MECHANISMS IN MIDFACE DEVELOPMENT AND DYSMORPHOLOGY

ESRA DENIZ CAMCI

A dissertation
submitted in partial fulfillment
of the requirements for the degree of

Doctor of Philosophy

University of Washington
2016

READING COMMITTEE
Timothy C. Cox, Chair
Susan W. Herring
Michael L. Cunningham
Carrie L. Heike

Program Authorized to Offer Degree:
Oral Biology

University of Washington

Abstract

Mechanisms in Midface Development and Dysmorphology
Esra Deniz Camci

Chair of the Supervisory Committee: Timothy C. Cox
Research Professor of Pediatrics,
University of Washington
and
Laurel Endowed Chair in Craniofacial Research,
Center for Developmental Biology and Regenerative Medicine,
Seattle Children's Research Institute

Craniofacial asymmetry and dysmorphology in the *sbse* mutant mouse resembles the spectrum of anomalies associated with branchial arch disorders in human patients. Although relatively common, little is known about their etiology. Such disorders are characterized by mid- and lateral facial malformations, and are typically thought to be the result of a genetic or epigenetic events or insults during embryogenesis. In the mutant *sbse*, variable midface asymmetry appears in concert with ectopic suture and synchondrosis fusion, postcranial defects, and ipsilateral ear phenotypes, within the first month after birth. In mutants, a rearrangement on Chromosome 4 disrupts the gene encoding Pleomorphic adenoma gene 1 (*Plag1*), a transcription factor associated with salivary gland tumor development. In this dissertation, I tested the role of *Plag1* deficiency in the development of midface dysmorphology, and investigated the effect of the *sbse* mutation on embryonic gene expression.

Dedicated to my parents, Esin and Cengiz Camcı,
my aunt, Gülin Ilikcik
and to the memory of Nevber Aki Ilikcik,
Emine Pakize Çakmakaya Camcı and Orhan Celalettin Camcı.

INSTITUTIONAL ACKNOWLEDGMENTS

I would like to sincerely thank my supervisor, **Tim Cox**, and the members of my committee, **Sue Herring**, **Kathy Rafferty**, **Michael Cunningham** and **Carrie Heike**. It is difficult to express how much I appreciate your guidance and support during my time at the UW and SCRI.

I was fortunate to work with my colleagues in **the Cox, Cunningham, and Herring labs**, including Christine Clarke, Emily Chu, Vincent Fok, Tina Fu, Negar Homayounfar, Mohamed Hasan, Yongzhao Huang, Cathy Koto, Matt Lacourse, Wenjie Li, Murat Maga, Monica Parada-Sanchez, Sara Parent, Sarah Park, Sara Rolfe, Jessica Rosin, Basma Tamasas, Kai Yu, Karen Zemplenyi, and especially **Sid Vora**.

I am grateful for the support of the following:

At the **University of Washington**, the program in Oral Biology (Jennifer Kohn, Kathy Hobson and Richard Presland) and the Department of Oral Health Sciences (Kseniya Saava, Mary Beth Cunningham, Eileen Kakida and Doug Ramsay) as well as the Oral Health Sciences training grant.

At **Seattle Children's Research Institute**, the Center for Developmental Biology and Regenerative Medicine (Wendy Kramer, Ellen Coyle, Andrew Timms, and David Beier), the Craniofacial Center (Jerrie Bishop), the Office of Animal Care (Brandon Ng and Maia Chan), Information Services, and Eugenia Thomas.

Thanks to Carol Schuurmans and Lata Adnani for providing the *Plag1*-null mice.

This work was supported by the UW Top Scholar Award, NIH R01-DE022561 and T90-DE021984-02.

PERSONAL ACKNOWLEDGMENTS

I'd like to acknowledge everyone who supported throughout this project, particularly Ed Lee-Eng, for hearing "I should be done today" so many times; Eric Driscoll, for 12 years of sage counsel; Tessa Folino, because the stars look very different today, Emily Chu and Sarah Park, for all the laughter; Julie Ho, because a circle has no beginning; Nadia Bahrami, for 36 degrees and dancing through Sunday; Mackenzie Krause because they move in herds; Anna Lindsay, Krista Geister, Seungshin Ha, Jennifer Gustafson, and Kristina Bernardi for the positivity; Jabier Gallego and Chris Brewer for the negativity; Alisha Mendonsa for running up that hill.

Most of all, I'd like to thank my parents, Esin and Cengiz Camcı, and my aunt, Gülin Ilikcik for their love, encouragement, sense of humor, and patience.

★

CONTENTS

LIST OF FIGURES

LIST OF TABLES

INTRODUCTION

1

LITERATURE REVIEW

The skull has been an object of interest for generations of scientists, clinicians, philosophers, and artists. Our brains are so attuned to the stereotypic facial pattern - two eye above a mouth - that we begin to "see" faces in inanimate objects or meaningless noise around eight months of age.[1] The symmetry and relative neoteny of a stranger's face influences how we perceive their personalities, and influences their quality of life.[2,3] Children with mixed craniofacial conditions were found to be more inhibited, depressed, anxious, and less socially adept, compared to a normative group. The authors suggest that these traits may be the result of personal dissatisfaction with, and bullying due to, their appearance and speech impediments, or having had repeated hospitalizations.[4,5] Unfortunately, some pediatric craniofacial malformations predict higher hospital use and medical spending before age 2, and are associated with more mortality risks over a lifetime than faced by unaffected controls.[6–9] Craniofacial dysmorphology may have significant social, functional, and medical significance.

CONGENITAL CRANIOFACIAL DYSMORPHOLOGY

Craniofacial malformations are present in a third of all children born with birth defects, and is associated with factors including heavy maternal consumption of alco-

hol, tobacco use, and use of teratogenic medications.[10] Fetal exposure to these common risk factors has been modeled in animal systems; the results of these studies highlight the significance of the cranial neural crest, a population of cells sometimes called the "fourth germ layer", to typical craniofacial development.[11–17] A more comprehensive understanding of embryonic development has allowed clinicians to offer evidence-based recommendations to patients.[18–20] Significant strides have been made towards recognizing the environmental causes of many preventable birth defects, however, many craniofacial conditions are caused by inherited or spontaneous mutations in the genome. The high degree of evolutionary conservation between the human and mouse genomes has made the latter a significant tool in study of typical and atypical development. The differences in the shape and size of the human and mouse skulls reflect the ≈96 million years since the divergence of the lineages.[21–24] Many of the genetic mechanisms contributing to craniofacial developmental are retained in both species, and regulate the developmental of functionally homologous bones from homologous embryonic tissues. A mutation causing a craniofacial malformation in a human can thus be studied in a mouse.

Tissue development may be disrupted directly by genetic or epigenetic insults, or indirectly due to the integration and inter-dependence of cranioskeletal tissues. Real life craniofacial conditions are rarely restricted to a single tissue, or to a single region. For example, midface and axial skeletal abnormalities are associated with different types of craniosynostosis, a relatively large group of conditions associated with premature calvarial suture fusion. Thorogood put forth a useful template for thinking about dysmorphology, focusing on six broad classes of physical defects that may cause changes in the topology of the embryonic face.[25]

- **Forebrain/frontonasal mass defects** Embryonic exposure to ethanol during neural crest cell migration causes defects in midline forebrain-derived structures.[26]

- **Epithelial fusion defects** A mutation affecting *Wnt9b* in the A/WySn inbred line predisposes them to cleft lip with or without cleft palate *Wnt9b* inhibits degradation of a transcriptional coactivator in the cells of the epithelial seam between the medial and lateral nasal processes, and may regulate lip fusion.[27,28]
- **Skeletal dysplasia** Craniofacial malformations in the *achondroplasic* (*an/an*) mutant are likely to be a result of reduced cellular proliferation at the cranial base synchondroses, nasal septal cartilage, and condylar cartilage.[29]
- **Disruption/deformation** Unilateral facial nerve ablation in rabbits resulted in ipsilateral bony deficiency and subsequent maxillary and mandibular asymmetry.[30]
- **Vascular crisis defects** Conditional knockout of *Vegfa* in the neural crest results in reduced vessel density in branchial arch 1, chondrocyte proliferation in Meckel's cartilage and atrophy of the mandibular artery. By E17.5, the mutant mandible and maxillae are hypoplastic.[31]
- **Branchial arch defects** Injection of the folic acid antagonist triazene into pregnant dams at E10.5 produced variably sized uni- or bilateral hemorrhages over the angle of the mandible at day 14, and progressive micrognathia and external ear defects from days 15-17, as well as defects in the bony parts of orbits in 100% of animals.[32]

A number of conditions are typically associated with malformations in the mid- and lateral facial structures, including Craniofacial Microsomia (CFM), Oculo-Auriculo-Vertebral Spectrum (OAVS), Hemifacial Microsomia, Goldenhar Syndrome, and Otomandibular Dystosis.[33–35] These conditions are highly variable in terms of severity, sidedness (symmetry/asymmetry), and etiology. The facial tissues affected are derived from the embryonic branchial arches, transient structures which are visible to the naked eye in mice around embryonic day (E)10.5, although postcranial defects are commonly observed.[35,36]

> *"The first and second branchial arch syndrome is made up of a constellation of congenitally malformed structures which arise from the embryonic first and second branchial arches, the intervening first pharyngeal pouch and first branchial cleft, and the primordia of the temporal bone. In its fullest expression, a patient with this syndrome would exhibit unilateral or occasionally bilateral underdevelopment of the external ear, middle ear, mandible, zygoma, maxilla, temporal bone, facial muscles, muscles of mastication, palatal muscles, tongue, and parotid gland, as*

> *well as macrostomia and a first branchial cleft sinus. Frequently, however, the complete syndrome is not fully expressed."* (W.C. Grabb, 1965[37])

With an estimated prevalence between 1:3000 and 1:5000 live births, Craniofacial Microsomia is one of the most commonly treated condition treated at most Craniofacial Centers, and is associated with a substantial health burden.[37–39] Many patients with CFM and similar conditions undergo multiple screening evaluations and surgical interventions throughout childhood to address the impacts of the primary anomalies, which can include hearing impairment, upper airway obstruction, altered speech, and difficulty with feeding. Surgical and other treatment outcomes vary widely.[35,40,41] A case for a heritable genetic etiology can be made in light of reported chromosomal aberrations in patients as well as the small proportion of the population showing distinct familial transmission.[42–48] Mid- and lateral facial dysmorphology in these conditions is variable in appearance and phenotype, may be associated with a number of different postcranial abnormalities, and is thought to be etiologically heterogenous. The idea that the spatial restriction of these malformations was related to a specific sensitivity of the embryonic facial primordia was articulated by the concept of the developmental field,[1] although the utility of that model is limited both by its broadness, and the fact that variable postcranial defects are frequently observed in patients. Mutations in genes with a variety of functionalities are known to affect the development of both branchial arch derivatives and a variety of postcranial structures.[50–53] More basic science research addressing the causes and development of congenital and spontaneous mid- and lateral facial dysmorphology is necessary, given the significant functional impact it may cause, as well as the frequency at which it occurs in patient populations.

1

> *"'Given that a specific malformation is demonstrated to occur as two or more causally different traits, then a developmental field defect has been defined in the sense of a dysmorphogenetically reactive unit, i.e., a set of embryonic primordia that reacted identically to different dysmorphogenetic causes. It then follows that these primordia must also constitute a morphogenetically reactive unit under normal circumstances.'"* (Optiz, 1985[49])

EMBRYONIC CRANIOFACIAL DEVELOPMENT

The conservation of embryonic spatial and temporal gene expression patterns between species has made mouse models a major tool to study both typical and atypical human craniofacial development.[54] At mouse embryonic day 10.5, the presumptive facial primordia, including the branchial arches, are visible to the naked eye. At the dorsal surface of the embryo, a population of ectodermally-derived cells at the segmented neural plate undergo an epithelial to mesenchymal transition, becoming cranial neural crest cells (CNCC), a vertebrate-defining cell population.[23] . This population, the "fourth germ layer", migrates into the branchial arches, having already acquired axial-level identities. Evolutionary conservation implies that homologous mechanisms control the development of homologous structures - in a recent model concerning jawed vertebrates, morphogen gradients are proposed to define quadrants of mandibular and maxillary outgrowth. The morphogen in question is a transcription factor and putative chromatin binding protein, SAT2B, which emanates towards the TMJ ("hinge") from the "caps" regions at the distal ends of BA1 and the frontonasal prominences. The authors suggest that conservation of this patterning mechanism produce jaws of different lengths in different species, extending and contracting the gradient field in a dose-dependent manner, and that *Sat2b* defines the jaw module (Placeholder for figure).

In the embryonic cranial base, aggregations of pre-chondrogenic cells differentiate into primary cartilages, some of which will form anlagen supporting endochondral ossification.[55,56] These tissues appear before, and are distinct from, secondary cartilages, which will form at the edges of intramembranously ossified bones.[57] The cells which produce and remodel bone, osteoblasts, are specialized matrix-forming fibroblasts; a second population, osteoclasts, resorb bone by dissolving the mineral matrix.

The activities of the cell populations determine the consistency of mineralized tisse throughout the body.. Intramembranous ossification occurs in the facial and calvarial regions by the aggregation of pre-osteogenic mesenchymal cells.[58,59] Notably, both the cartilage anlage and mesenchyme cell condensations remain avascular until just prior to ossification.[60] Mineralization results from differentiation and subsequent activity of osteoblasts in these precursor tissues, starting around E12.5 in the murine face and calvaria[61]

Simultaneously, the major cranial nerves and blood vessels develop, either from neural crest-derived mesenchyme, or from mesodermal cells influenced by neural crest-specific expression of vasculogenic growth factors.[31] One vessel arises, sequentially, from each branchial arch, between E8 and E13.5, and undergoes significant remodeling before it achieves its mature form. Craniofacial and endocranial vasculature arises from the first two branchial arches, eventually forming a dense network of vessels in the adult skull (Appendix A.11 and A.11).[62] Disruption to the formation or remodeling of the major branchial arch-derived vessels can have significant consequences for jaw extension.[63]

ETIOLOGY OF MID- AND LATERAL FACIAL DYSMORPHOLOGY

There are a number of theories regarding the development of hypoplastic, variably asymmetric mid- and lateral facial morphology.

The most popular theory rests on the work done by David Poswillo, using the folate antagonist triazene to induce hemorrhages over the remodeling stapedial artery in the second branchial arch. Embryonic vascular development from angioblasts in the

mesoderm; as the vascular network grows, it is continually remodeled by the creation of new vessels and the regression of pre-existing ones, a process which occurs around E9.5 through E11.5 in the mouse head (around the 6th week in humans). Poswillo hypothesized that craniovasculature is more sensitive to insult while it is remodeling, and that the result of such an insult would be localized hypoxia and/or necrosis sufficient to affect symmetrical growth.[32,64] Others have extended this theory to include genetic susceptibilities that predispose the BA tissues to more subtle loss of endothelial cell integrity or retardation of vessel development, secondary to a deficiency in neural crest mesenchyme that supplies the factors promoting vascular growth, such as *Vegfa*.[31,65] The extent and position of hemorrhage and subsequent disruption could explain observed inter-individual variability.greater involvement of facial structures, including the masticatory muscles, was seen. Such damage to cells is thought to lead to a local reduction in proliferation and/or necrosis, or adaptive functional changes that impact the symmetric development of both skeletal and non-skeletal elements of the face. The extent and position of disruption is could explain observed inter-individual variability. Additional support comes from observations of the impact of vasoactive drug use and the occurrence of vascular events in early pregnancy, as well as maternal diabetes (associated with circulation problems in severe cases) all of which increase the odds of having a child with facial asymmetry.[66,67], The significant increase in the incidence of branchial arch anomalies in populations living at high altitude (i.e. low oxygen) has also been interpreted as supportive of a vascular crisis etiology.[68] Because surgical damage to the first arch-derived Meckel's cartilage in the chick model system is sufficient to induce asymmetric beak formation, midface dysmorphology has been proposed to be a result of defects in early auriculofacial cartilages.[69,70] Clinical evidence showing deficiency in the muscles of mastication also exists.[71] A wide variety of chemical, physical, and genetic insults to facial primordia have been proposed to

cause of midface dysmorphology.

POSTNATAL CRANIOFACIAL DEVELOPMENT

Most theories concerning the etiology of congenital mid- and lateral facial dysmorphology focus on embryonic causes. The basic pattern of the adult cranioskeleton is established *in utero*, and is necessary but not sufficient for normal development: simple expansion would not produce mature cranioskeletal morphology on its own. Postnatal growth patterns - "geometric changes in morphology due to growth" - are responsible for the changes in size, shape, and arrangement that result in the adult skull.[72] Changes to the size and shape of the skull proceed with a considerable degree of synchronicity to maintain the function of the brain, sensory organs, airways, and oral cavity.[73] According to Donald Enlow, overall growth in the skull is imbalanced. For example, the resorptive field at the anterior midfacial region balances the deposition on the posterior and superior surfaces of the maxilla. Together, these processes enable the jaw to gain vertical height without developing a prognathic profile.[74] Melvin Moss, in a later refinement of his Functional Matrix hypothesis, discusses how epigenetic factors, specifically, mechanical loading, may affect local gene expression, recruitment of osteoblasts, and subsequent remodeling of bone.[75] Cranioskeletal morphology is the cumulative product of the genetic programs underlying embryonic development, epigenetic factors that might affect early patterning and development, genetic programs involved in postnatal physiology and function, and epigenetic factors that may arise after birth.

Bone is a living tissue, containing embedded networks of mechanosensory osteocytes, blood vessels, and nerves. Its functionality is determined, in part, by the tissues

surrounding it. The osteogenic fronts of intramembranous bones in the calvaria are separated by sutural mesenchyme and collagen fibers, overlain by periosteum resting on top of dura mater.[76–79] Within the cranial base and vertebrae, bones are connected by cartilaginous synchondroses. Premature loss of either sutural or cartilaginous growth sites is associated with dysmorphology in mouse models.

Craniofacial sutures are fibrous joints which are permissive to both motion and growth at their bony margins. Removing the active coronal suture tissue in New Zealand white rabbits (*Oryctolagus cuniculus*) ultimately did not affected anterior-posterior length, suggesting that they function as semi-mobile synathrotic joints and expansion sites, but have no intrinsic growth potential.[73,80,81] Experimental surgical obliteration of rabbit coronal sutures affects the shape of the midface, although it doesn't always cause hypoplasia.[82,83] Maxillary retrognathia was found 2 years after surgical obliteration of the temperozygomatic, sphenofrontal + temperozygomatic, sphenofrontal, palatomaxillary, vomerobasillary + pterygopalatine, and sphenooccipital + pterygopalatine + pterygomaxillary sutures of juvenile Chacma baboons (*Papio ursinus*). Although sample sizes were extremely low, these finding that loss of the ability to expand at facial sutures may affect midface outgrowth.[84] Sutures function as semi-mobile synathrotic joints and expansion sites, but have no intrinsic growth potential, i.e., premature or otherwise ectopic fusion might affect normal midface outgrowth, but cannot cause it.

Histologically, the synchondroses in the skull resemble bipolar growth plates, and are thought to drive anterior-posterior expansion in the cranial base.[73] Experimental fixation of the sphenooccipital synchondrosis (SOS) in rats resulted in a shortening of the anterior-posterior length of the skull in general, and the cranial base in particular. They noted an increased curvature of the cranium, consistent with the appearance of

many mouse models, but did not comment on the face.[85] Fixation of the SOS in rabbits resulted in a shortening of the face and reduced basal-maxillary and total cranial base angles, as well as a marked flattening of the cranial base. The authors of that study propose a model in which cranial base fixation creates a pivot point around the SOS, shortening of the anterior cranial base and decreasing upward facial projection.[83] (Interestingly, an early reduction in sphenoid length in human evolution is thought to have decreased facial projection in the human skulls.[86]) Midface phenotypes in mouse models with premature synchondrosis ossifications are sometimes attributed solely to the shortened cranial base. In one mutant line, *Brachyrrhine* (*Br*), cranial base and midface defects are typically attributed to defects in the presphenoid and surrounding synchondroses. Reports conflict about the state of the nasal septal cartilage in these mice, but at least one paper states that it is completely absent.[87]

The nasal septal cartilage is a remnant of the embryonic trabecular cartilage.[56,88] Recent work supports a role for it in the normal growth of the midface.[89] In a case report involving a set of monozygotic twins, early trauma to the nasal septum was thought to cause underdevelopment of the middle third of the nose and maxilla.[90] Dissection of this tissue has been shown to reduce midfacial growth, although it has been suggested that the cartilage is a passive participant in growth.[91,92] Later evidence to the contrary suggests that it has intrinsic growth potential: *in vitro*, the nasal septal cartilage of rats maintains its shape as it expands in the (anatomical) anterior-posterior dimensions.[93] In juvenile mice, the septum resembles a synchondrosis at its ethmoidal and presphenoidal surfaces, both histologically and in its rate of mineralization, and increases in size expansion is thought through interstitial growth.[94] These findings suggest that the nasal septal cartilage may play a major role in midface growth, and that congenital midface hypoplasia may occur as a result of reduced growth in this structure.

MODELS WITH MIDFACE ASYMMETRY

Several mouse models with heritable BA-related syndrome-like phenotypes have been reported in the literature, although little has been done to characterize the molecular mechanisms causing their malformations. An interesting distinction exists between these strains that may speak to diverse causes: their facial asymmetry appears either before birth (*Hfm* and *643*)[95,96], or after 2 weeks(*Far* and *Mb*)[97,98]. Mice from the *643* line are reported to develop asymmetric deformation of the maxilla and microtia following some embryological event resulting in hypoplasia of the second branchial arch at E9 and E10, malformation of the auricular hillocks, as well as transient hemorrhages observed to occur over the region.[96] A second line with similar defects is caused by a transgenic insertion on Chromosome 10, and is named *Hemifacial Microsomia* (*Hfm*). Defects are apparent by E9, which the authors propose is associated with embryonic defects of auriculofacial cartilages.[95] Another insertional mutation with a midface phenotype affects a regulatory region upstream of the transcription factor, *Zic family member 3* (*Zic3*); apparent up-regulation results in facial asymmetry, asymmetric and low set ears, as well as defects in the cricoid and hyoid cartilages. Interestingly, both these strains have lateral facial defects, including microtia, and no major mandibular asymmetry. Unlike *643* and *Hfm*, the deviation in the snout of the *Far* and *Mb* strains appears at least two weeks after birth. Unilateral premaxillary-maxillary suture fusion appears to be causative to asymmetry seen in the *First Arch* (*Far*) mutant, although the phenotype appears to cause defects in all the bones derived from the first arch. (Crossing out the BALB/cGaBc-far mutation onto a ICR/Bc inbred background resulted in a phenotypic shift from recessive to dominant, and an increased incidence of facial asymmetry in heterozygotes.)[98,99] The postnatal appearance of facial asymmetry is also a feature of the *Maxillary Bending* (*Mb*) strain, whose asymmetric phenotype is apparent two or more weeks after birth. *Mb* asymmetry is reported to be due to asymmetric shorten-

ing of the maxilla on the side of the fused premaxillary-maxillary suture.[97] Finally, a line with with low set ears, called *Low set ears* (*Lse*) was reported in 1986.[100] These models support the hypothesis that dysmorphology and asymmetry may be caused by many different mechanisms. In this dissertation, I focused on a mutant mouse, *small body, small ears* (*sbse*), which carries a mutation on Chromosome 4 causing significant mid- and lateral facial dysmorphology and asymmetry. The *sbse* mutant has several significant craniofacial and postcranial features in common with human conditions like Craniofacial Microsomia, Hemifacial Microsomia, and Oculo-Auriculo-Vertebral Spectrum (OAVS). Understanding the genetic, developmental, and postnatal developmental patterns of a single model may shed light on the factors regulating typical and atypical mid- and lateral facial morphogenesis.

2

MATERIALS AND METHODS

2.1 ANIMAL CARE AND USE

All animal-related work was carried out at Seattle Children's Research Institute (SCRI) in compliance with USDA guidelines under the oversight of the Office of Animal Care, following a protocol approved by the SCRI Institutional Animal Care and Usage Committee (IACUC; IACUC 13319). Mice were housed at standard temperature (22.8 $\pm$ 3° C) and humidity (30% $\pm$ 5%), with 12 hour light cycles. Water and pelleted chow (Pico Rodent Diet 20-5053) were provided *ad libitum*; breeding pairs were maintained on high fat, low carbohydrate diet (Pico Rodent Diet 20-5058). Litters were weaned onto the standard chow on or after postnatal day 21. Euthanasia was carried out in accordance with American Veterinary Medicine Association guidelines.[101] Mice were sacrificed via overdose of an inhalent agent, followed by a secondary exposure in CO_2-filled bag; primary exposure to gas was extended to 30 minutes for animals under P10. After secondary euthanasia of the dam, dissection of embryonic litters proceeded in ice-cold Phosphate-Buffered Saline (PBS). Embryonic age was calculated from the date the copulatory plug was observed; cervical dislocation or decapitation were used as a form of secondary euthanasia for pups over E15.

2.1.0.1 *Mutant mouse lines*

Three distinct lines of inbred mutant mice were required for this work. "*small body and small ear*" (*sbse*) [1] and "*froggy*" (*frg*) were obtained from the Jackson Laboratories (Bar Harbor, ME; JAX) in 2010 during the course of a project entitled "Genetic and developmental pathways causing midface hypoplasia" (NIH/NIDCR R01 DE022561 PI: T.C. Cox); colonies were initially established by M.G. Hasan and S.S. Park. I assumed responsibility for them, under the supervision of S.S. Park, and later S.R. Vora, in early 2013. While under my care, breeders from both lines were incrossed to background-matched wildtype C57BL/6J or A/J mice (obtained directly from JAX) with no notable effect on phenotype. *Plag1*-null mice (*tm1Wjmv*) were generously provided by Carol Schuurmans, currently at the University of Toronto (Table 2.1).[2]

OUTCROSSES F1 litters born to mixed genotype breeding pairs were sacrificed at P28 for 3D imaging, or dissected at embryonic stages for X-gal staining. Inbred mutant mouse lines and their derivative outcrosses are summarized in Table 2.1.

2.2 GENOTYPING AND GENE EXPRESSION

Sequence analysis and structural diagram rendering was done primarily using the Geneious v.7.1.7 software package (http://www.geneious.com). Wildtype reference sequences (*Mus musculus* strain C57BL/6J) were downloaded from National Center

1 *small body and small ear*, s.v. *small body and short ear pinna* through (at least) May 9th, 2011 on the associated JAX data sheet (004246).

2 Mice carrying the transgenic *Plag1*^{tm1Wjmv} (null) allele were generated by the laboratory of Wim J.M. Van de Ven at the University of Leuven and Flanders, c. 2004.[104] Ablation of gene expression in homozygotes is a result of a knock-in mutation at the start site of *Plag1*, which also places expression of a functional copy of the reporter gene β-*galactosidase* (*lacZ*) under the control of the *Plag1* promoter.

for Biotechnology Information (NCBI) RefSeq.[105] The Mouse Genome Browser at the University of California, Santa Cruz (UCSC) was used to explore data mapped to the mm9 (July 2007) build of the C57BL/6J wildtype mouse genome.[106,107]

2.2.0.1 *Genotyping*

PCR Polymerase chain reaction (PCR) was used to amplify regions of DNA for genotyping and other purposes. All endpoint PCR was carried out in an PTC-200 DNA-Engine Peltier Thermal Cycler (MJ Research/BioRad). Oligonucleotide primer pairs for all PCR applications were designed to fit standard criteria by E.D. Camci or T.C. Cox and synthesized by Thermo Fisher Scientific. Reaction products were separated by electrophoresis (0.5 μg/ml ethidium bromide in a 1.0-1.5% agarose gel, run at 110-160 mV in sodium borate buffer) and visualized under a UV lamp.

GENOTYPING Primer pairs for genotyping were designed to amplify across breakpoints in the *sbse* inversion and *Plag1*-null (*tm1Wjmv*) recombination sites in genomic DNA; sequences are listed in Table 2.2. Protocols, conditions, and expected band sizes are detailed in Appendix B.

sbse T.C. Cox and collaborators characterized the *sbse* mutation in 2010, working with J. Shendure and M. Kircher and M.G. Hasan. I used PCR to test and ultimately validate their findings, under the supervision of T.C. Cox and K Yu.

frg The Donahue group at the JAX mapped the *frg* mutation to a site between microsatellite markers D13Mit88 and D13Mit248 of mouse chromosome 13. Sequence from WGS was mapped to the July 2007 (mm9) assembly - based on the genome

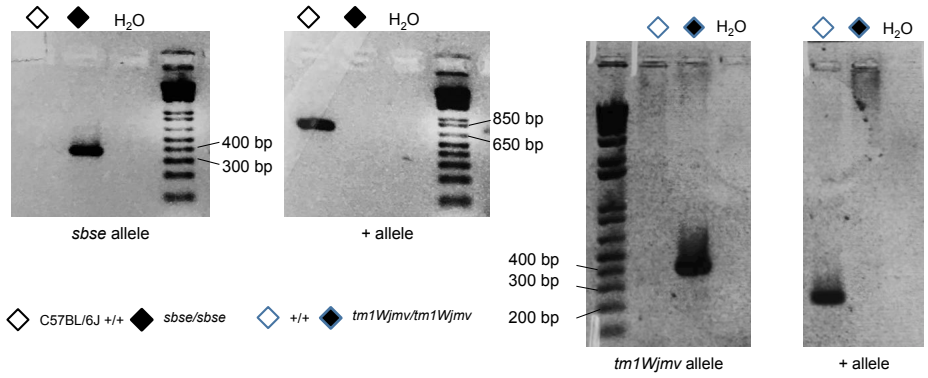

(a) *sbse* **(b)** *tm1Wjmv* (*Plag1*-null)

Figure 2.1: PCR genotyping of *sbse* and *Plag1*-null mice. PCR is used to amplify fragments of the gene *Plag1*; the size of the amplified fragment indicates the alleles present. Expected band sizes: (**a**) *sbse* mutant: 350 bp, wildtype: 700 bp. (**b**) *tm1Wjmv* (*Plag1*-null), *LacZ* knock-in) mutant: 400 bp, wildtype: 270 bp.

of C57BL/6J - of the mouse reference genome.[108] Sequence polymorphisms in two genes were validated using endpoint PCR, at which time the background-matched A/J reference sequence became available (Table 2.3). The attempt to identify the *frg* mutation is detailed in Chapter 4.

sry Embryonic sex was determined by primers amplifying a fragment of the Y chromosome (*Sry*).

2.2.0.2 *Gene expression*

Table 2.1: Mutant mouse lines used in this study

INBRED MUTANTS	
sbse[102]	*"Small body and small ear"*
	Background: C57BL/6J MGI ID: 3758822 JAX ID: 004246 Mutants arose at the JAX c. 2001. A colony was established at SCRI in 2010. Incrossed with wildtype C57BL/6J in 2013 and 2015, outcrossed with *froggy* mutants in 2015 (*sf*). Coat color: Black
frg[103]	*"Froggy"*
	Background: A/J MGI ID: 3767190 JAX ID: 003485 Mutants arose at the JAX c. 1992. A colony was established at SCRI in 2010. Incrossed with wildtype A/J in 2013 and 2015, outcrossed with *sbse* mutants in 2015 (*sf*). Coat color: White, red eyes
Plag1-null[104]	*"Pleomorphic adenoma gene 1; targeted mutation 1, Wim J.M. Van de Ven"*
	Background: S1Sv-129X1/SvJ-Swiss Webster MGI ID: 3580633129 JAX ID: N/A Mutants were created c. 2004 in the lab of W.J.M. Van de Ven. A colony was established at SCRI in 2015 with mice generously provided by Carol Schuurmans. Outcrossed with *sbse* mutants in 2015 (*sk*). Coat color: White, black eyes

OUTCROSSED/DOUBLE MUTANTS	
sf F1	*"Small body and small ear"* × *"Froggy"*
	Background: 50% C57BL/6J/ 50% A/J Coat color: Agouti
sk F1	*"Small body and small ear"* × *"Plag1*-null"
	Background: 50% C57BL/6J / 50% S1Sv-129X1/SvJ-Swiss Webster Coat color: Mixed white, agouti, black

Table 2.2: Primers designed for *sbse* and *Plag1*-null genotyping.

ALLELE		SEQUENCE 5′ TO 3′	SIZE
sbse mutant	*Plag1* genoR	CACTGCCAATTCTCTGGGTAAATGGG	350 bp
	Plag1 geno1	CAGGACACACTCTTGTGCTTTACATACG	
sbse wildtype	*Plag1* geno2	CCACATTGTCCAGAGTGGTAGGAGGC	700 bp
	Plag1 geno3	GCCTTCATGACCTTTTGGCAATGCTC	
tm1Wjmv mutant	*Plag1*-MT-F	CAGTTCCCAGGTGTCCAACAAG	400 bp
	Plag1-MT-R	AATGTGAGCGAGTAACAACCCG	
tm1Wjmv wildtype	*Plag1*-WT-F	CGGAAAGACCATCTGAAGAATCAC	270 bp
	Plag1-WT-R	CGTTCGCAGTGCTCACATTG	

Table 2.3: Primers designed to test *frg* polymorphisms.

ALLELE		SEQUENCE 5′ TO 3′	SIZE
Sema4d del	*Sema4d*-1	CTCTGGCTATCAGGCTATTGAAACAATGGACC	211 bp
	Sema4d-2	GGTCCACATGCTAAGCTGTCCAGGTCACGTG	
Sema4d	*Sema4d*-1	CTCTGGCTATCAGGCTATTGAAACAATGGACC	37 kb
	Sema4d-4	CTCTTGCTTCTTGGTCATGATGTTTGTGCAGG	
Kif13a	*Kif13a*-r1	GATTCAGGTGAAGAGAGTCGTG	755 bp
	Kif13a-f1	CTGCCCAAGGAACACGGCAGTC	

Table 2.4: Primers designed for quantitative real-time PCR

GENE		SEQUENCE 5′ TO 3′	SIZE	COVERAGE
Barx1	*mBarx1*-f	GGAGTCGCACCGTATTCACT	180 bp	E2-3-4
	mBarx1-r	GCCACCTTGCAGCACTATTT		
Chchd7	*mChchd7*-r	GAGATCCTGACATAAACCCTTGC	230 bp	E3-4-5
	mChchd7-f	GTAGGGCATCTTTTGCATTGCTC		
Crabp2	*mCrabp2*-f	CACGGAGATTAACTTCAAGATCGGGGAG	194 bp	E2-3-4
	mCrabp2-r	CTGTCATTGTCAGGATCAGCTCTCCATC		
Edn1	*mEdn1*-f	GTCAGTGCGCTCACCAAAAA	190 bp	E3-4-5
	mEdn1-r	TGGCCTCCAACCTTCGTAGT		
Efnb1	*mEfnb1*-f	CACCCGCACTATGAAGATCGTTATGAAG	191 bp	E3-4-5
	mEfnb1-r	CACTCTTCTCTTCCTGGTTCACAGTCTC		
Hivep1	*mHivep1*-f	CAGCTGGAAACCCTGCC	130 bp	E8-9
	mHivep1-r	GGGTGAGGTGAGACTGAGG		
Igf2	*mIgf2*-f	GATACCCTAAAGAAGCAGAAGAGACGCC	250 bp	E2-3
	mIgf2-r	AGAGATGAGAAGCACCAACATCGACTTC		
Jarid2	*mJarid2*-f	ATCACCATGGATGAGCTCCC	140 bp	E8-9
	mJarid2-r	CGCAGCATGTCTGCTAGTTTG		
Mos	*mMos*-F1	CTGTGTCGCTACCTCCCTC	230 bp	
	mMos-R1	ACCGTGGTAAGTGGCTTTATACA		
Omd	*mOmd*-f	AGAACTCAACGTTGGACACAAT	165 bp	E3-4
	mOmd-r	GGTCCACACGAAGGTATGTT		
Ogn	*mOgn*-f	ACGACCTGGAATCTGTGCCT	130 bp	E6-7
	mOgn-r	ATTCGCTCCCGAATGTAACGA		
Penk	*mPenk*-F1	GGACTGCGCTAAATGCAGCTA	247 bp	
	mPenk-R1	GAAGCCTCCGTACCGTTTCAT		
Pgf	*mPgf*-f	CTTGGATGAATACCCTGATGAGGTGTCTC	280 bp	E3-4-5-6
	mPgf-r	GTTTCTACTCCTCTTCCTCTTCCCCTTG		
Phactr1	*Phactr1*-f	GGCCCACAGTGGAAGAACTC	130 bp	E2
	Phactr1-r	TTGTCTGCAGCGGTGAGG		
Plag1	*mPlag1*-f	GGAGAGAGGCCCTACAAGTGCAC	175 bp	E4-5
	mPlag1-r	GGTCATGTGTATGGAGGTGATTC		
Sdr16c5	*mSdr16c5*-F2	TGGGAGCAGTGCTTGTTCTC	231 bp	
	mSdr16c5-R2	CATCTGGGCAGTCAAGGAAAT		
Sdr16c6	*mSdr16c6*-F1	ATGGAAACCTGTAGACTGGTCA	92 bp	
	mSdr16c6-R1	ACTCTGTAGACCTCTATCCTGCT		
Vegfa^{120}	*mVegfa*-f	GTGCAGGCTGCTGTAACGATGAAGC	190 bp	
	mVegfa120-r	CTTGGCTTGTCACATTTTTCTGGCTTTG		
Vegfa^{164}	*mVegfa164*-f	GAACAAAGCCAGAAAATCACTGTGAGCC	160 bp	
	mVegfa164-r	GGCTTGTCACATCTGCAAGTACGTTCG		

RNA EXTRACTION Embryonic litters from heterozygous crosses were dissected in ice-cold PBS at embryonic day 10.5. Whole embryo, whole head, or isolated branchial arch one and two tissue was snap-frozen on dry ice, and stored at -80°C. Genomic DNA was extracted from embryonic membrane or hindlimb tissue and used to determine the genotype and sex of all pups (Table 2.2 and Appendix B). Whole embryo and whole head RNA was isolated using the Maxwell 16 LEV Simply RNA Tissue kit (AS1280; Promega). Branchial arch RNA was isolated using the Qiagen RNeasy Mini Kit (74104; Qiagen). RNA concentration and purity was assessed with a Nanodrop UV-Vis spectrophotomer (Thermo Scientific); samples were rejected if $A_{260/280}$ ratios varied significantly from 2, or if nucleotide concentrations were low (Thermo Scientific). For branchial arch samples intended for RNAseq, RNA quality and concentration was assessed using the Agilent 2200 TapeStation system at the Genomics Core at Fred Hutchinson Cancer Research Center (Seattle, WA). All samples had a RIN greater than 8.

GENE EXPRESSION ANALYSIS cDNA for quantitative real-time PCR (qPCR) was generated at 50 ng/µl from isolated RNA using the High-Capacity cDNA Reverse Transcription Kit (Applied Biosciences/Thermo Fisher). *Holocytochrome C Synthase* (*Hccs*) was used as a housekeeping gene. Analysis of relative gene expression levels was carried out with the ABI 7500 Fast Real-Time PCR System (Applied Biosystems/Thermo Fisher) with SensiMix SYBRLow-ROX reagent (QT625-05; Bioline). Primers were designed by E.D. Camci or T.C. Cox and synthesized by Fisher Scientific; sequences are reported in Table 2.4.

RNASEQ Dissection and preparation of mouse branchial arch 2 tissue for RNAseq was carried out in parallel with J.M. Rosin, whose results I discuss in section 6. Branchial arches one and two were dissected separately following standard protocol and snap-frozen on the lids of PCR tubes before storage at -80°C; genotyping was carried out using embryonic membrane tissue. Genome-wide expression profilling was carried out using a total of 1 µg each of *sbse/sbse* and wildtype +/+ RNA, pooled from 3 pups of each genotype (333 ng of RNA from each individual, pooled). The samples were sent to the Genomic Services Lab at the Hudson Alpha Institute for Biotechnology (Huntsville, AL) for independant quality control and the preparation of indexed directional sequencing libraries ahead of Ribosomal Reduction RNA-seq. Samples were sequenced paired end with 250 million reads with an Illumina HiSeq v.4 PE100, and results were returned as FASTQ files. Andrew Timms (SCRI) used the Cufflinks software suite for transcriptome assembly and differential expression analysis of the mutant and wildtype data, the DESeq2 package to weight expression using count data, and the Integrative Genomics Viewer (IGV) to visualize sequences.[109,110] Results were returned to E.D. Camci and T.C. Cox for further analysis.Gene IDs and names were assigned according to records in the OMIM and MGI databases.[111,112]

Differentially expressed transcripts showing at least a $\log_2$ two-fold difference in expression between *sbse/sbse* and wildtype littermate samples were graphed using Plot.ly, a web-based tool well suited for visualization of large datasets (Montrèal, CA). The top 100 (Deseq-weighted) over- and under-expressed genes were subject to Gene Ontogeny (GO) analysis. Analysis was carried out using the Database for Annotation, Visualization and Integrated Discover (DAVID) v6.7, following the protocol described in Huang (2008) (https://david.ncifcrf.gov/).[113] Transcript IDs were mapped to known genes using the Official Gene Symbol tool. Functional classification and annotation were carried out using default analysis parameters. GO terms reported

were retrieved from the by the Gene Annotation Association functionality of the DAVID tool.

2.2.0.3 *Luciferase assay*

Reporter gene luminance in the luciferase assay is roughly proportional to mRNA expression. Using the Dual-Luciferase Reporter Assay system (Promega E1500), I tested the ability of the transcription factor *Plag1* to activate gene expression by binding to two putative *Vegfa*-regulatory regions containing its consensus binding motifs.

AMPLIFICATION OF THE *plag1* CDS The 1.5 kb *Plag1* protein coding region spans two exons. Amplification of this was attempted from embryonic wildtype mouse cDNA and genomic DNA, by both basic and and overlap extension PCR (OE-PCR). Primers designed to bind to the 3′ and 5′ ends of the predicted CDS did not amplify the expected 1.5 kb band; moving the forward primer 40 bp upstream of 5′, was also unsuccessful. Attempts were made to amplify the two regions of the CDS separately, from both cDNA and genomic DNA. Primers were designed to the 5′ end of exon 4 and the 3′ end of exon 5, with complementary tails to facilitate OE-PCR. Only the shorter fragment, covering first coding exon, was successfully amplified. After the failure of OE-PCR, we decided to move forward using a human PLAG1 ORF clone. Primer sequences are recorded in Table 2.5 and Figure 2.2; PCR was done using PrimeSTAR HS DNA polymerase reagent (Takara).

Table 2.5: Primers designed to amplify the *Plag1* CDS

ALLELE		SEQUENCE 5′ TO 3′	SIZE
Plag1 ORF	*mPlag1*ORF-f	ATGGCCACTGTCATTCCTGG	1.5 kb
	*mPlag1*ORF-r	CTACTGAAACGCCTGGTGGA	
Plag1 ORF 2	*mPlag1*ORF-f2	GCTGCGATGGCCACTGTCATTC	1.5 kb bp
	mPlag1ORF-r		
Plag1 OE-PCR	*mPlag1*OLr	GTAGCCATGTGCCTTTGTAATTTGTACTTAGAAACAAGGC	
		with ORF-f2	297 bp
Plag1 OE-PCR	*mPlag1*OLf	GTACAACTTACAAAGGCACATGGCTACTCCTCTCCTG	
		with ORF-r	1276 bp

Table 2.6: Primers designed to amplify putative *Plag1* binding sites upstream of *Vegfa*

Allele	Sequence ID	Sequence 5′ to 3′	Product	Restriction Site
Vegfa Fragment A	PuVA	TATCCATGGCGACTGGTCCGATGC	1 kb	*NcoI*
promoter insertion	PuVB	CTAAGGTACCTGGTTGGTCCCTCTCTTCC		*KpnI*
Vegfa Fragment A	MuVA	TTACTCGAGCGCGACTGGTCCGATGC	1kb	*XhoI*
MCS insertion	PuVB	CTAAGGTACCTGGTTGGTCCCTCTCTTCC		*KpnI*
Vegfa Fragment P	MuVP	AAGCTCGAGTCAGCCTTCCCTTAATCAACAGC	1kb	*XhoI*
MCS insertion	MuVR	GTGAGGTACCTAGTATTTGTCATCGCAACGAAAGG		*KpnI*

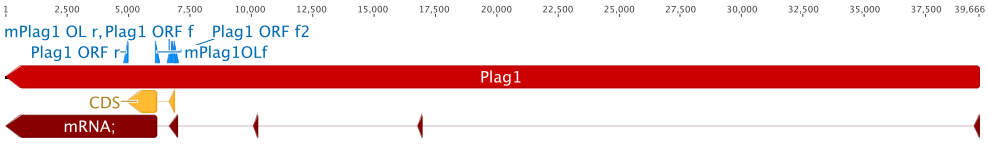

(a) Protein-coding sequence makes up a small fraction of the gene *Plag1*.

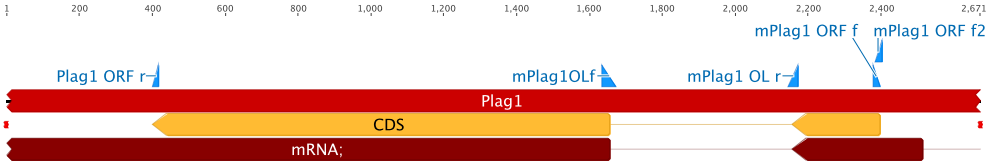

(b) Placement of primers designed to amplify the *Plag1* CDS Refer to Table 2.5.

Figure 2.2: Placement of primers designed to amplify the Plag1 CDS.

CONSTRUCTION OF THE PCDNA3.2/V5-PLAG1 EXPRESSION VECTOR A entry clone carrying the human PLAG1 sequence (pDONR221-hsPLAG1) was obtained from the DNASU plasmid repository (Tempe, AZ). Alignment of the reported insert sequence with the mouse mRNA sequence (XM 006538116.2 Mus musculus pleiomorphic adenoma gene 1 (*Plag1*), transcript variant X1, mRNA) found 90.4% identity over 1.5 kb of sequence. (Figure 2.3a) The PLAG1 fragment was transferred from the entry clone into the V5-tagged pDEST vector by the LR Clonase II reaction and propagated in homemade chemically competent TOP10 E. coli cells and SOC (Gateway Recombination Cloning system, Invitrogen/Thermo Fisher Scientific). Plasmid DNA was purified by spin miniprep (QIAprep Spin Miniprep Kit, Qiagen, 27104); restriction digests with FastDigest *Ndel* and *PvuII* (Thermo Scientific, FD0583 and FD0634) suggested that the PLAG1 sequence had been successfully ligated into the pcDNA3.2/V5 vector in both colonies (FastDigest Restriction enzymes, Thermo Scientific. Sequencing of the plasmid using CMVf and V5r primers confirmed the identity of the insert (Figure 2.3b).

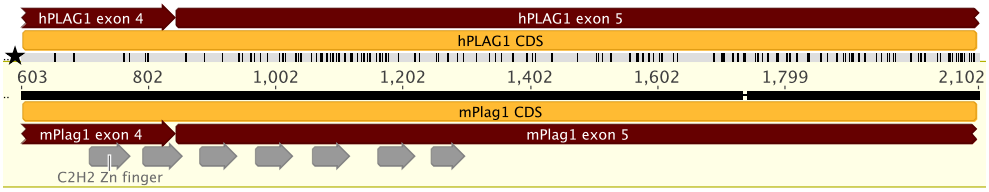

(a) Coding sequence sequence homology in human hPLAG1 and mouse *mPlag1*. Black star black lines indicate disagreements between human (top) and mouse (bottom) sequence; they are 90.4% homologous. **Gray**, DNA binding zinc finger motifs.

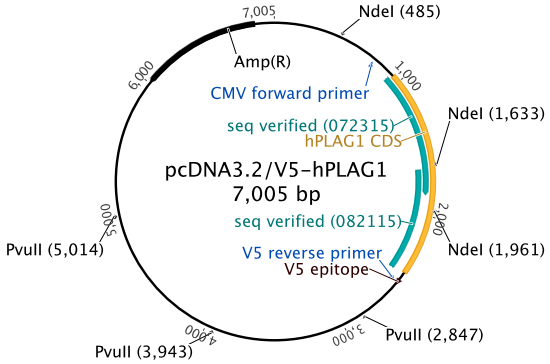

Plasmid map of the pcDNA3.2/V5-PLAG1 expression construct with *NdeI* and *PvuII* restriction sites. Yellow, hPLAG1 CDS. **Blue**, primers used to sequence insert. **Teal**, sequenced regions aligned with predicted insertion of hPLAG1. **Black**, Ampicillin resistance gene.

(b)

Figure 2.3: pcDNA3.2/V5-PLAG1 expression construct

IDENTIFICATION OF PUTATIVE *plag1* BINDING SITES Voz, et al. (2000) identified a consensus binding motif ($GRGGC(N)_{6-8}GGG$) in the promoters of PLAG1 target genes.[114] I used Geneious to find instances of this motif upstream of *Vegfa*. Two or three motifs were typically clustered together. Each motif was labeled alphabetically, starting 5′ to *Vegfa* (Figure 2.4a). Data available from the UCSC Genome Browser was used to assess the regulatory potential of the 16 identified regions of interest. Nucleotide conservation, histone modification, DNAse I hypersensitivity, and enhancer associated protein P300 binding sites in several embryonic cell types suggested that the sites are potentially functional. I selected Fragment A (within the *Vegfa* promoter, which covers *Plag1*-binding motifs A and B) and Fragment P (located 30 kb from the start site of *Vegfa*, covering motifs P, Q and R) for further analysis.[106,115–118]

AMPLIFICATION OF PUTATIVE *plag1* TARGET SEQUENCES The two regions of interest upstream of *Vegfa* were amplified from genomic DNA before cloning into the luciferase reporter vectors. Primers were designed to add directional restriction sites onto the amplified fragments. Table 2.6 lists primers and their restriction sites. PrimeSTAR HS DNA polymerase was used to amplify the sequences (Takara). Restriction digests were done with FastDigest *NcoI* (FD0573), *KpnI* (FD0524), and *XhoI* (FD0694) enzymes (Thermo Fisher Scientific. Cloning was carried out using T4 DNA ligase (Ambion). Plasmid DNA was purified by spin miniprep (QIAprep Spin Miniprep Kit, Qiagen, 27104); restriction digests with FastDigest *NdeI* and *PvuII* (Thermo Scientific, FD0583 and FD0634) suggested that the fragments has inserted into the plasmids per design.

CONSTRUCTION OF THE PGL4.23 LUCIFERASE REPORTER PLASMIDS Plasmids carrying reporter genes encoding different light-emitting enzymes are used to compare gene expression in the Dual-Luciferase Reporter Assay system (Promega). We selected constructs with low baseline expression levels, pRL-TK[*Rluc*] and pGL4.23[*luc2* minP]. The luciferase (*Rluc*) gene encoded by the pRL-TK vector (Promega) is derived from *Renilla reniformis* (sea pansy) and has weak constitutive expression; measurement of its luminance serves as an internal control. The sequences of interest were cloned into the pGL4.23[*luc2* minP] plasmid, which carries a luciferase gene *luc2* derived from *Photinus pyralis* (firefly), under the control of a minimal promoter.

Promoter construct The pGL4.23 map indicates the presence of a multiple cloning site with several restriction enzyme cut sites upstream of *P. pyralis Luciferase* (*luc2*) gene. I noticed an unannotated *NcoI* site at the start of (*luc2*), and used it to replace

the minimal promoter encoded in the plasmid with fragment A. (Fragment A has two putative *Plag1* binding motifs, and is within the canonical *Vegfa* promoter.)

Enhancer constructs Two fragments of interest were cloned into the pGL4.23 reporter plasmid upstream of a minimal promoter, to test its functionality as an enhancer in the presence of *Plag1*.

ANALYSIS OF LUMINANCE Luciferase analysis was carried out by JM Rosin, using plasmids and reagents designed and constructed by E.D. Camci. 250 ng of the pGL4.23/*Vegfa* (*P. pyralis luc2*) promoter or enhancer plasmids, 10 ng of pRL-TK (*R. reniformis Rluc*), and 250 ng of either pcDNA3.2/V5-PLAG1 or pcDNA3.2/V5 were incubated in 2.3% PolyJet (SignaGen) in Dulbecco's Modified Eagle Medium (DMEM). Cos-1 cells were incubated with the DNA/PolyJet/DMEM mixture at 37°for 5 hours. Cells were grown for 2 days in fresh DMEM at 37°C. Samples were lysed with PLB (Promega) before a two-step measurement of luminance. Cos-1 cell lysate was first mixed with firefly (*Photinus*) *luc2* substrate-containing Luciferase Assay Reagent II (LARII, Promega); the resulting luminance was measured in Relative Light Units (RLU) using a luminometer (Analytical Luminescence Laboratory Monolight luminometer, Berthold Technologies). Addition of Stop & Glo reagent (Promega) to the lysate/LARII samples quenched the *luc2* reaction and provided the substrate for baseline sea pansy (*R. reniformis*) *Rluc*-catalyzed luminance.

2.3 3D IMAGING AND MORPHOMETRIC ANALYSIS

µCT IMAGING The majority of skeletal images in this document are 2D screen grabs of 3D renderings, generated at SCRI's Small ANimal Tomographic Analysis Facility (SANTA). 17.21 µm resolution images of the skull and cervical vertebrae were acquired with a Skyscan 1076 µCT scanner (Bruker microCT), using the 0.5 mm Aluminum filter at 55 kV and 179 µA, settings optimized for mineralized tissue. BMP stacks were reconstructed using Skyscan Nrecon v.1.6.9.4 package. Reconstructions were visualized at full resolution without further modification in Drishi Volume Exploration and Presentation Tool 8.[119] Vertebrae and mandibles were segmented from reconstructions of µCT images using Mayo Clinic ANALYZE 9.0. Landmark-independant analysis of bilateral asymmetry in 23 hemimandible pairs was carried out using the tool described in Rolfe et al. (2013).[120]. µCT scan renderings in this document are representative; all efforts have been made to keep images to scale.

MORPHOMETRIC ANALYSIS Landmarks were digitized twice on the surface of µCT scan images using Drishti and averaged. Minimum sample size was calculated per Webster and Sheets 2010.[121] Linear distances, cranial base growth rates, and cranial angles were calculated from landmarks using Microsoft Excel. Procrustes superimposition, Principal Component Analysis and Discriminant Function Analysis were carried out in MorphoJ.[122] Procrustes coordinates exported from MorphoJ were subject to Goodall's F test in Chapter 3 using Simple3D 1.0.[123] Subsequent mean shape testing was carried out in R v3.2.1. Lateral profile landmarks were subject to Procrustes superimposition and analyzed using the *testmeanshapes* function of the *shapes* package, which includes a GPA step, using 1000 permutations. Significance in

all statistically tests was determined using an alpha of 0.01.[124,125]

2.4 QUALITATIVE METHODS

Qualitative traits - growth site loss, vertebral defects, and lateral facial defects - were assessed using a combination of μCT scan renderings and histological methods. Where applicable, group means were tested using Excel 2011, v.14.5.9 (Microsoft, Redmond, WA) or GraphPad QuickCalcs (GraphPad Software, La Jolla, CA;). Categorical data was analyzed using the VasserStats calculator (courtesy of R Lowry, Poughkeepsie, NY/Avon, CT).

ALCIAN BLUE/ALIZARIN RED SKELETAL PREPARATIONS Alcian blue and Alizarin red were used to differentially label cartilaginous (blue) and calcified (red) tissue in mice at P7 and P28. Ethanol-fixed tissue was defatted overnight in acetone and incubated sequentially in Alcian blue solution (Alcian blue 8GX (Acros Organics 400460100), 5% Acetic acid, 70% EtOH, pH 2.5), 1% Potassium hydroxide (KOH) and Alizarin red S solution (Acros Organics 400480250), with wash steps in between, following the protocol of Ovchinnikov (2009).[126]. Specimens were cleared in 1% KOH/20% glycerol solution for several days before being photographed.[126,127]

HISTOLOGY Following μCT scanning, 1 cm thick sections containing the cranial base were trimmed from P7 mouse crania and incubated in Bouin's fixative at room temperature overnight, decalcified for 2 weeks in 14% EDTA, changing solution every 2 days, and embedded in paraffin. 12 μm thick sections were cut in the transverse

plane on a Leica microtome and stained with Masson's Tri-chrome (Sigma-Aldritch HT15-1KT) or H&E before mounting on slides for imaging (Permount, Fisher Chemical SP15-100).

IMMUNOHISTOCHEMISTRY Whole mount immunostaining was used to differentially label vascular and neural cells after incubation and bleaching in Dent's fixative embryos between E9.0 and E15.5, following the protocol described in Vickerman et al. (2011)[128] Endothelial cells were labeled with rat α-mouse Endomucin antibody (Affymetrix, 14-5851). Neurons were labeled using the mouse α-rat neurofilament (2h3) antibody, deposited at the Developmental Studies Hybridoma Bank by T.M Jessell and J Dodd (Howard Hughes Medical Institute/Columbia University).[129] Both primary antibodies were detected with ImmPACT DAB Peroxidase (HRP) Substrate (Vector Labs SK-4105). Samples were cleared and photographed in BABB.

X-GAL DETECTION *lacz* *lacZ* positive embryos were fixed in 4% paraformaldehyde (PFA) and processed according to the protocol described in Nagy, et al. (2007).[130] β-Galactosidase activity was detected with x-gal staining solution (5mM $K_4[Fe(CN)_6]$*$3H_2O$, 5mM $K_3[Fe(CN)_6]$, 40mg/mL x-gal). Samples were postfixed in PFA and photographed in PBS.

2.4.0.1 *Technical guidance*

I would like to thank Sara S Park, Siddharth R Vora, Brandon Ng and Maia Chan for their guidance and assistance with the mice, Katherine Rafferty, Mei Deng, and Siddharth R Vora for their guidance regarding histology and skeletal preparations,

A. Murat Maga and Jill Weyers for their guidance regarding imaging, and Jessica M. Rosin for her guidance regarding whole mount immunohistochemistry, x-gal staining, cloning, and branchial arch dissection.

Particular thanks go to Jessica Rosin for carrying out the cell culture and luminance assay elements of luciferase experiment reported in Chapter 4 and to Andrew Timms for his help with RNAseq data analysis. .

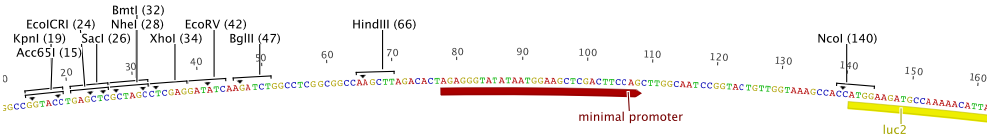

(a) There is a *NcoI* restriction enzyme cut site between the minimal promoter (red) and start of *luc2* (yellow) MCS with annotated enzyme cut sites.

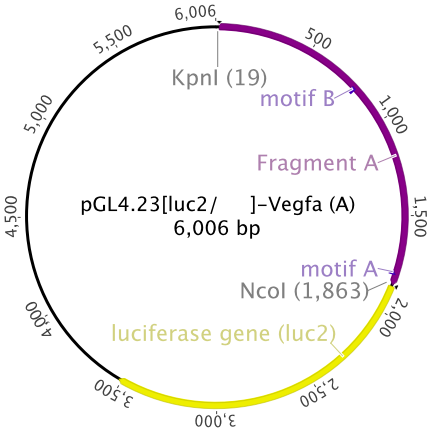

(b)

Promoter construct A.
Fragment A (**magenta**) (located within the *Vegfa* promoter) cloned into pGL4.23 luciferase reporter plasmid without a promoter. This construct tests the ability of *Plag1* to activate expression by binding directly to the promoter.

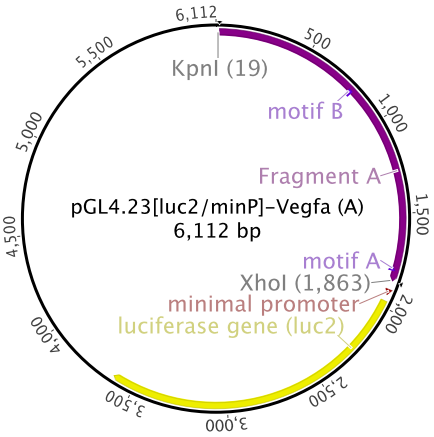

(c)

Enhancer construct A.
Fragment A (**magenta**) cloned into pGL4.23 luciferase reporter plasmid, 5′ to a minimal promoter; tests the ability of *Plag1* to activate expression by binding to an enhancer.

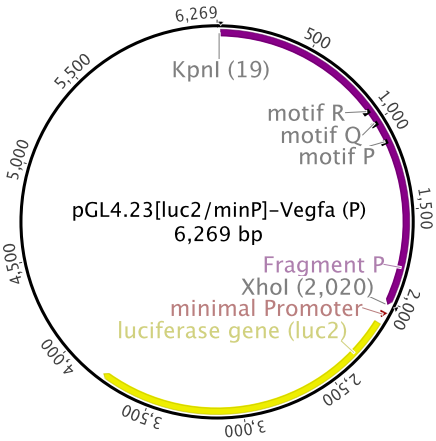

(d)

Enhancer construct P.
Fragment P (**magenta**) cloned into pGL4.23 luciferase reporter plasmid, 5′ to a minimal promoter; tests the ability of *Plag1* to activate expression by binding to an enhancer.

Figure 2.4: pGL4.23-*Vegfa* luciferase constructs

MORPHOLOGY

3

"SMALL BODY, SMALL EAR" (SBSE)

3.1 OVERVIEW

Research into the molecular mechanisms of postnatally relevant structural birth defects typically focuses on timepoints at or after embryonic organogenesis, without considering the effect of neonatal and juvenile growth patterns on adult skeletal morphology.[72,131] Craniofacial malformations have been found in mouse models of Apert syndrome, suggesting that a model of considering suture fusion as the primary cause of cranioskeletal dysmorphology is insufficient.[132] Suture fusion clearly affects morphology, but cannot explain the whole phenotype. Skeletal malformations and associated soft tissue defects in conditions like craniosynostosis disrupt both pre- and postnatal developmental patterns, and without treatment, may cause progressive deformities.[133,134] There is significant debate over the timing of medical and surgical interventions in such conditions.[135,136] In light of these debates, it is surprising how superficially the patterns of postnatal growth are typically characterized.

Detailed longitudinal analyses of shape changes during early development are rare. While developmental biologists are fastidious about the chronological and morphological age in their samples, they may be less concerned about the postnatal

events that might have contributed to their phenotype of interest. Murine cranioskeletal size, shape, and angulation change rapidly in the first month after birth, and aberrant expression of a mutated gene *in utero* may have a different effect when it is expressed postnatally. The interpretation of data on the molecular mechanisms affecting morphogenesis would be enriched by a more thorough understanding of the postnatal effects of that mutation.

The wildtype mouse skull undergoes immense changes in size and shape, following a predictable growth pattern, from birth through maturity, with half of expected adult anterior posterior length attained by P7. In wildtype C57BL/6J mice, 80% of expected anterior posterior growth occurs before P14 and P21 in the cranial base and facial regions, respectively[137]. Growth and development is controlled by genetic and epigenetic factors, and while embryonic defects may set the course towards normal adult morphology, disruptions in postnatal growth processes may sink the ship. In this chapter, I examine the development of the hypoplastic and asymmetric *small body, short ear* (*sbse*) cranium, and test the association between growth site defects and dysmorphology, with the aim of understanding the differential developmental patterns caused by the mutation.

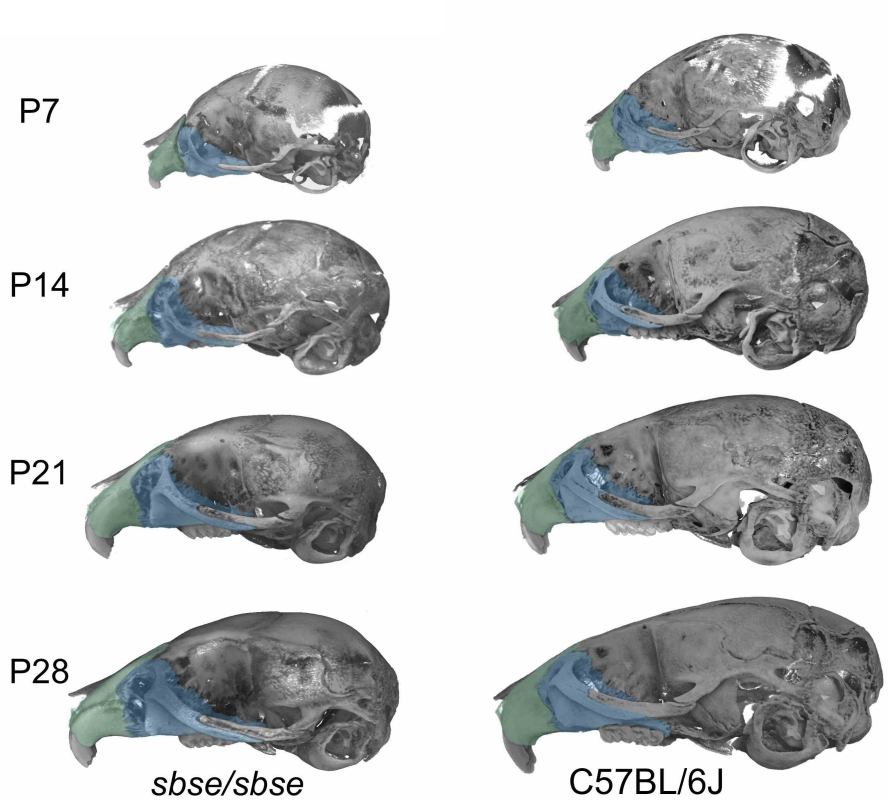

(a) Homozygous *sbse/sbse* mutants **(b)** Wildtype C57BL/6J +/+ controls

Figure 3.1: Cranioskeletal dysmorphology in the *sbse* develops from P7-P28. Lateral views of μCT scan renderings of representative animals at each of time points examined.

3.2 RESULTS

3.2.1 *Inheritance and body size*

3.2.1.1 *Average litter sizes are smaller in sbse mice*

Postnatal litter size, defined as the average number of viable pups, is significantly smaller in all *sbse* crosses compared to wildtype C57BL/6J +/+. Mutant litter sizes vary with the hetero- or homozygosity of the parents, although the difference between groups fails to reach significance. Homozygote crosses produce the fewest pups on average (■×●) (*sbse*/*sbse* × *sbse*/*sbse*; M= 4.4, SD= 1.4), followed by heterozygote crosses (◪×⊘) (*sbse*/+ × *sbse*/+; M= 5.2, SD= 1.4). Mixed homozygote-heterozygote crosses (◆×◇) resulted in the largest litter sizes (*sbse*/*sbse* × *sbse*/+ mice); M= 5.6, SD= 1.4, t(18)= 2.93) (Table 3.1).

The average embryonic litter resulting from a heterozygous cross (◪×⊘) contains 9 pups, and is larger than the average litter observed postnatally, suggesting that the *sbse* mutation has an embryonic lethal effect after E10.5.

3.2.1.2 *Genotype ratios change between E10.5 and birth*

Embryonic litters resulting from heterozygote *sbse* crosses (◪×⊘) dissected at E10.5 were significantly larger than comparable postnatal litters (*sbse*/+ × *sbse*/+; M= 9.0, SD= 2.3; t(14)= 4.1, $p<0.01$*) The Mendelian ratio of the embryonic litters was 1.0 : 1.9 : 1.4, close to the expected 1:2:1. The postnatal ratio, 1.9 : 3.8 : 1.0, skewed heavily towards mutants.

3.2.1.3 *Mendelian ratios in mixed crosses are normal*

The genotype ratios of litters born to mixed homozygote-heterozygote crosses (◆×◈) are normal, at exactly 1.0 : 1.0 : 0.0.

3.2.1.4 *There is no effect on the ratio of male to female pups born to mutants*

The ratio of sexes in each litter is only significantly different between the homozygous *sbse* (*sbse*/*sbse* × *sbse*/*sbse* M= 0.59, SD= 0.23, $n_{litters}$= 10) and wildtype C57BL/6J +/+ groups (C57BL/6J +/+ M= 0.39, SD= 0.16, $n_{litters}$= 11; z= -2.3, p= 0.02). The comparison between litters born to mixed homozygote-heterozygote crosses and the wildtype approaches, but does not reach significance (◪×◯)) (*sbse*/*sbse* × *sbse*/+ M= 0.58, SD= 0.28, $n_{litters}$=9; z= -1.8, p= 0.07) (Table 3.2).

3.2.1.5 *Cranioskeletal dysmorphology is inherited recessively*

The *sbse* phenotype can be identified by the overall external appearance and in μCT scan renderings of mice from postnatal day (P)14 onwards; it appears only the offspring of two *sbse* line mice. To test for recessive inheritance of the phenotype, I assigned each member of the P28 sample to "affected" and "unaffected" groups; "affected" group membership was 100% predictive of homozygosity (◆) by PCR-based genotyping results. i.e., the cranioskeleton of all *sbse* homozygotes are dysmorphic. All wildtype and heterozygote mice were classified as unaffected (*sbse*/*sbse* ◆ n= 20; *sbse*/+ ◈ n= 9; n= 20; C57BL/6J +/+ ◇ n= 16).

HETEROZYGOTE PHENOTYPE μCT scan renderings show that the skulls of mice heterozygous for the *sbse* mutation (*sbse*/+ ◈) are larger than homozygotes, and have a wildtype-like appearance. μCT scan renderings reveal the same growth site

defects and asymmetries seen in the homozygotes are present at P28, although they appear at lower levels (Table 3.17). No significant difference in average body weight was found between *sbse*/+ and C57BL/6J +/+ (*sbse*/+ ♢ n= 20; C57BL/6J +/+ ♢ n= 16; t(34)= 1.2 p= 0.24.) (Figure 3.3).

Inheritance of the *sbse* mutant phenotype is complex: the characteristic cranioskeletal dysmorphology and body weight phenotypes appear to be inherited recessively. Impaired reproductive ability, along with growth site defects and asymmetries, appear in heterozygotes at low levels, and may be semi-dominant.

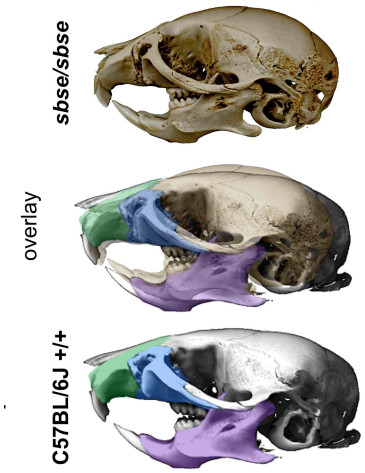

(a)

Comparison of lateral view, *sbse/sbse* (top, beige) and wildtype C57BL/6J +/+ (bottom, gray). Overlay aligned at the palatal surface and first molar, showing the length and cranial vault height differences between mutant and wildtype skulls.

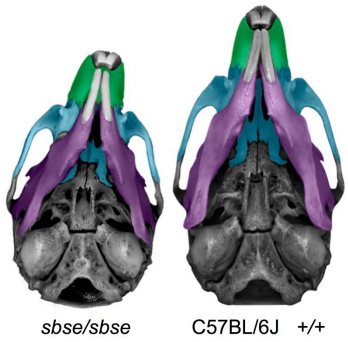

(b)

Deviation of the snout, relative to the midline of the cranial base.

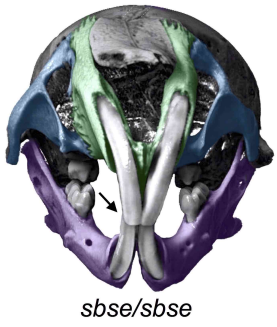

(c)

Frontal view of incisors in an asymmetric *sbse/sbse*. The lack of malocclusion in mutants with deviated snouts suggests that maxillary asymmetry is mirrored in the mandible.

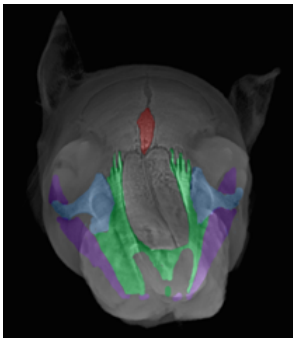

(d)

Soft tissue, with underlying cranioskeleton. Cranioskeletal asymmetry is reflected in the external appearance of the head.

Figure 3.2: The *sbse* cranioskeletal phenotype at P28 *Green*, premaxilla. *Blue*, maxilla. *Purple*, mandible. *Red*, Interfrontal bone. *White dots*, interfrontal suture. *Black arrow*, incisors. (μCT scan renderings.)

Table 3.1: Reduced litter size in *sbse* mice.

Cross	$n_{litters}$	n_{pups}	M ± SD	□×○ wildtype +/+	■×● homozygote *sbse/sbse*	◪×⊘ heterozygote *sbse/+*	
Post-natal							
C57BL/6J (+/+) × C57BL/6J (+/+)							
□×○	11	88	8.0 ± 2.1[1]	-	-	-	-
sbse/sbse × *sbse/sbse*							
■×●	10	44	4.4 ± 1.4	**t(19)=4.48,p<0.01***	-	-	
sbse/sbse × C57BL/6J (+/+)							
■×○	3	14	4.7 ± 2.9	-	-	-	
◪×○	4	23	5.8 ± 1.0	-	-	-	
sbse/+ × *sbse/+*							
◪×⊘	9	47	5.2 ± 1.4	**t(18)=3.34,p<0.01***	t(17)=1.27,p=0.22		
sbse/sbse × *sbse/+*							
◆ × ◇	9	50	5.6 ± 1.4	**t(18)=2.93,p<0.01***	t(17)=1.76,p=0.096	t(16)=0.77,p=0.45	
■×⊘	4	24	6.0 ± 0.82	-	-	-	
◪×●	5	26	5.2 ± 1.8	-	-	-	
Embryonic							
sbse/+ × *sbse/+*							
◪×⊘	7	63	9.0 ± 2.3	-	-	**t(14)= 4.07,p<0.01***	

*Significant difference, compared to WT, p<0.01

Table 3.2: Sex ratios in *sbse* litters

Cross	$n_{litters}$	Average % litter ♂ M ± SD	□×○ wildtype +/+	■×● homozygote *sbse/sbse*	◪×⊘ heterozygote *sbse/+*
Post-natal C57BL/6J +/+					
□×○	11	0.4 ± 0.2			
sbse/sbse × *sbse/sbse*					
■×●	10	0.6 ± 0.2	z=-2.29, p=0.022		
sbse/sbse/+ × *sbse/+*					
◪×⊘	9	0.4 ± 0.1	z=-0.85, p=0.39	z=1.87, p=0.061	
sbse/sbse/sbse × *sbse/+*					
◆ × ◈	9	0.6 ± 0.3	z=-1.81, p=0.071	z=0.085, p=0.93	z=-1.41, p=0.16
■×⊘	4	0.6 ± 0.3			
◪×●	5	0.6 ± 0.3			
Embryonic					
sbse/+ × *sbse/+*					
◪×⊘	7	0.5 ± 0.1			z=-1.07, p=0.29

*Significant difference, p <0.01, by two-sample z-test, two tailed.

Table 3.3: Genotype ratios in *sbse* litters

Cross	$n_{litters}$	n_{pups}	◆ homozygote *sbse/sbse*	◈ heterozygote *sbse/+*	◇ wildtype +/+	Mendelian ratios Observed	Expected
Post-natal							
sbse/sbse × *sbse/sbse*							
■×●	10	44	4	0	0	1.0 : 0.0 : 0.0	1.0 : 0.0 : 0.0
sbse/+ × *sbse/+*							
◪×⊘	9	47	13	27	7	1.9 : 3.8 : 1.0	1.0 : 2.0 : 1.0
sbse/sbse × *sbse/+*							
◆×◈	9	50	25	25	0	1.0 : 1.0 : 0.0	1.0 : 1.0 : 0.0
■×⊘	4	24	15	9	0	1.7 : 1.0 : 0.0	
◪×●	5	26	10	16	0	1.0 : 1.6 : 0.0	
Embryonic							
sbse/+ × *sbse/+*							
◪×⊘	7	63	14	27	20	1.0 : 1.9 : 1.4	1.0 : 2.0 : 1.0

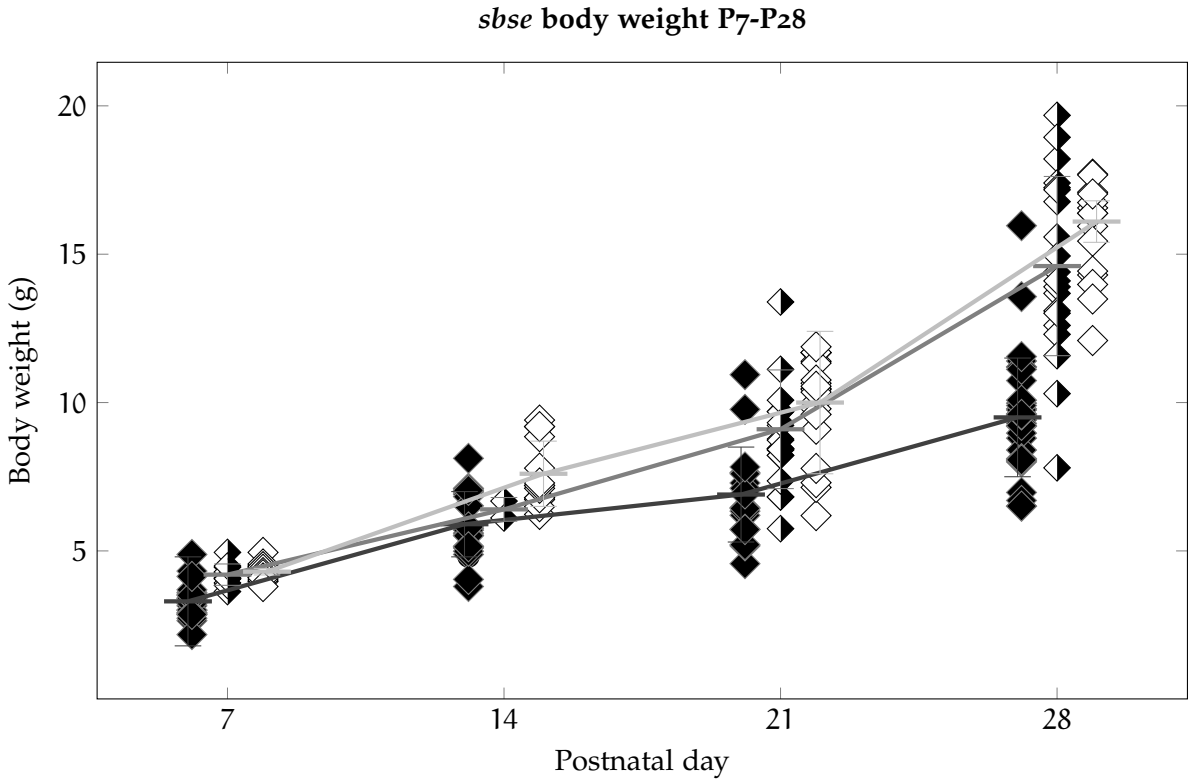

Figure 3.3: *sbse* body weight, P7-P28. *sbse*/*sbse* mice are lighter than *sbse*/+ and C57BL/6J +/+ at all ages.

Table 3.4: *sbse* body weight, P7-P28.

(Compared to wildtype)

	◆ homozygote *sbse*/*sbse*			◈ heterozygote *sbse*/+			◇ wildtype +/+	
Age	M ± SD	n_{pups}=		M ± SD	n_{pups}		M ± SD	n_{pups}
P7	3.3 ± 0.6	20	t(32)=5.7 p<**0.001***	4.2 ± 0.4	11	t(23)=0.72 p=0.48	4.3 ± 0.29	14
P14	5.9 ± 1.1	32	t(36)=4.6 p<**0.001***	6.4 ± 0.4	2	t(14)=1.49 p=0.16	7.6 ± 1.1	14
P21	6.9 ± 1.7	18	t(33)=5.6 p<**0.001***	9.1 ± 2.0	20	t(35)=1.6 p=0.11	10.1 ± 1.7	21
P28	9.6 ± 2.0	32	t(46)=10.4 p<**0.001***	14.6 ± 3.0	20	t(34)=1.2 p=0.24	15.6 ± 1.6	16

*Significant difference between genotypes by unpaired T-test, p<0.05

(Table of data presented in Figure 3.3)

Table 3.5: Reduced cranioskeletal size and abnormal proportions in the *sbse*, P28

Dimension		◆ homozygote *sbse/sbse* M ± SD	◇ wildtype +/+ M ± SD	Δ (mm)	Difference
Skull length	Internasal to basion	12.71±0.66	15.10±0.47	2.39	t(33)= 11.92 p < 0.001*
Snout length	Fused length of internasal suture	4.21±0.50	5.91±0.18	1.70	t(33)= 12.53 p < 0.001*
Snout height	Nasal suture to premax-max suture	4.32±0.17	4.36±0.21	0.04	t(33)= 2.02 p= 0.051
Vault height	Posterior interfrontal to basioccipital	6.43±0.24	7.23±0.15	0.80	t(33)= 11.33 p < 0.001*
Snout width	Lateral premax-max suture (pair)	3.75±0.22	3.91±0.089	0.17	t(33)= 6.65 p < 0.012*
Vault width	Point of zygomatic-temporal union (pair)	10.32±0.28	10.87±0.17	0.55	t(33)= 6.72 p < 0.001*
Orbital width	Anterior zygomatic-max suture (pair)	8.54±0.43	9.57±0.26	1.03	t(33)= 8.20 p < 0.001*
Alveolar width	Anterior alveolar crest (pair)	3.43±0.15	3.45±0.11	0.03	t(33)= 0.44 p = 0.67

sbse/sbse n= 20; C57BL/6J +/+ n= 15 *Significant difference, $p < 0.05$, by two-sample *z*-test, two tailed.

Figure 3.4: Linear dimensions measured at P28.

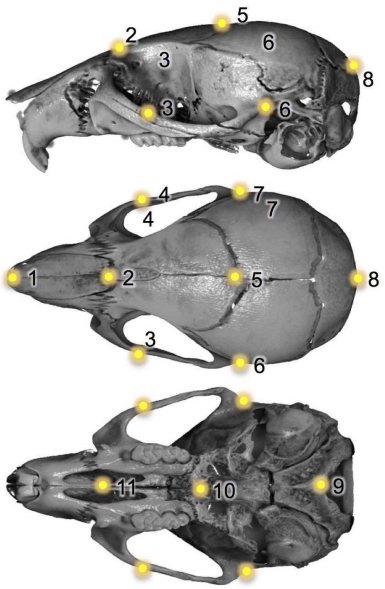

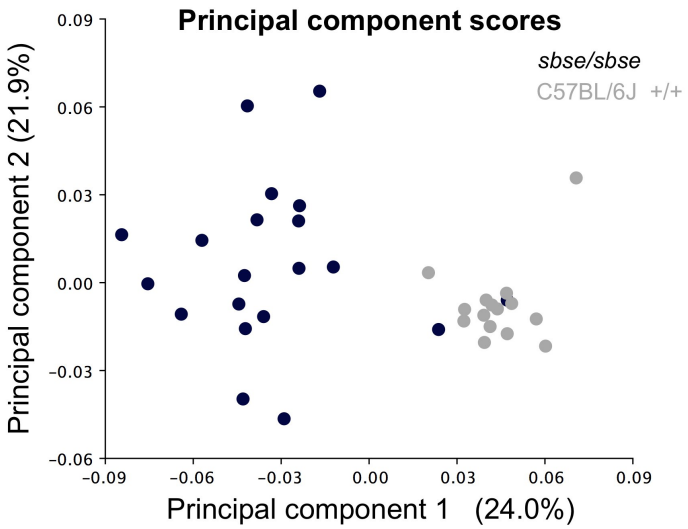

(a) k=11 landmark points used to test for a difference in overall cranioskeletal shape at P28 by Goodall's F-test, Principle Component Analysis (PCA), and Discriminant Function Analysis (DFA). **(b)** Separation of *sbse/sbse* and C57BL/6J +/+ along the first PC of shape.

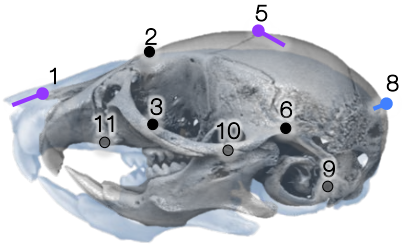

(c) PC1 (24.0% of var.)

Principal component (PC) 1 accounts for 24.1% of variation in the sample. Purple, #1 tip of the snout (rhinion) and #5 cranial vault (bregma). Blue, posterior cranium.

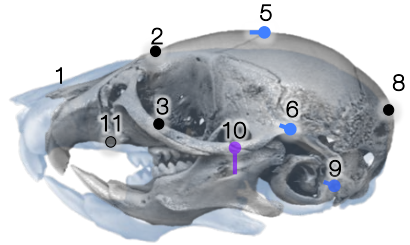

(d) PC2 (21.9% of var.)

Principal component (PC) 2 accounts for 21.9% of variation in the sample. Purple, point #10 at the SOS.

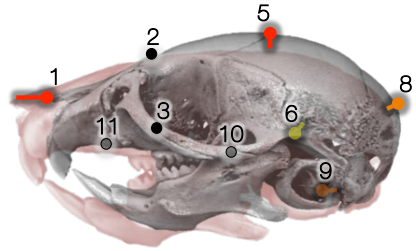

(e) (DFA)

Characteristic features of the *sbse/sbse*, identified by DFA: Red, #1 tip of the snout (rhinion) and #5 cranial vault (bregma). Orange, posterior cranium.

Figure 3.5: Overall shape differences in the shape of the *sbse* cranium, P28

Norma verticalis (superioris)

(a) Dorsal view, *sbse/sbse*. **(b)** C57BL/6J +/+

Norma basalis (inferioris)

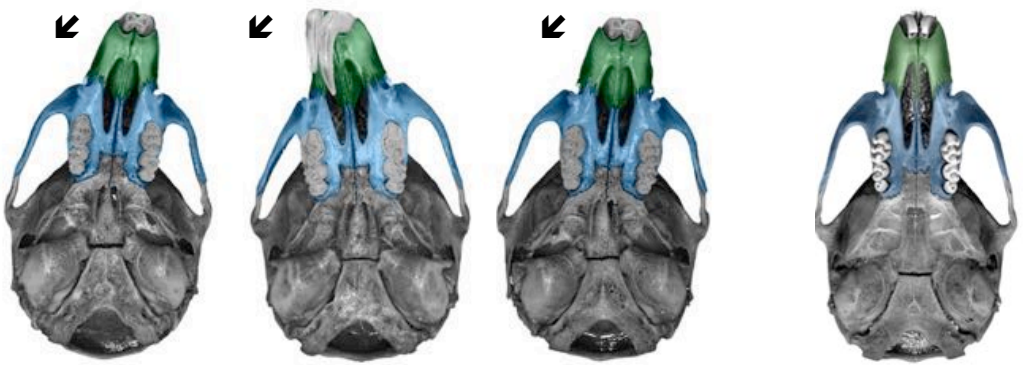

(c) Ventral view, *sbse/sbse*. **(d)** C57BL/6J +/+

Norma basalis (exterior)

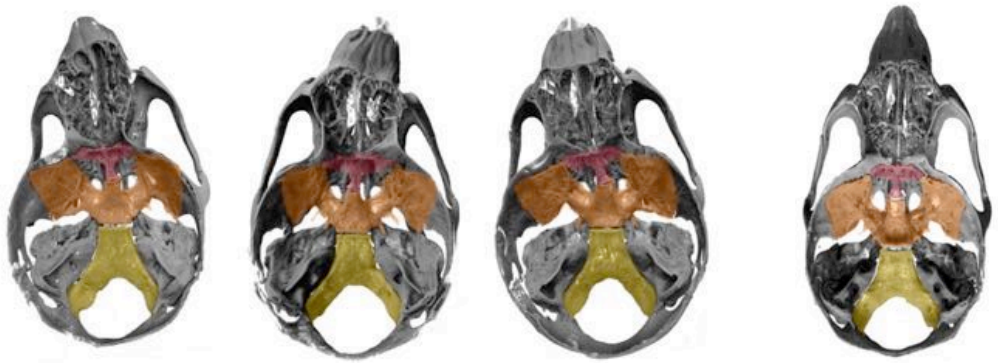

(e) Endocranial view, *sbse/sbse*. **(f)** C57BL/6J +/+

Figure 3.6: Variability in *sbse/sbse* cranioskeletal morphology. (a, c) Midface hypoplasia, asymmetry and **(e)** abnormal cranial base morphology in in the mutant *sbse/sbse* is highly variable. **(b, d, f)** Wildtype C57BL/6J +/+ morphology.

Stars, dorsal asymmetry relative to the sagittal plane. *Arrows*, ventral asymmetry relative to the midline of the basioccipital. *Green*, premaxilla. *Blue*, maxilla. *Red*, Presphenoid. *Yellow*, Basisphenoid. *Orange*, Basioccipital. (µCT scan renderings.)

3.2.2 *Craniofacial size, shape, and asymmetry*

I examined μCT scan renderings of *sbse* mice sacrificed at postnatal day (P)28.[2] The overall appearance of the mutant skull is more rounded, with a short premaxilla/-maxilla and doming of the cranial vault (Figures 3.2a and 3.6). The maxilla deviates from the midline of the cranial base in 73.3% of mutants, and from the plane of the sagittal suture in 34.4% of mutants (Figures 3.2b and 3.2d). Within the cranial base, the presphenoid deviates from the midline of the cranial base in 71.9% of mutants (Figure 3.11c). Malocclusion was observed in one animal (3.3%) (*sbse*/*sbse* ◆ n= 32) (Figure 3.2c). Neither maxillary asymmetry nor malocclusion is observed in the wildtype C57BL/6J +/+ sample (n= 15). Further analysis of asymmetry in the lateral facial tissues is reported in Chapter 6.

3.2.2.1 *Differences in mean size and shape*

REDUCTION OF AVERAGE SKULL SIZE, P28 The reduction in size of the *sbse* skull is more pronounced in the anterior-posterior dimension. To quantify the difference between mutant and wildtype cranioskeletal size at P28, I compared animals at P28, and found a significant reduction in six of eight linear dimensions (*sbse*/*sbse* n= 20; C57BL/6J +/+ n= 15). The most pronounced differences in the mutant are in average anterior-posterior (AP) skull length (Δ= 2.4 mm) and average dorsal snout length (Δ= 1.70 mm), where the average *sbse* reaches only 84% and 71% of mutant length, respectively. In contrast, of the three significantly reduced average widths, only average orbital width is a 10% reduction in size (Δ= 1.03 mm). The genotype-invariant

2 Bone mineral density, cortical area, and other measures of skeletal maturity are reported to reach their maximum values ("skeletal maturity") in the tibia of C57BL/6J mice between three and six months of age.[139] The Cox lab has found that mice scanned at P28 are old enough to have attained a mature cranioskeletal shape.

measurements are the average width of the anterior alveolar crest (measurement E, Δ= 0.03 mm) and the average height of the snout (measurement F, Δ= 0.04 mm) (Table 3.5).

CHANGES TO MEAN SKULL SHAPE, P28 The mutant *sbse/sbse* has a significantly different shape that that of the C57BL/6J +/+. 11 landmarks were digitized on μCT scan renderings and aligned using the partial Procrustes superimposition function in `MorphoJ` or the `shapes` package for `R` (Figure 3.5).[122] Goodall's F-test reports a statistically significant difference in shape (sum of squared Procrustes distances) between mutant and wildtype groups ($F_{26,858}$= 31.99, p< 0.001).

The shape of the mutant cranioskeleton appears significantly more variable than the wildtype in μCT scan renderings; no laterality is detected (Figure 3.6). Principal Component Analysis (PCA) identified 26 Principal Components (PC) of shape variation, describing 90% of variance in the first 9. Plotting individual scores on axes representing by the first two PC (totaling 45.9% of variation) shows clean separation between *sbse/sbse* and C57BL/6J +/+ (Figure 3.5b). Landmarks most affected in PC1 include shortening of the distance between the snout and the top and back of the cranial vault, and the width of the zygomatic arch (Figure 3.5c). Landmarks most affected in PC2 include the dropping of the posterior part of the palate, deviation of the midline points including the snout, and the length of the zygomatic arch (Figure 3.5c).

Discriminant function analysis (DFA) identified the anterior most point of the snout and the most posterior point of the interfrontal suture as characteristic elements of sbse mutant shape (Figure 3.5e red). A secondary group of landmarks with shorter deformation vectors was also identified around the posterior neurocranium (Figure

3.5 orange and yellow). While there is a statistically significant difference between group means by Procrustes distance (Goodall's F-test) and Mahalanobis distance, cross validation of the DF resulted in correct reclassification of 73% and 85% of wildtype and mutant crania, respectively.[121]

3.2.3 *Postnatal phenotypic progression*

The mean size and shape phenotype in the *sbse* is variable and worsens with age. Mild midface hypoplasia is visible in μCT scan renderings of the cranioskeleton at P7; midfacial asymmetry is only apparent in mice at P14 and older ages (Figure 3.1). The full expression of the mutant phenotype is not seen until P28 (Figure 3.6). There is a significant difference between the body weight of *sbse*/*sbse* mutants and age matched samples of wildtype mice at all time points from P7 through P28; at P28, the average weight of heterozygotes is not significantly different from the wildtype. Although lighter, on average, mutant and wildtype mice gain weight at a comparable rate through rate from P7 through P14. From P14 through P21, weight gain plateaus in the mutant (Figure 3.3 , Table 3.3).

3.2.3.1 *Associations between sided traits*

Pronounced dorsal asymmetry is first observed at P24, and is present in 34.4% of the homozygote population at P28, favoring the right side in 66.0% of affected animals. Two χ^2 tests of independence was performed to examine the relation between the side of sagittal plane/interfrontal suture (dorsal deviation) and the side of presphenoid tilting and deviation. The relationship between these variables was significant ($\chi^2(2, n= 90)= 71.94$, $p < 0.01$), suggesting that there is a non-random association between

asymmetry in the snout and deviation in the cranial base at the presphenoid. Comparison of the side of dorsal deviation and the side of maxillary asymmetry, relative to the midline of the cranial base (ventral asymmetry) was also significant ($\chi^2(2, n=90) = 19.63$, $p < 0.0001$). Both presphenoid and ventral asymmetry are found in 71.9% of *sbse* mice at P28.

3.2.3.2 *Growth site defects and dysmorphology*

SUTURAL DEFECTS The zygomatic maxillary suture is located bilaterally on the rim of the mouse orbit, and appears patent in μCT scan renderings of wildtype mice; uni- or bilateral obliteration of the suture is found in 62.5% of *sbse/sbse* at P28 3.11a). μCT scan renderings show a mineralized surface "sunken" between the posterior part of the interfrontal suture in 93.8% of mutants at P28 (*sbse/sbse* n=32). Coronal slices through the reconstructed volume suggest that the endocranial plate is ossifying abnormally, and compared to C57BL/6J controls, prematurely. In the wildtype, the bony fronts of the endocranial and ectocranial plates abut one another evenly at this age (Figure 3.11b).

Weak association between suture loss and dysmorphology

There is a statistically significant association between dorsal deviation and ectopic fusion of the interfrontal suture (p= 0.016). There is no association between dorsal deviation and premature fusion of the zygomatic-maxillary suture (p= 0.14), or between maxillary asymmetry, relative to the cranial base (ventral asymmetry) and loss of either the zygomatic-maxillary (p= 0.823) or interfrontal sutures (p=0.25) in the age-pooled *sbse/sbse* sample.

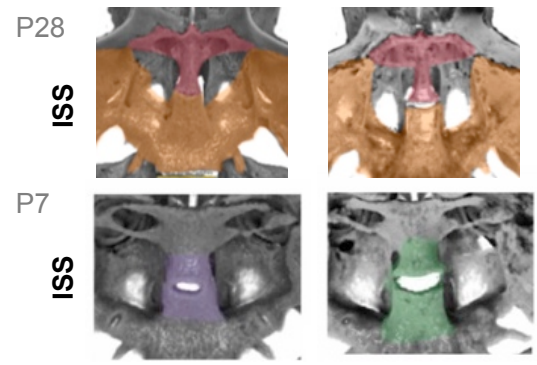

(a)

Premature ossification of the intersphenoidal synchondrosis (ISS). Complete loss of the ISS occurs in 96.9% of *sbse/sbse* mutants by P28. (μCT scan renderings.)

Red, presphenoid. *Orange*, basisphenoid.

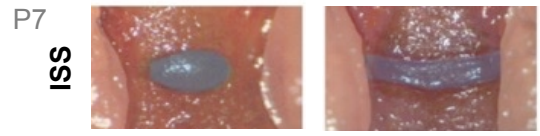

(b)

"Bulging" at the endocranial surface of the intersphenoidal synchondrosis. Skeletal preparations show that the endocranial surface of the synchondrosis "bulges" out of the fusing synchondrosis. (Photographs of ISS tissue, stained with Alcian blue to label cartilage, and Alizarin red to label mineralized tissue, at P7.)

Blue, cartilage. *Pink*, mineralized tissue.

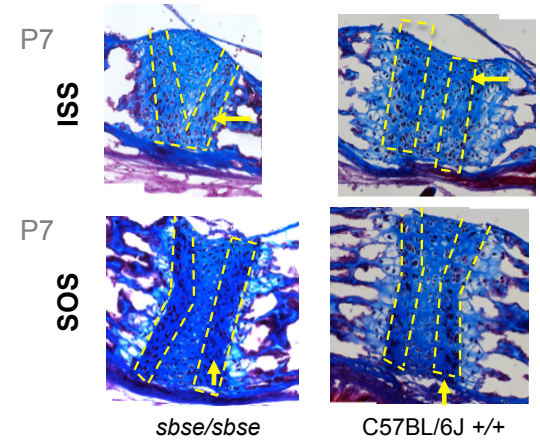

(c)

Chondrocyte disorganization in the intersphenoidal synchondrosis. Histological sections cut in the sagittal plane through the midline of the fusing *sbse/sbse* ISS show a loss of polarity in proliferative chondrocytes, and general disorganization of resting chondrocytes at P7. The spheno-occipital synchondrosis is morphologically and histologically normal in most mutants from P7-P28. (18 μm paraffin sections, stained with Masson's trichrome.)

Black, nuclei. *Blue*, collagen. *Pink*, muscle.

Figure 3.7: Ectopic ossification of the intersphenoidal synchondrosis in *sbse* mice.

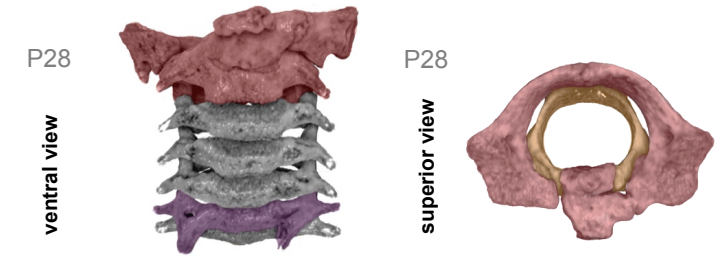

(a)

Vertebral clefts. Vertebral clefts form at the sites of the late-ossifying synchondroses on either side of the vertebral centra and between and can extend through the bone. Left: Cleft at C1, and fusion with the dental process of C2. Right: Superior view of cleft at C1.

Red C1, and C1-C2 fusion. *Purple* C6.

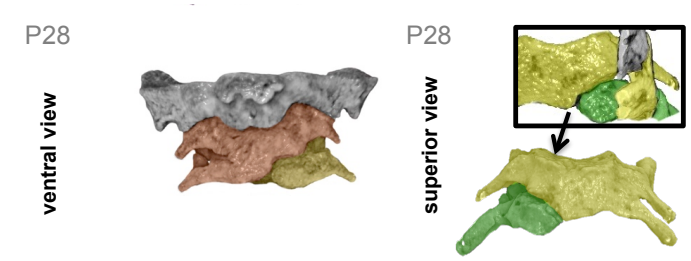

(b)

Hemivertebrae. Hemivertebrae form between the late-ossifying synchondroses on either side of the vertebral centra. Left: Fusion between C2 and C3. Right: Fusion between C3 and C4 extends through both bones.

Orange Hemivertebra formed by fusion of C2 and C3. *Yellow* Hemivertebra formed by fusion of C3 and C4. *Green* C4.

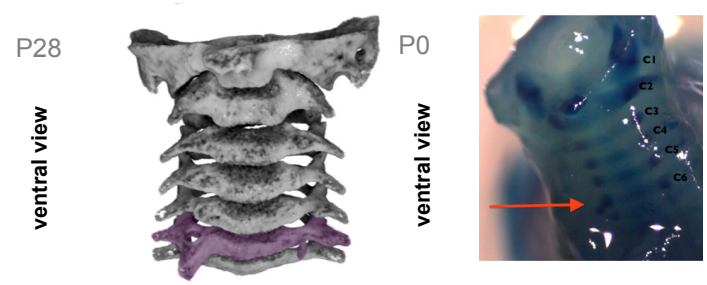

(c)

Carotid tubercle abnormalities.
Left: the left carotid (Chassaignac) tubercle on the anterior face of C6 is missing in a µCT scan rendering at P28. Right: the cartilaginous anlage of the left tubercle is missing in an Alcian blue-stained skeletal preparation of mutant at P0.

Purple, C6. *Blue*, cartilage.

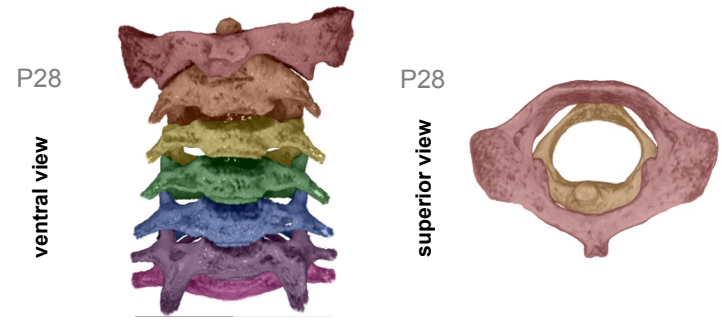

(d)

C57BL/6J +/+ reference.

Red, C1. *Orange*, C2. *Yellow*, C3. *Green*, C4. *Blue*, C5. *Purple*, C6. *Pink*, C7.

Figure 3.8: Defects in the cervical vertebrae of *sbse/sbse* mutants. Defects occur at the site of the anterior synchondroses between the centrum and vertebral body, dental process, and in the anterior carotid tubercles. No abnormalities were observed in the posterior neural arch.

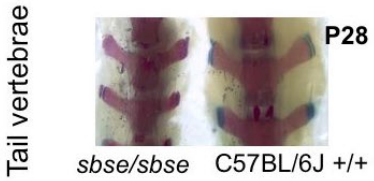

Figure 3.9: Defects in the tail vertebrae and sternum of *sbse/sbse* mutants.

Top: mutant *sbse/sbse* mice have smaller tail vertebrae. The cartilaginous growth plates on the transverse processes of the vertebrae are thinner or absent.

Bottom: Defects in the ossification pattern of neonatal sternebrae resemble a defect reported in a craniofacial microsomia patient.[140]

Blue, cartilage. *Pink*, mineralized tissue.

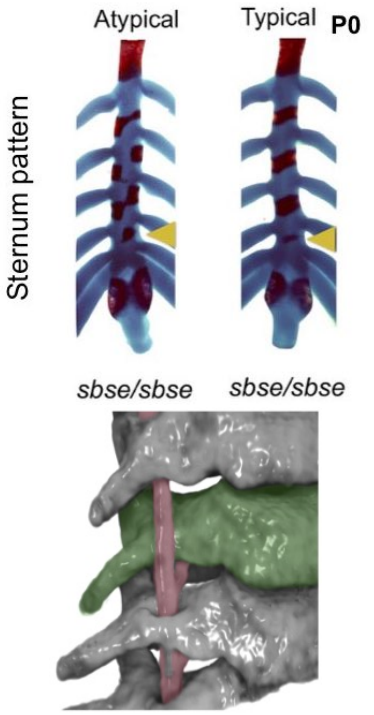

Figure 3.10: Incomplete closure of vertebral foramina in *sbse/sbse* mutants. The foramina on the transverse process of the cervical vertebrae are frequently incompletely ossified; μCT scan renderings of *sbse/sbse* mice following the post-mortem injection of contrast media into the the left ventricle of the heart show that the vertebral artery itself is intact. The defects do not follow a discernible pattern.
Red, vertebral artery. *Green*, C4.

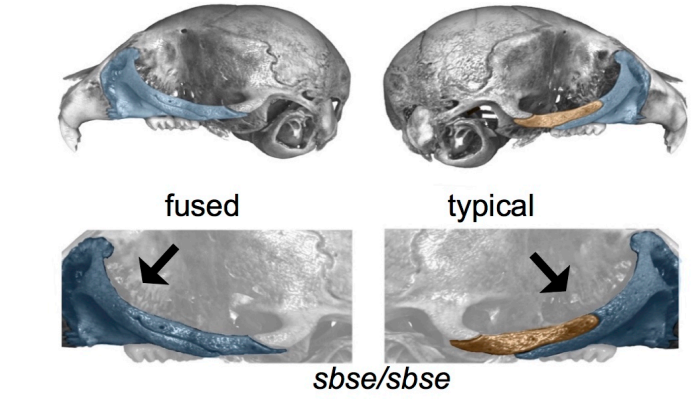

(a) Ectopic fusion of the zygomatic-maxillary suture. Uni- or bilateral premature fusion occurs at the orbital zygomatic-maxillary suture.

Blue, maxilla. *Orange*, jugal bone

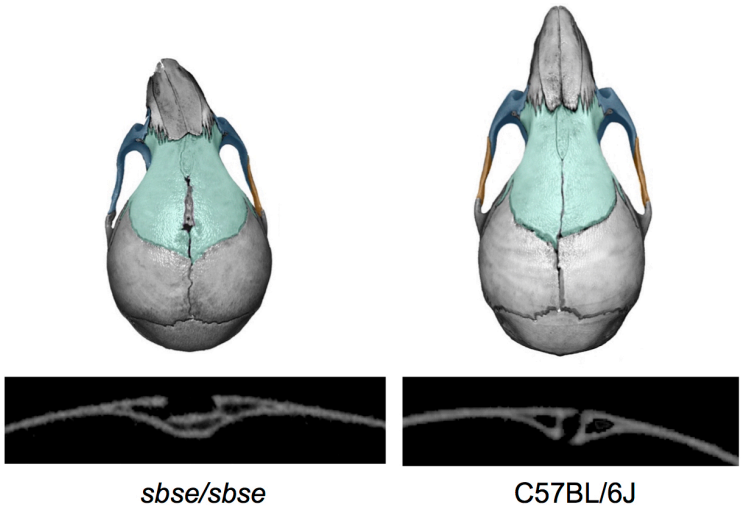

(b) Abnormal fusion at the posterior interfrontal suture.

Light green, frontal bones. *Green*, premaxilla. *Blue*, maxilla.

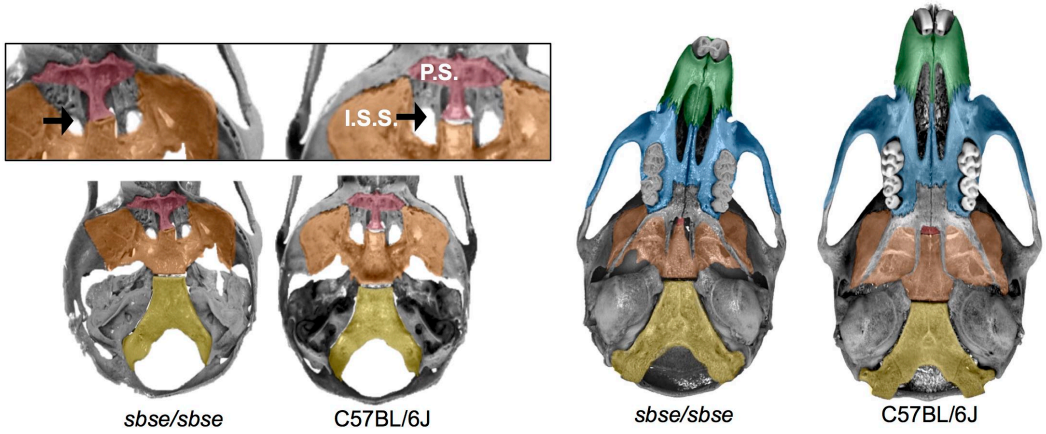

(c) Cranial base abnormalities. Asymmetry and ectopic ossification in the ISS of the mutant *sbse/sbse* cranial base. Left: endocranial surface of the cranial base. Right: ectocranial surface of the cranial base. *Green*, premaxilla. *Blue*, maxilla. *Orange* basisphenoid *Light green*, frontal bones. *Yellow*, basioccipital.

Figure 3.11: Growth site defects in the *sbse*
(μCT scan renderings.)

SYNCHONDROSIS / CARTILAGE DEFECTS *Intersphenoidal synchondrosis ossification*

Ossification of the intersphenoidal synchondrosis (ISS) at P7 is observed in 61.9% of *sbse* mice, and increases in the population with age. Unlike the spheno-occipital synchondrosis, ossification at this site proceeds by the extension of mineralized tethers at the lateral margins. Cartilage within the bilaterally enclosed ISS appears to bulge outwards, as though it is under compression. Sagittal sections show an abnormal union of the proliferating layers at the ventral surface, forming a "V" shape filled with resting chondrocytes. (Figure 3.7c, yellow boxes). At P28, the ISS has ossified prematurely in 96.9% of mutants. Anterior to the ISS, the *sbse* presphenoid bone is deviated out the the midline 71.9% of mutants (Figure 3.11c). Overall, the mutant sphenoid appears smaller and less robust than the wildtype, with thinner bone and incompletely ossified foramina. Foramina defects are also observed in the cervical vertebrae (Figure 3.10). Defects at the vertebral synchondroses (hemivertebrae, abnormal clefting) are observed in 28.1% of mutants at P28. Postcranially, defects have been observed in pattern of mineralized tissue in the neonatal sternum (Figure 3.9) (*sbse*/*sbse* n= 32).

Incomplete ossification of the vertebral foramina observed at P28 *sbse/sbse* suggested that the integrity of the vertebral artery, a major blood source, may be compromised. upμCT imaging with contrast media demonstrated that vessels of normal thickness and morphology were transmitted through the defective foramina.

No association between ISS ossification and asymmetry

There is no association between premature ISS ossification and dorsal (p= 0.34) or ventral (p= 0.27) asymmetry (n= 90, Fisher's Exact Test). Average overall, and posterior cranial base length increased at roughly the same rate in the mutant and wildtype between P7 and P21 (Figure 3.15); echoing the trend observed in mutant

body weight, *sbse* growth slowed to 0.2 mm/week, compared to 1.4 mm/week in the wildtype (*sbse*/*sbse* n= 12; C57BL/6J +/+ n= 12; t(22)= 8.28 p< 0.001).

THE RATE OF AP GROWTH IN THE MUTANT IS UNAFFECTED UNTIL P21 Compared to the C57BL/6J +/+ wildtype, basion to incisors incisor length is significantly reduced in the mutant at all time points. I examined the association between ossification of the intersphenoidal synchondrosis and the rate of anterior-posterior growth. Echoing a trend observed in bodyweight, average anterior-posterior cranial dimensions increased at roughly the same rate in the mutant and wildtype between P7 and P21 (Figure). Between P21 and P28, growth in the mutant slowed to 0.2 mm/week, compared to 1.4 mm/week in the wildtype (Figure 3.15). (*sbse*/*sbse* n= 12; C57BL/6J +/+ n= 12; t(22)= 8.28 p< 0.001).

CRANIAL BASE ANGLE MAY BE AFFECTED BY ISS OSSIFICATION Both the angle made by the snout between the ISS, crista galli, and the incisors (*sbse*/*sbse* n= 12; C57BL/6J +/+ n= 12; t(22)= 3.23 p= 0.0038) and the angle of the cranial base, between crista galli, the ISS and basion are significantly different in mutants. Gradual flexion between P7 and P28 in the wildtype mouse skull make the cranial base-nasomaxillary complex flatter over time. In the mutant, the cranial base angle does not change significantly (Figure 3.18).

The range of angular values measured in the mutant is larger, and in the measurement of the cranial base angle, appears to separate into subgroups based on ossification of the intersphenoidal synchondrosis. Although sample sizes are too low to test for significance, lack of ectopic ossification of this site at P14 and P21 is

predictive of a more acute, wildtype-like cranial base angle. (Figure 3.14).

Incidence of abnormal suture, synchondrosis, symmetry, and ear phenotypes in the *sbse/sbse*, P7-P28.

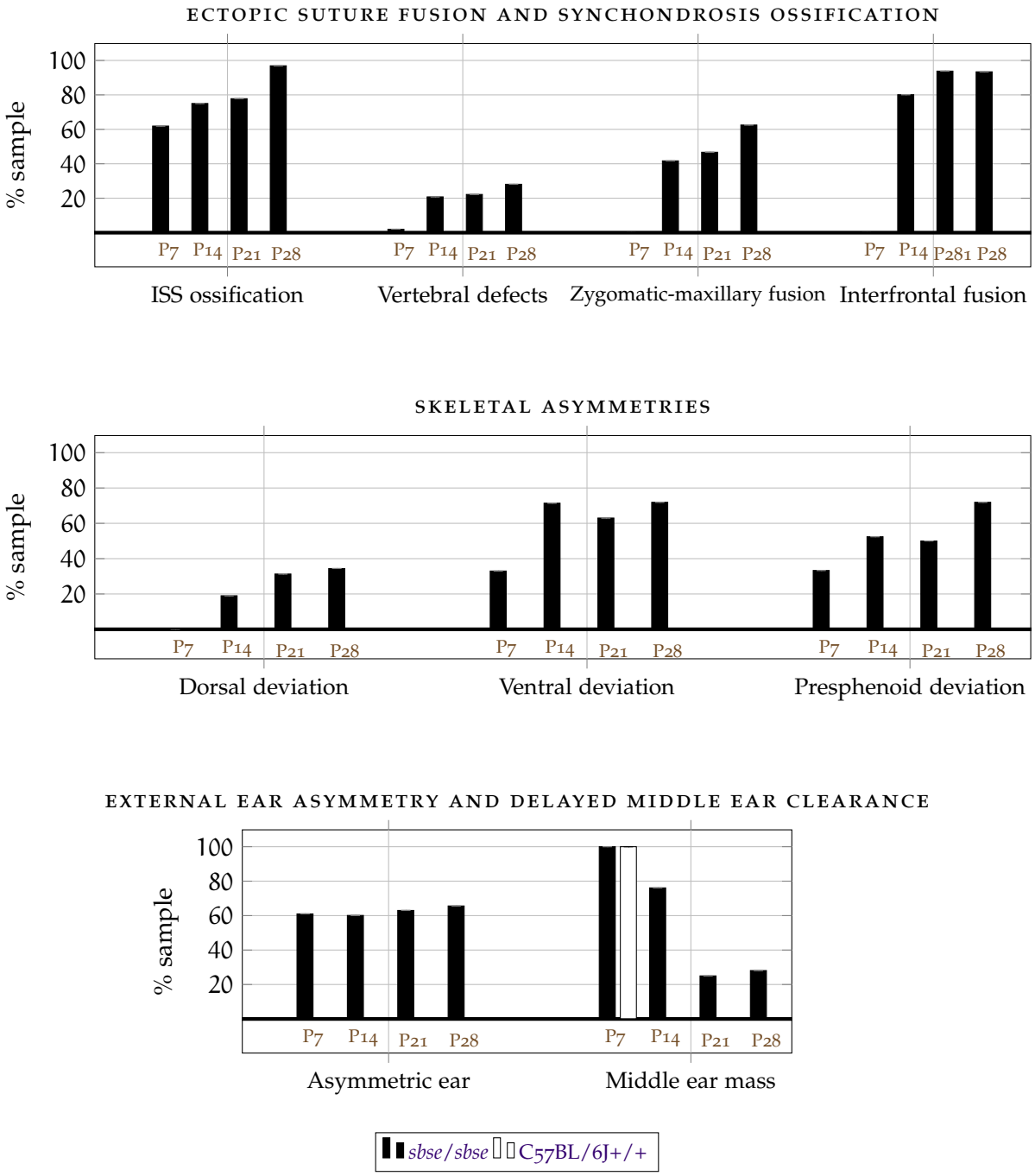

Figure 3.12: Timeline of *sbse* trait development

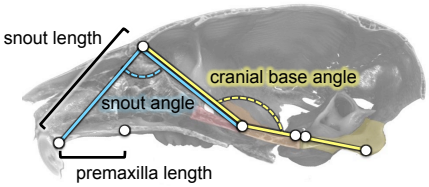

(a) AP dimension landmarks, lateral.

Black lines, premaxillary and snout lengths. *Blue*, snout and *Yellow*, cranial base angles.

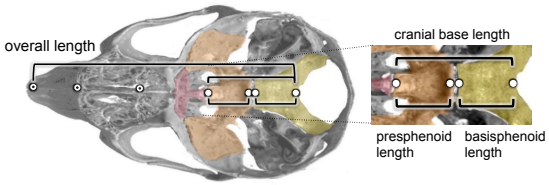

(b) AP dimension landmarks, dorsal.

Black lines, overall, crania base, basisphenoid and basioccipital length.

Figure 3.13: Anterior-posterior growth and angulation measurements. µCT scan rendering of a representative P28 C57BL/6J +/+ skull showing linear measurements and cranial angles.

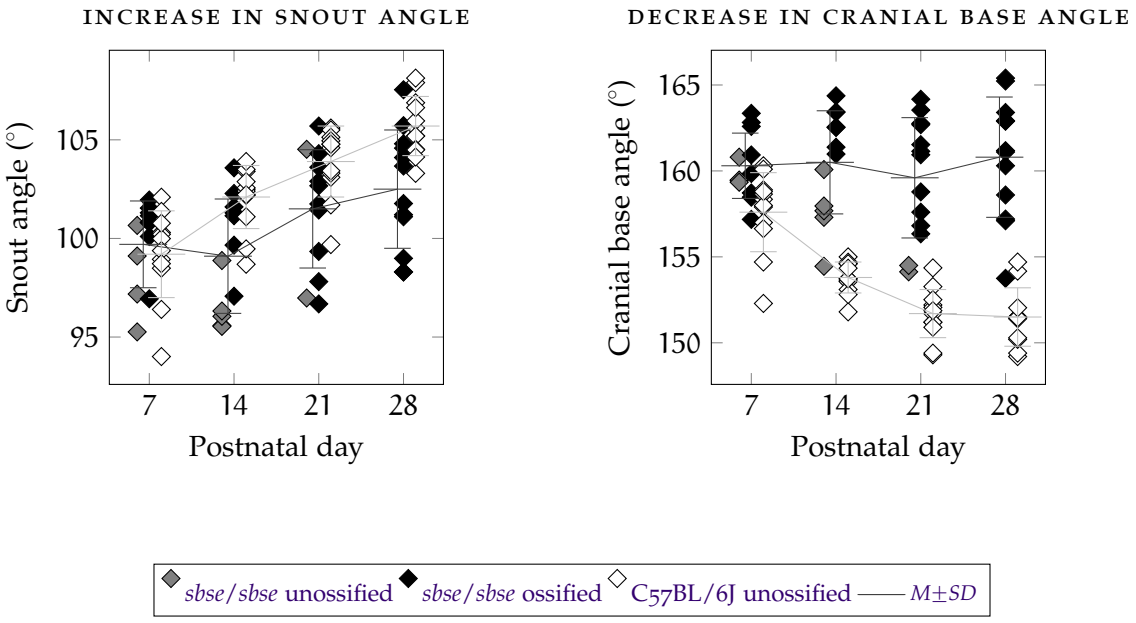

Figure 3.14: Changes in the angle of the snout and cranial base in *sbse/sbse*, P7-P28. Cranial base angle becomes more acute in the wildtype mouse (average Δ= 6.2° between P7 and P28) with minimal change in the mutant (average Δ= 0.5°) (*sbse/sbse* n=12; C57BL/6J +/+ n=12; $t(22)$=8.28 p<0.0001) In mutant animals without ossification of ISS, cranial base angle appears to change normally.

Anterior-posterior growth in the *sbse/sbse*, P7-P28.

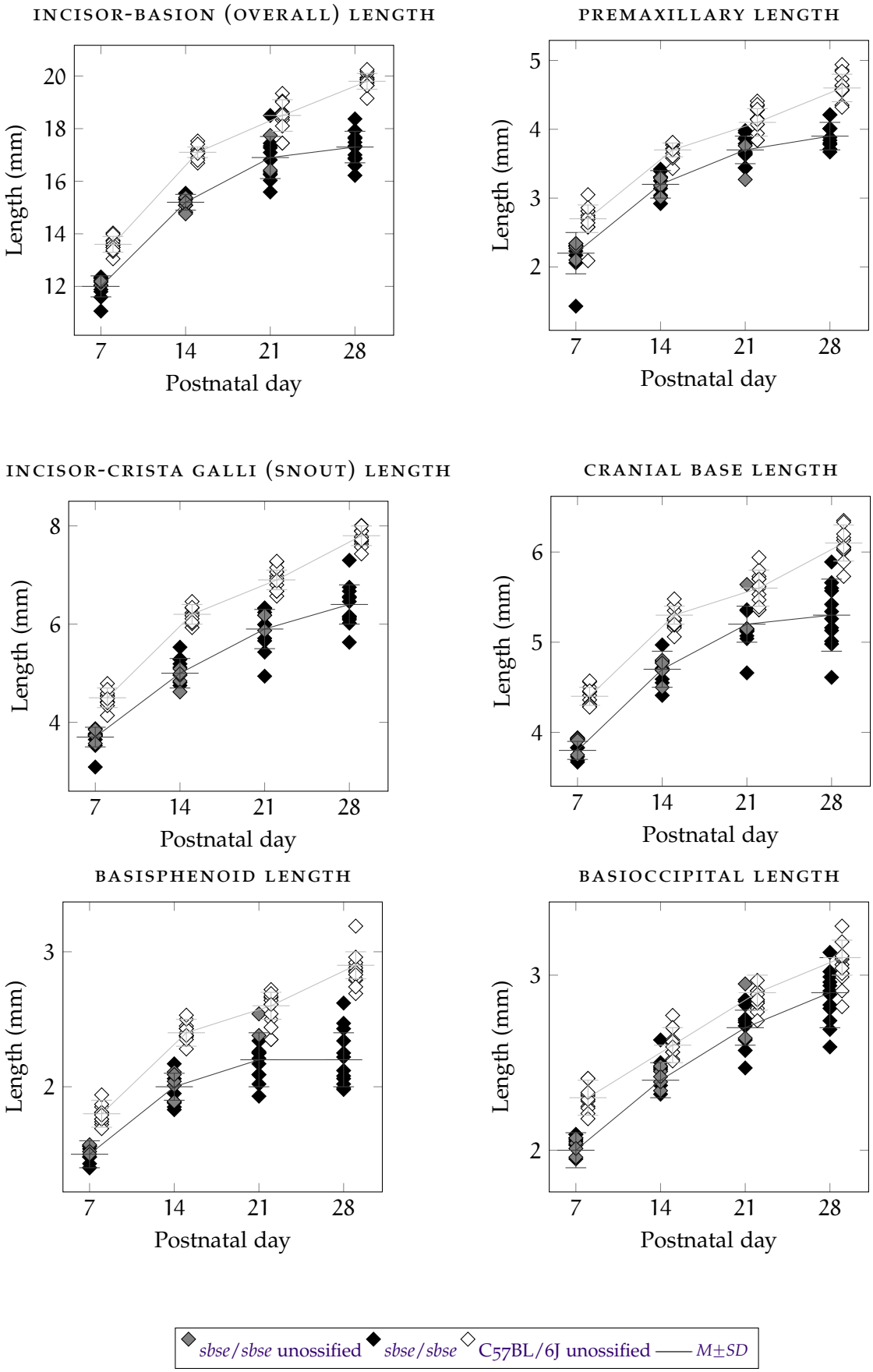

Figure 3.15: Anterior-posterior cranial growth in the *sbse*, P7-P28 Postnatal growth in the anterior-posterior dimension is abnormal in the *sbse/sbse* mutant.

The anterior-posterior length of the *sbse/sbse* mutant is significantly shorter in all dimensions at all ages. Between postnatal day (P)7 and P14, the average wildtype C57BL/6J +/+ controls and mutant *sbse/sbse* grow at similar rates. Between P14 and P28, the rate of overall anterior-posterior growth and growth in the cranial base decreases in the mutant.

3.2.4 *Lateral facial asymmetry in the sbse*

3.2.4.1 *Mandibular asymmetry is concentrated in the condyle*

Given the pronounced deviation of the *sbse* maxilla, there must be a region of unilateral deficiency in the mandibl that helps the lower jaw adapt. I quantified the difference between left and right bones in the hemimandible pairs of mutant and wildtype mice using a landmark-independent analysis tool devised by SM Rolfe. Both global and local asymmetry rankings correlated highly with visual ranking of mandibular asymmetry (n= 23; $r(21) = 0.92$ and $r(21) = 0.91$, respectively). *Post hoc* comparison found that the skulls of all *sbse* with dorsally apparent maxillary asymmetry have mandibular asymmetry scores above the global and local thresholds, suggesting that differential growth at the condyle may be enough to compensate for maxillary asymmetry.

3.2.4.2 *External ear hypoplasia is a fully penetrant phenotype*

Size and position of the external ears was assessed based on visual appearance in animals before μCT scanning. Hypoplasia of the external ears is present in all homozygote *sbse*, one of the most consistent phenotypes in terms of both expressivity and penetrance 3.19). In 65.6% of mutants at P28, the left and right ears are placed asymmetrically relative to the sagittal and anterior-posterior axes, e.g., one ear may be further forward and slightly above or below the other, relative to the sagittal and transverse planes (Figures 6.4). Asymmetry is present at P7, and remains at between 60% and 65% of the population through P28. Categorical comparisons found that the side towards which the maxilla deviates, relative to the sagittal plane, is strongly associated with side of dropped ear placement by the chi-square test of independence (χ^2 (2, n= 90)= 31.7, $p < 0.001$) .

Table 3.6: Anterior-posterior growth in the *sbse/sbse*, P7-P28.

	POSTNATAL DAY			
DIMENSION	P7	P14	P21	P28
Average incisor-basion (overall) length (mm)				
sbse/sbse	12.00 ± 0.38	15.16 ± 0.27	16.86 ± 0.79	17.27 ± 0.60
C57BL/6J +/+	13.58 ± 0.27	17.07 ± 0.24	18.45 ± 0.58	19.83 ± 0.29
	p < **0.001***	p <**0.001***	p <**0.001***	p= **0.012**
Average premaxillary length (mm)				
sbse/sbse	2.18 ± 0.25	2.42 ± 0.16	2.77 ± 0.22	3.10 ± 0.19
C57BL/6J +/+	2.69 ± 0.23	2.95 ± 0.11	3.30 ± 0.2	3.67 ± 0.19
	p < **0.001***	p <**0.001***	p= 0.03	p= **0.012***
Average incisor-crista galli (snout) length				
sbse/sbse	3.67 ± 0.21	4.00 ± 0.26	4.48 ± 0.43	5.59 ± 0.22
C57BL/6J +/+	4.48 ± 0.17	4.95 ± 0.16	5.59 ± 0.22	6.16 ± 0.17
	p < **0.001***	p <**0.001***	p <**0.001***	p= **0.012***
Average cranial base length				
sbse/sbse	3.84 ± 0.10	4.03 ± 0.15	4.31 ± 0.18	4.60 ± 0.35
C57BL/6J +/+	4.41 ± 0.10	4.63 ± 0.11	4.92 ± 0.19	5.23 ± 0.17
	p < **0.001***	p <**0.001***	p <**0.001***	p= **0.012***
Average basisphenoid length				
sbse/sbse	1.50 ± 0.06	1.61 ± 0.11	1.76 ± 0.13	1.92 ± 0.21
C57BL/6J +/+	1.80 ± 0.07	1.96 ± 0.07	2.18 ± 0.13	2.40 ± 0.13
	p < **0.001***	p <**0.001***	p <**0.001***	p= **0.012***
Average basioccipital length				
sbse/sbse	2.04 ± 0.05	2.13 ± 0.08	2.26 ± 0.12	2.41 ± 0.15
C57BL/6J +/+	2.29 ± 0.07	2.36 ± 0.08	2.47 ± 0.06	2.61 ± 0.12
	p < **0.001***	p <**0.001***	p=**0.04***	p= **0.012***

n= 12 for all groups *p <**0.05**

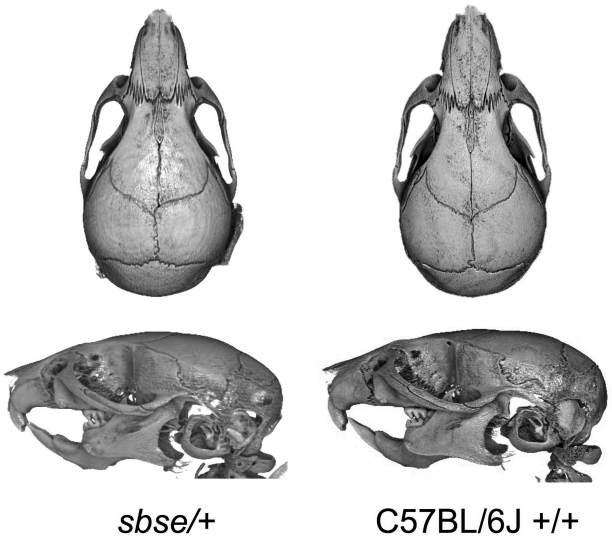

Figure 3.16: The *sbse*/+ phenotype. Dorsal and lateral views, *sbse*/+ ⟡ and C57BL/6J +/+ ◇ at P28. μCT scan renderings.

Figure 3.17: Comparison of *sbse*/*sbse*, *sbse*/+, and +/+ phenotypes.

	◆		⟡		◇	
Trait	#*sbse*/*sbse*	n= 32	# *sbse*/+	n= 20	C57BL/6J +/+	n= 16
Cranioskeletal asymmetries						
Maxillary deviation						
Dorsal	11	34.4%	2	10.0%	0	0.0%
Ventral	23	71.9%	10	50.0%	0	0.0%
Presphenoid deviation	23	71.9%	9	45.0%	0	0.0%
Suture defects						
Zygomatic-maxillary suture fusion	20	62.5%	2	10.0%	0	0.0%
Posterior interfrontal suture fusion	30	93.8%	8	40.0%	0	0.0%
Synchondrosis/cartilage defects						
Ectopic synchondrosis ossification						
Intersphenoidal synchondrosis	31	96.9%	9	45.0%	0	0.0%
Spheno-occipital synchondrosis	2	6.3%			0	0.0%
Vertebral synchondrosis	9	28.1%	3	15.0%	0	0.0%
Ear defects						
Middle ear mass	21	28.1%	3	15.0%	0	0.0%
Asymmetric external ear position	21	65.6%	5	25.0%	0	0.0%

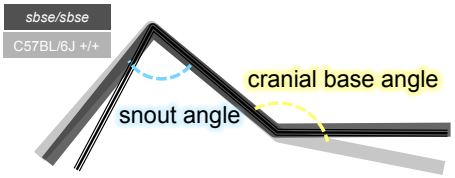

Figure 3.18: Model of angle changes in the *sbse*. *Triple black line*, *sbse* and C57BL/6J snout and cranial base angles at P7. *Dark gray*, *sbse* at P28. *Light gray*, Wildtype at P28.

3.2.4.3 *Radio-opacity in the middle ear*

µCT scan reconstructions of *sbse/sbse* crania at P28 revealed radio-opacity in one or both middle ear chambers in 28% of homozygotes (Figures 3.19a and 3.19c). This mass is present in 100% of wildtype animals at P7, but completely disappears by P14 (Figure 3.12). A two-tailed Fisher's exact test revealed a significant association between asymmetric placement of the external ear and radiopacity within the middle ear at P28 (n= 32, p= 0.04).

3.2.4.4 *The shape of the auditory ossicles is normal in mutants*

Age-related hearing loss is reported in the *sbse*. Curtain et al. (2001) found a 20 db higher threshold in mutants at 7 weeks of age, by auditory brainstem response threshold analysis.[102] Examination of the auditory ossicles at P28 by µCT scan rendering revealed no morphological abnormalities (*sbse/sbse* n= 32 +/+ n= 3).

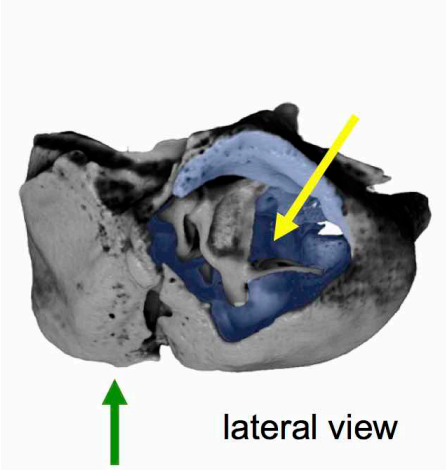

(a) Lateral view looking into the external auditory meatus. µCT scan rendering of a disarticulated mouse tympanic bulla. *Blue*, the surface of the middle and inner ear.

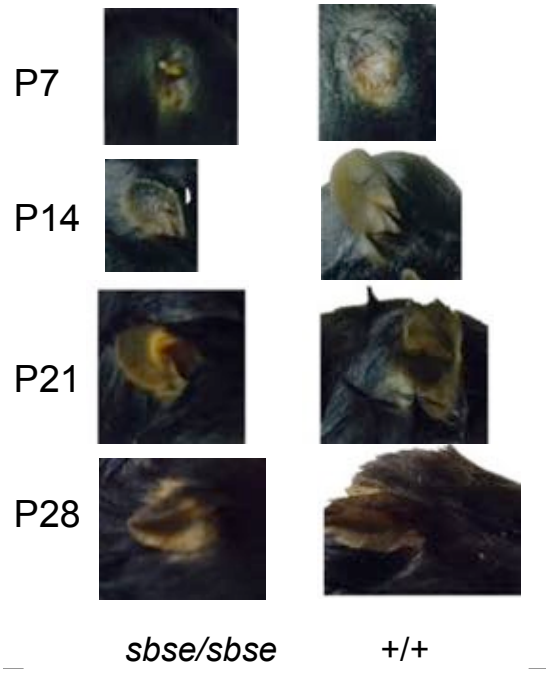

(b) External ears morphology, P7-P28 *sbse/sbse* mutant ears are smaller at birth, and do not catch up with those of wildtype C57BL/6J +/+.

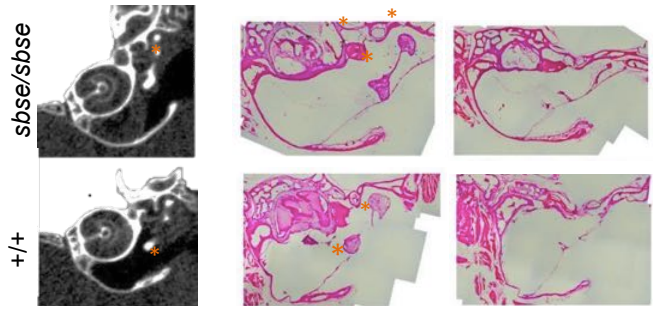

(c) Radio-opacity in the *sbse* middle ear.

Figure 3.19: Ear phenotypes in *sbse* mice. (a) µCT scan rendering of a C57BL/6J +/+ mouse tympanic bulla, looking through the external auditory meatus and middle ear. *Green arrow* rostral end. *Yellow arrow*, ossicles. **(b)** *sbse* homozygote ears are noticeably hypoplastic at P7, and do not catch up to those of the wildtype. Radio-opacity in the mutant and wildtype middle ear, P7 through P28. **(c)** Histology is inconclusive on the identity of the radio-opaque tissue within the mutant middle ear.

3.3 DISCUSSION

The *sbse* mouse carries a recessive mutation causing malformations homologous to those occurring in patients with BA syndromes. Mutants are difficult to visually differentiate without μCT scan renderings at postnatal day (P)7. By P14, asymmetry relative to the sagittal suture begins to manifest. At P28, the mutant is clearly differentiable from heterozygotes and wildtype animals. While the mutation associated with the phenotype has not been identified in any human craniofacial malformations, *sbse* serves as a model relating the appearance of skeletal asymmetry, anterior-posterior growth, and cranial base flexion through the development of the young adult skull. In this chapter, I describe the effect of the mutation on basic characteristics and outline growth pattern of these mice and test the association of growth site defects with facial asymmetry and outgrowth.

3.3.0.1 *Reduced fecundity and body size suggest that the sbse mutation may affect expression of the candidate gene Plag1*

Curtain, et al. (2001) mapped the *sbse* mutation to the neighborhood of the transcription factor *Pleomorphic adenoma gene 1* (*Plag1*), variants of which have been found to regular body size differences across multiple species.[102,141] Both *Plag1*-null and *sbse* homozygotes are significantly smaller than controls, and produce fewer pups per litter (■×●) than wildtypes cross.[102,104] *Plag1*-null reproductive ability issues are thought to be influenced in both male and female reproductive systems. *Plag1*-null males are less fecund; when successful, litter size is reported to be normal. In contrast, fewer pups were counted in litters born to mutant *sbse/sbse* or *sbse*/+ and C57BL/6J (+/+) dams, suggesting that there is a paternal effect on *sbse* reproductive ability. In female *Plag1*-null mice, reduced uterine capacity is thought to contribute to reproductive

ability defects; relative size and genotype of uterine tissue, along with placental size and vascular density are considered to regulate litter size and postnatal body weight in the offspring.[141–145] *Post hoc* analysis of the *sbse* colony records, comparing the effects of maternal genotype on body size, weight, embryonic lethality, and eventual reproductive productivity might be fruitful in light of findings presented in Chapters 5 and 6. Reduced body size and reproductive ability in knockout mice suggest that the mutation causing the *sbse* phenotype may include a loss of function or hypomorphic dysregulation of *Plag1*.

Compared to control animals, the bones of the *sbse/sbse* midface are deficient at P7, morphologically immature at P28, and shorter in length at all timepoints. Midfacial deficiency and cranial vault doming in homozygotes is present soon after birth, before the majority of defects affecting the sutures, synchondroses, and lateral facial tissues arise. In this chapter, I examine the timing of cranioskeletal malformations in the *sbse* and test the relationship between ectopic postnatal fusion or ossification in the face or cranial base and asymmetry, anterior-posterior growth, and cranial flexion.

Asymmetry is a frequent feature of the homozygote phenotype, affecting the maxillary, cranial base and lateral facial regions in 34%-71.9% of homozygotes animals at P28; asymmetric defects in an individual typically affect the same side. In the *sbse* mouse, the paired zygomatic-maxillary and midline posterior interfrontal suture begin to fuse ectopically between P7 and P14. Surprisingly, there was no relationship with asymmetry and fusion of the orbital suture. I found a significant posterior interfrontal (IF) suture fusion and asymmetry relative to the sagittal plane (dorsal deviation). If fixation is a functional adaptation, the (chronological or developmental) timing at which it occurs may be critical.

Midfacial asymmetry is presented in several publications reporting on Apert mutant mice.[3] If dysregulation of interfrontal suture fusion timing affects the geometry of the anterior cranial vault, it may influence the symmetric outgrowth of the snout. While statistically significant, no evidence exists that premature fusion at this site affects midface development, although it might provide an interesting environment to test the role of the dura mater on suture fusion and interfrontal bone formation.

Normal fusion of the posterior interfrontal (IF) suture occurs through endochondral ossification.[148–150] A number of cartilaginous defects are present throughout the mutant skeleton, affecting the ossification of cranial base and vertebral synchondroses, the midline elements of the sternum, and deficiencies of growth plate tissue at the sacral vertebrae. These defects are important in light of the vertebral defects that characterize OAVS.

Defects in the cranial base synchondroses are typically considered the cause of craniofacial malformations in mice with skeletal dysplasias.[29]. Both surgical and congenital fixation of synchondroses affect the length of the cranial base, a trait which is highly correlated with cranial and facial shape in neonates.[83,147,151,152] Cartilage undergrowth in *brachymorph* (*bm*) mice results in cranial base and snout shortening, cranial vault doming, and in at least one published image,[4] facial asymmetry.[153,154] In a related model, a local defect in presphenoidal chondrocyte proliferation in the *Brachyrrhine* (*Br*) strain is sufficient to cause defects in the anterior cranial base, midface hypoplasia and subtle fluctuating asymmetry in the cranium.[155–157] A early reduction in sphenoid length in human evolution is thought to have decreased facial projection in our skulls.[86] The reduction in basisphenoid length in the *sbse* may

3 ($Fgfr2^{S252W}$, Wang et al. (2005) Figure 3C.[146] $Fgfr2^{P253R}$ Yin et al. 2008, Figure 4B.[147]).
4 *bm/bm* Hallgrímsson, et al. 2006 Figure 2.[153]

have a similar effect, supporting the hypothesis that fixation at the intersphenoidal synchondrosis affects cranial base length. There is insufficient evidence to suggest that shortening of the cranial base is causative to any midface phenotype.

The angle of the murine cranial base increases during the first month of development to accomodate the growing brain[158] In the mutant *sbse*, the average remains the same from P7 though P28. (ISS fixation may have a direct effect on cranial base flexion: although more datapoints are necessary, *sbse* without synchondrosis ossification trend towards a more wildtype-like cranial base angle. Restriction of the interfrontal suture, fixation of the intersphenoidal synchondrosis, and abnormal flexion of the cranial base may affect the process of secondary displacement in the *sbse*. Without normal growth and morphogenesis in the neurocranium, movement and subsequent growth of the maxilla and premaxilla of the *sbse* is restricted.

In this chapter, I examined the postnatal growth pattern in the *sbse* mutant, and tested the association of various growth site defects on the progressive development of its phenotype. Further work on the postnatal mechanisms influencing midface dysmorphology may test the effect of interfrontal suture and intersphenoidal synchondrosis fixation on cranioskeletal morphology in wildtype animals. A combination of dietary and surgical interventions could be utilized to try and rescue asymmetry in mutants. Finally, the variety and frequency of cartilaginous defects observed in the *sbse* suggest further histological study of the chondrocyte populations in the cartilaginous nasal septum.

4

"FROGGY" (FRG)

4.1 OVERVIEW

Craniofacial malformations occur in a third of all children born with birth defects, and are associated with mutations affecting components of many major signaling pathways, including genes associated with *fibroblast growth factor* (FGF), *sonic hedgehog* (SHH), *wingless* (WNT), and Rho signaling.[10,159] Complex signaling cascades may be sensitive to mutations affecting individual pathway members, as well as the epistatic effect of wildtype modifiers or distinct mutations in interacting genes.

Complementation tests are used to determine if phenotypically similar mutations mapped to the same region in the genome affect the same gene, or to test if two mutations on different chromosomes interact. Mutations affecting expression of a member of the WNT signaling pathway predisposes mice to nonsyndromic cleft lip with and without cleft palate.[28] Compound heterozygosity of the clefting-associated locus *clf1*, which includes the gene *Wnt9b*, with a null allele of *Wnt9b* replicates the predisposition of inbred A/WySn mice to orofacial clefting. The genotype of a second locus (*clf2*) on a different chromosome was shown affect the penetrance of the clefting phenotype in these mice.[27] The *clf2* gene has not been identified, although it thought

to regulate methylation of the *Wnt9b/clf1* locus. The interaction of *clf1* and *clf2* is an example of "unlinked non-complementation," a state in which concurrence of two otherwise silent heterozygous mutations at different, but interacting loci "cause the phenotypic threshold to be exceeded".[160].

This chapter focuses on the asymmetric craniofacial phenotypes of two lines of mutant mouse, "*Small body, small ear*" (*sbse*) and "*Froggy*" (*frg*). Both lines arose as spontaneous mutants at the Jackson Laboratories (Bar Harbor, ME, USA), and carry recessive mutations that cause cranioskeletal dysmorphology. Notably, both have highly penetrant premaxillary-maxillary asymmetry, but are able to maintain the dental occlusion. (Asymmetry affecting both the upper and lower jaws is rarely reported in mouse models of these conditions.)

The *frg* mutation has not been definitively identified, but was mapped between the microsatellite markers D13Mit88 and D13Mit248, a 14 Mb stretch of mouse chromosome 13, by the Donahue lab at the JAX, while the *sbse* mutation has been identified as a rearrangement on mouse chromosome 4, affecting the *Plag1-Chchd7* locus.[102,103] In this chapter, I compare the phenotype of the *frg* mouse with the *sbse*, attempt to identify its causative mutation, and test if the maxillary and mandibular asymmetry trait is due to genetic interaction between the *frg* and *sbse* loci. for unlinked non-complementation.

MUTANT MOUSE NOMENCLATURE The name of the strain, *frg* ("*froggy*") may refer to the unusual, frog-like appearance of their limbs and their invariably wide-set eyes.

Table 4.1 defines the two mutant alleles and three final genotypes of interest presented

this study.

Table 4.1: Key to *frg* and *sf* mutant strain IDs

STRAIN	GENOTYPE	WT			BACKGROUND
sbse	*sbse/sbse*	+/+	spontaneous	JAX[102,108]	C57BL/6J
frg	*frg/frg*	+/+	spontaneous	JAX[103,108]	A/J
sf	*sbse/frg*	+/+		JAX	C57BL/6J-A/J

4.2 RESULTS

4.2.1 *Inheritance and body size*

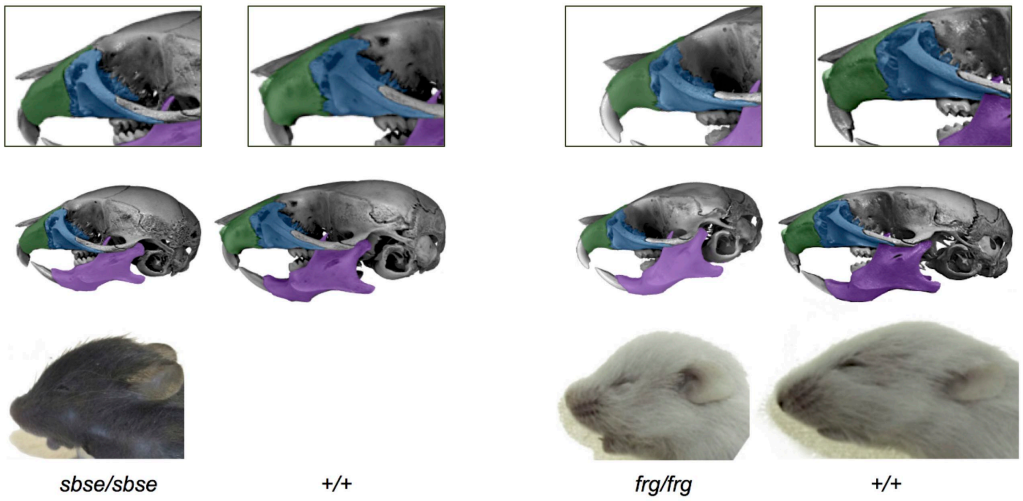

(a) Midface deficiency and cranial doming.

Top row: dysmorphology and hypoplasia (MFH) of the premaxilla and maxilla. Middle and bottom rows: MFH and cranial doming

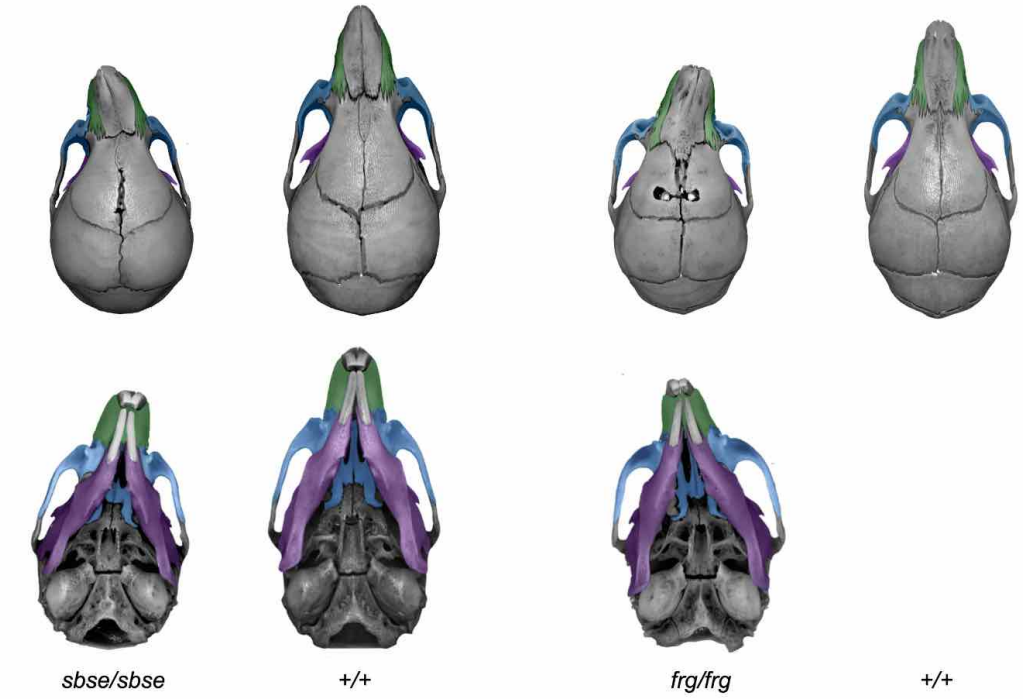

(b) Midface deficiency and cranial doming.

Top row: dorsal view, showing maxillary deviation in the **(a)** *sbse* and **(b)** *frg*, alongside background-match wild-type controls. Bottom row: ventral view, showing mandibular deviation, mirroring the maxilla, in the mutants.

Figure 4.1: Comparison of *sbse* and *frg* midface morphology. The *sbse* and *frg* mutations cause similar facial phenotypes. μCT scan renderings and photographs of representative mutants and wildtype controls (P28).

Blue, maxilla. *Green*, premaxilla. *Purple*, mandible.

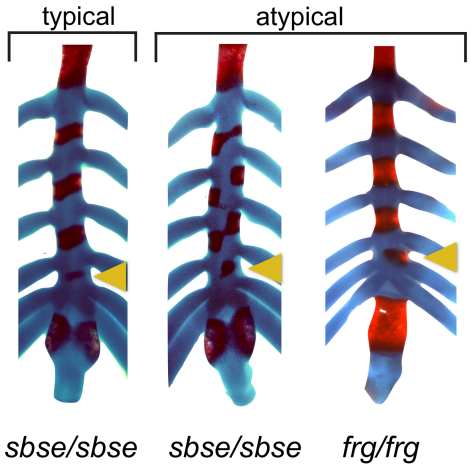

Figure 4.2: Ossification defects in the body of the sternum occur in both the *sbse* and *frg* mutants.
(a) An atypical checkerboard-like pattern has been found in the sternum of *sbse/sbse* neonates; incomplete ossification of S4 (yellow arrow) in *frg/frg*. **(b)** Typical appearance of the body of the sternum. S, sternebra (1-5). M, manubrium. Z, ziphoid process. (*sbse/sbse* n=4, *frg/frg* n=3). (Po)

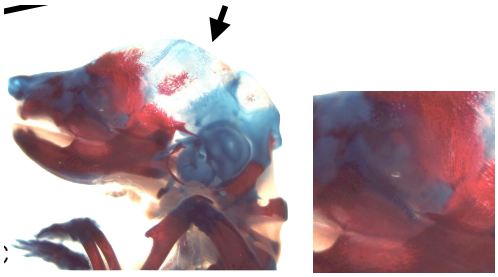

(a) Severely affected *frg/?*

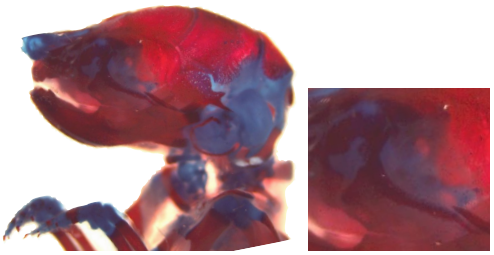

(b) Typical *frg/?*

(c) *sbse/sbse*

Figure 4.3: Calvarial and zygomatic defects in *frg*. *frg* pups born to a mixed (◆×◇) cross. **(a)** Typical morphology in a *frg*/?. **(b)** Absence of the calvarial bones and lack of mineralization in the zygomatic process of the maxillary in an affected *frg*/?. **(c)** The *sbse/sbse* calvaria and zygomatic process of the maxillary appear ossified as expected. Alcian *blue* (cartilage) and Alizarin *red* (mineralized tissue) staining, E18.5.

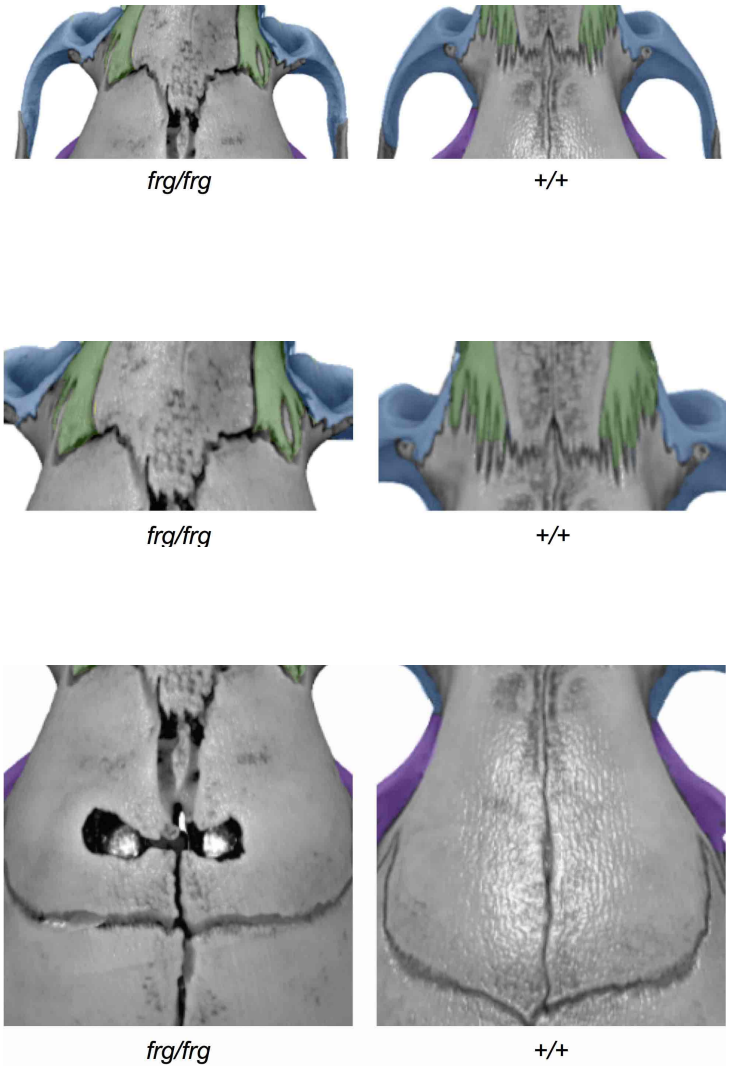

(a) Curvature of the zygomatic arch.

Unusual curvature of the zygomatic arch, with a particular robust maxillary process.

(b) No interdigitation in the *frg/frg* frontal-maxillary suture.

(c) Large gaps in the bone near the interfrontal suture.

Figure 4.4: Craniofacial phenotypes unique to the *frg*.

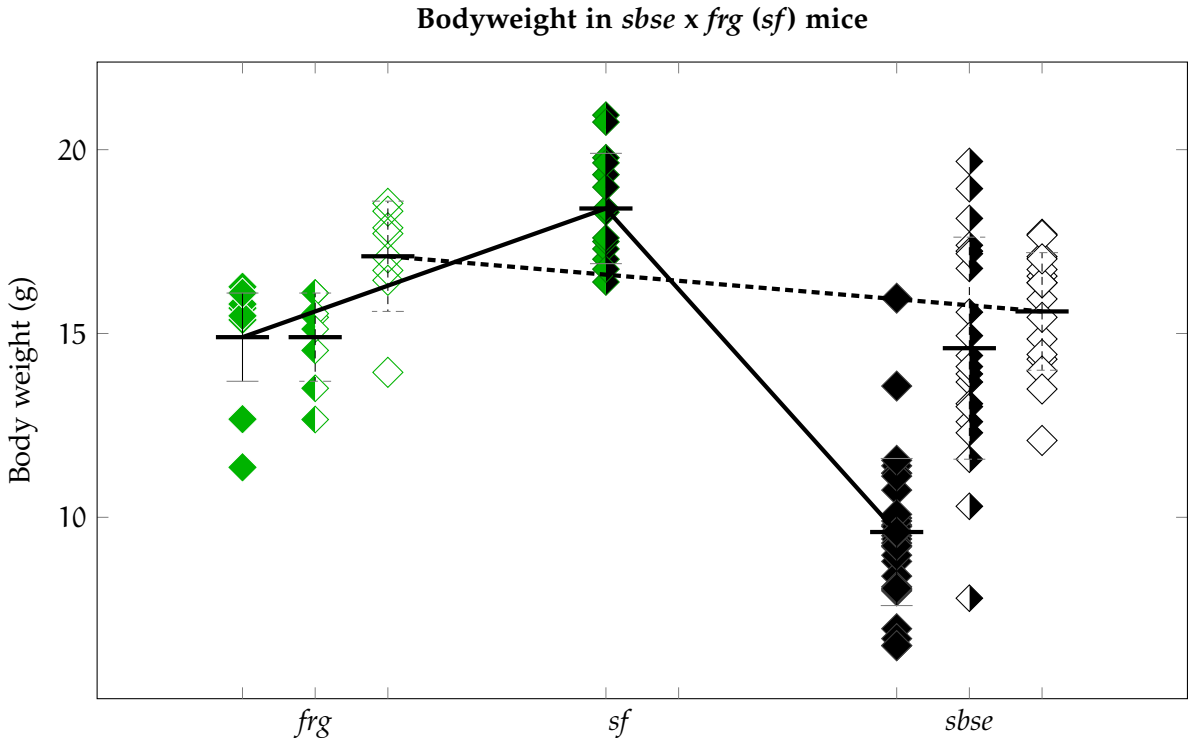

Bodyweight in the *frg*, *sf*, and *sbse* lines *Solid horizontal lines* Animals homozygous for *sbse* and

(a) Bodyweight in the *frg*, *sf*, and *sbse* lines

frg mutations are typically lighter than wildtype controls. *sf* mutants are heavier than wildtype C57BL/6J or A/J wildtype controls. (Table 4.2).

Table 4.2: Bodyweight in the *frg*, *sf*, and *sbse* lines

	◆			◈			◇	
	M ± *SD*	*n*=		*M* ± *SD*	*n*=		*M* ± *SD*	*n*=
frg	*frg/frg*			*frg/+*			**+/+**	
	14.7 ± 1.9	4	***t*(13)=2.7 p=0.02***	14.9 ± 1.2	22	***t*(14)=-3.23 *p*=0.006***	17.1 ± 1.5	10
sf				*sbse/frg (sbse/+ +/frg)*				
				18.5 ± 1.5				
sbse	*sbse/sbse*			*sbse/+*			**+/+**	
	9.5 ± 2.0	32	***t*(46)=10.6 *p*<0.001***	14.6 ± 3.0	20	*t*(34)=1.2 *p*=0.24	15.6 ± 1.6	16

*Significant difference between mutant and wildtype by unpaired T-test, p<0.05

4.2.1.1 *Variable reproductive capacity and reduced litter size in frg mutants*

The *frg* phenotype appears in all pups born to affected parents, and appears to be inherited in a recessuve fashion.[103]. The offspring of presumed heterozygous crosses (sibling-sibling matings of the F2 generation) showed a *frg*-like phenotype below expected ratios, although it is currently not possible to confirm the genotype of unaffected animals by PCR (Figure 4.5).

Both *frg* and *sbse* mutants suffer from reduced fertility. Over 6 months, 19 pups were born in 4 litters to 2 homozygous (*frg*/*frg*) breeding pairs, for an average of 4.8 pups/litter; 2 cages of siblings set up as homozygous crosses at 6-8 weeks old bore no pups. This trend was observed throughout the time we maintained this line. Over 6 months, 44 pups were born in 7 litters to 4 heterozygous *frg*/+ breeding pairs, for an average of 6.3 pups/litter. No unproductive heterozygous breeding pairs were observed (Table 4.3).

Both homozygous and heterozygous *frg* mice weigh less than wildtype controls (Figure 4.5a).

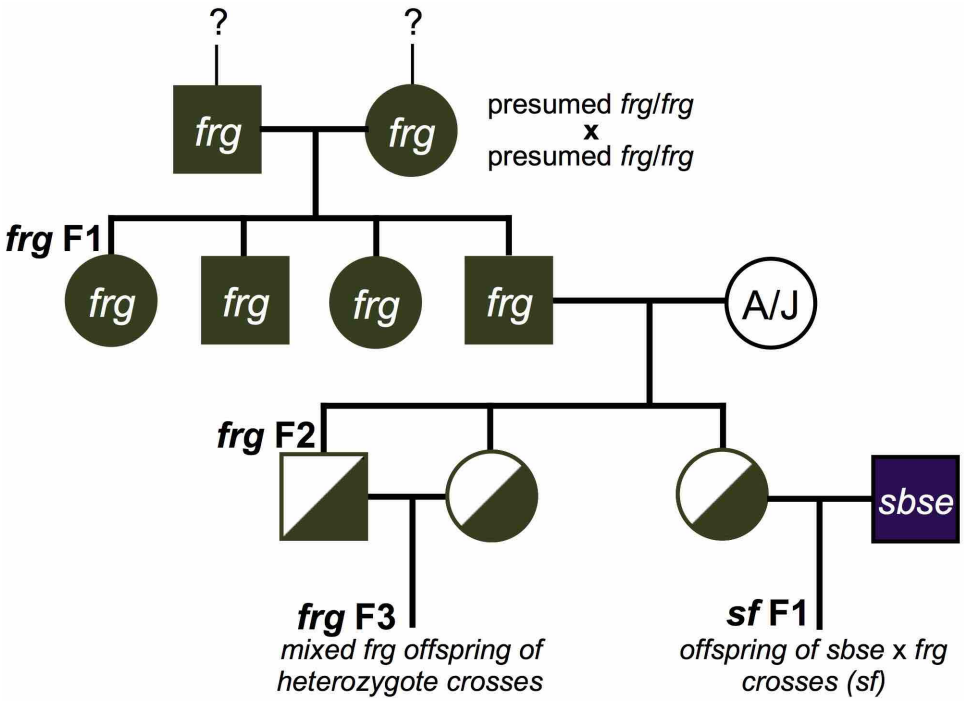

Figure 4.5: Representative pedigree, *frg* and *sf* colonies. A phenotype-specific breeding strategy was required in the absence of a PCR-testable genotype for *frg*. *sf* mutants were generated by crossing a heterozygous *frg* dam with a homozygous *sbse* sire.

Table 4.3: Litter size in *frg* mice.

Cross	# Litters	# Pups	M ± SD
Post-natal *frg*			
frg/*frg* × *frg*/*frg*			
■×●	4	19	4.8
frg/+ × *frg*/+			
◪ × ⊘	7	44	6.3
frg/*frg* × *frg*/+			
◆ × ◇	7	38	5.4
Double heterozygote *sf*			
sf sbse/*sbse* × *frg*/+			
■×⊘	3	20	6.7
Postnatal single heterozygote *sbse*			
sbse sbse/*sbse* × *sbse*/+			
◪×⊘	4	24	6

4.2.2 *The frg and sbse mutants have similar midface phenotypes*

4.2.2.1 *Comparison of the frg and sbse mutants*

The characteristic *sbse* and *frg* midface phenotypes are inherited recessively, and feature variable craniofacial defects (Figure 4.1a). In both lines, the midface frequently appears deviated or bent away from the midline, affecting the symmetry of the upper and lower jaws and allowing the incisors to occlude (Figure 4.1b). Hearing loss is reported in both lines, although it is likely to be a background-specific effect in the *frg*; atypical hearing loss is reported in the *sbse*.[102,103,161] Postcranial defects include abnormal ossification in the body of the sternum, and limb size and shape defects (*sbse*) and position (*frg*) (Figure 4.2)

The maxillary process of the zygomatic arch has a robust, squared-off appearance in the *frg*, compared to the wildtype A/J (Figure 4.4a). In the *sbse*, the orbital phenotypes

(width and premature fusion of the zygomatic-maxillary suture) do not affect overall morphology. In differentially stained skeletal preparations of mice at E18.5, the region of the *frg* maxillary process remains cartilaginous in some samples suggesting that mineralization of the anlage may be delayed; mineralization in calvarial bones is also completely absent (Figure 4.3).

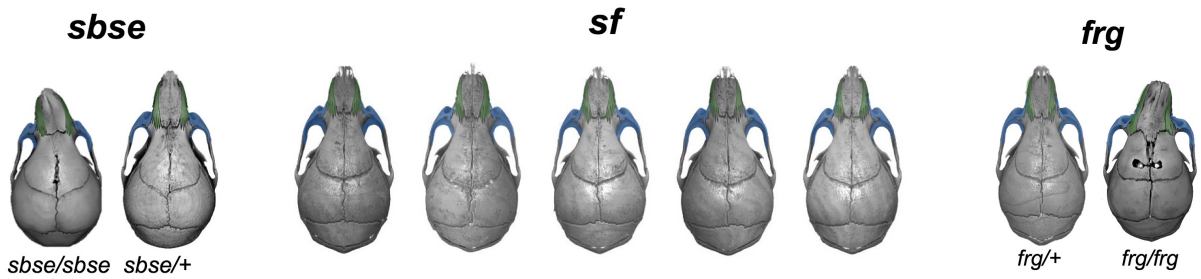

(a) *sbse* **(b)** *sbse* **x** *frg* **(*sf*) double and single heterozygotes.** **(c)** *frg*

Figure 4.6: μCT scan renderings of *sf*, *sbse* and *frg* mutant crania
Dorsal views: **(a)** The cranioskeleton of the average homozygous *sbse/sbse* is dysmorphic, compared to the average heterozygous *sbse/+*. (*purple*) **(b)** There is no significant asymmetry or other dysmorphology apparent in double heterozygote *sf* litters. *sbse/frg* and *sbse/+*. **(c)** The cranioskeleton of the average homozygous *frg* is dysmorphic, compared to the average heterozygous *frg/+*(*green*).

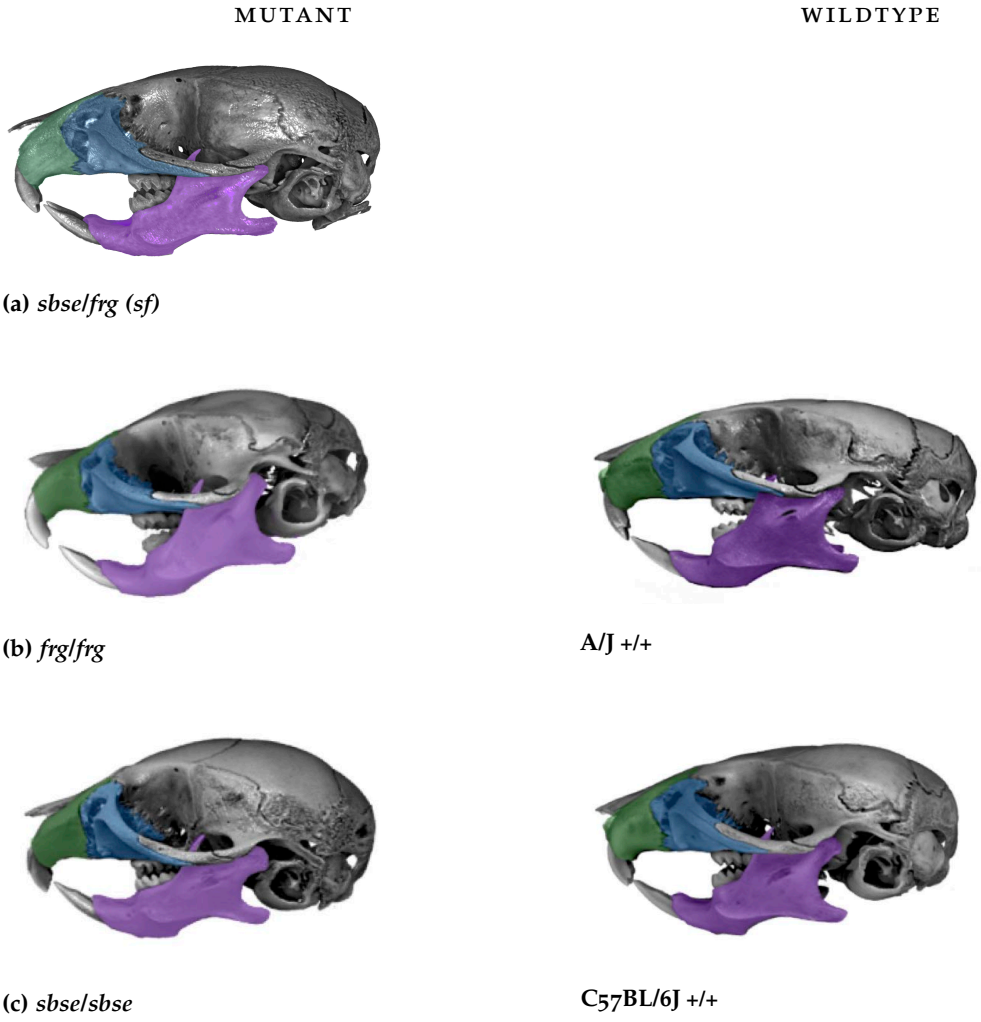

Figure 4.7: μCT scan renderings of *sf*, *sbse* and *frg* mutant crania
Lateral views: **(a)** *sbse/frg (sf)* double heterozygotes do not have significantly dysmorphic cranioskeletal phenotype. **(b)** *frg/frg* and wildtype A/J (+/+). **(c)** *sbse/sbse* and wildtype C57BL/6J (+/+) (Not to scale.)

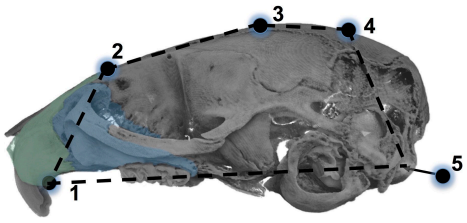

Figure 4.8: Landmarks used to test differences in lateral cranial profile.

Table 4.4: Pairwise comparison of lateral shape: *sbse*, *frg*, and *sf* mutants.

Wildtype controls for *sbse* and *frg* mice are not significantly different at P28.

***p^{perm}<0.01**	*sbse* WT ◇ C57BL/6J+/+
frg WT ◇ A/J+/+	*F*= 6.5 *p*= 0.02

Compound heterozygote *sf* mutants are not significantly different at P28.

***p^{perm}<0.01**	*sf* ◆ *sbse/frg*		*sbse* ◆ *sbse/sbse*		*frg* ◆ *frg/frg*	
sbse WT ◇ C57BL/6J +/+	**F= 6.9**	**p^{perm}= 0.004***	**F= 10.6**	**p^{perm}<0.001***	-	-
frg WT ◇ A/J+/+	**F= 9.9**	**p^{perm}= 0.007***	-	-	**F= 7.8**	**p^{perm}= 0.007***
sf ◆ *sbse/frg*	-	-	**F= 17.7**	**p^{perm}<0.001***	**F= 35.6**	**p^{perm}<0.001***
sbse ◆ *sbse/sbse*	-	-	-	-	**F= 16.2**	**p^{perm}<0.001***

Goodall's F statistic. 1000 permutations. n= 37 Landmarks, Figure 4.8.

A number of defects affect the dorsal surface of the snout, including obliteration of the internasal suture and a pronounced lack of interdigitation at the frontal-maxillary suture (Figure 4.4b). The length of the contiguous naso-maxillary suture is disproportionately wide, relative to the width of the snout. Notably, the nasal bones may form a triangular process extending into the interfrontal region.[1](Figure 3.2d). Gaps in the frontal bones are often continuous with (and sometimes symmetric across) the interfrontal suture (Figure 4.4c).

4.2.3 *The sf double heterozygote is different, but not dysmorphic*

Double and single heterozygotes (*sf* F1) were generated by crossing proven homozygous *sbse* sires with proven heterozygous *frg* dams (■×⊘) (Figure 4.5). Renderings of μCT scan images of the *sf* pups at P28 show no obvious difference in cranioskeletal morphology within the litter (Figure 4.7) (*sbse*/+ *frg* unffected and *sbse*/+ n= 19).[2]

4.2.3.1 *sf double heterozygosity affects mean cranioskeletal shape*

Pairwise comparison of landmark configuration established that the profile of background matched C57BL/6J +/+ and A/J +/+) wildtype crania are not significantly different from one another at P28 (Figure 4.8, Table 4.4). Significant differences were found in the shape of the mutant *sbse* and *frg* profiles compared to their wildtype controls, as well as when compared to one another. Although no significant midface hypoplasia or asymmetry was observed in the *sf* compound heterozygote, shape was

1 A/J and other A-derived mice do not typically have an interfrontal bone.
2 Initial crosses between homozygous *frg* dams and homozygous *sbse* sires were non-productive. The heterozygous dams were selected from members of the F2 generation and crossed with a sibling; at least one pups in the resulting litters had a homozygous phenotype.

found to differ from both the wildtype and mutant crania (Table 4.4; Goodall's F test, n= 37).

4.2.3.2 *Effect of double heterozygosity on body weight*

There is a significant difference between the average body weight of phenotypically affected *frg/frg* mutants (14.8 ± 1.8g, n= 8) and A/J wildtype controls (17.1g ± 1.5g, n= 8) at P28. This 2.3 g difference in average weight is less than the 6 g difference between the *sbse* and C57BL/6J wildtype. The average body weight of the *sf* compound heterozygote group (17.1g ± 1.5g, n= 16) is higher than that the pure mutants and wildtype control groups, possibly a result of hybrid vigor (Figure 4.5a).

4.2.4 *Efforts to identify the mutation causing the frg phenotype*

4.2.4.1 *Putative variants in Sema4d and Kif13a in the frg locus were identified as A/J background-specific polymorphisms*

Analysis of whole genome sequence by Timothy Cox and Andrew Timms identified four possible rearrangements involving three genes (Table 4.5). I tested two of the irregularities identified, affecting the genes *Semaphorin-4D* (*Sema4d*; Figure 4.9a) and *Kinesin family member 13A* (*Kif13a*; Figure 4.9b). Both were confirmed to be background-specific polymorphisms by end-point PCR (PCR results are in the captions of Figure 4.9).

Seven putative structural variants genes were selected for further testing based on their physical location within the *frg* locus and reported expression in the maxillary and mandibular processes of wildtype CD1 mouse embryos at E10.5. (Reported ex-

Table 4.5: Validation of variants predicted in the *frg* genome by WGS (Whole Genome Sequencing)

Gene	Location	Predicted Variant	Finding
Kif13a	x	intronic deletion	A/J-specific polymorphism)
Sema4d	x	2 possible insertions	x A/J-specific polymorphism

pression data was obtained from the FaceBase 24 Sample Types Averaged dataset, available through the University of California Santa Cruz (UCSC) Genome Browser tool.[162]) No significant difference in expression was found in whole embryo tissue at E10.5 in *Hivep1*, *Edn1*, *Phactr1*, *Jarid2*, *Barx1*, *Omd*, or *Ogn* (Figure 4.10).

(a) A/J-specific polymorphism in *Sema4d*
Primers designed to cover a region of intron 2 amplified a 200 bp band in C57BL/6J DNA, and nothing in A/J and *frg*. Primers placed in introns 1 and 2 amplify bands at 300 bp and 500 bp. In the A/J, they amplify bands at 200 bp and 500 bp. In the *frg*, the amplify bands at 200 bp and just below 100 bp.

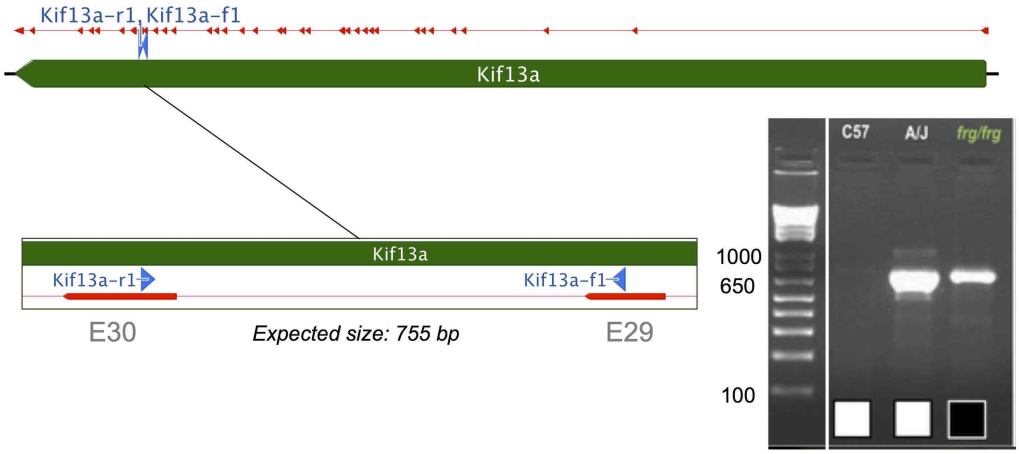

(b) A/J-specific polymorphism in *Kif13a*
Primers were designed to amplify a 755 bp region between exons 29 and 30 amplified a faint band of the expected size in C57BL/6J genomic DNA. In the A/J, this band is much brighter, and two more bands are visible around 1000 bp and 500 bp. Only the expected band appears in *frg*.

Figure 4.9: Background-specific polymorphisms in A/J (a) *Sema4d* **(b)** *Kif13a*

Figure 4.10: *frg* mutation candidate genes within the Chr 13 locus.

4.3 DISCUSSION

small body-short ear (*sbse*) and *froggy* (*frg*) arose spontaneously at the Jackson Laboratories, and were selected for further study based on their dysmorphic (and frequently asymmetric) midface phenotype at postnatal day (P)28. The key shared *sbse* and *frg* phenotypes are midface hypoplasia and dysmorphology, and in particular, the high frequency of asymmetry observed in the upper and lower jaws. Closer examination of the *frg* phenotype revealed several unique phenotypes not present in the *sbse*. Unlike the *sbse*, major deficiencies of mineralization are present in the calvaria and the zygomatic process of the maxillary at E18.5. Reproductive impairment in the strains follows different patterns. In *sbse* mice, the average size of litters born to dams are smaller, but the dams are typically fecund. In the *frg* mutant, while litter sizes are small when crossed with male *frg* sires, the ability of the dams to conceive or carry a litter to birth is impaired.

If the *sbse* and *frg* phenotypes are caused by mutations in unlinked but non-complementary genes, compound heterozygotes (*sf*) would be predicted to have pronounced midface hypoplasia, asymmetry, and cranial vault doming (Figure 4.7). Visual inspection of μCT scan renderings of *sf* crania show minimal dysmorphia and little variability in the mutant skull. Landmarks placed on the lateral cranial profile show a significant difference in mean shape between all the mutants by Goodall's F test. There is no difference in mean shape between A/J and C57BL/6J, suggesting that the landmarks are capturing a real difference in the mutant crania. The body of the *sf* is heavier at P28, although that may be a result of hybrid vigor. It is not possible to differentiate between mutant and background-specific effects on shape or body weight without a C57BL/6J +/+ × A/J control, although reduced variability in the sample, which should contain only *sbse/frg* and *sbse*/+ genotypes, suggests that the genes

involved in the mutations do not interact strongly. (For comparison, see the images of representative *sbse*/+ and C57BL/6J +/+ skulls in Figure 3.16.) It is likely that the mutations causing the *sbse* and *frg* phenotypes act on distinct developmental pathways.

MOLECULAR MECHANISMS

5

PLAG1

5.1 OVERVIEW

Embryonic cranioskeletal development does not occur in a vacuum. The soft tissue surrounding bones - loose mesenchyme, perichondrium, periosteum, musculature, and others - is required to regulate every step from initial ossification through remodeling of mature bones. In the skull, ossification occurs in two distinct populations of mesenchymal precursor cells. In the cranial base and ethmoid, condensations of cells differentiate into cartilaginous anlage before mineralizing; condensations in the facial and calvarial regions mineralize directly.[73] The genetically determined program of tissue growth and development of tissues is reactive to genetic and environmental cues, including blood-borne factors like signaling molecules and oxygen. Hypoxia disrupts cellular respiration, the conversion of biochemical energy sources into usable energy, and thus impairs normal growth and morphogenesis of the embryo. Disruptions in oxygen homeostasis induce rapid physiological responses, including the reduction of oxygen consumption by the cell as well as extension and remodeling of existing vasculature.[163,164] In human populations, fetuses exposed to hypoxic conditions during gestation are at higher risk for malformations of structures derived from the branchial arches.[34,66] The arches are transient structures which undergo rapid growth

and morphogenesis, and give rise to mid- and lateral facial tissues. Experimental evidence suggests that chemical and genetic disruption of the remodeling pharyngeal arch arteries can also to induce facial hypoplasia and asymmetry in murine and primate model systems.[31,32,64,165]

The *sbse* phenotype is inherited in a recessive fashion, and is associated with a mutation on the distal end of mouse chromosome four. The mutation appears to affect the expression of multiple genes within a 700 kb locus on mouse chromosome 4, centered on a breakpoint in *Pleomorphic adenoma gene 1* (*Plag1*). *Plag1*) encodes a transcription factor known to regulate normal embryonic growth and reproduction, overexpression of which causes *Insulin-like growth factor-2* (*Igf2*)-mediated tumor formation.[141,166–168] Expression profiling of *Plag1*-associated tissues suggest that it may directly regulate several genes associated with vascular development, a critical process in both tumorigenesis and embryonic development.[169] In this chapter, I tested the hypothesis that the embryonic transcription factor *Plag1* regulates craniofacial vascular development, and that vascular insufficiency caused by *Plag1* deficiency is responsible for the *sbse* cranioskeletal phenotype.

Supporting work

The *sbse* mutant appeared spontaneously in a production line at the Jackson Laboratories (JAX; Bar Harbor, ME) in 2001. The mutation was mapped to a 2.5 Mb region between the centromere of mouse chromosome 4 and the microsatellite marker D4Mit316, which includes the transcription factor *Pleomorphic adenoma gene 1* (*Plag1*); the body size and fertility phenotypes reported in *Plag1* null mice made it a plausible candidate. Exome sequencing at the JAX failed to identify the mutation.[102] The mutation was later identified by whole genome sequencing, carried by the Cox lab in collaboration with M. Kircher and J. Shendure (Department of Genome Sciences,

University of Washington).[108] Sequence analysis by T.C. Cox identified a rearrangement and deletion in the non-coding region of the *Plag1-Chchd7* locus (Figure C.1). The structure of the *sbse* mutation was verified by PCR product size and sequence after amplifying across breakpoints.

Mutant mouse nomenclature

The name of the strain, *sbse* ("*small body-short ear*"), predates precise characterization of the mutation, a large inversion physically disrupting the first intron of the gene *Plag1*. No other (known) genes are (structurally) disrupted. Griffiths, et al. (2000) define an allele as "(o)ne of the different forms of a gene that can exist at a single locus."[170] For the sake of clarity, I refer to the *sbse* mutation as an allele of *Plag1*, following the nomenclature conventions established by the International Committee on Standardized Genetic Nomenclature for Mice.[171] A second mouse line carrying a null allele (*tm1Wjmv*) of *Plag1* was utilized in this study. Crossing the *Plag1*-null line with the *sbse* resulted in a third genotype of interest, a compound heterozygote carrying one of each allele.[104] It is necessary to note that *sbse* and *Plag1*-null mice are on different inbred genetic backgrounds. Table 5.1 defines the two alleles and three final genotypes of interest used in this study.

Table 5.1: Key to *Plag1* mutant strain IDs.

***Plag1* mutant alleles utilized in this study.**

Strain	Genotype	WT			Background
sbse	*Plag1*$^{sbse/sbse}$	*Plag1*$^{+/+}$	spontaneous	JAX[102 108]	C57BL/6J
***Plag1*-null**	*Plag1*$^{tm1Wjmv/tm1Wjmv}$	*Plag1*$^{+/+}$	*lacZ* knock-in	KU Leuven U of Calgary	129S1/Sv-129X1

Experimental cross, *Plag1* mutants

Strain		Genotype	WT		Background
sk	*Plag1*$^{sbse/tm1Wjmv}$	*Plag1*$^{+/+}$			C57BL/6J-129S1/Sv-129X1

(a) Wildtype: *Plag1*$^{+}$ Wildtype *Plag1-Chchd7* locus.

(b) *sbse*: *Plag1*^{sbse} Structural disruption of the 5′ end of *Plag1* in *sbse* mice.

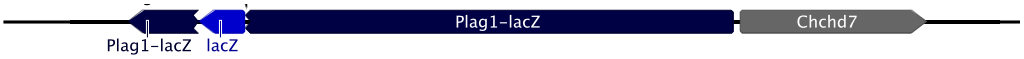

(c) *Plag1*-null: *Plag1*^{tm1Wjmv} *Plag1*-null allele generated by knock-in of the reporter gene *LacZ*.

Figure 5.1: Mutant *Plag1* alleles.

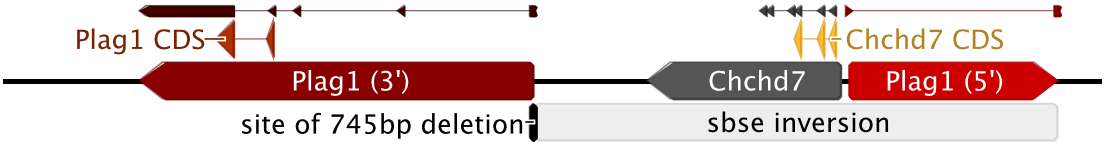

Figure 5.2: Rearrangement of *Plag1-Chchd7* locus in *sbse* mice. The abutting 5′ ends of *Plag1 (red)* and *Chchd7 (gray)* are separated by a 440 bp region harboring markers of a bidirectional promoter.[172] The *sbse* rearrangement flips the orientation of the promoter region and displaces it by approximately 33 kb *(white)*. A 745 bp deletion within exon 1 of *Plag1* flanks the inverted sequence *(black)*. The CDS of both genes remain intact *(dark red and gold triangles)*, although the linearity of *Plag1* mRNA *(5′ red, 3′ dark red)* is disrupted.

5.2 RESULTS

5.2.1 *Structural disruption of the Plag1-Chchd7 locus in sbse mice*

The mutation associated with the *sbse* phenotype is a rearrangement of mouse chromosome 4, affecting a region harboring two genes[1] *Plag1*, a transcription factor, and *Chchd7*, a gene encoding components of mitochondrial protein import machinery.[141,173]

The *sbse* mutant allele differs from the wildtype sequence in two ways:

- an inversion, approximately 33 kb in length, with one breakpoint within the intron of *Plag1* and the other 3.5 kb from the 3′ end of *Chchd7* and
- a 745 bp deletion within intron 1 of *Plag1* (Figures 5.1b, 5.2).

It was found that mice with the full *sbse* cranioskeletal phenotype were always homozygous for the mutation. Isolated growth site defects, which have a have minimal effect on overall cranioskeletal shape, are found at low levels in confirmed heterozygotes (Table 3.17, Figure 3.16).

1 The 5′ regions of *Plag1* and *Chchd7* abut, sharing a promoter region, and are transcribed from opposite strands.

5.2.1.1 *Sequence analysis identifies potentially functional regions of the Plag1-Chchd7 locus*

I used wildtype references sequences and experimental datasets available from NCBI and the UCSC Genome Browser to search for predicted or validated functional regions that might be disrupted by the *sbse* mutation.

INVERSION AND DISPLACEMENT OF *chchd7*, THE *plag1-chchd7* PROMOTER REGION, AND EXON 1 OF *plag1* In the *sbse* mutation, a 33kb stretch of DNA containing the first exon of *Plag1*, an intergenic region, all of the gene *Chchd7*, and its 3′ UTR are inverted *in situ* (Figure 5.2). In the wildtype locus, the 5′ ends of the genes *Plag1* and *Chchd7* are separated by 426 bp, which an orthology-based method implemented by Yang, et al. identified as a bidirectional promoter.[106,118,172,174] (Figure 5.1a, star). Markers of histone modification in several cell types suggest that the conformation of chromatin at this site can be modified to accommodate transcriptional activity.[115–117,175] The presence of core promoter sequences, validated POL2 and TBP transcription factor binding site, and a CpG island suggest that this region acts as a promoter, i.e., the mutation displaces the canonical *Plag1-Chchd7* promoter.

Deletion in the first intron *Plag1* The *Plag1* end of the *sbse* inversion a region 13.5 kb from its start site, within the first intron, where a 745 bp deletion was detected, bordering the breakpoint. The USCSC Genome Browser's BLAT search function was used to locate the missing region in the reference sequence. Markers of functional importance, including sequence conservation, were higher in the deletion than the surrounding regions (Figure 5.3a).[107] [2] Regulatory protein binding at this site has

2 In this study, I used protein binding and enzymatic activity marker datasets, available from large-scale studies of embryonic tissue and cell culture, to inform early analysis of the mutation. While it is not specific to either the *sbse* mutation or embryonic tissue, this data demonstrates that the predicted regulatory

been validated via ChIPseq in mouse embryonic day 11.5 craniofacial tissue (P300 binding) and immortalized B-cell lymphoma-derived erythroleukemia (MEL) cells (P300, POL2, CTCF binding).[115,176] Strong DNase I hypersensitivity peaks are present in embryonic mesoderm.[177] P300 enhancer-associated protein binding is reported at the deletion site in MEL and CJH12 cells (Figure 5.3b).

5.2.1.2 *Expression of Plag1, but not Chchd7, is nearly ablated in the sbse*

The truncation of *Plag1* between exons 1 and 2, before the start of the CDS, suggests that mRNA expression may be deficient in the mutant. Preliminary reverse-transcription PCR (RT-PCR) results confirmed that *Plag1* mRNA expression is dramatically suppressed in the $Plag1^{sbse/sbse}$ head and body. RT-PCR failed to detect differences in *Chchd7* expression in the $Plag1^{sbse/sbse}$ head at E11.5. (RT-PCR, embryonic whole-head tissue, E11.5. Biological replicates, n= 2; technical replicates, n= 2).

mRNA expression was quantified in whole head tissue at E10.5 using quantitative real-time PCR (qRT-PCR). The expression of *Plag1* mRNA was significantly reduced in $Plag1^{sbse/sbse}$ and $Plag1^{sbse/+}$ embryos, compared to wildtype controls ($t(6)= 11.1$, $p< 0.001$ and $t(6)= 5.2$, $p= 0.002$*, respectively). No significant difference was observed in the expression of *Chchd7* in the same group (Figure 5.4a). (qRT-PCR, embryonic whole-head tissue, E10.5. Biological replicates, n= 4; technical replicates, n= 2.)

5.2.1.3 *Plag1 is expressed in the embryonic face, ear, and forelimbs*

After validating that *Plag1* expression is suppressed in the embryonic head, I used X-gal staining to visualize its spatial expression pattern of in $Plag1^{lacZ}$ transgene in

activity occurs in nature. Where relevant, I have provided an image of the UCSC Genome Browser tracks reporting the data, which indicates the cell or tissue from which it was derived.

mice. Tissues labeled blue are actively transcribing the *Plag1* CDS. At E10.5, *lacZ* staining is particularly strong in branchial arches (BA) 1 and 2, and as well as in the forelimb (Figure 5.5). Staining is also observed in BA2, the hindlimb, and the spinal cord region. At E12.5, expression is strong in the forebrain, the snout, external ear precursor tissues, the distal limbs and phalanges, the spinal cord, and the umbilical cord.

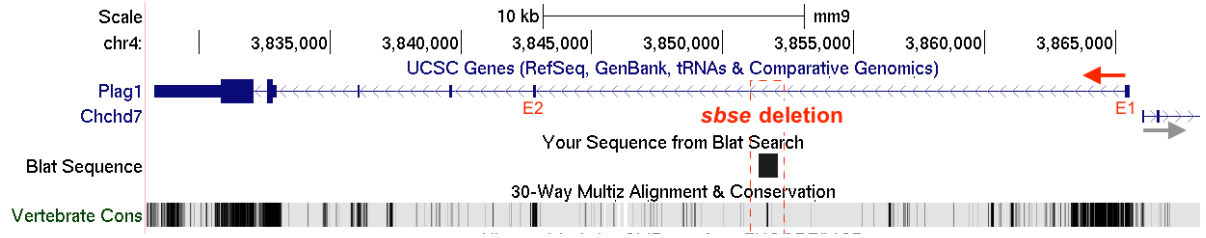

(a) The *sbse* deletion covers an unusually conserved region of intron 1. Deleted region identified by BLAT search.

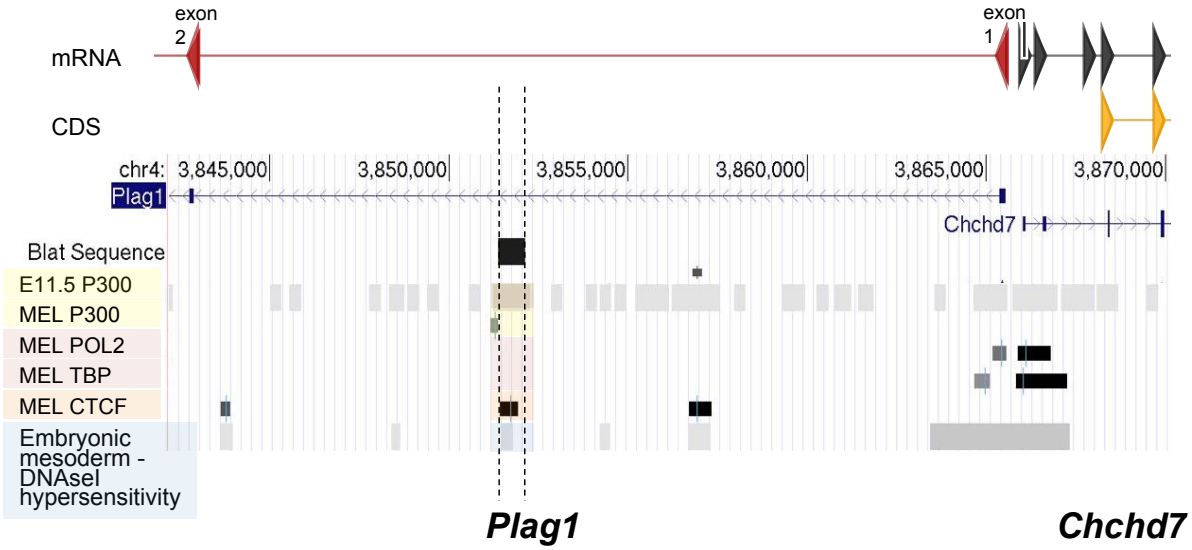

(b) Chromatin markers in the deleted region suggestive of regulatory potential. *Black box,* BLAT-localized sequence from *Plag1* deletion. *Yellow* P300 binding is associated with enhancer activity.[178] *Red* Binding sites for transcriptional machinery. *Orange* CTCF binding is associated with insulators and definition of transcriptional domains.[115] *Blue* Hypersensitivity to DNAse I is associated with local relaxation of chromatin structure and regulatory activity.[179] A representative ChIPseq track shows DNAse I hypersensitivity hotspots in mesoderm derived from E11.5 mice.[177]

Figure 5.3: Markers of regulatory potential within the *sbse* deletion Figures generated using the UCSC Genome Browser.

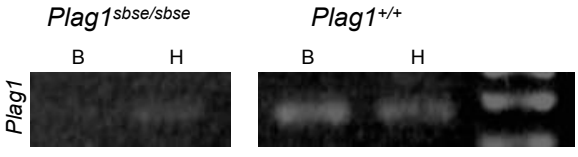

(a) Deficient *Plag1* mRNA expression in *Plag1*$^{sbse/sbse}$ at E11.5.

(b) Normal *Chchd7* mRNA expression in *Plag1*$^{sbse/sbse}$ at E11.5.

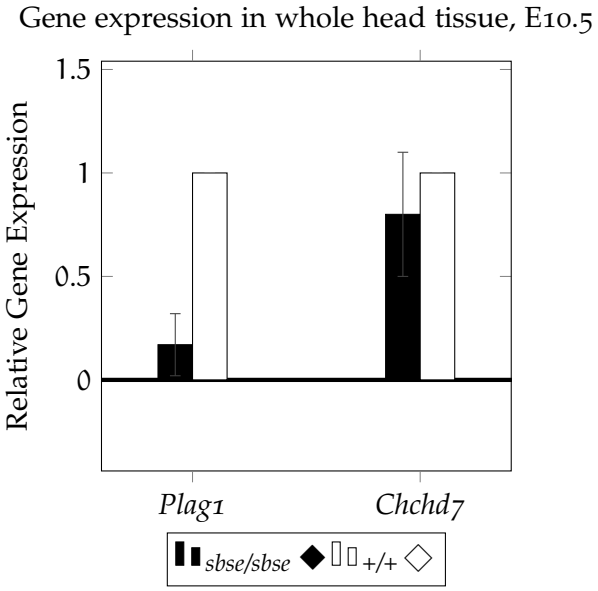

(c) No difference in *Chchd7* mRNA expression.

Figure 5.4: Expression of *Plag1* and *Chchd7* mRNA in *sbse* mutants. The *sbse* mutation affects expression of *Plag1* mRNA, but does not affect *Chchd7* in whole head tissue.

Table 5.2: Relative expression of *Plag1* and *Chchd7* mRNA, E10.5.

◆ *Plag1*$^{sbse/sbse}$	M ± SD	
Plag1	0.17±0.15	t(6)= 11.1, p< **0.001***
Chchd7	0.80±0.29	t(6)= 1.4, p= 0.22

Biological replicates, n=4; technical replicates, n=2 . *Unpaired T-test, p<0.05

The *sbse* mutations reduces expression of *Plag1*, but not *Chchd7* **(a)** mRNA expression at E11.5. **(b)** A statistically significant difference was found in the expression of *Plag1* in mutant embryos at E10.5, relative to littermate controls. No significant change was observed in the expression of *Chchd7* in the same group.

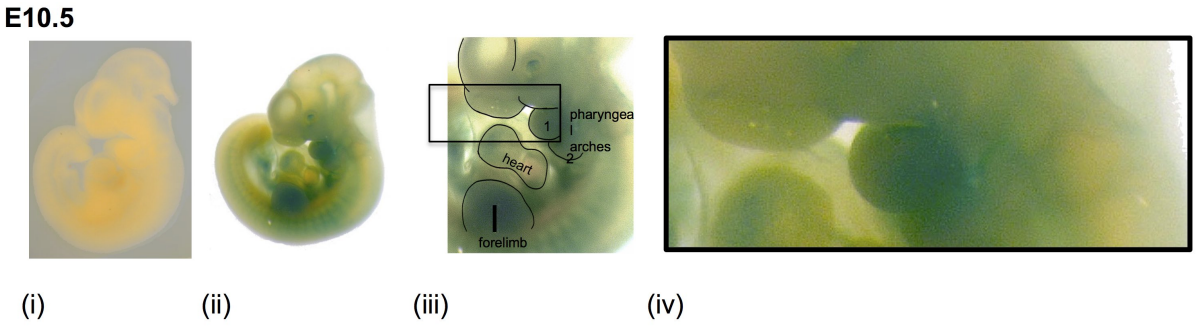

(a) X-gal-staining suggests that *Plag1* is typically expressed in branchial arch 1, the forelimb, and the region dorsal to the heart at E10.5. *(i) Plag1*$^{+/+}$ *(ii-iv) Plag1*$^{tm1Wjmv/+}$ (*Plag1*$^{tm1Wjmv/+}$ n= 4 *Plag1*$^{+/+}$ n= 2).

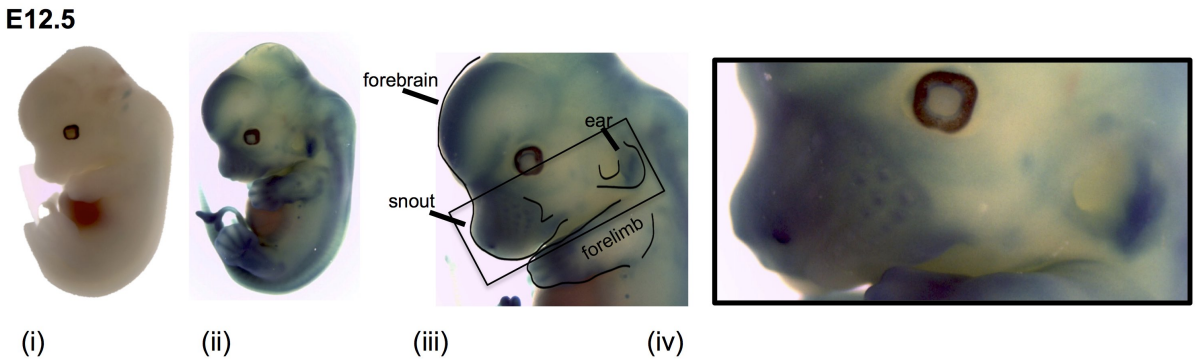

(b) X-gal-staining suggests that *Plag1* is typically expressed in the forebrain, the snout, the pinna, the distal limbs, and the spinal cord region at E12.5. *(i) Plag1*$^{+/+}$ *(ii-iv) Plag1*$^{tm1Wjmv/+}$ (*Plag1*$^{tm1Wjmv/+}$ n= 3 *Plag1*$^{+/+}$ n= 6).

Figure 5.5: *Plag1* is expressed in the craniofacial precursors at E10.5 and E12.5 X-gal-staining of *lacZ* knock-in embryos (*Plag1*-null; *Plag1*$^{tm1Wjmv/+}$) reveals a that expression is strong in the facial precursors at E10.5, results which agrees with previously published wholemount RNA *in situ* hybridization findings.[180] Expression at E12.5 has spread through the developing craniofacial region, notably, in the jaw and developing external ear.

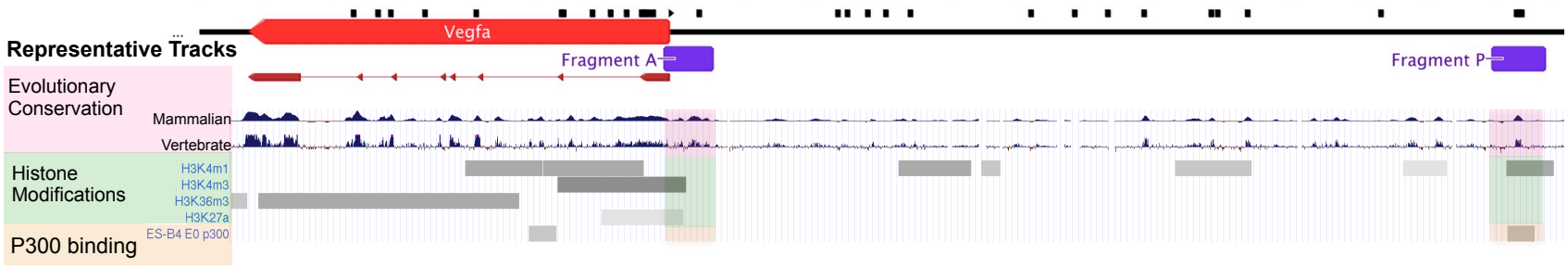

(a) Predicted *Plag1* binding motifs appear in doublet or triplet clusters (black) throughout the 50kb region upstream of *Vegfa*. The 1kb stretches (Fragments A and P) were selected for luciferase testing based on the presence of the *Plag1* consensus binding motif, their proximity to validated markers of regulatory function, as well as the neighboring and motif-specific sequence conservation, and are marked with purple boxes. Representative tracks showing features suggestive of regulatory activity: *Pink* Conserved non-coding regions *Green* Histone modifications typically found near open chromatin structure and transcriptionally active genes (H3K36Me3) or near active promoters (H3K4me1, H3K4me3, H3K27ac) in mouse embryonic stem cell line E14. *Orange* P300 binding in mouse embryonic stem cell line Bruce4.

(b) *Plag1* consensus binding sites (`GRGGC(N)`$_{6-8}$`GGG`) are conserved through opossum.

Figure 5.6: Markers suggesting that *Plag1* may regulate *Vegfa* expression

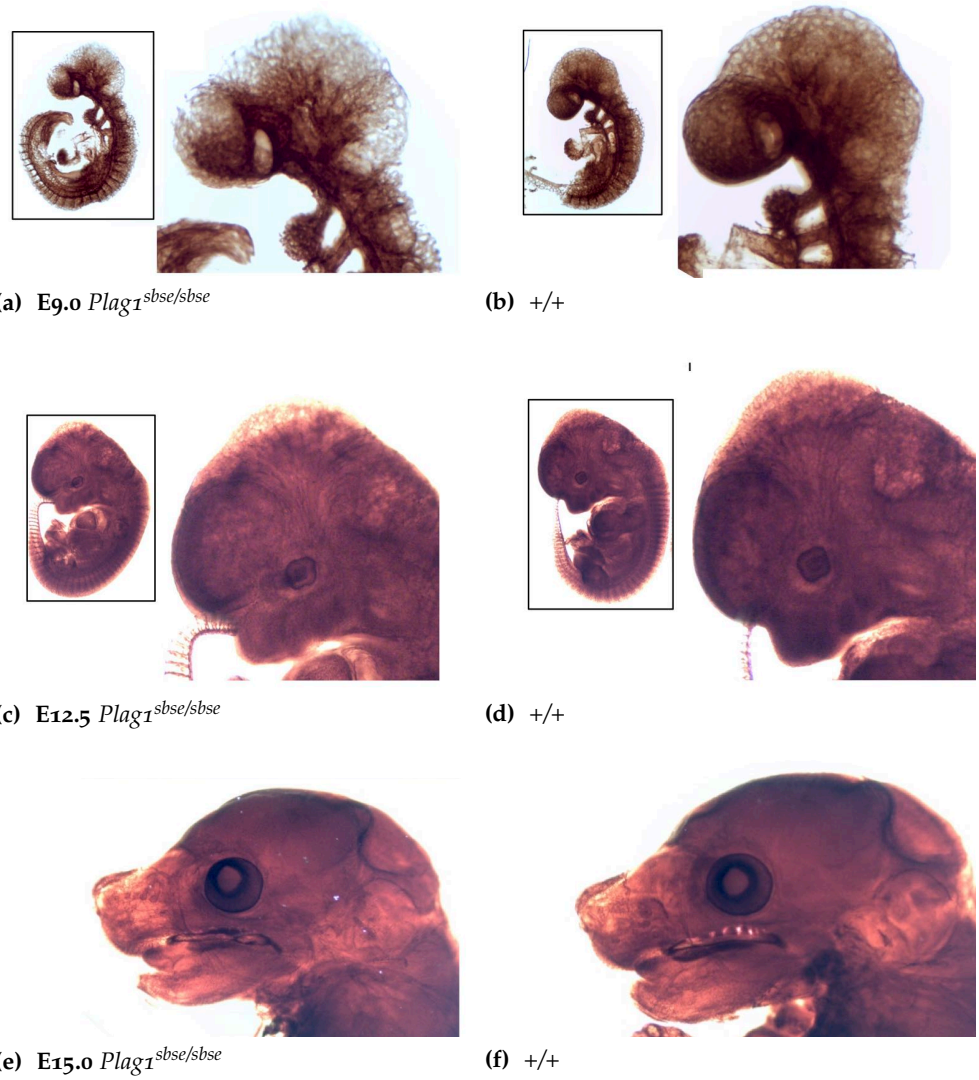

(a) **E9.0** *Plag1*$^{sbse/sbse}$ **(b)** +/+

(c) **E12.5** *Plag1*$^{sbse/sbse}$ **(d)** +/+

(e) **E15.0** *Plag1*$^{sbse/sbse}$ **(f)** +/+

Figure 5.7: Vascular density in the *Plag1*$^{sbse/sbse}$ embryo, E9.0 - E15.5 Early differences in mutant craniofacial vascular and lymphatic density do not persist in the mutant through late gestation. The intensity of brown signal is proportional to the density of α-Endomucin-labeled endothelial cells in embryos. **(a,b) E9.0.** Endothelial cell networks in the mutant fore-, mid- and hindbrain are less dense than in wildtype controls. There is no difference in the branchial arches. **(c, d) E12.5.** The intensity of endothelial cell staining varies between mutant *Plag1*$^{sbse/sbse}$ and wildtype *Plag1*$^{+/+}$ at E12.5. **(e,f) E15.0.** No superficial difference in signal intensity.

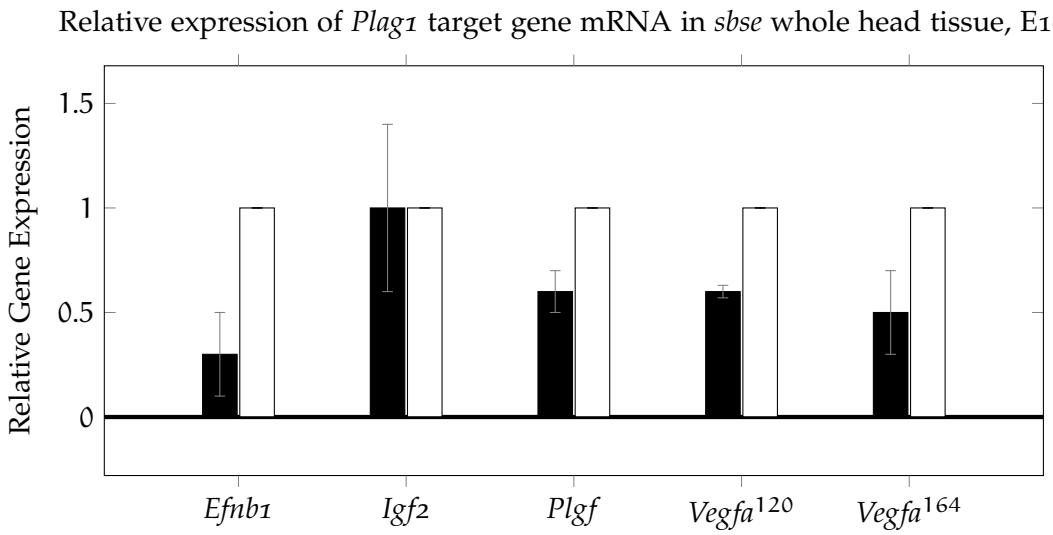

Figure 5.8: Relative expression of *Plag1* target gene mRNA in *sbse*.

5.2.2 *PLAG1 may regulate expression of Vegfa*

5.2.2.1 *Disrupted expression of genes associated with vascular development in the sbse*

Candidate target genes were prioritized by local *Plag1* binding motif density and reported expression levels in embryonic craniofacial tissues. Four genes were selected for further testing: *Ephrin B1* (*Efnb1*), *Insulin-like growth factor 1* (*Igf1*), *Placental growth factor* (*Plgf*) and *Vascular endothelial growth factor A* (*Vegfa*). In light of known differential activity on vascular development and chondrogenesis, I tested both the *Vegfa120* and *Vegfa164* isoforms of *Vegfa*[3] mRNA expression in whole-head tissue at E10.5 was significantly reduced in $Vegfa^{120}$ ($t(2)= 23.57$, $p= 0.0018$*) and in *Efnb1* ($t(2)= 4.95$, $p= 0.039$) in mutant embryos. No significant difference found in the expression of *Igf2*, *Plgf* or $Vegfa^{164}$ (Biological replicates, $n= 2$; technical replicates, $n= 2$.) (Figure 5.8).

3 Isoforms of *Vegfa* are known to vary in terms of diffusibility and activity; *Vegfa164* has been shown to be specifically required for normal branchial arch development in mice.[181]

Table 5.3: Relative expression of *Plag1* target gene mRNA in *sbse* whole head tissue, E10.5.

	motifs/100kb		$M \pm SD$	s
Ephrin B1	113	***Efnb1***	0.3 ± 0.2	$t(2)$=4.95, ***p*=0.039***
Insulin-like growth factor 2	73	***Igf2***	1.0 ± 0.6	$t(2)$=0, p=1.0
Placental growth factor	57	***Plgf***	0.6 ± 0.1	$t(2)$=5.66, p=0.30
Vascular endothelial growth factor A	69	***Vegfa*^{120}**	0.5 ± 0.03	$t(2)$=23.57, ***p*=0.0018***
		***Vegfa*^{164}**	0.6 ± 0.2	$t(2)$=2.83, p=0.11

*Significant difference between genotypes by unpaired T-test, p<0.05

5.2.2.2 *PLAG1 activates the Vegfa promoter*

I used a luciferase assay to test the hypothesis that the transcription factor *PLAG1* directly binds to and activates *Vegfa* expression. A total of 17 candidate *Plag1* binding site regions exist in the 50 kb region upstream of *Vegfa*. Markers of regulatory potential[4], including sequence conservation, reported histone modification at those sites, and reported P300 binding sites, were used to prioritize two fragments of interest. (Figure 5.6, 5.6a). Fragment A is within the classical *Vegfa* promoter and contains a pair of *Plag1* binding motifs.[183] Both enhancer and promoter configurations of Fragment A were tested. In the promoter configuration, Fragment A increased gene expression by 2.5 fold in the presence of PLAG1, a statistically significant increase (technical replicates n= 3, p= 0.032) (Figure 5.9a). No statistically significant increase in luciferase activity was observed in Fragment A in the enhancer configuration (technical replicates n= 3, p= 0.27) (Figure 5.9b). Fragment P is located 30 kb from the start site of *Vegfa*, and contains a pair of Plag1 binding motifs. Luciferase activity increased by 1.25 fold in the presence of the *Plag1* expression vector (technical replicates n= 3, p= 0.015) (Figure 5.9c).

4 Retrieved from tracks available at UCSC Genome Browser.[182]

5.2.2.3 *Early differences in vascular density in the sbse embryo do not persist*

Vascular network density in the heads of *Plag1*$^{sbse/sbse}$ and *Plag1*$^{+/+}$ embryos was assessed at E9.0, E12.5 and E15.5 by whole mount immunohistochemistry. The intensity of brown signal in photographs is proportional to the density of α-Endomucin-labeled endothelial cells in embryos. Staining appears to be less intense in the mid- and hindbrain of *Plag1*$^{sbse/sbse}$ at E9.0, compared to littermate controls. There was no difference the intensity of staining in mutant and wildtype mice at E12.5 and E15.5. Within the mutant groups, staining pattern variability was no longer notable, although morphological differences persist (E9.0, E12.5 and E15.5: Biological replicates n= 3/genotype/age, technical replicates n= 2/age.)

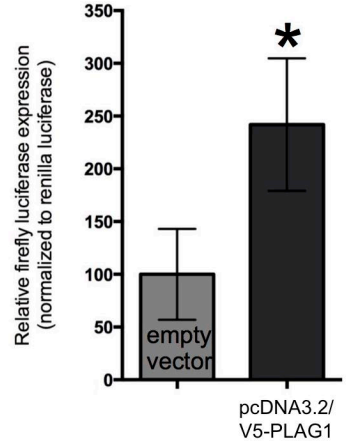

(a) Promoter A-*luc2*
A statistically significant 2.5 fold increase in fragment A-*luc2* activity in the presence of PLAG1 (p= 0.032).

Plasmid map: 2.4b

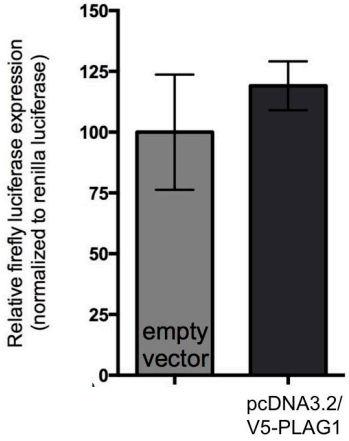

(b) Enhancer A minP-*luc2*
No significant increase in fragment A-minP-*luc2* activity in the presence of PLAG1 (p=0.27).

Plasmid map: 2.4c

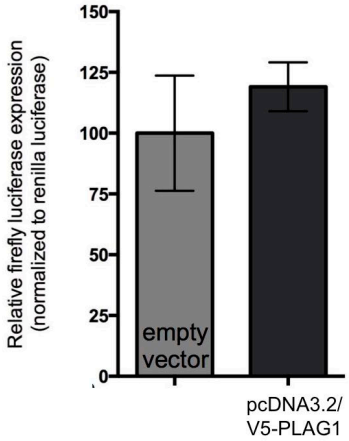

(c) Enhancer P-minP-*luc2*
A statistically significant 1.25 fold increase in fragment A-minP-*luc2* activity in the presence of PLAG1 (p=0.032)

Plasmid map: 2.4d

Figure 5.9: PLAG1 activates the *Vegfa* promoter

Table 5.4: *Plag1*-null (*tm1Wjmv*) litter sizes

Cross	# Litters	# Total pups	# Pups/litter
Plag1$^{tm1Wjmv/+}$ × *Plag1*$^{tm1Wjmv/+}$			
◪×⊘	5	60	12

*Significant difference, compared to WT, p <0.05

Table 5.5: Genotype ratios in *Plag1*-null (*tm1Wjmv*) mice

Cross	#Litters	#Pups	◆ *tm1Wjmv/tm1Wjmv*	◈ *tm1Wjmv/+*	◇ +/+	Mendelian ratios Observed	Expected
Plag1$^{tm1Wjmv/+}$/+ × *Plag1*$^{tm1Wjmv/+}$/+							
◪×⊘	3	36	4	22	10	1.0 : 5.5 : 2.5	1.0 : 2.0 : 1.0

*Significant difference, compared to WT, p<0.05

Table 5.6: Bodyweight in the *Plag1*-null, *sk*, and *sbse* lines

	◆ $M \pm SD$	n		◈ $M \pm SD$	n		◇ $M \pm SD$	n
	tm1Wjmv/tm1Wjmv			*tm1Wjmv/+*			**+/+**	
Plag1-null	11.6 ± 1.1	4	$t(12)=7.2$ $\mathbf{p<0.0001}$*	20.2 ± 2.8	22	$t(30)=1.2$ $p=0.22$	21.5 ± 2.6	10
	sbse/tm1Wjmv						**+/+**	
sk	16.5 ± 2.9	9	$t(12)=2.7$ $\mathbf{p= 0.019}$*				21.7 ± 4.4	5
	sbse/sbse			*sbse/+*			**+/+**	
sbse	9.5 ± 2.0	32	$t(46)=10.6$ $\mathbf{p<0.0001}$*	14.6 ± 3.0	20	$t(34)=1.2$ $p=0.24$	15.6 ± 1.6	16

*Significant difference between mutant and wildtype by unpaired T-test, $p<0.05$

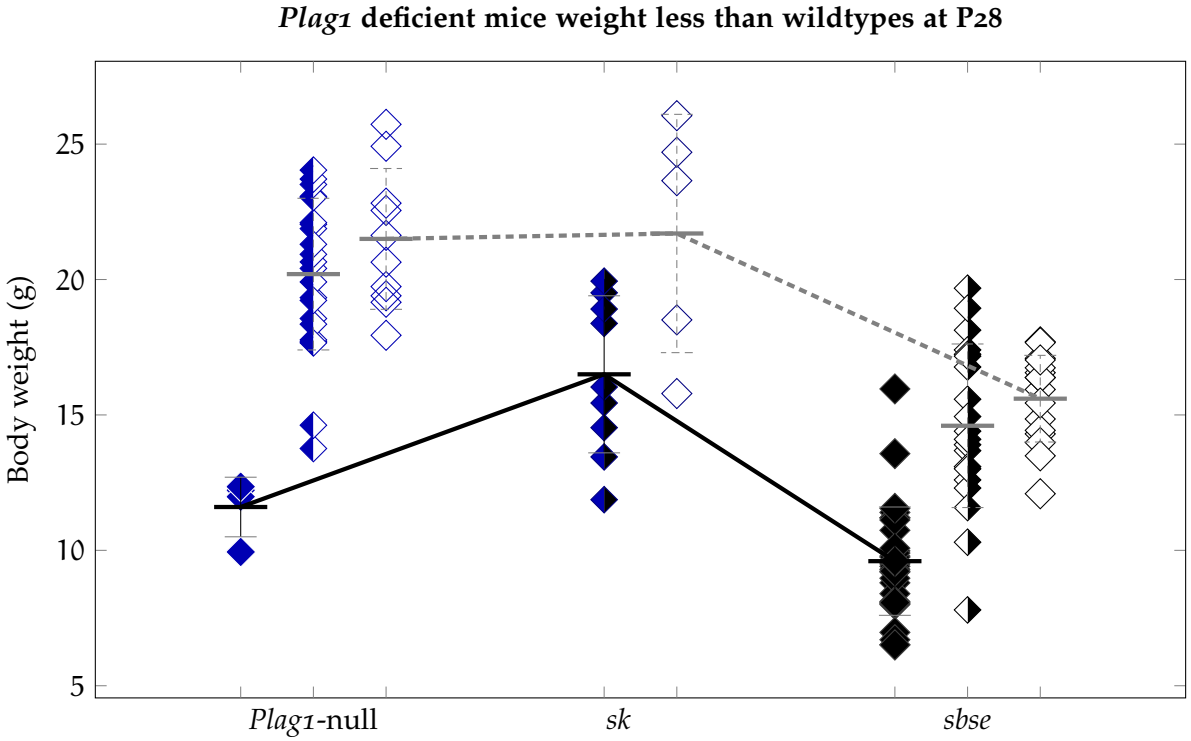

Figure 5.10: Bodyweight in the *Plag1*-null, *sk*, and *sbse* mutants.
Average body weight is reduced only when mice are homozygous or compound heterozygous for *Plag1*-deficient alleles.

Solid horizontal lines The average weight of mice carrying two *Plag1*-deficient alleles is significantly lighter than their wildtype controls at P28. *Dashed horizontal lines* There is no difference between the average weight of mice heterozygous for a *Plag1*-deficient allele and their wildtype controls (Table 5.6).

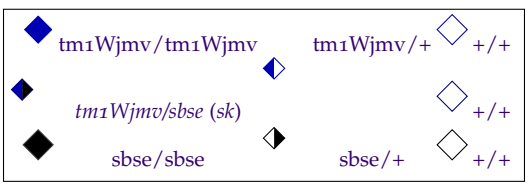

MUTANT WILDTYPE

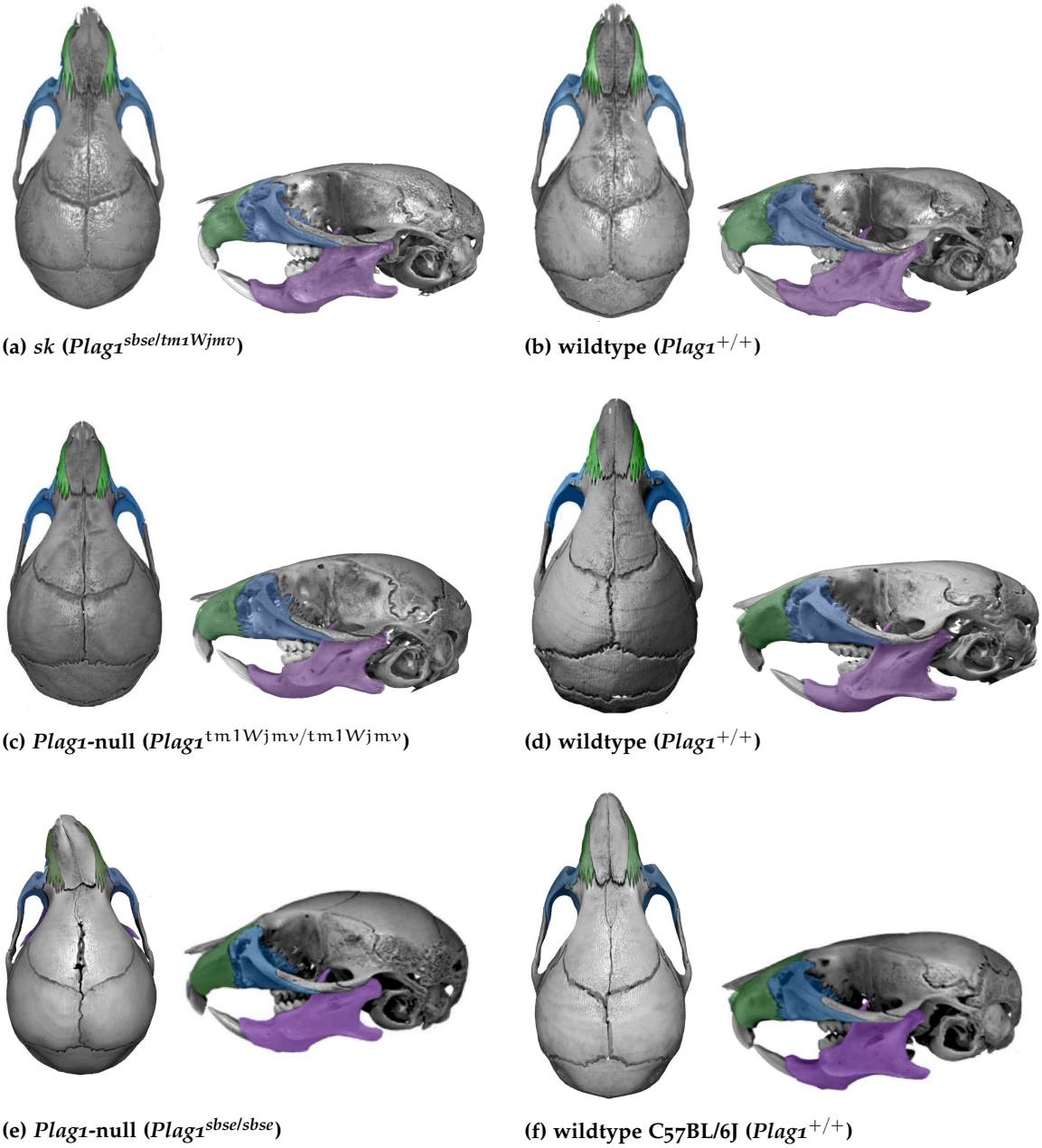

(a) ***sk*** **(*Plag1*$^{sbse/tm1Wjmv}$)** **(b) wildtype (*Plag1*$^{+/+}$)**

(c) ***Plag1*****-null (*Plag1*$^{tm1Wjmv/tm1Wjmv}$)** **(d) wildtype (*Plag1*$^{+/+}$)**

(e) ***Plag1*****-null (*Plag1*$^{sbse/sbse}$)** **(f) wildtype C57BL/6J (*Plag1*$^{+/+}$)**

Figure 5.11: μCT scan renderings of *Plag1* deficient mutant crania. Mutant (left) and wildtype (right) crania are shown from the dorsal and lateral perspectives.
Green, premaxilla. *Blue*, maxilla. *Purple*, mandible. (Not to scale.)

Table 5.7: Pairwise comparison of lateral shape: *Plag1* deficient mutants.

Compound heterozygote *sk* mutants are not significantly different at P28.

$*p^{perm}<0.01$	*sk* ◆ *sbse/tm1Wjmv*		*sbse* ◆ *sbse/sbse*		*Plag1*-null ◆ *tm1Wjmv/tm1Wjmv*	
sk WT ◇ +/+	**F= 5.5**	**p^{perm}= 0.003***	-	-	-	-
sbse WT ◇ C57BL/6J +/+	F= 0.7	p^{perm}= 0.6	**F= 8.2**	**$p^{perm}<0.001$***	-	-
Plag1-null WT ◇ +/+	**F= 6.6**	**$p^{perm}<0.001$***	**F= 17.4**	**$p^{perm}<0.001$***	**F= 3.6**	**$p^{perm}<0.001$***
sk ◆ *sbse/tm1Wjmv*	-	-	**F= 8.2**	**$p^{perm}<0.001$***	F= 1.6	p^{perm}= 0.2
sbse ◆ *sbse/sbse*	-	-	-	-	**F= 2.7**	**p^{perm}= 0.007***
Plag1-null ◆ *tm1Wjmv/tm1Wjmv*	-	-	-	-	-	-

Goodall's F statistic. 1000 permutations. n=36.

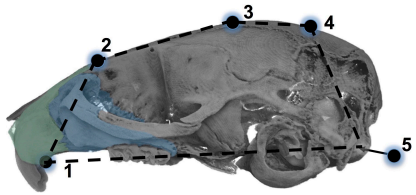

Figure 5.12: Landmarks used to test differences in lateral cranial profile.

The lateral profile shape of wildtype controls does not vary significantly at P28

$*p^{perm}<0.01$	*sbse* WT ◇ C57BL/6J +/+		*Plag1*-null WT ◇ +/+	
sk WT ◇ +/+	F= 1.6	p^{perm}= 0.2	F= 0.9	p^{perm}= 0.5
sbse WT ◇ C57BL/6J +/+	-	-	F= 1.7	p^{perm}= 0.2

5.2.3 *Complementarity of Plag1^{tm1Wjmv} and Plag1^{tm1Wjmv}*

5.2.4 *Body size deficiencies in both Plag1-null and Plag1$^{sbse/sbse}$ mice*

Mice homozygous for either the *Plag1^{sbse}* and *Plag1^{tm1Wjmv}* mutant alleles are smaller in size, and either hypomorphic or completely null for *Plag1* expression, while heterozygotes are normal weight.[104] In *Plag1$^{sbse/tm1Wjmv}$* (*sk*) compound heterozygotes, the *sbse* allele is in *trans* with the null allele. The observed reduction in *sk* body size suggests that the effect of the *sbse* mutation on *Plag1* expression is non-complementary. (Figure 5.10).

5.2.5 *Cranioskeletal dysmorphology in Plag1 deficient mice*

Genetic complementation of the hypomorphic *Plag1^{sbse}* and null *Plag1^{tm1Wjmv}* alleles supports a role for Plag1 the reduced body weight phenotype. μCT scan renderings reveal that the overall shape of both the *Plag1*-null (*Plag1$^{tm1Wjmv/tm1Wjmv}$*) and *sk* cranioskeletons are not notably dysmorphic, with no midface deficiency or asymmetry in either strain (Figure 5.11). Landmark-based shape analysis was designed to quantitatively test differences in the mean shape of the lateral cranial profile (Figure 5.12). Pairwise comparison using the `shapes` package in R established that the profile of background matched (*sbse*: C57BL/6J +/+) or littermate (*Plag1*-null, *sk*: +/+) wildtype crania are not significantly different from one another at P28 (Table 5.12).[124,125] Significant differences were found, however, in the shape of the mutant *sbse* and *Plag1*-null profiles, when compared to one another, as well as when compared to all wildtype samples. Pairwise comparison of landmark points showed no significant difference between the shape of the *sk* compound heterozygote and the

C57BL/6J +/+ or the *Plag1*-null (Goodall's F test, $p^{perm} < 0.05$, k= 5, n= 37) (Table 5.7). Furthermore, no difference was observed in the size or position of the *sk* external ear, a fully penetrant element of the *sbse* phenotype.

5.3 DISCUSSION

In this chapter we examined the effect of the *sbse* mutation on the expression of the transcription factor *Plag1* and mitochondrial transport protein *Chchd7*, and tested a mechanism by which *Plag1* deficiency might affect craniovascular cranioskeletal development in mutant embryo. Although deficiency in the mutant embryos appears to affect body size and fertility, *Plag1* was determined to be the sole cause of the *sbse* cranioskeletal phenotype.

5.3.0.1 *The sbse mutation disrupts expression of Plag1 in the embryo*

Specific polymorphisms in the bidirectional *Plag1-Chchd7* promoter have been associated with differences in cattle (*Bos taurus*) body size. *in vitro* experimental manipulations, which inverted stretches of the intergenic region containing the mutations caused changes to the expression level of *Plag1* and *Chchd7*.[184] PLAG1, the human ortholog to murine *Plag1*, was first identified as a common participant in spontaneous promoter swapping in samples of human Pleomorphic adenoma tumor tissues, forming a fusion gene with the promoter region of β-catenin (CTNNB1). CTNNB1 is a significantly more active and widely expressed gene, and under the control of its promoter, PLAG1 is overexpressed in the salivary glands.[185] Subsequent studies of pleomorphic adenoma, cavernous angiomatosis, myxoid chondrosarcoma, hepatoblastoma, and lipoblastoma tumors identified 10+ tumor-associated PLAG1

fusion genes formed by promoter swapping at the same site.[186–191] The number and diversity of of PLAG1 intron 1 promoter swapping rearrangements reported in the literature suggests that this region is particularly sensitive to breakpoints.[5]

In the *sbse*, a mutation splits *Plag1* into two pieces at the first intron, separating the protein coding region on exons 4 and 5 from the canonical transcriptional start site (TSS) at exon 1 The breakpoint forms one flank of a 33kb inversion, displacing the first exon of *Plag1*, a 426 bp intergenic region and the nearby mitochondrial gene, *Chchd7*. Although the *Plag1* TSS-promoter sequence remains intact, the loss of linearity before exon 2 and the downstream protein-coding sequence of the gene should result in total loss of PLAG1 mRNA and protein production. [6] This model of altered gene expression was supported by the reduction of *Plag1* expression in the head of $Plag1^{sbse/sbse}$ embryos at E10.5.

5.3.0.2 *Plag1 deficiency may affect bodyweight and fertility in the sbse*

The literature suggests that the major downstream targets of *Plag1* include genes associated with cellular proliferation. It has been proposed that the loss of expression during the transition from undifferentiated neuroepithelial rosettes into committed neural precursors, accounts for their subsequent limited proliferative capabilities. In culture, siRNA knockdown of PLAG1 expression in SH-SY5Y cells[7] suppressed their proliferative ability.[193] Regulation of cell proliferation in the embryo may be the underlying mechanisms accounting for the body size and fertility pheno-

5 Experimental insertion of a highly active EGFP provirus within intron 2 was able to massively transactivate expression.[192]

6 *Plag1* and *Chchd7* are thought to share a bidirectional promoter within the 426 bp space between them. The sequence of both the intergenic space and the gene *Chchd7* are intact, and should have no effect on *Chchd7* expression.

7 A cell line derived from human neuroblastoma tissues, and often used in studies of neuron function and differentiation.

types observed in the *Plag1*$^{tm1Wjmv/tm1Wjmv}$ knockout mice, which are recapitulated in the *Plag1*$^{sbse/sbse}$ mouse. Compound heterozygotes, carrying one allele each of *Plag1*^{sbse}and *Plag1*^{tm1Wjmv}, are significantly smaller than wildtype controls or single heterozygotes of either genotype, suggesting that the causative pathway is affected by both mutations. In addition, the litters born to *Plag1*$^{sbse/sbse}$ dams are smaller than expected from animals on a C57BL/6-derived background, a trait also observed in the *Plag1*$^{tm1Wjmv/tm1Wjmv}$.[194,195] These phenotypes suggest that the reduction in *Plag1* expression observed in *Plag1*$^{sbse/sbse}$ embryos at E10.5 may affect the same pathways as *Plag1*^{tm1Wjmv} knockout.

5.3.0.3 *Plag1 is expressed in craniofacial precursors at E10.5*

The E10.5 wildtype expression domain of the transcription factor *Plag1* includes the first two pharyngeal arches (BA), tissues which form the precursors to many midfacial structures. This localization suggests that it regulates processes critical to craniofacial development. I hypothesized that *Plag1* deficiency may result in abnormal cranioskeletal morphogenesis, such as that seen in the *sbse*. The first two BA, which will give rise to many of the vessels, bones, nerves, and cartilages of the face, are visible on the ventral side of the embryo at E10.5. *lacZ* staining under control of the wildtype *Plag1* promoter is specific and strong in both BA 1 and 2 at this timepoint. Homozygous *Plag1*$^{sbse/sbse}$ mutant morphology is more variable compared to *Plag1*$^{+/+}$ littermates at E10.5, suggesting that the *sbse* phenotype is initiated early in development (Figure 5.7). The *sbse* mutation, which significantly reduces expression of the transcription factor *Plag1* at this stage, causes mid- and lateral facial dysmorphology in homozygotes. I propose that the loss of *Plag1* is sufficient to disrupt downstream expression of factors critical to normal cranioskeletal development.

5.3.0.4 *Plag1 may regulate Vegfa expression*

Plag1-nucleotide binding sites, required for the transcriptional activation of a putative target, are very common in the mammalian genome. Identification of these consensus sequence motifs ($\texttt{GRGGC(N)}_{6-8}\texttt{GGG}$) within a regulatory region suggests that *Plag1* may help induce expression of a nearby gene, and is therefore a helpful tool when screening for potential direct downstream targets.[196] Expression analysis of tissue derived from Pleomorphic adenomas of the salivary gland identified 40+ upregulated putative targets of PLAG1, including a number of genes associated with angiogenesis or vasculogenesis.[166] It was hypothesized that *Plag1* directly regulates expression of one or more of these genes, and that abnormalities in the pathway in the *sbse* causes vascular insufficiency in the pharyngeal arches.

Embryonic vascular defects are thought to be a cause of cranioskeletal deficiency and asymmetry. A number of major putative *Plag1* targets are associated with vascular development. Significant reductions in *Vegfa*[120] and *Efnb1* expression in the mutant suggested that such a mechanism may be causative to the *sbse* phenotype. Using a luciferase assay, I tested the ability of a *Plag1* expression plasmid to bind to and activate expression at two putative binding sites upstream of *Vegfa*. My findings support a direct regulatory relationship between the two genes and suggest that the transcription factor may bind at the canonical promoter of *Vegfa*, however, I found no evidence for a defect in embryonic vascular density or in the major arteries of the mice at postnatal stages.

5.3.0.5 *Plag1 deficiency is not sufficient to cause of the sbse cranioskeletal phenotype*

Mice homozygous for the *Plag1*^{tm1Wjmv} null allele were smaller in size and lighter in weight than wildtype littermates. Shape analysis of *Plag1*$^{tm1Wjmv/tm1Wjmv}$ (*Plag1*-null) crania show a statistically significant difference in form, compared to wildtype con-

trols, suggesting that *Plag1* loss affects cranioskeletal morphology to a some degree. The vectors of shape change identified in my analysis show a slightly different and less significant pattern of dysmorphology in *Plag1*-null mice, compared to the $Plag1^{sbse/sbse}$. A genetic complementation test provided final confirmation that *Plag1* deficiency on its own does not cause the $Plag1^{sbse/sbse}$ phenotype. No phenotype was observed in single heterozygotes of either strain. If *Plag1* deficiency alone is sufficient to cause cranioskeletal defects, compound heterozygosity of the *sbse* and $Plag1^{tm1Wjmv/tm1Wjmv}$ alleles should functionally replicate the phenotype of the $Plag1^{sbse/sbse}$. $Plag1^{sbse/tm1Wjmv}$ (*sk*) double heterozygotes are significantly smaller in size than their littermate controls, supporting the role of *Plag1* as a modulator of growth, but morphometric analysis found no difference in shape by Goodall's F test, and no significant asymmetry in the crosses, unlike the $Plag1^{sbse/sbse}$.

In this study, I examined the effect of the $Plag1^{sbse/sbse}$ inversion on the most directly affected gene, *Plag1*, and tested the effect that it's loss may have on normal craniofacial morphogenesis. Despite strong expression in embryonic facial precursor tissues at critical timepoints, the loss of *Plag1* expression does not cause the characteristic craniofacial asymmetry or midface hypoplasia observed in the *sbse*. (While cranioskeletal morphology is largely unaffected, *Plag1* deficiency may play a role in the small body size and reduced fertility phenotypes observed in the mutant.) Further work should test the regulatory functionality of the deleted and rearranged sequences in the *sbse* locus. Although *Plag1* is the only directly disrupted gene in the *sbse* mutation, large stretches of sequence are either deleted or rearranged. Such rearrangements may affect chromatin organization, altering the boundaries of functionally shielded gene expression units, altering the local regulation of gene expression.[197,198]

6

DYSREGULATION OF GENE EXPRESSION IN THE SBSE LOCUS

6.1 OVERVIEW

All-*trans* retinoic acid (RA), a metabolite of vitamin A, modulates early embryonic gene expression; both maternal vitamin A deficiency and elevated embryonic exposure to RA are risk factors for structural birth defects.[13,199,200] RA binding activates a specialized class of transcription factors (retinoic acid receptors (RARs)) known to induce the expression of many *Homeobox* (*Hox*) gene family members in a tissue-specific fashion.[201–204] Insufficient or inappropriately large amounts of RA-bound RAR activity can disrupt normal cellular identity and embryonic patterning.[205] The embryo is buffered against small fluctuations in RA levels by enzymatic synthesis and degradation, as well as by binding proteins modulating activation of RARs in the cytoplasm and blood.[206–208] Regulation of RA levels in the embryo is critical to pattern the tissue that will develop into the facial primordia.[209]

In vertebrates, groups of epithelial cells near the neural tube delaminate to become mesenchymal cranial neural crest cells (CNCC), a secondary mesenchymal population thought to be a defining feature of vertebrates.[23] CNCC identity is programmed by their origin along the anterior-posterior (AP) axis, and is maintained through

migration into the branchial arches.[210–212] Altering retinoic acid levels can respecify anterior-posterior segmental identity before migration: RA, FGF and WNT8B, when expressed together, can induce ectopic formation of CNCC, while knockout of the gene encoding *Retinaldehyde dehydrogenase 2* (*Raldh2*) changes gene expression in rhombomeres 3-5, and results in significant cell death before or just after the start of migration (Figure 6.2).[213,214] After formation, chemotactic signals in the lateral regions restrict the migration of CNCC to the branchial arches. From arch 1, these cells will eventually give rise to the maxilla and mandible. From arch 2, CNCC will form the cartilaginous external ear, and the epithelial cell lining of the middle ear cavity.[215,216] (Figure 6.4e). The embryo remains sensitive to RA long after axis specification: low doses have been able to rescue inner ear defects caused by *Hoxa1* deficiency mid-gestation.[217]

It is likely that RA-mediated disruptions of CNCC are among the etiological causes of Branchial arch-related (BA) syndromes.[35,135,218] In this chapter, I present data from preliminary RNAseq experiments on the branchial arch 2 tissue of *sbse* mice, suggesting that the mutation at the *Plag1-Chchd7* locus affects the expression of two enzymes involved in vitamin A metabolism, and suggest that a nearby chromatin domain boundary with putative insulating activity may be disrupted. I suggest that the "rewiring" of the *sbse* locus on chromosome 4 by the deletion of this boundary element upregulates conversion of vitamin A to retinoic acid, and that the neural crest-derived precursors of the mid- and lateral facial tissue in the mouse are united by a shared developmental sensitivity to retinoic acid exposure.[197]

6.2 RESULTS

6.2.1 *Differential gene expression in lateral facial precursors*

6.2.1.1 *RNAseq*

RNA was extracted from branchial arch 2 tissue, pooled, and submitted for RNAseq at the Hudson Alpha Institute for Biotechnology (Huntsville, AL). Assembly and preliminary analysis was carried out by Andrew Timms (SCRI) using the Cufflinks software suite. 19848 genes were expressed in the second branchial arch at E10.5. Comparison of embryonic *sbse* and wildtype expression patterns found 411 genes with $\log_2$ fold change below -2 (2.1% of total), and 494 genes with $\log_2$ fold change over +2 (2.5% of total). Further analysis was carried out using the DEseq tool, which weights expression and count data, to help compensate for small sample size.[110,219]

6.2.1.2 *Fold change-weighted expression analysis of the sbse locus*

Expression levels of *Plag1* and *Chchd7* were consistent with previous findings. Within the *sbse* locus[1], I found significant up-regulation of the genes *Epidermal Dehydrogenase/Reductase Family 16C, Member 5 (Sdr16c5)* and *Epidermal Dehydrogenase/Reductase Family 16C, Member 6 (Sdr16c6)* in the mutant[2]. No significant changes were observed in the genes *Ribosomal Protein S20 (Rps20), LYN proto-oncogene, Src family tyrosine kinase (Lyn), Trimethylguanosine synthase 1 (Tgs1)* or *Transmembrane Protein 68 (Tmem68)* (Figure 6.1b) RNAseq results were validated via real time qPCR (Table 6.1).

1 1 kb surrounding the start site of *Plag1*.
2 *Sdr16c5* and *Sdr16c6* are the murine homologues of human short chain dehydrogenase/reductases RDHE2 and RDHE2S, respectively.[208]

DYSREGULATION OF RETINOID METABOLISM? Short Chain Dehydrogenase/Reductase Family 16C members 5 and 6 are murine homologues of human RDHE2 and RDHE2S enzymes.[208] They are components of the highly redundant retinoic acid (RA) pathway, which catalyze the conversion of all-*trans*-retinol to all-*trans*-retinaldehyde/retinal. I used GO terms "retinol dehydrogenase activity" (GO:0004745) and “retinal dehydrogenase activity” (GO:0001758) to identify other members of this pathway. Figure D.1 shows the differential expression of these enzymes, as well as RA binding proteins and receptors. Only *Sdr16c5* and *Sdr16c6* appear to be perturbed.

I searched the under- and over-expressed gene sets for proven direct targets of retinoic acid, identified by Balmer and Blomhoff (2002) and Fremantle, et al (2002).[203,220] RNAseq suggests that expression of homeobox genes *Homeobox protein Hox-B4 (Hoxb4), Hoxd8, Hoxa11as, Hoxa10*, as well as *Reproductive homeobox 6 (Rhox6), Rhox9, and Paired Like Homeobox 2a (Phox2a)* are perturbed. Known retinoic acid targets *Interferon Induced Transmembrane Protein 1 (Ifitm1), Claudin 10 (Cldn10), Neurogranin (Nrgn)* and *Serpin Family B Member 8 (Serpinb8)* also appear to be abnormally expressed. Misexpression of these RA target genes may disrupt normal development or morphogenesis (Figure 6.3).

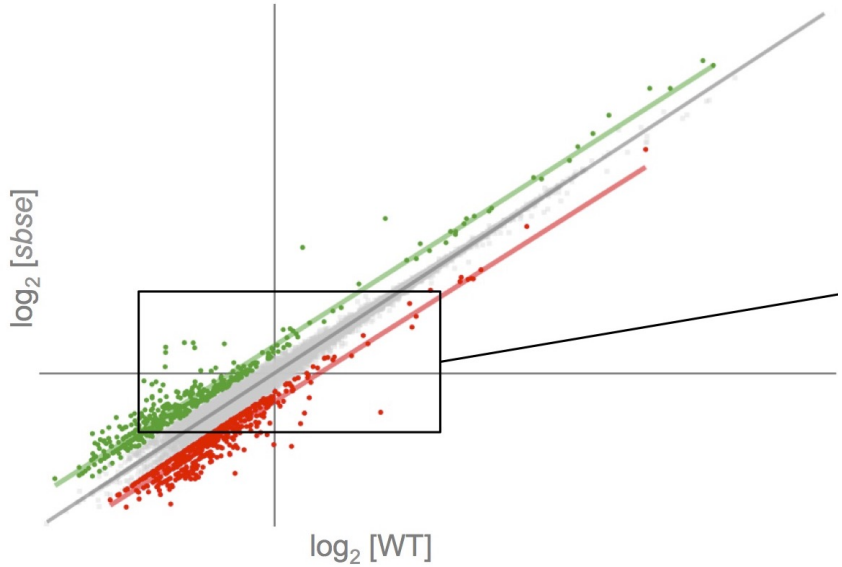

(a) All transcripts.

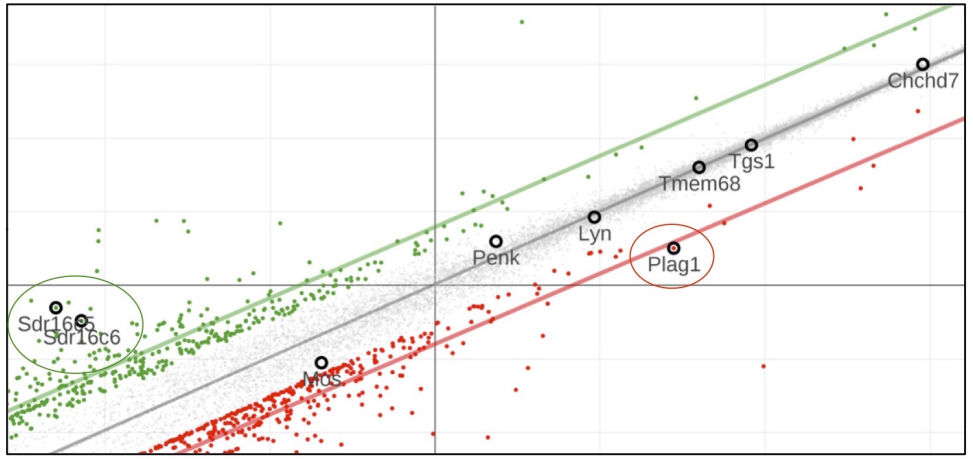

(b) Genes within the 700 kb *sbse* locus.

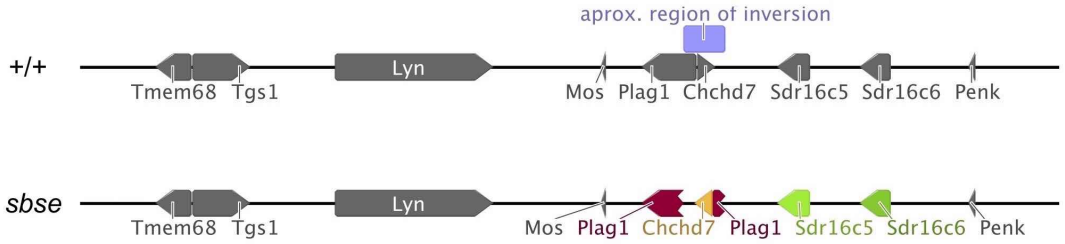

(c) Rearrangement of the locus caused by the *sbse* mutation.

Figure 6.1: Differential expression of *Sdr16c5* and *Sdr16c6* in the *sbse* locus. (a) Differentially expressed genes, represented by points on the graph, are coded by $\log_2$ fold change values: *Red*, $L_2$2FC $\leqslant$ -1. *Gray*, -1 $<$ $L_2$2FC $>$ +1. *Green*, $L_2$2FC $\geqslant$ +1. Lines of best fit have been drawn through each $L_2$2FC group. **(b)** Close-up showing the positions of genes within the *sbse* mutation locus. *Plag1* (circled in red) is under-expressed; *Sdr16c5* and *Sdr16c6* (circled in green) are overexpressed. **(c)** Rearrangement of the locus caused by the *sbse* mutation, color-coded to reflect changes in expression.

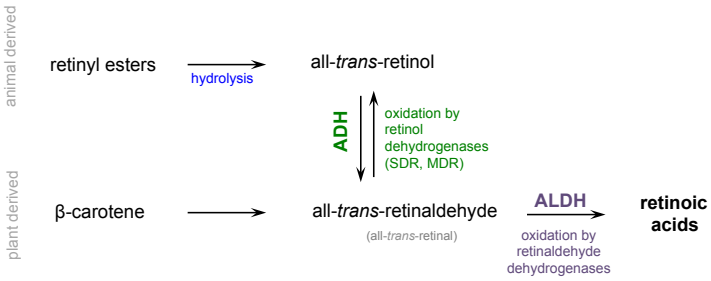

Figure 6.2: Metabolic relationships between retinoids. Metabolism of vitamin A derivatives (retinyl esters and β-carotene) to the active form, retinoic acid. *Sdr16c5* and *Sdr16c6* act at step labeled "ADH".

Table 6.1: qPCR validation of select genes expressed within 1 kb of *Plag1*

	Tmem68	*Tgs1*	*Lyn*	*Rps20*	*Mos*	*Plag1*	*Chchd7*	*Sdr16c5*	*Sdr16c6*	*Penk*
$\log_2$ FC										
RNAseq	0.00	-0.02	-0.08	+0.05	-0.73	-1.88	+0.01	3.32	4.00	0.46
RTqPCR		1.80				-3.50	0.40		7.62	0.18

Technical replicates n= 2, biological replicates *sbse/sbse* n= 3 +/+ n= 2

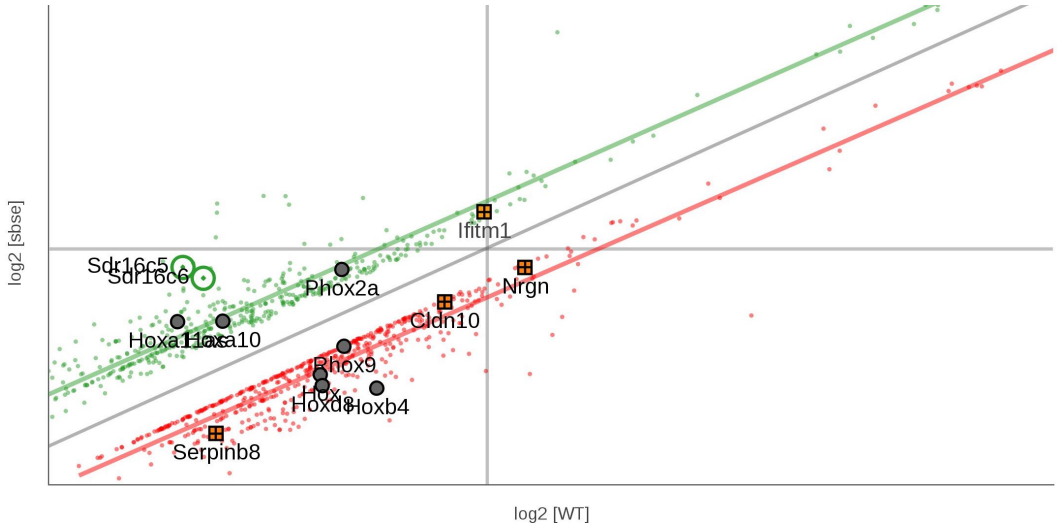

Figure 6.3: Differential expression of retinoic acid receptor targets in the *sbse* Differentially expressed genes, represented by points on the graph, are coded by $\log_2$ fold change values: *Red*, $L_2$2FC $\leqslant$ -1. *Gray*, -1 $<$ $L_2$2FC $>$ +1. *Green*, $L_2$2FC $\geqslant$ +1. Lines of best fit have been drawn through each $L_2$2FC group. *Green circle*, *Sdr16c5* and *Sdr16c6*, overexpressed in the *sbse* mutant. *Gray*, *Homeodomain*-containing genes. *Orange*, validated non-*Hox* targets of retinoic acid.

Table 6.2: Summary of annotation clusters, top 100 under- and overexpressed genes Full results in appendix D. Prioritized clusters have an enrichment scores (Enr. Score) over 1.

	Under-expressed	E.S.		Over-expressed genes	E.S.
1	nucleosome, chromatin formation	6.99	1	translation, ribosomal activity	7.68
2	location: within the lumen	2.20	2	nucleosome, chromatin formation	6.25
3	oxygen binding and transport in the blood	2.19	3	extracellular matrix	1.88
4	reproductive, urogenital development	1.11	4	cell morphogenesis	1.26
5	nucleotide and ribonucleotide binding	1.08	5	cytoskeletal structure	1.00
6	signal transduction, embryonic morphogenesis	1.03	6	apoptosis/cell death	0.46
7	cytoplasmic and membrane bound vesicles	0.94	7	apoptosis/cell death	0.45
8	redox	0.86	8	cell cycle	0.32
9	epithelial development, urogenital development	0.74	9	negative regulation of gene expression	0.26
10	phosphorylation, protein modification	0.65	10	metal binding	0.20
11	extracellular matrix	0.62	11	location: within the lumen	0.018
12	adenine/purine (nucleotide, ATP) binding	0.58	12	adenine/purine (nucleotide, ATP) binding	0.015
13	protein catabolism	0.56			
14	guanine/purine (nucleotide, GTP) binding	0.55			
15	cell cycle control	0.53			
16	neuron development	0.51			
17	protein catabolism	0.51			
18	mRNA modification	0.48			
19	vascular development	0.42			
20	negative regulation of gene expression	0.41			
21	positive regulation of gene expression	0.33			
22	metal binding	0.31			
23	ionic and chemical homeostasis	0.19			
24	protein phosphorylation	0.038			

E.S. Enrichment score

6.2.1.3 *Gene Ontogeny (GO) analysis*

Gene Ontogeny (GO) analysis was carried out using the top 100 under- and over-expressed genes, as identified by DEseq (Appendix D.1). Functional classification clustering grouped genes involved in biological processes, molecular functions, and cellular compartments[3] that might be affected by the *sbse* mutation.[221] The results of these analyses are summarized in Table 6.2, and reported in full in Appendix D.

3 *"**Cellular Component**, the parts of a cell or its extracellular environment; **Molecular Function**, the elemental activities of a gene product at the molecular level, such as binding or catalysis; and **Biological Process**, operations or sets of molecular events with a defined beginning and end, pertinent to the functioning of integrated living units: cells, tissues, organs, and organisms."* (http://geneontology.org/)

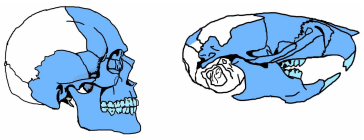

(a) Neural crest-derived bones. *Blue*, neural crest-derived bones in the skull.[222,223]

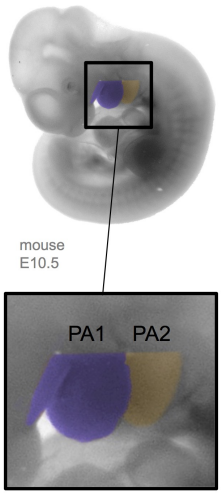

(b) BA 1 and 2, E10.5.

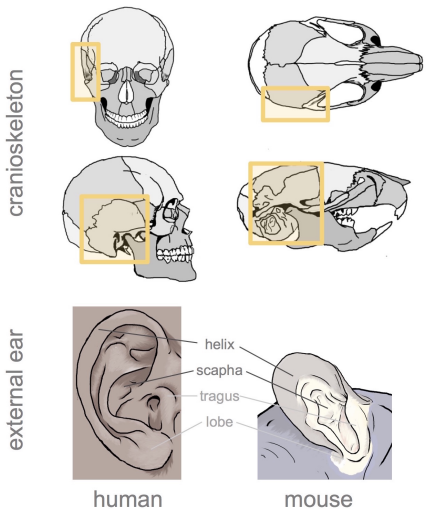

(c) Lateral facial region.

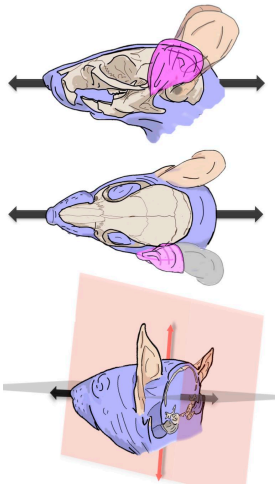

(d) Ear asymmetry.

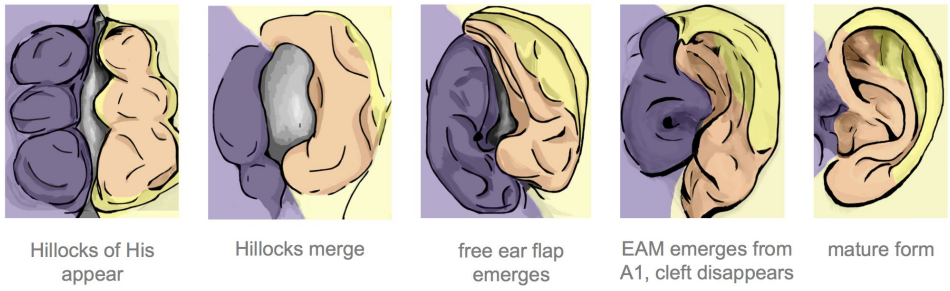

(e) and (b) Embryonic origin of the external ear: *Purple*, BA1. *Yellow orange*, BA2.

Figure 6.4: Lateral facial tissues and cranial neural crest cells(a) Neural crest-derived bones in human and mouse crania. **(b)** Branchial arches 1 (purple) and 2 (yellow) on a photograph of a mouse embryo at E10.5. **(c)** The lateral facial region on the adult human and mouse skulls is indicated by the yellow box. External ear diagram showing analogous structures in the adult human and mouse.[218] **(d)** Axis along which external ear placement varies in the *sbse* mouse. **(e)** Diagram of the current model of external ear morphogenesis. *Yellow-orange*, tissue derived from BA2.[216,218,224] (Figures *(c)* and *(e)* were adapted from my figure in Cox, et. al (2014).)

FUNCTIONAL CLASSIFICATION CLUSTERS, UNDER-EXPRESSED GENES. 24 annotation clusters were identified in the list of under-expressed genes in the mutant. Terms describing the 6 clusters with enrichment scores over 1 are:

- **biological processes:** chromosome structure, gene regulation, reproductive and urogenital development
- **molecular functions:** oxygen binding and transport, nucleic acid binding, signal transduction
- **cellular compartments:** intracellular lumens.

FUNCTIONAL CLASSIFICATION CLUSTERS, OVER-EXPRESSED GENES. 12 annotation clusters were identified in the the list of over-expressed genes in the mutant. Clusters with enrichment scores over 1 include:

- **biological processes:** chromosome structure, gene regulation, cell morphogenesis
- **molecular functions:** protein translation
- **cellular compartments:** extracellular matrix, cytoskeletal structure.

CHROMOSOME STRUCTURE AND GENE REGULATION Two annotation clusters with high enrichment scores (No. 1 under-expressed, ES 6.99; No. 2 over-expressed, ES 6.25) included 45 genes associated with chromosome structure and function, as well as regulation of gene expression (Figure D.4). Members of the *Histone H1* family are heavily represented in both the under- and over-expression sets, along with orthologs in the H2, H3 and H4 families.[225,226] Functional classification clustering identified differential expression in two groups of genes with GO terms associated with cell cycle regulation, including *Cyclin D2* (*Ccnd2*) and *Marker of proliferation 67* (*Mki67*) (Figure D.4).

CHROMOSOME 4 The top 100 under- and over-expressed genes included six located on mouse chromosome 4, of which two (*Plag1* and *Tenascin C, (TNC)*) are under-regulated (Figures D.4, D.1). None are within likely regulatory range: *Tnc*, approximately 60Mb from the *sbse* locus, is the closest to *Plag1* and the site of the mutation.[105] The four over-expressed genes on chromsome 4 are, in increasing distance from the *sbse* locus, *FRAS1 Related Extracellular Matrix 1 (Frem1)* (80 Mb), *Aldo-Keto Reductase Family 1, Member A1 (Akr1a1)* (112 Mb), *Lin-28 Homolog A (Lin28a)* (130 Mb), and *Inhibitor Of DNA Binding 3, (Id3)* (132 Mb).

COMPARATIVE GENE EXPRESSION, *sbse* AND *dumbo* MUTANTS The *Hmx1*$^{dm/dm}$ mouse carries a mutation in a distal enhancer element. In rats, this mutation causes an external ear phenotype.[227] To see if there are any shared gene expression patterns, I compared the top 100 under- and over-expressed genes in the *sbse* BA2 with that of the *Hmx1*$^{dm/dm}$ "*dumbo*" mutant, both at E10.5 .[4] 5 and 8 genes are shared between the under- and over-expression sets, respectively (Table 6.3). GO analysis identified a single annotation cluster, with terms referring to nucleosome, chromatin and DNA assembly, organization, and binding, which was composed entirely of *Histone H1* family members. The remaining common genes are have nucleic acid-related functionalities.

4 Both datasets are derived from analysis of tissue prepared in parallel at SCRI. E.D.C. performed the dissections and genotyping for *sbse*, while J.M.R. performed the dissections and genotyping for *dumbo*.

Table 6.3: Shared differences in gene expression, *sbse* and *dumbo* mutants.

Under-expressed in both *sbse* and *dumbo* BA2	
Lars2	Leucyl-tRNA synthetase 2
Hist1h1d	Histone gene cluster 1, H1 histone family, member D
Hist1h4d	Histone gene cluster 1, H4 histone family, member D
Hist1h1e	Histone gene cluster 1, H1 histone family, member E
Tnc	Tenascin
Over-expressed in both *sbse* and *dumbo* BA2	
Kcnq1ot1	KCNQ1 overlapping transcript 1
Rpph1	Ribonuclease P, component H1
Snord15b	small nucleolar RNA, C/D box 15B
4930470H14Rik	RIKEN cDNA 4930470H14 gene
Mir17hg	MicroRNA 17 host gene
Hist1h4a	Histone gene cluster 1, H4 histone family, member A
Rmrp	mitochondrial RNA-processing endoribonuclease, RNA component
Scarna10	Small Cajal body-specific RNA 10

6.3 DISCUSSION

DISRUPTION OF CHROMATIN STRUCTURE MAY DYSREGULATE RETINOIC ACID SIGNALING Preliminary data from an RNAseq analysis of the second branchial arch tissue dissected at E10.5 revealed a pattern of misexpression of multiple genes located within a 700 kb region on chromosome 4. Of the 10 genes found within this region, only one (*Plag1*) is structurally disrupted by the mutation; the locus is separated from other protein-coding genes by more than 400 kb of DNA (Figure C.1). Interestingly, we found significant over-expression of two genes located between 80 and 140 kb upstream from the wildtype *Plag1* start site (Figure 6.1b, 6.1c). *Epidermal retinol dehydrogenase 2* (*Sdr16c5*) and *Epidermal retinol dehydrogenase 2-similar (Sdr16c6)* are enzymes that catalyze the conversion of all-*trans*-retinol (Vitamin A) to all-*trans*-retinaldehyde and all-*trans*-retinal, precursors to the transcriptional activator retinoic

acid (Figure D.2). Embryonic overexpression of the *Xenopus laevis* (African clawed frog) homolog of *Sdr16c5*, rdhe2, results increased RA metabolism and produced modest morphological defects. Supplementation with the substrate all-*trans*-retinol and exogenous rdhe2 RNA results in dramatic defects including reductions in the size of the head and overall length of the body.[228,229] This may be consistent with a neural crest cell patterning defect-related etiology for the *sbse* phenotype.

Evidence exists suggesting that the effect of RA on cranial neural crest cell proliferation and survival is more pronounced than it is on those neural crest cells fated to migrate into the trunk.[230] *In vitro* over-exposure to RA in mid-gestation has shown that growth of the first two branchial arches is significantly impaired by persistent exposure to RA.[231]. While RAR binding motifs are common throughout the genome, their accessibility may be limited. Tissue-specific sensitivities to epigenetic factors (original definition) are influenced by epigenetic modifications (more recent definition), i.e., modifications to genomic structure is a major determinant of cellular identity.[232] Crudely, factors like histone modifications and DNA methylation in a given region of the genome determine its accessibility to cellular transcription machinery, and therefore, regulate which genes can be expressed in that cell. (The same principle applies to transcription factors, like those activated by RA.) Various sequencing technologies are used, with great success, to test the tissue-specific binding ability of individual DNA binding proteins across the genome, and might be used to compare the relative availability of RAR binding sites between tissue types at different points in embryogenesis.[178,233]

Sequence analysis and ChIPseq data from the UCSC genome browser suggests that the *sbse* mutation may disrupt functional motifs, including CTCF, that often define boundary regions required to maintain higher order chromatin structure and that are

a significant regulator of gene expression (CTCF binding motifs in the *sbse* deletion are in Appendix E).[117,198] Disruption of such domains is thought to interfere with the normal interaction of genes, promoters, and enhancers. The *sbse* mutation deletes a validated CTCF binding site with other regulatory markers in the first intron of *Plag1*. If the deletion is a functional component of an insulating boundary region or or an enhancer, aberrant local chromatin architecture may result in over-expression of the retinoid metabolism enzymes *Sdr16c5* and *Sdr16c6*, located nearby.

RETINOIC ACID DYSREGULATION ON MID- AND LATERAL FACIAL MORPHOGENESIS *sbse* mice have significant defects in the cartilaginous components of the cervical vertebrae and sternum, which are particularly interesting in light of the postcranial defects commonly associated with Craniofacial microsomia, Hemifacial microsomia, Oculo-Auriculo-Vertebral Spectrum (OAVS), and other craniofacial conditions associated with branchial arch defects (Figures 3.7, 3.8, and 3.9). A high incidence of vertebral anomalies, and in at least one reported case, sternal anomalies have been reported in this population.[34,41,140,234] Experimental exposure to single dosages of RA *in utero* are sufficient to induce anomalies of the vertebrae, similar to those seen in the *sbse*, in the Syrian hamster.[235] Dysregulation of retinoic acid metabolism is a plausible cause of cartilage and other tissue patterning abnormalities in mutants.

Three structural anomalies affect the lateral facial region of the *sbse* mutant, of which only one, external ear hypoplasia, is fully penetrant and minimally variable. In a mouse model of Treacher Collins/mandibulofacial dysostosis, maternal hypervitaminosis A is reported to cause death in pre-otic neural crest cells and a reduction in local mesenchymal cell populations, consistent with evidence that growth in

the branchial arch tissues differentially reduced in the presence of the vitamin A metabolite, RA.[236] The placement of the external ears are asymmetric in 60-65% of animals at all ages: in affected animals, one ear is "dropped", or set low along the axis of expected migration (Figure 6.4d)[5]. In the normal human embryo, it is thought that the relative position of the ear shifts laterally due to differential growth of the surrounding tissue, which in the mouse, is the temporalis muscle.[242,243] The migration, patterning, and differentiation of myogenic paraxial mesoderm has been shown to depend on cranial neural crest-derived instructions, and deficiency could therefore be a secondary effect of retinoic acid exposure.[244]

The third lateral facial anomaly in the *sbse* is consistent with a defect in the cavitation of the middle ear. The decreasing incidence of radio-opacity in the mutant middle ear over time suggests that cavitation is delayed, rather than arrested, although inflammation (otitis media) may be an additional or alternative cause that could follow such a pattern. The neural crest derived cells involved in the cavitation event undergo a mesenchymal to epithelial transition, and become the epithelial lining of the middle ear cavity in the upper region of the bulla. Endodermally-derived epithelia forms the lining of the shell-like part of the bulla.[245,246]

Persistence of the human meatal plug in hemifacial microsomia patients has been suggested to cause both soft tissue and mineralized obstructions in the ear, and while

5 In 1922, George Streeter suggested that the external ear may be entirely derived from the hyoid arch (second) arch, foreshadowing the findings of a study by Minoux, et al. (2013) by 91 years. In the same manuscript, Streeter's interpretation of Wilhelm His's 1885 model of EAM formation suggests that both were aware of a "transverse elevation in the floor of the fossa angularis", a "swelling of the closure plate of the first gill cleft". This structure, called *tuberculum central*, was reported to contain parts of the hyoid cartilage and stapedial artery.[224] Soon after the work of His was published, Kastschenko (1887) reported that the EAM was associated with, but secondary to, the branchial cleft in pigs.[237]. Nearly a century after His, Streeter, and Kastschenko's publications, Mangold et. al (1981) and Theiler and Sweet (1986) describe tissue bridging between the first and second arches (*membrana obturans*) before the formation of the EAM.[100,238] Despite these and other studies, at some point, the collective scientific unconscious rejected a model of EAM formation by invagination of the *tuberculum central* or *membrana obturans*, in favor of a persistent branchial cleft model. The latter is described in a range of modern textbooks (Nanci/Ten Cate (2013),[239] Sperber et al. (2010),[150] Kaufman and Bard (1999),[240] Enlow (1990)[241]) as the canonical model of EAM formation.

no systematic study has been made of older *sbse* middle ear scans, such a phenotype may contribute to the hearing loss reported in the line.[247–249] Retinol has been shown to induce apoptosis in cells in a mitochondria-dependent fashion.[250,251] If the retinoic acid hypothesis is causative of the craniofacial phenotype, the progressive hearing loss reported in the *sbse* by Curtain, et. al (2001) might be a consequence of retinoic acid toxicity in neural crest derived auditory hair cell mitochondria.[251,252] Further work is necessary to confirm that the *sbse* mutation causes dysregulation of retinoic acid metabolism, and that such dysregulation is sufficient to disrupt morphogenesis and physiological function in homozygotes.

CONCLUSIONS AND FUTURE DIRECTIONS

7

DISCUSSION

This thesis examined the genetic and developmental mechanisms that result in mid- and lateral craniofacial dysmorphology and asymmetry in a mouse model of Branchial arch-related syndromes, using a combination of 3D imaging and molecular biology techniques . The cranioskeletal phenotype of the *small body-small ear* (*sbse*) mouse is highly variable, and shows a significant incidence of asymmetry in the midface, cranial base, and lateral facial tissues. My first major goal was to characterize the development of the *sbse* phenotype from birth through maturity, and identify which, if any, growth site defects influence symmetry, outgrowth, and overall changes in shape in the mutant skull. The second major goal of this project was to identify the genetic and developmental mechanisms causing those changes in shape.

POSTNATAL FACIAL ASYMMETRY

Premature fusion at the maxillary/premaxillary suture in Apert $Fgfr2^{S252W}$ and Muenke $Fgfr3^{P244R}$ syndrome models, both of which have significant midface hypoplasia, inspired the initial hypothesis, which related midface hypoplasia and asymmetry in the *sbse* mice to facial suture fusion. Surprisingly, there was no associ-

ation between zygomatic-maxillary suture fusion and dorsally apparent asymmetry (i.e., deviation of the snout relative to the sagittal plane).

Mid- and lateral facial asymmetry are characteristics of Branchial arch-related syndromes (BAS) like Hemifacial microsomia, Craniofacial microsomia, and Oculo-Auriculo-Vertebral Spectrum. Like in human BAS, midface hypoplasia and asymmetry in the *sbse* mouse model involves both the maxilla and mandible, and tends to appear ipsilateral to any apparent external or middle ear defects. A set of classic experiments demonstrated that injection of a teratogen - in this case, the folate antagonist triazene (N_2H_2) - into a mouse dam at 10.5 dpc produced focal hemorrhages of variable size over the second branchial arch. The resulting damage to the remodling stapedial artery and lateral facial region caused the widespread damage to derivatives of the brachial arches found at E17:

> "...on the affected side, marked undedevelopment of the orbital frame and zygomatic portion of the malar bone, absence of the zygomatic portion of the temporal bone, distortion and diminution of the ramus of the mandible with absence of the condylar prcess, and reduction of the coronoid process..." (DE Poswillo, 1973[32])

This experiment shows how local tissue damage can affect both the upper and lower jaws, in utero.[1]

1 In that publication, Poswillo notes that similar injections of Vitamin A in rats had no effect on the bony facial skeleton. I expect that the gestational stage at which it was introduced to the dam, as well as the form, prevented widespread teratogenic effects on pups. (Vitamin A must be metabolized to all-*trans*-retinol before it can activate retinoic acid receptors signaling.[208])

POSTNATAL MIDFACE HYPOPLASIA

Compared to the mice in the triazene experiments, the phenotype observed in the *sbse* are mild. Comparison of hemimandible pairs found that maxillary asymmetry predicts inter-pair differences in the shape of the ossified condylar region, and that the body of the mandible is straight and symmetric. Maxillary asymmetry in mutants, when present, appears no earlier than P8, well after the incisors - concurrent with (or slightly before) the eruption of the molars and the transition from nursing to solid foods.[253] Throughout this time, the growth of soft tissue, including the masticatory muscles, displaces the mandible forward, permitting ossification at the condylar cartilage.[74] If subtle asymmetry in the bony maxilla or the size of the masseter muscle is present at birth, the growing midface might force pups to gradually adapt their bite, changing the mechanical forces acting on each condyle, resulting in asymmetric ossification. An embryonic defect in the maxilla with a slow progress towards asymmetry may provide the time for biomechanical adaptation of the mandible, a trait observed in the *sbse* and *froggy* (*frg*) mice. Midface hypoplasia and asymmetry develop in the genetic, developmental, and biomechanical context of the skull, and may be adaptations to other primary defects.

A search for the term "midface hypoplasia" in the Online Mendelian Inheritance in Man database returned 207 genes and associated conditions, including several types of syndromic craniosynostosis. In the *sbse*, premature fusion of the interfrontal suture is significantly associated with dorsal asymmetry. The interfrontal suture in mice is the equivalent of the human metopic suture, raising the question of whether or not the *sbse* phenotype qualifies as craniosynostosis. A 2011 publication reporting interfrontal suture fusion in a model of metopic synostosis, caused by the hypomorphic *Frem1*^{bat} allele suggests that it might be an appropriate label. Abnormalities

at the interfrontal suture seems to be common in mice with maxillary asymmetries, both those with with premature fusion - *sbse*, *froggy* (reported in chapter 4), and two models of metopic craniosynostosis, *Frem1*^{bat} and *Gli3*$^{Xt-J}$[2] - and with delayed ossification in Apert syndrome *Fgfr*^{S252W} and *Fgfr*^{P253R} models.[146,147,254,255] While an interesting correlation, it brings to mind the morphological differences found in late embryonic stage Apert syndrome pups[3], which occur long before coronal suture fusion.[132] In both cases, suture fusion may have a postnatal effect, but do not explain dysmorphology on their own.

Altered tension in the dura mater has been proposed to act as a switch for calvarial suture fusion.[256] Basicranial asymmetry has been reported in patients with metopic synostosis, the development of which might cause shift dural attachement points in the skull, and provide abnormally tensed conditions.[257] Interestingly, both the cranial base and the interfrontal suture contain neural crest-derived cartilage. Ectopic ossification of the cartilaginous intersphenoidal synchondrosis in the *sbse* is associated with shortening and impaired flexion of the cranial base; shortening of the cranial base is often cited as the cause of midface hypoplasia in Apert and Crouzon syndrome patients, and in mice carrying their mutations.[136,147,258,259] The incidence of premature intersphenoidal synchondrosis ossification increases in the *sbse* from P7 through P28. (In humans, the intersphenoidal synchondrosis is typically no longer patent at birth; pathological ossification typically occurs in the spheno-occipital synchondrosis.[260,261]) In *sbse*, the overall length of the cranial base, the length of the sphenoid, and the angle between the cranial base and the cribiform plate of the ethmoid are significantly affected. Curiously, the growth rates of the mutant presphenoid (at the surface of the oral cavity) and the snout (from crista galli to the incisors) remain close to the wildtype through P21, while the changes to the angle of the snout relative to the

2 *Frem1*^{bat}, Vissers, et al. (2011) Figure 4.[254] and *Gli3*$^{Xt-J}$, Veistinen et al. (2012) Figure 1r,s.[255]
3 Specifically, Apert syndrome-associated *Fgfr2*^{P253R} and *Fgfr2*^{S252W} mutants.

cribiform plate of the ethmoid are delayed. A possible interpretation of these trends, in light of Enlow's model of maxillary growth, might be that secondary displacement of the maxilla is impaired by a short cranial base, and that primary growth at the nasal septum is slightly reduced.[241] While this does not account for bony deficiency in the dorsal nasal region, it would explain the delay in snout "lifting" observed in the mutant.

Genetic models support a link between cartilage growth and midface morphology: two of the best-characterized mutant lines with midface phenotypes, *Brachymorph* (*Bm*) and *Brachyrrhine* (*Br*) are the result of distinct defects disrupting chondrocyte proliferation in the cranial base.[155–157] Mice carrying the *Brachymorph* (*Bm*) mutation also have a hypoplastic midface and short cranial base, thought to be due to a global defect in cartilage matrix biochemistry.[262] Both the *Br* and *Bm* mice have short cranial bases and hypoplastic midfaces; images of the *Bm* mouse show notable maxillary asymmetry[4]. The *Br* mutant line was first reported by Lozanoff in 1993, and is thought to be a result of dysregulation of the homeobox transcription factor *Six2*.[87]. It is homozygous lethal, but adult *Br*/+ mice show a frontonasal dysplasia-like phenotype with facial clefting, ocular hypertelorism, and maxillary retrognathism. The presphenoid is severely hypoplastic or absent in these animals, a result of decreased chondrocyte proliferation in the region and a reduction in cranial base length.[155–157,263]

ENDOCHONDRAL OSSIFICATION, *plag1*, AND RETINOID METABOLISM

Many of the defects in the *sbse* mouse are directly or indirectly related to cartilaginous tissues, The vertebral synchondrosis defects found in the mutant support the idea that

4 *bm/bm* Hallgrímsson, et al. 2006 Figure 2.[153]

it may specifically model OAVS, Oculo-Auriculo-Vertebral spectrum. Disruption of both major vessel development and overall vascular density have been shown to affect craniofacial development, and in major disrupts, to cause BA-related syndrome-like phenotyes.[31,32,60] In the second chapter, I tested the connection between the *sbse* phenotype and the activity of the gene *Plag1*, over-expression of which has been shown to induce expression of angiogenic factors like *Vegfa*. Disruption of both major vessel development and overall vascular density have been shown to affect craniofacial development.[5] While I found that that expression of both *Vegfa*^{120} and *Vegfa*^{164} isoforms were reduced in the mutant, and was able to show that *Plag1* may activate expression of *Vegfa*, a complementation test demonstrated that *Plag1* deficiency was not sufficient to cause the *sbse* cranioskeletal phenotype on its own. Although the known phenotypes of *Plag1* deficiency - small body size and reduced fertility - are present in the *sbse*, we found that its loss is not sufficient to cause all the cranioskeletal abnormalities observed in the mutant[6]. Subsequent experiments identified a pattern of aberrant gene expression in the *sbse* locus that suggesting that over-expression of two enzyme involved in retinoid metabolism (*Sdr16c5* and *Sdr16c6*) may sensitize the *sbse* to the known teratogenic effects of Vitamin A derivatives.[13]

Retinoic acid is both a potent regulator of developmental patterning, as well as a potent teratogen. Free retinoic acid (all-*trans*-retinol, a metabolite of Vitamin A and its derivatives) activates specialized transcription factors known to regulate the spatial expression of *Hox* and other patterning genes, cellular differentiation, as well

5 Interestingly, *Fgfr1* and *Fgfr2*, the genes associated with Apert, Pfeiffer, and Crouzon syndromes, are expressed at high levels during intramembranous ossification. Endothelial-specific conditional heterozygosity for the Apert syndrome *Fgfr2*^{P253R} mutation affects the early volume and density of the facial bones, but does not affect their adult morphologies, suggesting that a vascular mechanism is not a major cause of midface hypoplasia in craniosynostosis.[60]

6 Genome-wide association studies (GWAS) have identified the *Plag1* locus as a conserved modulator of mammalian stature; comparative analysis found that copy number variants (CNVs) at the equine *Plag1* locus modulate stature across several breeds of horses.[264–268] Molecular analysis of stature-associated polymorphisms in the 5′ region of the bovine *Plag1* homolog has shown that they are sufficient to modify expression levels of *Plag1* and its conserved transcriptional partner, *Coiled helix-coiled helix 7* (*Chchd7*).

as chondrocyte maturation and endochondral bone formation in the limbs.[269] The structures involved in mid- and lateral facial phenotypes in the *sbse* - facial and anterior cranial base bones, the intersphenoidal synchondrosis, interfrontal sutural mesenchyme, the external ear, the meatal plug of the middle ear - are largely of neural crest origin, while the vertebrae and rib cartilage are derived from *Hox*-patterned mesodermal sclerotomes.[270] These patterns of malformation, and the variability present in the *sbse* phenotype, are consistent with a congenital sensitivity to dietary Vitamin A and its derivatives. In the *sbse*, this may be caused by an over-expression of the enzymes *Sdr16c5* and *Sdr16c5*.

FUTURE DIRECTIONS

Initial analysis of the *sbse* mutation found that, although over 30 kb of genomic DNA are rearranged, only one gene is structurally disrupted. Deficiency of that gene, a transcription factor called *Pleomorphic adenoma gene 1* (*Plag1*), was reported to cause small body size and reduced reproductive ability.[271] Ultimately, I found that *Plag1* deficiency alone is not sufficient to cause the cranioskeletal abnormalities observed in the mutant *sbse*, although it may contribute to the body weight and reproductive phenotypes. The structural defect reducing expression of *Plag1* in the *sbse* functionally ablated the activity of the the canonical promoter by shifting its position by 30 kb. The breakpoint that facilitated the inversion is one of many known to exist in the first intron of *Plag1*, which make the region vulnerable to rearrangement events during cell division.[185,191] Flanking the intronic break is a deletion covering a highly conserved region, 745 bp in length. Initially, the presence of validated P300 and POL2 binding sites, as well as DNAse I hypersensitivity sites, suggested that it may have a regulatory functionality. Further analysis may focus on the putative regulatory

elements at this site.

In tumor tissues, the loss of the first exon of human PLAG1 to promoter swapping does not prevent expression, suggesting that exon 1 is not required for transcription initiation. In addition, promoter- and enhancer-associated epigenetic markers have been reported in the *Plag1* sequence in mouse erythroleukemia (MEL) cells, E11.5 tissue, and embryonic mesoderm[7]. The effect of the mutation on local gene expression should be studied further. Two likely causes of dysregulation in the mutant may be the deletion of the conserved putative enhancer sites in intron 1 of *Plag1*, or the disruption of a silencer/boundary domain marker, *CTCF*. *CTCF* binding guides local local chromatin confirmation, defining Topologically Associated Domains (TAD). Loss of genomic boundary definition has been shown to result in ectopic gene enhancer-driven gene expression.[198] Transcription factor binding tracks in the UCSC Genome Browser identifies *CTCF* binding peaks within the breakpoint region of *Plag1* in C2C12, CH12, and MEL cells, as well as 3' repeating sequences, both considered markers of TAD boundaries. Dysregulation of genes on one side of the *sbse* inversion may be a result of this local disruption in chromatin folding, the loss of enhancer sites, or both.

The *sbse* mouse has an unusual and complex phenotype, which has features of both metopic craniosynostosis and Branchial arch-related syndromes, and is caused by a novel regulatory mutation in a locus typically associated with cancer. In this study, I examined the development of the cranioskeletal and external ear phenotype, and found that ipsilateral facial malformations and cranial base growth defects were associated with interfrontal suture and cranial base synchondrosis fusion. The *sbse* mutation appears to disrupt a Topological Chromatin Domain, a recently-discovered organizational unit of the genome.[198] The structural disruption of the gene *Plag1*, is not

7 While the data reported by USCS are not from *sbse* tissue, ChIP seq binding in any cell type proves that is is a functional motif.

causative to the craniofacial phenotype; rather, the mutation aappears to have a regulatory effect on nearby genes encoding enzymes involved in Vitamin A metabolism. Retinoids can modulate activities as diverse as embryonic patterning, neural crest cell formation, the proliferation, growth, differentiation, and migration of vascular smooth muscle cells, chondrocyte maturation and endochondral ossification, but seems to have a more tissue-specific effect on the embryonic branchial arches.[200,231,269,272] The human homolog of the two affected enzymes retains its position 5'of *Plag1* and its breakpoint-heavy first intron. I propose that the *sbse* mutation, or something similar, may cause congenital retinoic acid sensitivity and the characteristic mid- and lateral facial malformations seen in patients with Branchial arch-related syndromes.

APPENDICES

A

MOUSE ANATOMY REFERENCE (C57BL/6J +/+)

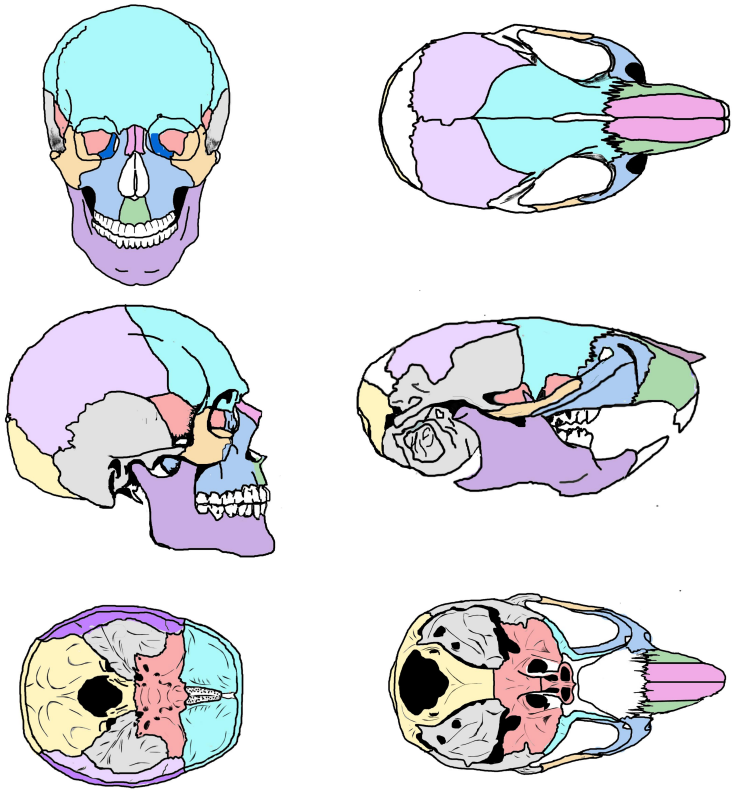

Figure A.1: Human and mouse cranioskeletal homology.[24,273]

Green, premaxilla. *Blue*, maxilla. *Purple*, mandible. *Pink*, nasal bones. *Light blue*, frontal bones. *Yellow-orange*, zygomatic. *Salmon*, sphenoid. *Gray*, temporal bones and bulla. *Light purple*, parietal bones. *Light yellow*, occipital. *White*, mouse interfrontal and interparietal bones.

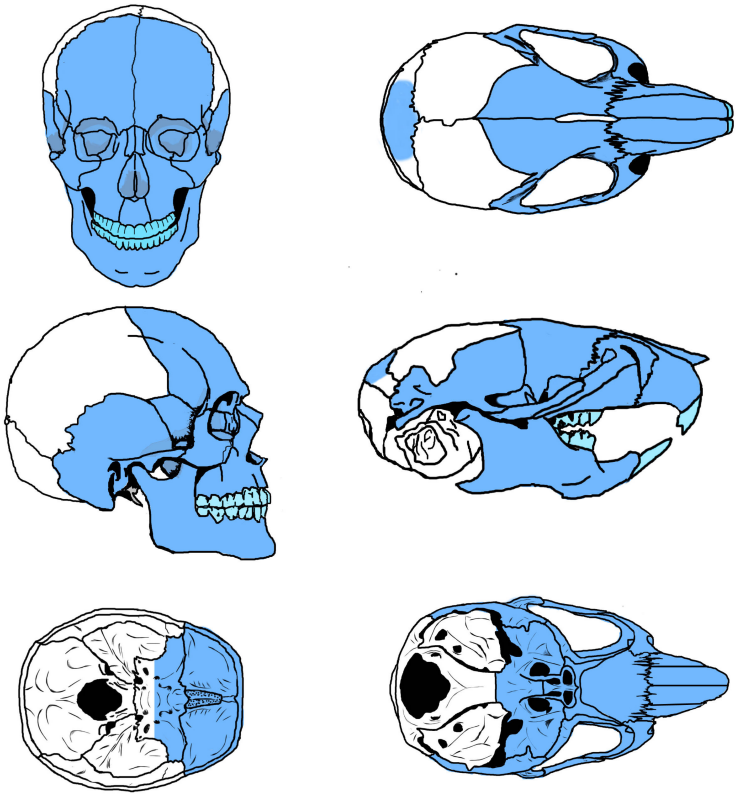

Figure A.2: Bones derived from cranial neural crest cells (blue).[56,150]

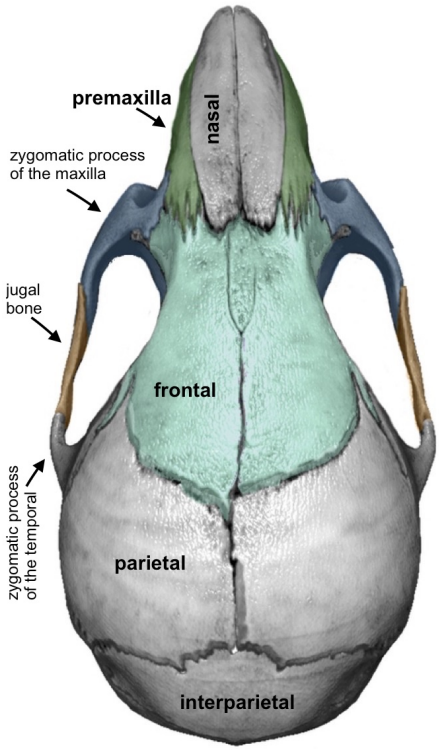

(a) *Norma verticalis (superioris)*/**dorsal view**

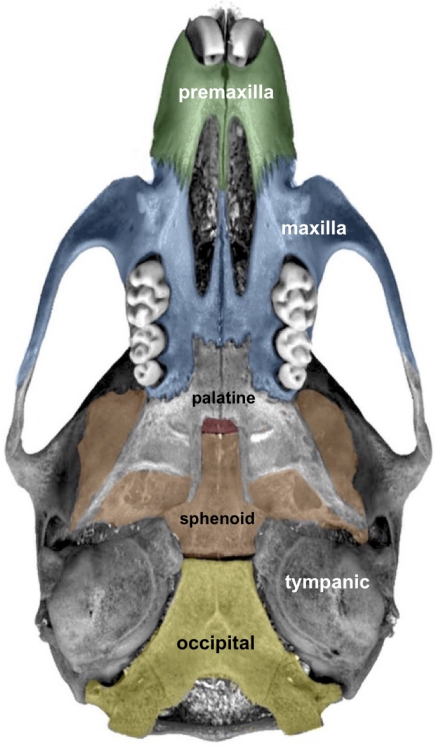

(b) *Norma basalis (inferioris)*/**ventral/ectocranial view**

(d) *Norma basalis (exterior)*/**dorsal endocranial view**

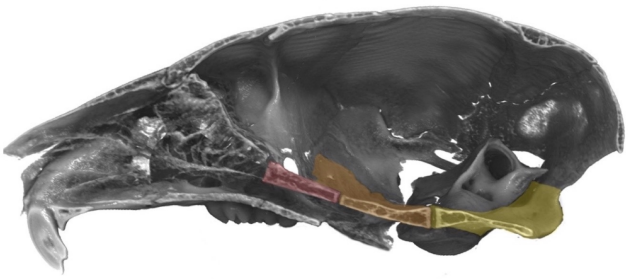

(c) *Norma sagittalis*/**lateral hemisected view**

(e) *Norma lateralis (temporalis)*/**lateral view**

Figure A.3: Wildtype external cranioskeleton P28. μCT scan rendering of a wildtype C57BL/6J +/+ at P28. *Green*, premaxilla. *Blue*, maxilla. *Light green*, frontal and interfrontal bones. *Red*, presphenoid. *Orange*, basisphenoid. *Yellow*, basioccipital. *Dark blue*, middle ear (inside surface, disarticualted tympanic bulla). *Slightly different orange*, jugal bone.

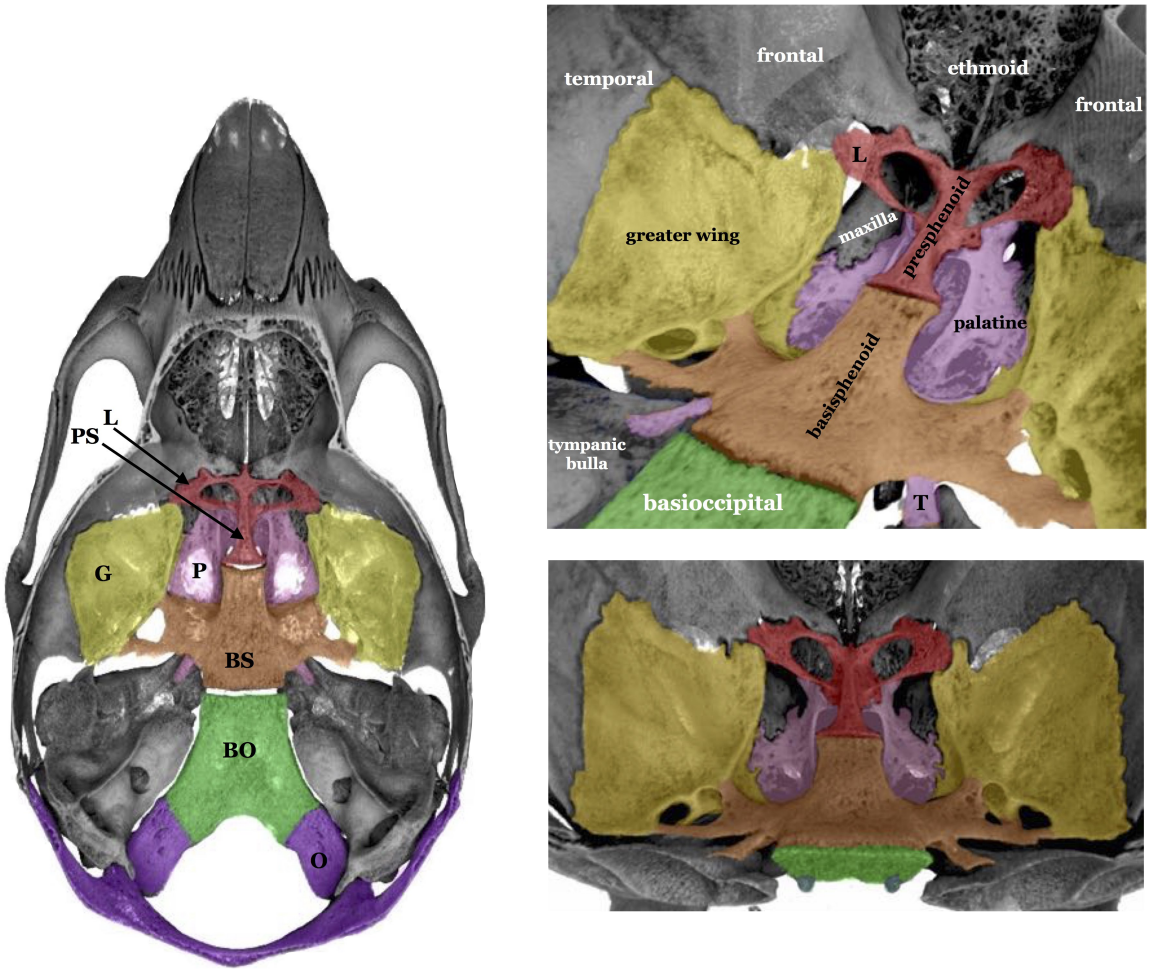

Figure A.4: Wildtype C57BL/6J +/+ cranial base, P28. Changing cranial base morphology the wildtype. µCT scan rendering of *Norma basalis (exterior)*/endocranial surface view.

Red, presphenoid. *Orange*, basisphenoid with *Yellow*, greater wing of the sphenoid. *Pink*, palatine. *Green*, basioccipital. *Purple*, exoccipital.

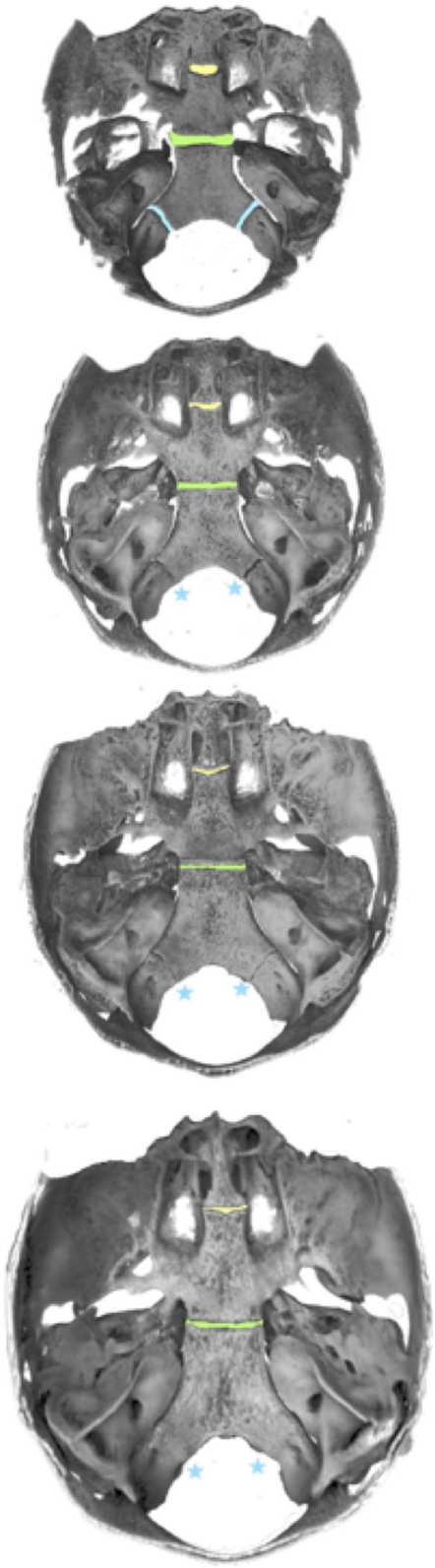

Figure A.5: Wildtype C57BL/6J +/+ cranial base synchondroses, P7-P28. μCT scan rendering of the *Norma basalis (exterior)*/dorsal endocranial view of the cranial base in C57BL/6J +/+ , P7-P28.

Yellow, intersphenoidal synchondrosis (ISS). *Green*, spheno-occipital synchondrosis (SOS). *Blue*, exoccipital-basioccipital synchondrosis (EO-BO).

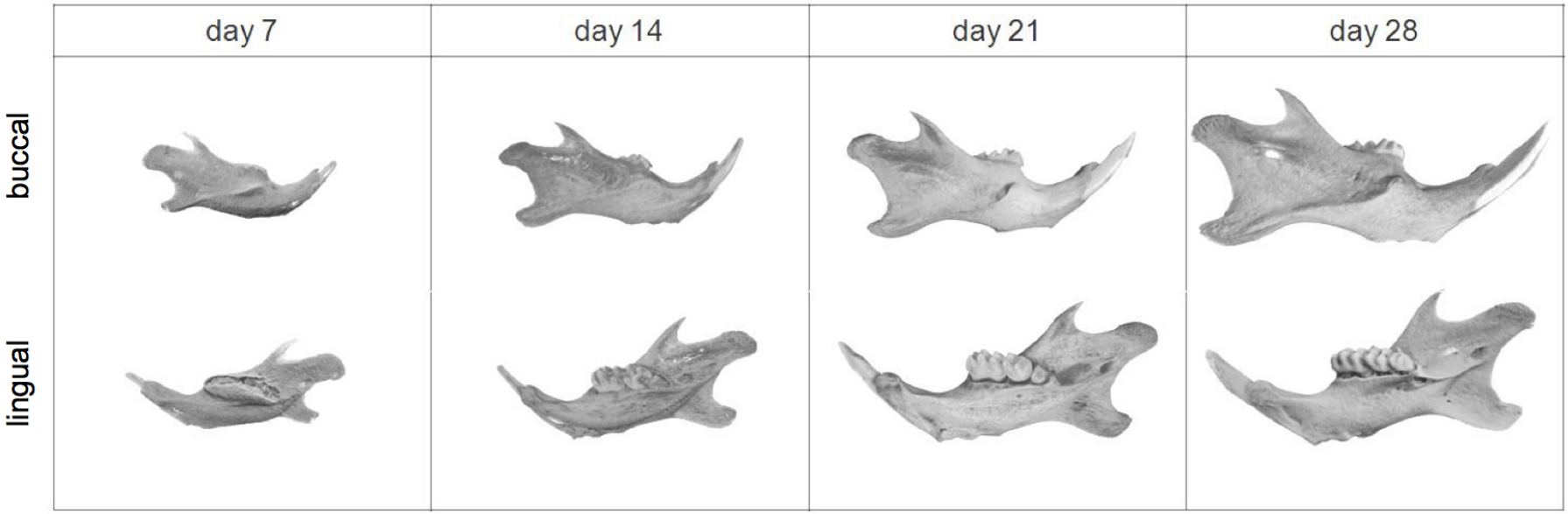

Figure A.6: Wildtype C57BL/6J +/+ hemimandibular morphology, P7-P28. Significant changes in molar count and hemimandibular morphology occur between postnatal days 7 and 28.

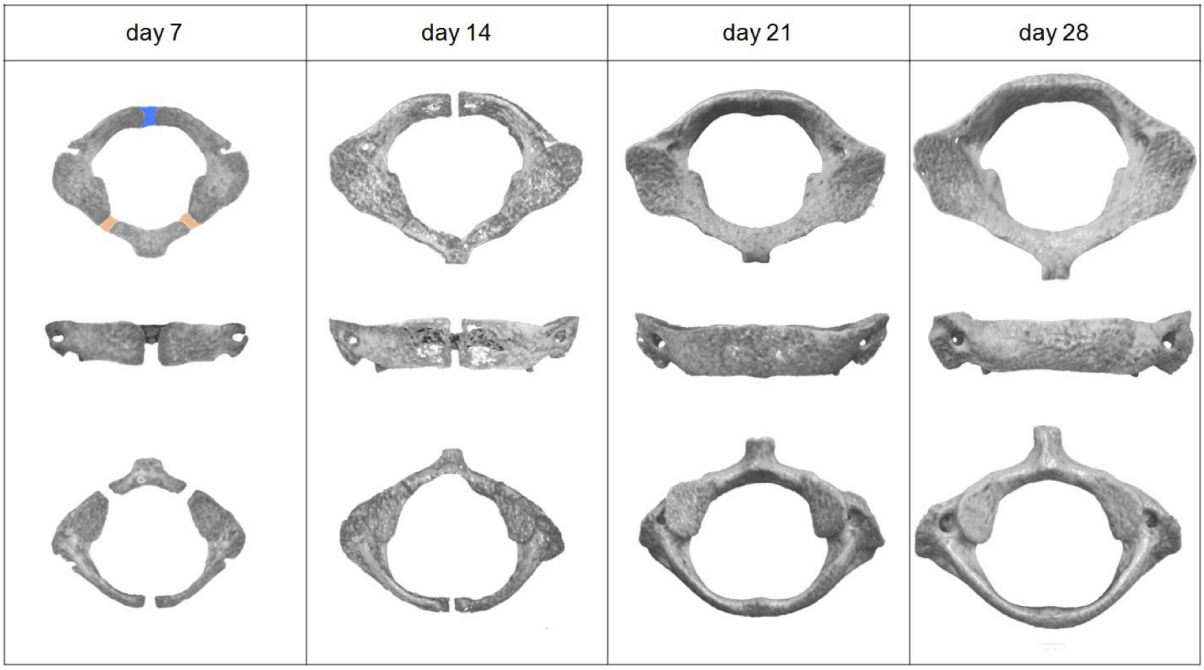

Figure A.7: Morphogenesis of the first cervical vertebra in C57BL/6J +/+ mice, P7-P28.

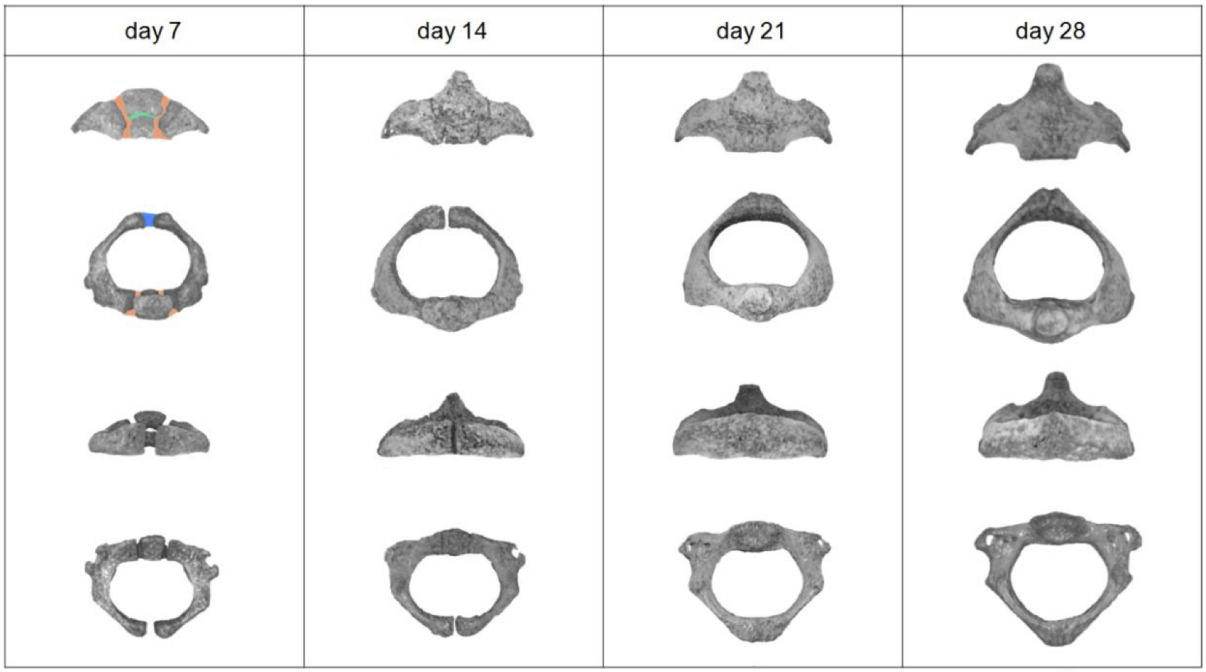

Figure A.8: Morphogenesis of the second cervical vertebra in C57BL/6J +/+ mice, P7-P28.

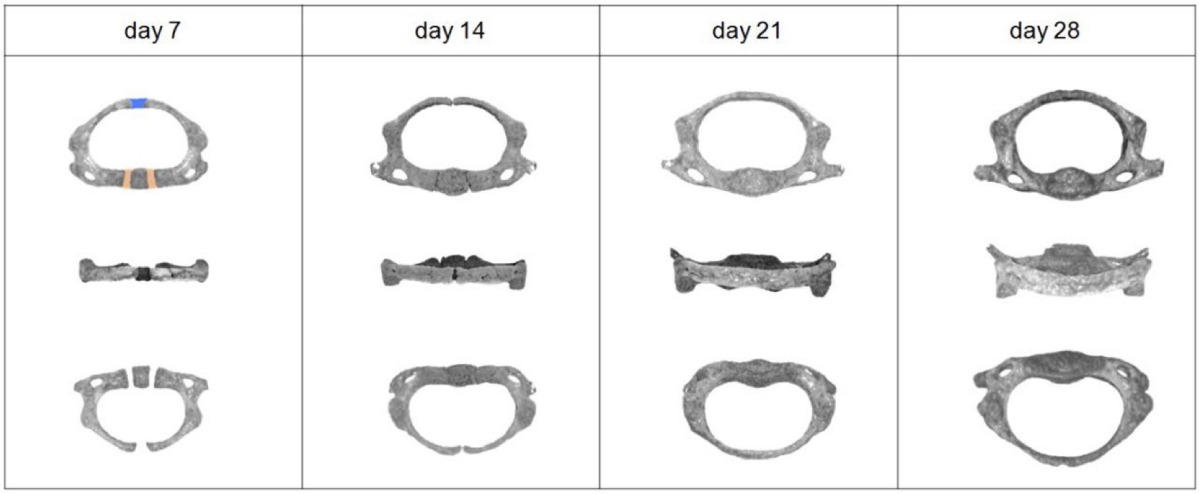

Figure A.9: Morphogenesis of the third cervical vertebra in C57BL/6J +/+ mice, P7-P28.

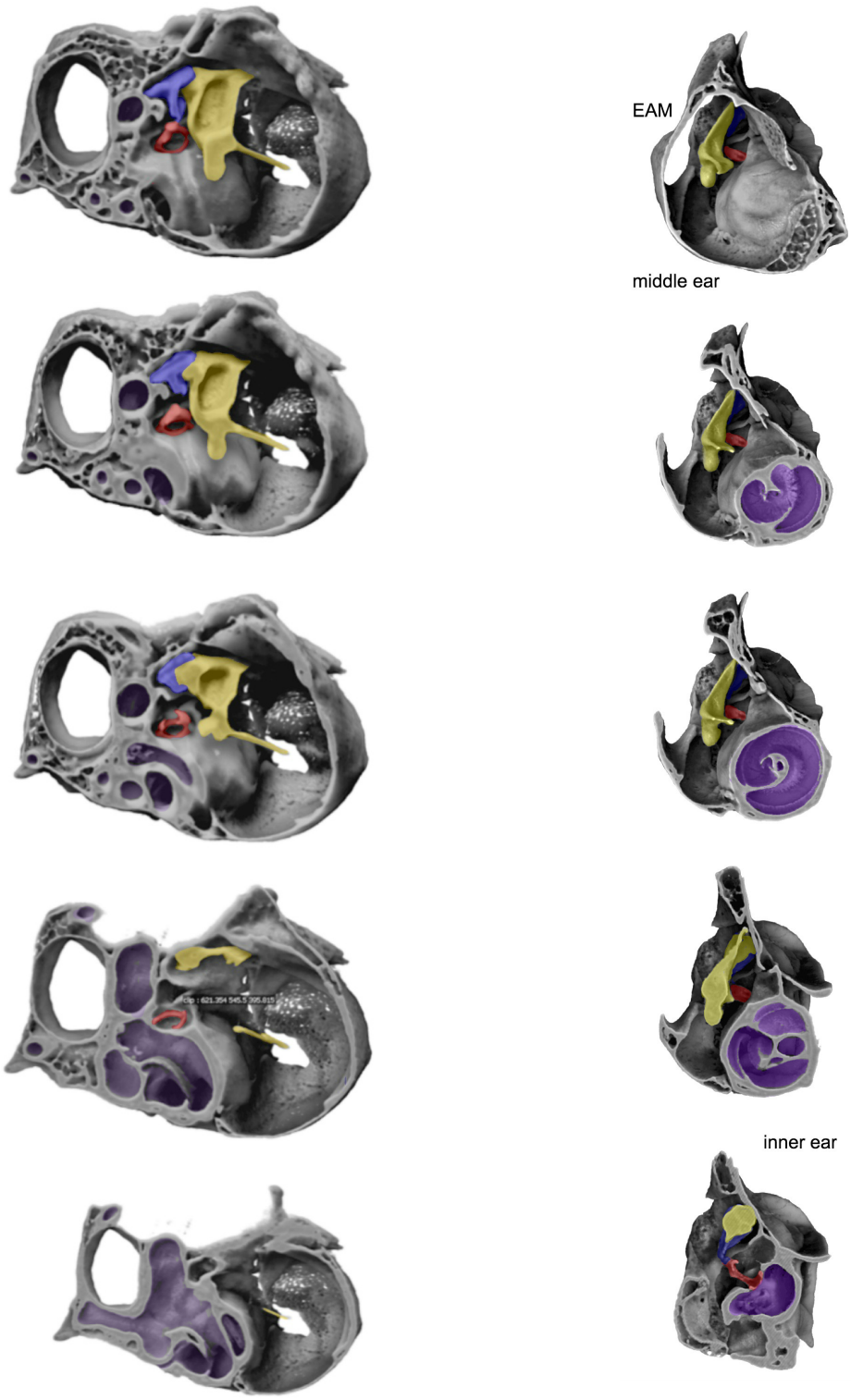

(a) Parasagittal sections. **(b) Paracoronal sections.**

Figure A.10: Sections through μCT scan rendering of the C57BL/6J +/+ tympanic bulla at P28. (a) Parasagittal sections progressing from the lateral towards the midline. Ossicles are show in the middle ear cavity. **(b)** Paracoronal sections progressing from the posterior to the anterior. Ossicles are shown in the middle ear cavity.

Yellow, incus. *Blue*, malleus. *Red*, stapes. *Purple*, inner ear.

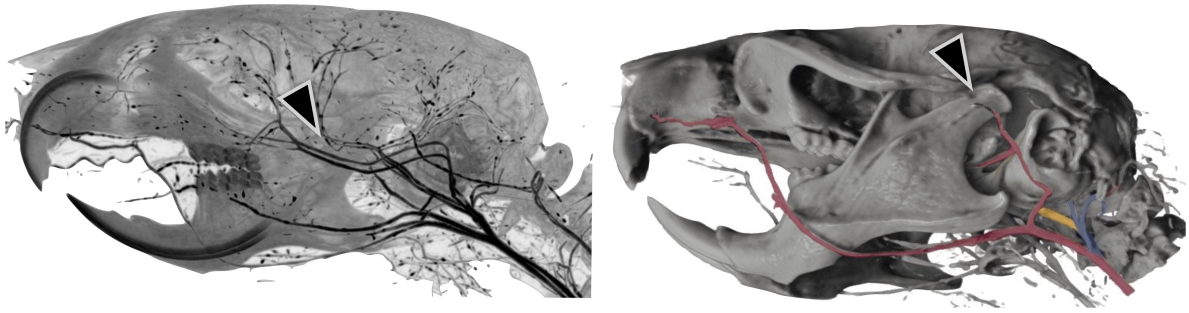

Figure A.11: Major vessels supplying the head and neck in C57BL/6J +/+ mice, P145.

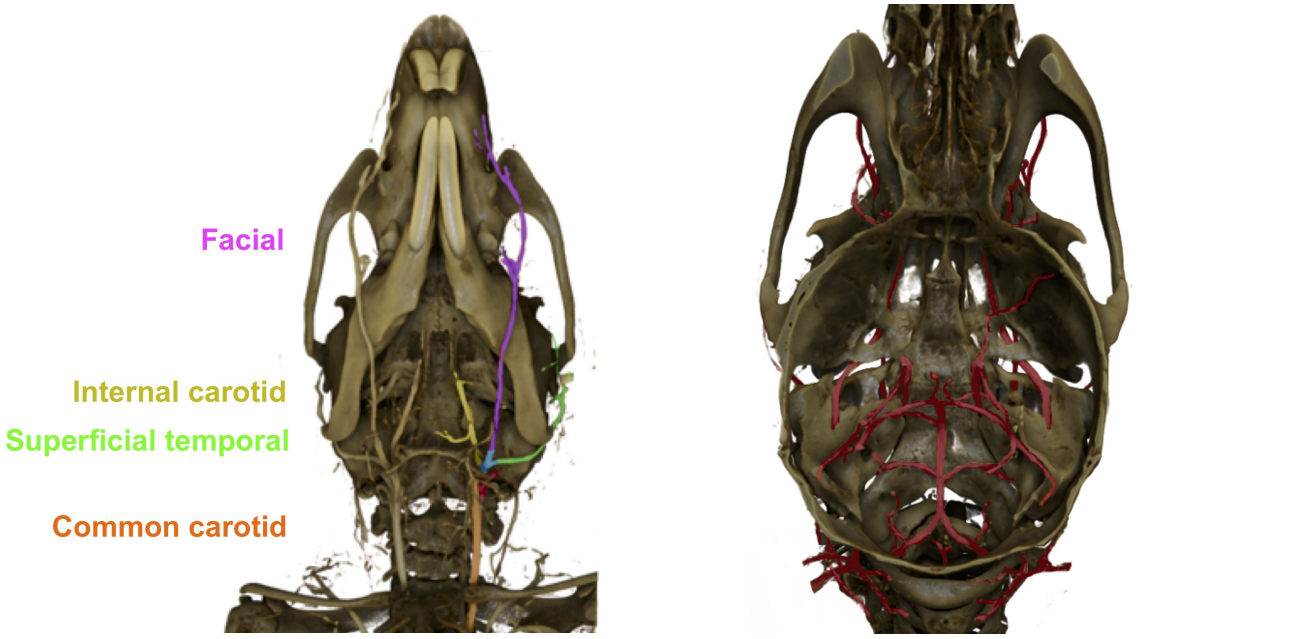

(a) *Norma basalis (inferioris)*/ventral/ectocranial view

(b) *Norma basalis (exterior)*/dorsal endocranial view

Figure A.12: Major vessels entering at the cranial base in C57BL/6J +/+ mice, P145 *Red*, carotid artery. μCT scan rendering following injection of contrast media.

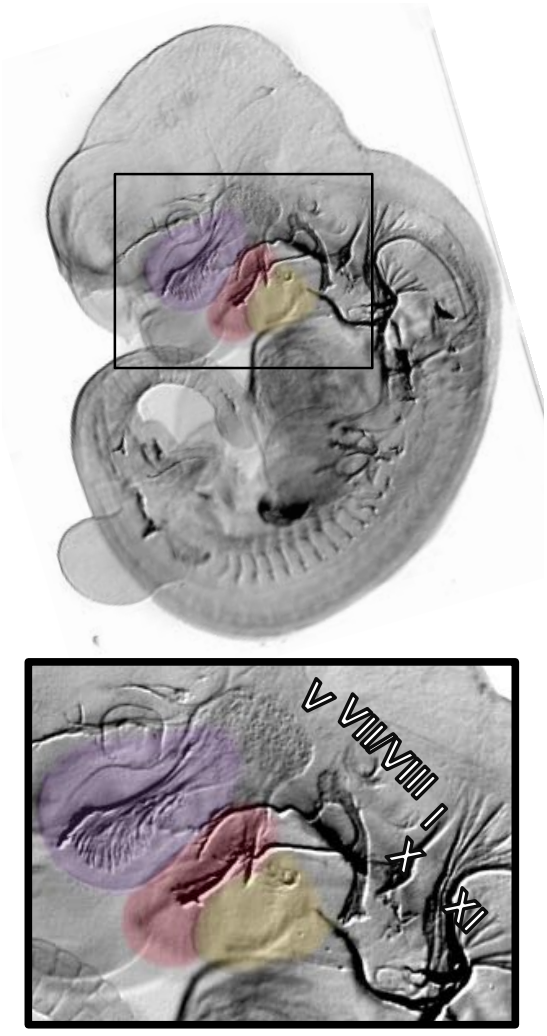

Figure A.13: Mouse cranial nerves, embryonic day 11.

Whole-mount immunohistochemistry, using anti-2H3 antibody to label neurofilament.

Purple and red, first branchial arch. *Yellow*, second branchial arch.

CN V (trigeminal), CN VII (facial), CN VIII (vestibulocochlear), CN IX glossopharyngeal, and CN XI (accessory).

B

GENOTYPING PROTOCOL

PCR genotyping protocol for *sbse* and *tm1Wjmv* alleles of *Plag1*.

Extraction of genomic DNA:

Digest embryonic membrane or ≈2 mm mouse tail tip tissue in 500 µl 50 mM NaOH at 95°C for 30 min.

Vortex, add 50 µl 1 M Tris-HCl (pH 7), vortex, spin briefly

Use immediately or freeze.

Amplification of target sequence:

0.5x reaction	Cycling conditions	
6.3 µl KAPA reagent*		3′ 95° C
4.5 µl H_2O	35x	15″ 95° C
0.5 µl forward primer (10 nM starting)		15″ Ta° C
0.5 µl forward primer (10 nM starting)		15″ 72° C
1.0 µl DNA digest		1′ 72° C

*KAPA HotStart Mouse Genotyping Kit, KAPA Biosystems KK7302

Primers

Allele	Sequence ID	Sequence 5′ to 3′	Product
sbse mutant	*Plag1* genoR	CACTGCCAATTCTCTGGGTAAATGGG	350 bp
	Plag1 geno1	CAGGACACACTCTTGTGCTTTACATACG	
sbse wildtype	*Plag1* geno2	CCACATTGTCCAGAGTGGTAGGAGGC	700 bp
	Plag1 geno3	GCCTTCATGACCTTTTGGCAATGCTC	
tm1Wjmv mutant	*Plag1*-MT-F	CAGTTCCCAGGTGTCCAACAAG	400 bp
	Plag1-MT-R	AATGTGAGCGAGTAACAACCCG	
tm1Wjmv wildtype	*Plag1*-WT-F	CGGAAAGACCATCTGAAGAATCAC	270 bp
	Plag1-WT-R	CGTTCGCAGTGCTCACATTG	

C

SBSE LOCUS SEQUENCE FEATURES

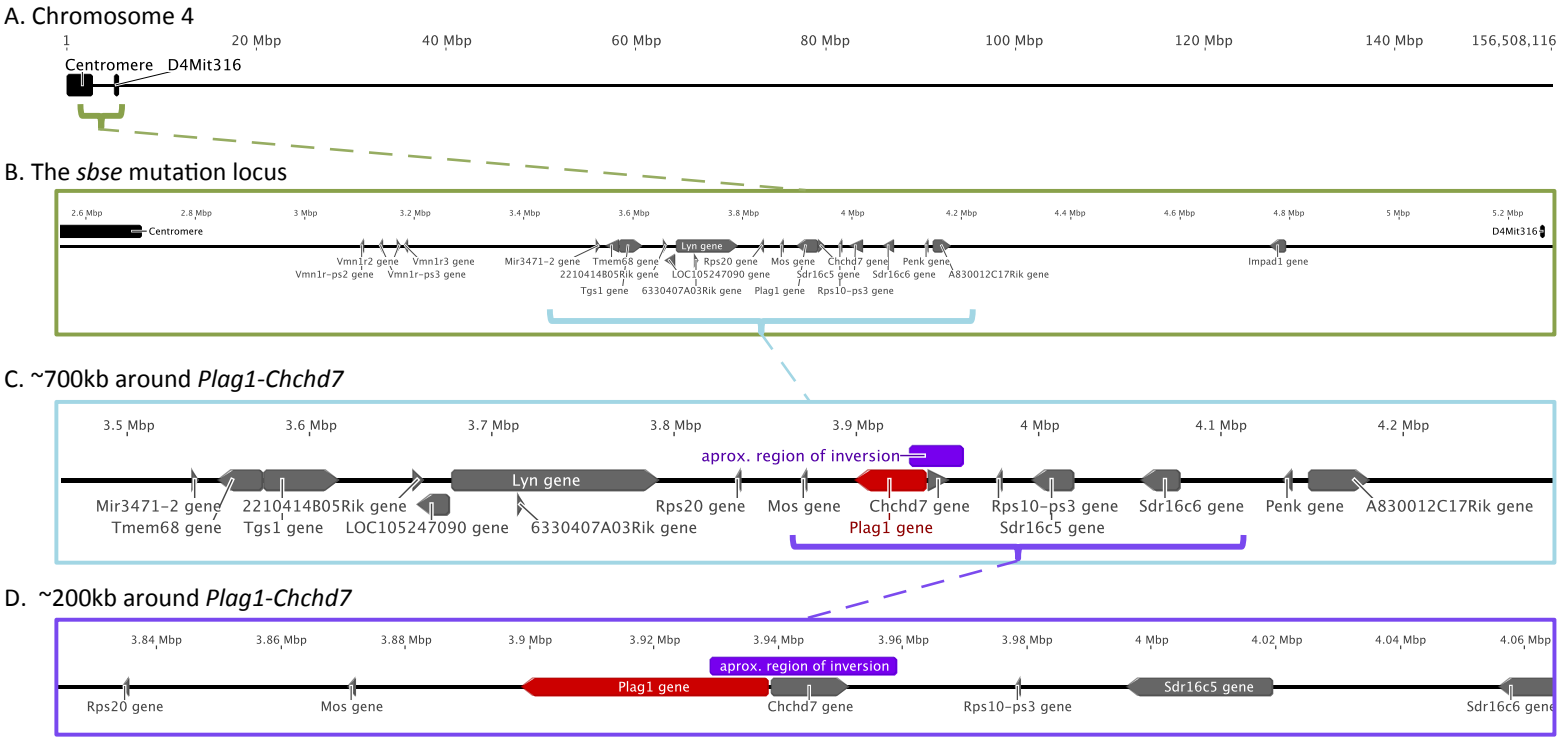

Figure C.1: Chromosomal context of the *sbse* mutation (a) Curtain, et al. (2001) mapped the mutation between the centromere of chromosome 4 and the microsatellite marker D4Mit316, near the gene *Plag1*. Bracket indicate region of detail in **(b)** ~2.6 Mbp centered on *Plag1* **(c)** ~700kb, annotated to show the *sbse* mutation, as well as *Sdr16c5* and *Sdr16c6*.

Table C.1: Functional regions in the PLAG1 protein.

Feature	Type	Relevance	Source
C_2H_2 zinc finger motif	protein-DNA binding	required for DNA-binding	168,271
lysine residues required for:			
- SUMO protein binding	regulatory	post-transcriptional modification regulates PLAG1 transactivation levels	196
-acetylation	regulatory	P300-mediated acetylation regulates transactivation capacity	274
Karyopherin α2 recognition site	Protein-DNA binding	Binding of transport protein Karyopherin α2 is required for nuclear localization of *Plag1*	275

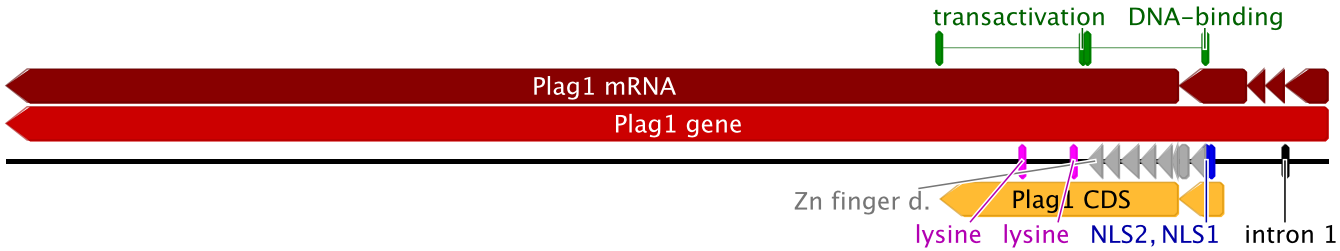

Figure C.2: Functional domains in the PLAG1 protein. Dark red, spliced exons of *Plag1*. **Gold**, Protein-coding sequence (CDS). **Pink**, lysines required for regulation by SUMO- and acetylation. **Gray**, seven zinc finger DNA-binding domains and **blue**, nuclear localization signals, both critical to *Plag1*'s transcription factor activity. **Black mark**, Cancer-associated rearrangements in human PLAG1, as well as the *sbse* rearrangement, occur at breakpoints within the first intron. **Green**, discrete transactivation and DNA-binding domains.

Table C.2: Predicted sequence features in the wildtype *Plag1-Chchd7* locus.

Feature	Type	Relevance	Source
Predicted bidirectional promoter	regulatory	May control expression of both *Plag1* and *Chchd7*	172 174
Conserved region within intron 1 of *Plag1*	regulatory	Highly conserved stretches of sequence may function as *cis*-regulatory elements	276 118
Evidence of P300, POL2 binding between *Plag1* and *Chchd7*, and within the first intron of *Plag1*	protein:DNA binding	P300 binding is associated with enhancer elements; POL2 binding is a signifier of active RNA transcription at that site	115 117
Histone modification at the 5′ ends of *Plag1* and *Chchd7*	Epigenetic modification	epigenetic modification of histones, particularly trimethylation of H3K4 and H3K36, are associated with active transcription at those sites	116

D

GENE ONTOGENY (GO) ANALYSIS RESULTS

Functional classification groups genes on the basis of annotation term co-occurrence, and may reflect participation in common biological networks.

Genes listed below reflect RNAseq results, restricted to transcripts expressed in the mutant at log2 fold change levels above 2 or below -2. Analysis was carried out using tools freely available from the Database for Annotation, Visualization and Integrated Discover (DAVID) v6.7, supported by the National Institute of Allergy and Infectious Disease (NIAID) at the National Institutes of Health (NIH).[221]

Figure D.1: Differential expression of retinoic acid pathway members.] Over-expression of the genes *Sdr16c5* and *Sdr16c6*. No change was observed in expression of other retinoic acid pathway enzymes, binding proteins, or receptors.

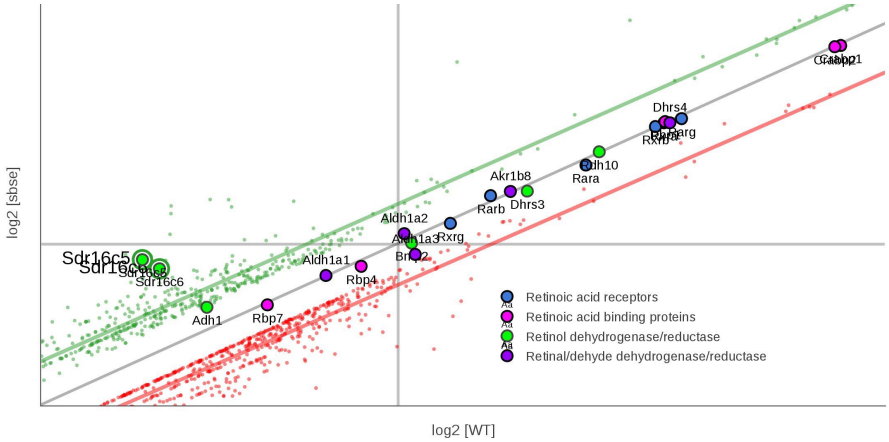

Blue, retinoic acid receptors. *Pink*, retinoic acid binding proteins. *Green*, Retinol dehydrogenases/reductases. *Purple*, Retinaldehyde dehydrogenases/reductases.

Figure D.2: Evidence suggeting misexpression of retinoic acid pathway genes in the *sbse* Differentially expressed genes, represented by points on the graph, are coded by $\log_2$ fold change values: *Red*, $L_2$2FC $\leqslant$ -1. *Gray*, -1 $<$ $L_2$2FC $>$ +1. *Green*, $L_2$2FC $\geqslant$ +1. Lines of best fit have been drawn through each $L_2$2FC group. *Green circle*, *Sdr16c5* and *Sdr16c6*, overexpressed in the *sbse* mutant.

Table D.1: Top 100 under- and over-expressed genes in the second branchial arch tissue of *sbse*, by DEseq. Genes listed in descending order, largest to smallest Log_2 fold change.

Under-expressed	Over-expressed
Xist, Gas7, Ubb, Ptchd1, Hist1h3e , Tuba1b, Eif2s3x, Plag1, Hist1h2bl , Mki67, Hist1h1e , Zfhx4, Lars2, Ubc, Kctd12, Hbb-y, Igf1r, Tnc, Hist1h2be , Rapgef4, Kdm6a, Hist1h2an , Prrc2c (Bat2d1), Ccnd2, Zdbf2, 2810417H13Rik, Hist1h1d , Oc90, Beta-s (Hbb-b1), Hbb-bh1, Scd2, Hist1h2bj , Zfp871, Dlx6as1 (Dlx6os1), Wbp5, Hsp90b1, Fbln2, Naa50, Zfml, Gas1, Farp1, Tnrc6b, Peg10, Ssb, Dek, Nup188, H1fo, Pbrm1, Hist1h4d , Ahnak, Srsf2 (Sfrs2), Ddx6, Eif5, Atad2, Top2b, Hmgb2, Huwe1, Pds5b, Cbx5, Ubxn7, Hmcn1, Fzd1, Tcf4, Smad4, Rsl1d1, Prrx1, Lrrc58, Zfp275, Tfrc, Pcdhgc3, Ubqln4, Zfp36l1, Hsp90aa1, Idi1, Cdc42, Hmgn2, Rpl19, Med13, Axl, Naa15, 3110099E03Rik, Azin1, Ptma, Usp9x, Cdk12, Ubr4, Lrrn1, Kdm5c, Ybx1, Nap1l1, Nucks1, Atad5, Mn1, Slc4a1, Zfr, Lnpep, Prpf40a, Gmps, Fnip1, Timp3	*Rmrp, Rpph1, Hist1h4a , Scarna10, Kdm5d, Snord15b, Ddx3y, Uty, Malat1, Hist1h4c , Hist1h4k , Sulf1, Scarna2, Snord22, Hist1h2ah , Eif2s3y, Hist4h4, H19, Rn45s, Hist1h3a , Hist2h2bb, Hist1h4j , Hist1h2ag , Rps15a, Hist1h4f , Hist3h2a, Hist1h2bm , Gas5, Rpl41, A2m, Rps5, Gnb2l1, Rplp2, Hist2h4, Rps15, Hist1h3c , Rplp1, Dusp9, Hist1h3f , Snrpg, Mir17hg, Hist1h3b , Tspan12, Hist1h3g , Id3, Bcam, Cgnl1, Col18a1, Mtch1, Rpl13a, Pfkl, Dact1, Gpc2, Fkbp9, Ctla2a, Aplp2, Dsp, Hist2h2ac, Lap3, Myh9, Rpl8, Gm1821, Snora78, Lama5, Cd2bp2, Unc5b, Hist1h3h , Nmral1, Bub3, Igfbp2, Gpr98, Tmem132a, Frem2, Hist1h3d , Limch1, Hk2, Nefl, Lin28a, Rps14, Wdr1, Id1, Fam129b, Dlk1, Snora61, Cnn2, Kcnq1ot1, Snhg8, Frem1, Erdr1, Myl6, Fndc3c1, Wdr6, 4930470H14Rik, Rpl37, Flna, Pmf1, Dohh, Mpnd, Rpl5, Akr1a1*

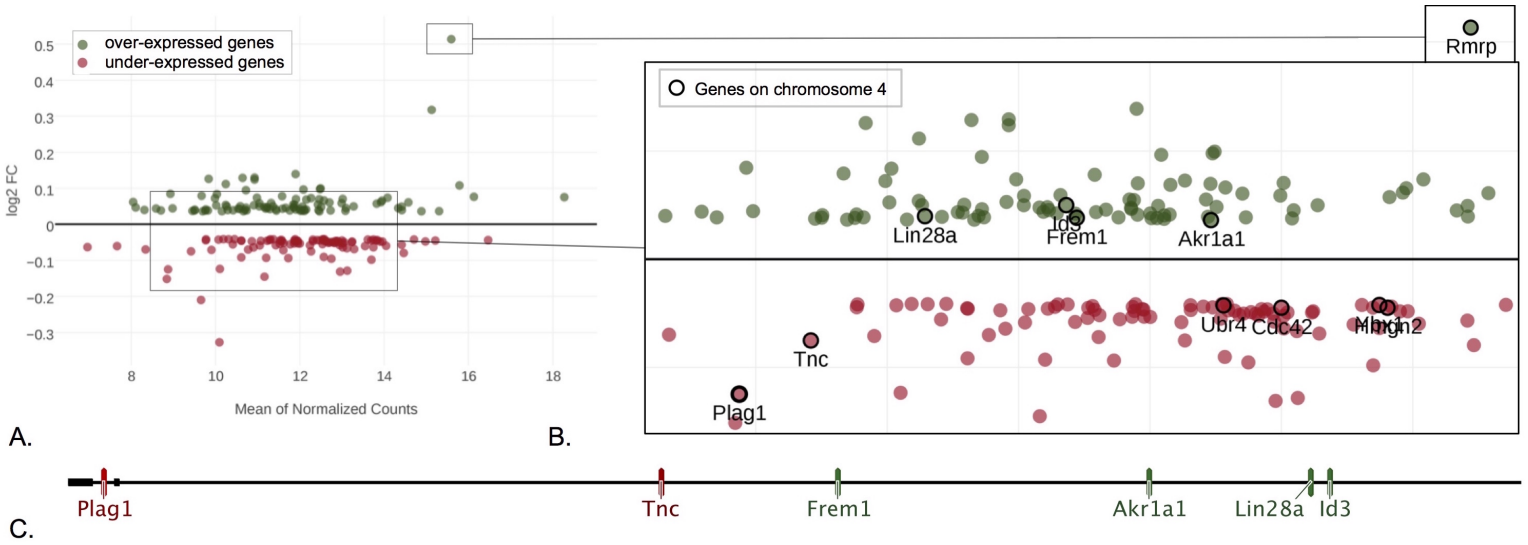

Figure D.3: Genes on Chr 4 and GO Analysis cluster: blood/vascular development. (A, B) Genes from the DEseq set, represented by points on the graph, are coded by expression pattern. Dark red, top 100 under-expressed transcripts. Dark green, top 100 over-expressed transcripts. **(C)** Differentially expressed genes from the DEseq set on chromosome 4.

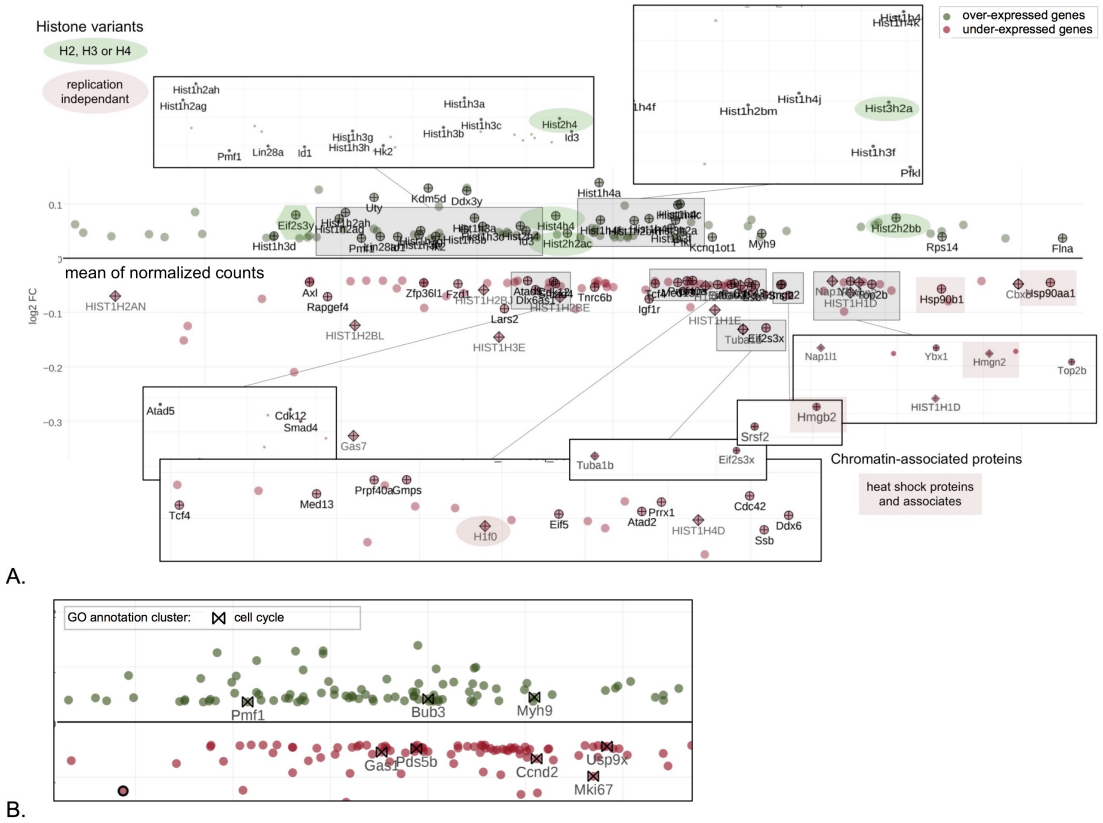

Figure D.4: GO Analysis cluster: Chromatin structure and cell cycle regulation (A) Differentially expressed genes involved in chromatin structure and gene regulation. **(B)** Genes from the DEseq set with GO terms associated with cell cycle regulation (hourglass).

Functional classification clustering, under-expressed genes in *sbse* PA2 at E10.5

Category	Term	Genes	Fold Enrichment
Annotation Cluster 1		**Enrichment Score: 6.99**	
GOTERM_BP_FAT	GO:0006334~nucleosome assembly	H1F0, HIST1H1E, HIST1H1D, HIST1H2BE, HIST1H2BL, HIST1H2BJ, NAP1L1, HIST1H4D, HIST1H3E, HIST1H2AN	21.21
GOTERM_BP_FAT	GO:0031497~chromatin assembly	H1F0, HIST1H1E, HIST1H1D, HIST1H2BE, HIST1H2BL, HIST1H2BJ, NAP1L1, HIST1H4D, HIST1H3E, HIST1H2AN	20.64
GOTERM_BP_FAT	GO:0034728~nucleosome organization	H1F0, HIST1H1E, HIST1H1D, HIST1H2BE, HIST1H2BL, HIST1H2BJ, NAP1L1, HIST1H4D, HIST1H3E, HIST1H2AN	20.37
GOTERM_BP_FAT	GO:0065004~protein-DNA complex assembly	H1F0, HIST1H1E, HIST1H1D, HIST1H2BE, HIST1H2BL, HIST1H2BJ, NAP1L1, HIST1H4D, HIST1H3E, HIST1H2AN	20.37
GOTERM_BP_FAT	GO:0006333~chromatin assembly or disassembly	H1F0, HIST1H1E, HIST1H1D, HIST1H2BE, HIST1H2BL, HIST1H2BJ, NAP1L1, HIST1H4D, HIST1H3E, HIST1H2AN, CBX5	15.78
GOTERM_CC_FAT	GO:0000786~nucleosome	H1F0, HIST1H1E, HIST1H1D, HIST1H2BE, HIST1H2BL, HIST1H2BJ, HIST1H4D, HIST1H3E, HIST1H2AN	24.08
GOTERM_BP_FAT	GO:0006323~DNA packaging	H1F0, HIST1H1E, HIST1H1D, HIST1H2BE, HIST1H2BL, HIST1H2BJ, NAP1L1, HIST1H4D, HIST1H3E, HIST1H2AN	15.33
GOTERM_CC_FAT	GO:0032993~protein-DNA complex	H1F0, HIST1H1E, HIST1H1D, HIST1H2BE, HIST1H2BL, HIST1H2BJ, HIST1H4D, HIST1H3E, HIST1H2AN	19.91
GOTERM_CC_FAT	GO:0000785~chromatin	H1F0, HIST1H1E, HMGN2, HIST1H1D, HIST1H2BE, HIST1H2BL, HIST1H2BJ, HIST1H4D, HIST1H3E, HIST1H2AN, CBX5	11.31
GOTERM_BP_FAT	GO:0034622~cellular macromolecular complex assembly	H1F0, HIST1H1E, HIST1H1D, HIST1H2BE, HIST1H2BL, HIST1H2BJ, NAP1L1, HIST1H4D, HIST1H3E, GAS7, TUBA1B, HIST1H2AN	8.72
GOTERM_BP_FAT	GO:0034621~cellular macromolecular complex subunit organization	H1F0, HIST1H1E, HIST1H1D, HIST1H2BE, HIST1H2BL, HIST1H2BJ, NAP1L1, HIST1H4D, HIST1H3E, GAS7, TUBA1B, HIST1H2AN	7.72
GOTERM_BP_FAT	GO:0065003~macromolecular complex assembly	H1F0, IGF1R, HIST1H1E, HIST1H1D, HIST1H2BE, HIST1H2BL, HIST1H2BJ, NAP1L1, HIST1H4D, HIST1H3E, GAS7, TUBA1B, HIST1H2AN	6.11
GOTERM_BP_FAT	GO:0043933~macromolecular complex subunit organization	H1F0, IGF1R, HIST1H1E, HIST1H1D, HIST1H2BE, HIST1H2BL, HIST1H2BJ, NAP1L1, HIST1H4D, HIST1H3E, GAS7, TUBA1B, HIST1H2AN	5.62
Annotation Cluster 2		**Enrichment Score: 2.20**	
GOTERM_CC_FAT	GO:0070013~intracellular organelle lumen	KDM6A, MKI67, SMAD4, MED13, LARS2, CBX5, SFRS2, RSL1D1, HSP90B1, ZFML, CDK12, TCF4, TOP2B, PRPF40A	2.31
GOTERM_CC_FAT	GO:0043233~organelle lumen	KDM6A, MKI67, SMAD4, MED13, LARS2, CBX5, SFRS2, RSL1D1, HSP90B1, ZFML, CDK12, TCF4, TOP2B, PRPF40A	2.30
GOTERM_CC_FAT	GO:0031981~nuclear lumen	RSL1D1, KDM6A, MKI67, ZFML, SMAD4, CDK12, MED13, TOP2B, TCF4, CBX5, SFRS2, PRPF40A	2.54
GOTERM_CC_FAT	GO:0031974~membrane-enclosed lumen	KDM6A, MKI67, SMAD4, MED13, LARS2, CBX5, SFRS2, RSL1D1, HSP90B1, ZFML, CDK12, TCF4, TOP2B, PRPF40A	2.23
Annotation Cluster 3		**Enrichment Score: 2.19**	
GOTERM_CC_FAT	GO:0005833~hemoglobin complex	HBB-BH1, HBB-B1, HBB-Y	69.99
GOTERM_MF_FAT	GO:0005344~oxygen transporter activity	HBB-BH1, HBB-B1, HBB-Y	47.06
GOTERM_BP_FAT	GO:0015671~oxygen transport	HBB-BH1, HBB-B1, HBB-Y	46.91
GOTERM_BP_FAT	GO:0015669~gas transport	HBB-BH1, HBB-B1, HBB-Y	39.69
GOTERM_MF_FAT	GO:0019825~oxygen binding	HBB-BH1, HBB-B1, HBB-Y	36.98
GOTERM_CC_FAT	GO:0044445~cytosolic part	HBB-BH1, RPL19, HBB-B1, HBB-Y	11.85
GOTERM_MF_FAT	GO:0020037~heme binding	HBB-BH1, HBB-B1, HBB-Y	3.60
GOTERM_MF_FAT	GO:0046906~tetrapyrrole binding	HBB-BH1, HBB-B1, HBB-Y	3.43
Annotation Cluster 4		**Enrichment Score: 1.11**	
GOTERM_BP_FAT	GO:0030850~prostate gland development	PLAG1, IGF1R, TNC	13.23
GOTERM_BP_FAT	GO:0048608~reproductive structure development	PLAG1, IGF1R, HMGB2, TNC	5.29
GOTERM_BP_FAT	GO:0001655~urogenital system development	PLAG1, IGF1R, TNC, SMAD4	4.71
GOTERM_BP_FAT	GO:0022612~gland morphogenesis	PLAG1, IGF1R, TNC	6.14
GOTERM_BP_FAT	GO:0003006~reproductive developmental process	PLAG1, IGF1R, HMGB2, TNC	2.61
GOTERM_BP_FAT	GO:0048732~gland development	PLAG1, IGF1R, TNC	2.62
Annotation Cluster 5		**Enrichment Score: 1.08**	
GOTERM_MF_FAT	GO:0000166~nucleotide binding	EIF2S3X, HSP90AA1, EIF5, AXL, ATAD2, ATAD5, SSB, LARS2, GMPS, SFRS2, DDX6, CDC42, IGF1R, HSP90B1, CDK12, RAPGEF4, TOP2B, TNRC6B, TUBA1B	1.50
GOTERM_MF_FAT	GO:0032555~purine ribonucleotide binding	EIF2S3X, HSP90AA1, EIF5, AXL, ATAD2, ATAD5, LARS2, GMPS, DDX6, CDC42, IGF1R, HSP90B1, CDK12, RAPGEF4, TOP2B, TUBA1B	1.54
GOTERM_MF_FAT	GO:0032553~ribonucleotide binding	EIF2S3X, HSP90AA1, EIF5, AXL, ATAD2, ATAD5, LARS2, GMPS, DDX6, CDC42, IGF1R, HSP90B1, CDK12, RAPGEF4, TOP2B, TUBA1B	1.54
GOTERM_MF_FAT	GO:0017076~purine nucleotide binding	EIF2S3X, HSP90AA1, EIF5, AXL, ATAD2, ATAD5, LARS2, GMPS, DDX6, CDC42, IGF1R, HSP90B1, CDK12, RAPGEF4, TOP2B, TUBA1B	1.48
Annotation Cluster 6		**Enrichment Score: 1.03**	
GOTERM_BP_FAT	GO:0060021~palate development	SMAD4, PRRX1, GAS1	14.74
GOTERM_BP_FAT	GO:0009967~positive regulation of signal transduction	IGF1R, SMAD4, PRRX1, GAS1	4.00
GOTERM_BP_FAT	GO:0010647~positive regulation of cell communication	IGF1R, SMAD4, PRRX1, GAS1	3.64
GOTERM_BP_FAT	GO:0048598~embryonic morphogenesis	SMAD4, PRRX1, GAS1	1.44
Annotation Cluster 7		**Enrichment Score: 0.94**	
GOTERM_CC_FAT	GO:0042470~melanosome	HSP90B1, HSP90AA1, TFRC, NAP1L1	8.78
GOTERM_CC_FAT	GO:0048770~pigment granule	HSP90B1, HSP90AA1, TFRC, NAP1L1	8.78
GOTERM_CC_FAT	GO:0031982~vesicle	LNPEP, HSP90B1, HSP90AA1, TFRC, NAP1L1	1.80

GOTERM_CC_FAT	GO:0016023~cytoplasmic membrane-bounded vesicle	HSP90B1, HSP90AA1, TFRC, NAP1L1	1.80
GOTERM_CC_FAT	GO:0031988~membrane-bounded vesicle	HSP90B1, HSP90AA1, TFRC, NAP1L1	1.78
GOTERM_CC_FAT	GO:0031410~cytoplasmic vesicle	HSP90B1, HSP90AA1, TFRC, NAP1L1	1.47
Annotation Cluster 8		**Enrichment Score: 0.86**	
GOTERM_MF_FAT	GO:0016702~oxidoreductase activity, acting on single donors with incorporation of molecular oxygen, incorporation of two atoms of oxygen	KDM6A, NUP188, KDM5C	7.61
GOTERM_MF_FAT	GO:0016701~oxidoreductase activity, acting on single donors with incorporation of molecular oxygen	KDM6A, NUP188, KDM5C	7.50
GOTERM_BP_FAT	GO:0055114~oxidation reduction	KDM6A, SCD2, NUP188, KDM5C	1.02
Annotation Cluster 9		**Enrichment Score: 0.74**	
GOTERM_BP_FAT	GO:0001655~urogenital system development	PLAG1, IGF1R, TNC, SMAD4	4.71
GOTERM_BP_FAT	GO:0060429~epithelium development	IGF1R, TNC, SMAD4, FZD1	2.54
GOTERM_BP_FAT	GO:0002009~morphogenesis of an epithelium	IGF1R, TNC, SMAD4	2.98
GOTERM_BP_FAT	GO:0048729~tissue morphogenesis	IGF1R, TNC, SMAD4	2.17
Annotation Cluster 10		**Enrichment Score: 0.65**	
GOTERM_BP_FAT	GO:0001932~regulation of protein amino acid phosphorylation	SMAD4, RAPGEF4, HBB-B1	4.26
GOTERM_BP_FAT	GO:0042325~regulation of phosphorylation	CDC42, SMAD4, RAPGEF4, HBB-B1	2.37
GOTERM_BP_FAT	GO:0031399~regulation of protein modification process	SMAD4, RAPGEF4, HBB-B1	3.13
GOTERM_BP_FAT	GO:0019220~regulation of phosphate metabolic process	CDC42, SMAD4, RAPGEF4, HBB-B1	2.29
GOTERM_BP_FAT	GO:0051174~regulation of phosphorus metabolic process	CDC42, SMAD4, RAPGEF4, HBB-B1	2.29
Annotation Cluster 11		**Enrichment Score: 0.62**	
GOTERM_CC_FAT	GO:0005578~proteinaceous extracellular matrix	HMCN1, FBLN2, TNC, TIMP3, OC90	3.14
GOTERM_CC_FAT	GO:0031012~extracellular matrix	HMCN1, FBLN2, TNC, TIMP3, OC90	3.02
GOTERM_CC_FAT	GO:0044421~extracellular region part	HMCN1, FBLN2, TNC, TIMP3, OC90	1.21
GOTERM_CC_FAT	GO:0005576~extracellular region	HMCN1, FBLN2, TNC, TIMP3, OC90	0.56
Annotation Cluster 12		**Enrichment Score: 0.58**	
GOTERM_MF_FAT	GO:0032559~adenyl ribonucleotide binding	IGF1R, HSP90B1, HSP90AA1, CDK12, AXL, ATAD2, ATAD5, RAPGEF4, LARS2, TOP2B, GMPS, DDX6	1.42
GOTERM_MF_FAT	GO:0030554~adenyl nucleotide binding	IGF1R, HSP90B1, HSP90AA1, CDK12, AXL, ATAD2, ATAD5, RAPGEF4, LARS2, TOP2B, GMPS, DDX6	1.35
GOTERM_MF_FAT	GO:0001883~purine nucleoside binding	IGF1R, HSP90B1, HSP90AA1, CDK12, AXL, ATAD2, ATAD5, RAPGEF4, LARS2, TOP2B, GMPS, DDX6	1.34
GOTERM_MF_FAT	GO:0001882~nucleoside binding	IGF1R, HSP90B1, HSP90AA1, CDK12, AXL, ATAD2, ATAD5, RAPGEF4, LARS2, TOP2B, GMPS, DDX6	1.33
GOTERM_MF_FAT	GO:0005524~ATP binding	IGF1R, HSP90B1, HSP90AA1, CDK12, AXL, ATAD2, ATAD5, LARS2, TOP2B, GMPS, DDX6	1.32
Annotation Cluster 13		**Enrichment Score: 0.56**	
GOTERM_BP_FAT	GO:0009057~macromolecule catabolic process	ZFP36L1, LNPEP, HSP90B1, HUWE1, USP9X, UBC, UBR4, UBB	1.84
GOTERM_BP_FAT	GO:0030163~protein catabolic process	LNPEP, HSP90B1, HUWE1, USP9X, UBC, UBR4, UBB	1.86
GOTERM_BP_FAT	GO:0006508~proteolysis	LNPEP, PEG10, HSP90B1, HUWE1, USP9X, UBC, UBR4, UBB	1.16
Annotation Cluster 14		**Enrichment Score: 0.55**	
GOTERM_MF_FAT	GO:0003924~GTPase activity	CDC42, EIF2S3X, TUBA1B	4.04
GOTERM_MF_FAT	GO:0005525~GTP binding	CDC42, EIF2S3X, EIF5, TUBA1B	1.95
GOTERM_MF_FAT	GO:0019001~guanyl nucleotide binding	CDC42, EIF2S3X, EIF5, TUBA1B	1.90
GOTERM_MF_FAT	GO:0032561~guanyl ribonucleotide binding	CDC42, EIF2S3X, EIF5, TUBA1B	1.90
Annotation Cluster 15		**Enrichment Score: 0.53**	
GOTERM_BP_FAT	GO:0022402~cell cycle process	PDS5B, MKI67, CCND2, USP9X, GAS1	2.19
GOTERM_BP_FAT	GO:0022403~cell cycle phase	PDS5B, MKI67, CCND2, USP9X	2.10
GOTERM_BP_FAT	GO:0007049~cell cycle	PDS5B, MKI67, CCND2, USP9X, GAS1	1.41
Annotation Cluster 16		**Enrichment Score: 0.51**	
GOTERM_BP_FAT	GO:0030182~neuron differentiation	CDC42, SMAD4, GAS1, TOP2B, GAS7	2.16
GOTERM_BP_FAT	GO:0000902~cell morphogenesis	CDC42, GAS1, TOP2B, GAS7	2.23
GOTERM_BP_FAT	GO:0048812~neuron projection morphogenesis	GAS1, TOP2B, GAS7	2.93
GOTERM_BP_FAT	GO:0030030~cell projection organization	CDC42, GAS1, TOP2B, GAS7	2.16
GOTERM_BP_FAT	GO:0048858~cell projection morphogenesis	GAS1, TOP2B, GAS7	2.55
GOTERM_BP_FAT	GO:0032989~cellular component morphogenesis	CDC42, GAS1, TOP2B, GAS7	1.96
GOTERM_BP_FAT	GO:0032990~cell part morphogenesis	GAS1, TOP2B, GAS7	2.43
GOTERM_BP_FAT	GO:0031175~neuron projection development	GAS1, TOP2B, GAS7	2.37
GOTERM_BP_FAT	GO:0048666~neuron development	GAS1, TOP2B, GAS7	1.77
Annotation Cluster 17		**Enrichment Score: 0.51**	
GOTERM_BP_FAT	GO:0030163~protein catabolic process	LNPEP, HSP90B1, HUWE1, USP9X, UBC, UBR4, UBB	1.86
GOTERM_BP_FAT	GO:0044265~cellular macromolecule catabolic process	ZFP36L1, HSP90B1, HUWE1, USP9X, UBC, UBR4, UBB	1.69
GOTERM_BP_FAT	GO:0043632~modification-dependent macromolecule catabolic process	HSP90B1, HUWE1, USP9X, UBC, UBR4, UBB	1.69

GOTERM_BP_FAT	GO:0019941~modification-dependent protein catabolic process	HSP90B1, HUWE1, USP9X, UBC, UBR4, UBB	1.69
GOTERM_BP_FAT	GO:0051603~proteolysis involved in cellular protein catabolic process	HSP90B1, HUWE1, USP9X, UBC, UBR4, UBB	1.61
GOTERM_BP_FAT	GO:0044257~cellular protein catabolic process	HSP90B1, HUWE1, USP9X, UBC, UBR4, UBB	1.60
Annotation Cluster 18		**Enrichment Score: 0.48**	
GOTERM_BP_FAT	GO:0016071~mRNA metabolic process	ZFP36L1, YBX1, SFRS2, PRPF40A	2.28
GOTERM_BP_FAT	GO:0008380~RNA splicing	YBX1, SFRS2, PRPF40A	2.57
GOTERM_BP_FAT	GO:0006397~mRNA processing	YBX1, SFRS2, PRPF40A	1.97
Annotation Cluster 19		**Enrichment Score: 0.42**	
GOTERM_BP_FAT	GO:0048514~blood vessel morphogenesis	ZFP36L1, PRRX1, NAA15	2.61
GOTERM_BP_FAT	GO:0001568~blood vessel development	ZFP36L1, PRRX1, NAA15	2.11
GOTERM_BP_FAT	GO:0001944~vasculature development	ZFP36L1, PRRX1, NAA15	2.06
Annotation Cluster 20		**Enrichment Score: 0.41**	
GOTERM_BP_FAT	GO:0010629~negative regulation of gene expression	FZD1, PRRX1, TNRC6B, TCF4, CBX5	2.10
GOTERM_BP_FAT	GO:0010605~negative regulation of macromolecule metabolic process	FZD1, PRRX1, TNRC6B, TCF4, CBX5	1.70
GOTERM_MF_FAT	GO:0016564~transcription repressor activity	PRRX1, TCF4, CBX5	2.45
GOTERM_BP_FAT	GO:0016481~negative regulation of transcription	FZD1, PRRX1, TCF4, CBX5	1.85
GOTERM_BP_FAT	GO:0045934~negative regulation of nucleobase, nucleoside, nucleotide and nucleic acid	FZD1, PRRX1, TCF4, CBX5	1.73
GOTERM_BP_FAT	GO:0051172~negative regulation of nitrogen compound metabolic process	FZD1, PRRX1, TCF4, CBX5	1.72
GOTERM_BP_FAT	GO:0010558~negative regulation of macromolecule biosynthetic process	FZD1, PRRX1, TCF4, CBX5	1.65
GOTERM_BP_FAT	GO:0031327~negative regulation of cellular biosynthetic process	FZD1, PRRX1, TCF4, CBX5	1.60
GOTERM_BP_FAT	GO:0009890~negative regulation of biosynthetic process	FZD1, PRRX1, TCF4, CBX5	1.59
GOTERM_BP_FAT	GO:0045892~negative regulation of transcription, DNA-dependent	PRRX1, TCF4, CBX5	1.68
GOTERM_BP_FAT	GO:0051253~negative regulation of RNA metabolic process	PRRX1, TCF4, CBX5	1.66
Annotation Cluster 21		**Enrichment Score: 0.33**	
GOTERM_BP_FAT	GO:0045944~positive regulation of transcription from RNA polymerase II promoter	HMGB2, DLX6OS1, SMAD4, MED13	1.92
GOTERM_BP_FAT	GO:0051173~positive regulation of nitrogen compound metabolic process	HMGB2, DLX6OS1, HSP90AA1, SMAD4, MED13	1.63
GOTERM_BP_FAT	GO:0031328~positive regulation of cellular biosynthetic process	HMGB2, DLX6OS1, HSP90AA1, SMAD4, MED13	1.56
GOTERM_BP_FAT	GO:0009891~positive regulation of biosynthetic process	HMGB2, DLX6OS1, HSP90AA1, SMAD4, MED13	1.54
GOTERM_BP_FAT	GO:0045893~positive regulation of transcription, DNA-dependent	HMGB2, DLX6OS1, SMAD4, MED13	1.65
GOTERM_BP_FAT	GO:0051254~positive regulation of RNA metabolic process	HMGB2, DLX6OS1, SMAD4, MED13	1.64
GOTERM_BP_FAT	GO:0045941~positive regulation of transcription	HMGB2, DLX6OS1, SMAD4, MED13	1.45
GOTERM_BP_FAT	GO:0010628~positive regulation of gene expression	HMGB2, DLX6OS1, SMAD4, MED13	1.41
GOTERM_BP_FAT	GO:0045935~positive regulation of nucleobase, nucleoside, nucleotide and nucleic acid metabolic process	HMGB2, DLX6OS1, SMAD4, MED13	1.35
GOTERM_BP_FAT	GO:0010557~positive regulation of macromolecule biosynthetic process	HMGB2, DLX6OS1, SMAD4, MED13	1.30
GOTERM_BP_FAT	GO:0010604~positive regulation of macromolecule metabolic process	HMGB2, DLX6OS1, SMAD4, MED13	1.09
Annotation Cluster 22		**Enrichment Score: 0.31**	
GOTERM_MF_FAT	GO:0046914~transition metal ion binding	PLAG1, KDM6A, HBB-BH1, SCD2, UBR4, NUP188, ZFR, ZFP871, HBB-Y, LNPEP, ZFP36L1, PEG10, ZFHX4, ZFML, UBC, HBB-B1, UBB, ZFP275, KDM5C	1.19
GOTERM_MF_FAT	GO:0046872~metal ion binding	PLAG1, KDM6A, HBB-BH1, SCD2, UBR4, NUP188, PCDHGC3, ZFR, ZFP871, HBB-Y, OC90, LNPEP, ZFP36L1, PEG10, HSP90B1, ZFHX4, FBLN2, ZFML, UBC, HBB-B1, UBB, IDI1, ZFP275, KDM5C	1.03
GOTERM_MF_FAT	GO:0043169~cation binding	PLAG1, KDM6A, HBB-BH1, SCD2, UBR4, NUP188, PCDHGC3, ZFR, ZFP871, HBB-Y, OC90, LNPEP, ZFP36L1, PEG10, HSP90B1, ZFHX4, FBLN2, ZFML, UBC, HBB-B1, UBB, IDI1, ZFP275, KDM5C	1.02
GOTERM_MF_FAT	GO:0043167~ion binding	PLAG1, KDM6A, HBB-BH1, SCD2, UBR4, NUP188, PCDHGC3, ZFR, ZFP871, HBB-Y, OC90, LNPEP, ZFP36L1, PEG10, HSP90B1, ZFHX4, FBLN2, ZFML, UBC, HBB-B1, UBB, IDI1, ZFP275, KDM5C	1.01
Annotation Cluster 23		**Enrichment Score: 0.19**	
GOTERM_BP_FAT	GO:0050801~ion homeostasis	LNPEP, SCD2, TFRC	1.76
GOTERM_BP_FAT	GO:0048878~chemical homeostasis	LNPEP, SCD2, TFRC	1.41
GOTERM_BP_FAT	GO:0042592~homeostatic process	LNPEP, SCD2, TFRC	0.88
Annotation Cluster 24		**Enrichment Score: 0.038**	
GOTERM_MF_FAT	GO:0004672~protein kinase activity	IGF1R, CDK12, AXL	0.89
GOTERM_BP_FAT	GO:0006468~protein amino acid phosphorylation	IGF1R, CDK12, AXL	0.81
GOTERM_BP_FAT	GO:0016310~phosphorylation	IGF1R, CDK12, AXL	0.72
GOTERM_BP_FAT	GO:0006793~phosphorus metabolic process	IGF1R, CDK12, AXL	0.60
GOTERM_BP_FAT	GO:0006796~phosphate metabolic process	IGF1R, CDK12, AXL	0.60

Functional classification clustering, over-expressed genes in *sbse* PA2 at E10.5

Category	Term	Genes	Fold Enrichment
Annotation Cluster 1		**Enrichment Score: 7.68**	
GOTERM_MF_FAT	GO:0003735~structural constituent of ribosome	RPL41, RPL13A, RPS14, RPLP1, RPL8, RPS15, RPLP2, RPS15A, RPL5, RPL37, RPS5	16.69
GOTERM_CC_FAT	GO:0005840~ribosome	RPL41, RPL13A, RPS14, RPLP1, RPL8, RPS15, RPLP2, RPS15A, RPL5, RPL37, RPS5	13.52
GOTERM_MF_FAT	GO:0005198~structural molecule activity	MYL6, COL18A1, RPS15A, RPLP2, RPL37, RPS5, RPL41, RPL13A, RPS14, RPS15, RPL8, RPLP1, RPL5, NEFL	7.13
GOTERM_BP_FAT	GO:0006412~translation	EIF2S3Y, RPL41, RPL13A, RPS14, RPLP1, RPL8, RPS15, RPLP2, RPS15A, RPL5, RPL37, RPS5	8.66
GOTERM_CC_FAT	GO:0030529~ribonucleoprotein complex	RPL41, RPL13A, RPS14, RPLP1, RPL8, RPS15, RPLP2, RPS15A, RPL5, RPL37, LIN28A, RPS5, SNRPG	6.64
Annotation Cluster 2		**Enrichment Score: 6.25**	
GOTERM_CC_FAT	GO:0000786~nucleosome	HIST4H4, HIST1H4K, HIST1H2AG, HIST2H4, HIST1H2BM, HIST2H2BB, HIST1H4A, HIST2H2AC, HIST1H3A, HIST1H3B, HIST1H2AH, HIST1H4F, HIST1H3C, HIST1H4C, HIST1H3D, HIST3H2A, HIST1H3F, HIST1H4J, HIST1H3G, HIST1H3H	30.44
GOTERM_CC_FAT	GO:0032993~protein-DNA complex	HIST4H4, HIST1H4K, HIST1H2AG, HIST2H4, HIST1H2BM, HIST2H2BB, HIST1H4A, HIST2H2AC, HIST1H3A, HIST1H3B, HIST1H2AH, HIST1H4F, HIST1H3C, HIST1H4C, HIST1H3D, HIST3H2A, HIST1H3F, HIST1H4J, HIST1H3G, HIST1H3H	25.17
GOTERM_BP_FAT	GO:0006334~nucleosome assembly	HIST4H4, HIST1H4K, HIST1H2AG, HIST2H4, HIST1H2BM, HIST2H2BB, HIST1H4A, HIST2H2AC, HIST1H3A, HIST1H3B, HIST1H2AH, HIST1H4F, HIST1H3C, HIST1H4C, HIST1H3D, HIST3H2A, HIST1H3F, HIST1H4J, HIST1H3G, HIST1H3H	25.24
GOTERM_BP_FAT	GO:0031497~chromatin assembly	HIST4H4, HIST1H4K, HIST1H2AG, HIST2H4, HIST1H2BM, HIST2H2BB, HIST1H4A, HIST2H2AC, HIST1H3A, HIST1H3B, HIST1H2AH, HIST1H4F, HIST1H3C, HIST1H4C, HIST1H3D, HIST3H2A, HIST1H3F, HIST1H4J, HIST1H3G, HIST1H3H	24.57
GOTERM_BP_FAT	GO:0034728~nucleosome organization	HIST4H4, HIST1H4K, HIST1H2AG, HIST2H4, HIST1H2BM, HIST2H2BB, HIST1H4A, HIST2H2AC, HIST1H3A, HIST1H3B, HIST1H2AH, HIST1H4F, HIST1H3C, HIST1H4C, HIST1H3D, HIST3H2A, HIST1H3F, HIST1H4J, HIST1H3G, HIST1H3H	24.24
GOTERM_BP_FAT	GO:0065004~protein-DNA complex assembly	HIST4H4, HIST1H4K, HIST1H2AG, HIST2H4, HIST1H2BM, HIST2H2BB, HIST1H4A, HIST2H2AC, HIST1H3A, HIST1H3B, HIST1H2AH, HIST1H4F, HIST1H3C, HIST1H4C, HIST1H3D, HIST3H2A, HIST1H3F, HIST1H4J, HIST1H3G, HIST1H3H	24.24
GOTERM_BP_FAT	GO:0006323~DNA packaging	HIST4H4, HIST1H4K, HIST1H2AG, HIST2H4, HIST1H2BM, HIST2H2BB, HIST1H4A, HIST2H2AC, HIST1H3A, HIST1H3B, HIST1H2AH, HIST1H4F, HIST1H3C, HIST1H4C, HIST1H3D, HIST3H2A, HIST1H3F, HIST1H4J, HIST1H3G, HIST1H3H	18.24
GOTERM_BP_FAT	GO:0034622~cellular macromolecular complex assembly	HIST4H4, HIST1H4K, HIST1H2AG, FLNA, HIST2H4, HIST1H2BM, HIST2H2BB, HIST1H4A, HIST2H2AC, RPS14, HIST1H3A, HIST1H3B, HIST1H2AH, HIST1H4F, HIST1H3C, HIST1H4C, HIST1H3D, HIST3H2A, HIST1H3F, HIST1H4J, HIST1H3G, HIST1H3H	10.61
GOTERM_BP_FAT	GO:0006333~chromatin assembly or disassembly	HIST4H4, HIST1H4K, HIST1H2AG, HIST2H4, HIST1H2BM, HIST2H2BB, HIST1H4A, HIST2H2AC, HIST1H3A, HIST1H3B, HIST1H2AH, HIST1H4F, HIST1H3C, HIST1H4C, HIST1H3D, HIST3H2A, HIST1H3F, HIST1H4J, HIST1H3G, HIST1H3H	16.90
GOTERM_BP_FAT	GO:0034621~cellular macromolecular complex subunit organization	HIST4H4, HIST1H4K, HIST1H2AG, FLNA, HIST2H4, HIST1H2BM, HIST2H2BB, HIST1H4A, HIST2H2AC, RPS14, HIST1H3A, HIST1H3B, HIST1H2AH, HIST1H4F, HIST1H3C, HIST1H4C, HIST1H3D, HIST3H2A, HIST1H3F, HIST1H4J, HIST1H3G, HIST1H3H	9.40
GOTERM_CC_FAT	GO:0000785~chromatin	HIST4H4, HIST1H4K, HIST1H2AG, HIST2H4, HIST1H2BM, HIST2H2BB, HIST1H4A, HIST2H2AC, HIST1H3A, HIST1H3B, HIST1H2AH, HIST1H4F, HIST1H3C, HIST1H4C, HIST1H3D, HIST3H2A, HIST1H3F, HIST1H4J, HIST1H3G, HIST1H3H	11.44
GOTERM_BP_FAT	GO:0006325~chromatin organization	HIST4H4, HIST1H4K, HIST1H2AG, UTY, HIST2H4, HIST1H2BM, HIST2H2BB, HIST1H4A, HIST2H2AC, HIST1H3A, HIST1H3B, HIST1H2AH, HIST1H4F, HIST1H3C, HIST1H4C, HIST1H3D, HIST3H2A, HIST1H3F, HIST1H4J, HIST1H3G, HIST1H3H, KDM5D	7.31
GOTERM_BP_FAT	GO:0065003~macromolecular complex assembly	HIST4H4, HIST1H4K, HIST1H2AG, FLNA, HIST2H4, HIST1H2BM, HIST2H2BB, HIST1H4A, HIST2H2AC, RPS14, HIST1H3A, HIST1H3B, HIST1H2AH, HIST1H4F, HIST1H3C, HIST1H4C, HIST1H3D, HIST3H2A, HIST1H3F, HIST1H4J, HIST1H3G, HIST1H3H	6.81
GOTERM_BP_FAT	GO:0043933~macromolecular complex subunit organization	HIST4H4, HIST1H4K, HIST1H2AG, FLNA, HIST2H4, HIST1H2BM, HIST2H2BB, HIST1H4A, HIST2H2AC, RPS14, HIST1H3A, HIST1H3B, HIST1H2AH, HIST1H4F, HIST1H3C, HIST1H4C, HIST1H3D, HIST3H2A, HIST1H3F, HIST1H4J, HIST1H3G, HIST1H3H	6.28
GOTERM_CC_FAT	GO:0044427~chromosomal part	HIST4H4, HIST1H4K, HIST1H2AG, PMF1, HIST2H4, HIST1H2BM, HIST2H2BB, HIST1H4A, HIST2H2AC, HIST1H3A, HIST1H3B, HIST1H2AH, HIST1H4F, HIST1H3C, HIST1H4C, HIST1H3D, HIST3H2A, HIST1H3F, HIST1H4J, HIST1H3G, HIST1H3H	6.68
GOTERM_CC_FAT	GO:0005694~chromosome	HIST4H4, HIST1H4K, HIST1H2AG, PMF1, HIST2H4, HIST1H2BM, HIST2H2BB, HIST1H4A, HIST2H2AC, HIST1H3A, HIST1H3B, HIST1H2AH, HIST1H4F, HIST1H3C, HIST1H4C, HIST1H3D, HIST3H2A, HIST1H3F, HIST1H4J, HIST1H3G, HIST1H3H	5.62
Annotation Cluster 3		**Enrichment Score: 1.88**	
GOTERM_CC_FAT	GO:0005604~basement membrane	COL18A1, LAMA5, FREM2, FREM1	12.93
GOTERM_CC_FAT	GO:0044420~extracellular matrix part	COL18A1, LAMA5, FREM2, FREM1	10.26
GOTERM_CC_FAT	GO:0005578~proteinaceous extracellular matrix	COL18A1, GPC2, LAMA5, FREM2, FREM1	3.97
GOTERM_CC_FAT	GO:0031012~extracellular matrix	COL18A1, GPC2, LAMA5, FREM2, FREM1	3.82
Annotation Cluster 4		**Enrichment Score: 1.26**	
GOTERM_BP_FAT	GO:0000902~cell morphogenesis	COL18A1, LAMA5, ID1, MYH9, NEFL	3.73
GOTERM_BP_FAT	GO:0000904~cell morphogenesis involved in differentiation	COL18A1, ID1, MYH9, NEFL	4.35
GOTERM_BP_FAT	GO:0032989~cellular component morphogenesis	COL18A1, LAMA5, ID1, MYH9, NEFL	3.28
Annotation Cluster 5		**Enrichment Score: 1.00**	
GOTERM_CC_FAT	GO:0016459~myosin complex	MYL6, CGNL1, MYH9	11.60
GOTERM_CC_FAT	GO:0015629~actin cytoskeleton	MYL6, CGNL1, WDR1, MYH9	4.60
GOTERM_MF_FAT	GO:0003774~motor activity	MYL6, CGNL1, MYH9	4.98
GOTERM_CC_FAT	GO:0044430~cytoskeletal part	MYL6, CGNL1, MYH9, NEFL	1.22
Annotation Cluster 6		**Enrichment Score: 0.46**	
GOTERM_BP_FAT	GO:0006915~apoptosis	UNC5B, ID1, MTCH1, SULF1	1.98
GOTERM_BP_FAT	GO:0012501~programmed cell death	UNC5B, ID1, MTCH1, SULF1	1.95
GOTERM_BP_FAT	GO:0008219~cell death	UNC5B, ID1, MTCH1, SULF1	1.82

GOTERM_BP_FAT	GO:0016265~death	UNC5B, ID1, MTCH1, SULF1	1.77
Annotation Cluster 7		**Enrichment Score: 0.45**	
GOTERM_BP_FAT	GO:0043065~positive regulation of apoptosis	COL18A1, MTCH1, ID3	2.79
GOTERM_BP_FAT	GO:0043068~positive regulation of programmed cell death	COL18A1, MTCH1, ID3	2.76
GOTERM_BP_FAT	GO:0010942~positive regulation of cell death	COL18A1, MTCH1, ID3	2.74
GOTERM_BP_FAT	GO:0042981~regulation of apoptosis	COL18A1, MTCH1, ID3, NEFL	1.67
GOTERM_BP_FAT	GO:0043067~regulation of programmed cell death	COL18A1, MTCH1, ID3, NEFL	1.65
GOTERM_BP_FAT	GO:0010941~regulation of cell death	COL18A1, MTCH1, ID3, NEFL	1.64
Annotation Cluster 8		**Enrichment Score: 0.32**	
GOTERM_BP_FAT	GO:0000279~M phase	PMF1, MYH9, BUB3	2.44
GOTERM_BP_FAT	GO:0022403~cell cycle phase	PMF1, MYH9, BUB3	2.11
GOTERM_BP_FAT	GO:0022402~cell cycle process	PMF1, MYH9, BUB3	1.76
GOTERM_BP_FAT	GO:0007049~cell cycle	PMF1, MYH9, BUB3	1.13
Annotation Cluster 9		**Enrichment Score: 0.26**	
GOTERM_BP_FAT	GO:0010629~negative regulation of gene expression	ID1, ID3, LIN28A, KCNQ1OT1	2.25
GOTERM_BP_FAT	GO:0010033~response to organic substance	PFKL, ID1, ID3, LIN28A	1.82
GOTERM_BP_FAT	GO:0006355~regulation of transcription, DNA-dependent	ID1, ID3, LIN28A	0.47
GOTERM_BP_FAT	GO:0051252~regulation of RNA metabolic process	ID1, ID3, LIN28A	0.46
Annotation Cluster 10		**Enrichment Score: 0.20**	
GOTERM_MF_FAT	GO:0046872~metal ion binding	MYL6, COL18A1, FKBP9, PFKL, UTY, RPL37, DLK1, LIN28A, GPR98, LAP3, FREM2, DOHH, FREM1, LIMCH1, SULF1,	1.01
GOTERM_MF_FAT	GO:0043169~cation binding	MYL6, COL18A1, FKBP9, PFKL, UTY, RPL37, DLK1, LIN28A, GPR98, LAP3, FREM2, DOHH, FREM1, LIMCH1, SULF1,	1.00
GOTERM_MF_FAT	GO:0043167~ion binding	MYL6, COL18A1, FKBP9, PFKL, UTY, RPL37, DLK1, LIN28A, GPR98, LAP3, FREM2, DOHH, FREM1, LIMCH1, SULF1,	0.99
Annotation Cluster 11		**Enrichment Score: 0.018**	
GOTERM_CC_FAT	GO:0070013~intracellular organelle lumen	FKBP9, RPL5, LIN28A	0.62
GOTERM_CC_FAT	GO:0043233~organelle lumen	FKBP9, RPL5, LIN28A	0.62
GOTERM_CC_FAT	GO:0031974~membrane-enclosed lumen	FKBP9, RPL5, LIN28A	0.60
Annotation Cluster 12		**Enrichment Score: 0.015**	
GOTERM_MF_FAT	GO:0005524~ATP binding	PFKL, DDX3Y, HK2, MYH9	0.64
GOTERM_MF_FAT	GO:0032559~adenyl ribonucleotide binding	PFKL, DDX3Y, HK2, MYH9	0.63
GOTERM_MF_FAT	GO:0032555~purine ribonucleotide binding	EIF2S3Y, PFKL, DDX3Y, HK2, MYH9	0.64
GOTERM_MF_FAT	GO:0032553~ribonucleotide binding	EIF2S3Y, PFKL, DDX3Y, HK2, MYH9	0.64
GOTERM_MF_FAT	GO:0030554~adenyl nucleotide binding	PFKL, DDX3Y, HK2, MYH9	0.60
GOTERM_MF_FAT	GO:0017076~purine nucleotide binding	EIF2S3Y, PFKL, DDX3Y, HK2, MYH9	0.61
GOTERM_MF_FAT	GO:0001883~purine nucleoside binding	PFKL, DDX3Y, HK2, MYH9	0.59
GOTERM_MF_FAT	GO:0001882~nucleoside binding	PFKL, DDX3Y, HK2, MYH9	0.59
GOTERM_MF_FAT	GO:0000166~nucleotide binding	EIF2S3Y, PFKL, DDX3Y, HK2, MYH9	0.52

E

USEFUL SEQUENCES

Annotated, Fasta-formatted sequences.

745 bp deleted in the *sbse* mutation, annotated with putative CTCF binding sites (CTCFBSDB 2.0[277])

```
>sbse deletion | 745bp
GCTCTCAGGCACAGGATTCAGACTGCAAGAGCCAGGGTCTTGCTTCTACTGCCCATGTCTTCATCTCAGCATTTA
GAATCCGGAACACATAGGAGGAATGTGATCGAGTGTTTGCTGAGTGAATAGAAAAGAGGGAGAGGAA GGAAGGGC
AAGAGGGCCCTTTCTACTCTGTTGGCCCAACGGATAAGGAAGACAGTTGTCTCTACAAACGACTGAGGATGGACA
GATTGGAAAATTCTCTGCATGTTCCATGCATATTTAACATTTAAGGAGATAAGACCTTTTTCTTGAGTTGGCCAA
TTCTCAATGGATACCAGAAAGCTGTAGTCATTG TGCCACCTTGTGGT CATGACTAGAAAGTTCCTCTTCCTTAAT
GGAATAGATATTCTCCTCCCCCTCACCTGCACAAAGGTATTAGTAGAAGCTTAGAGACAAACAAATGTCAATCAT
CCCATGTAAAGTCAAACTTTTAGAGTCTGTACTTTTAGGAAAGACCTAAAACAATATACAAATGACATGAAACAA
TTTTATATCAAACGATCTCCATGAGGCGGCTGTATTTGGGTGGGGGAGTGGTTGAAGCAAGCCTAACTGCTCTGG
AGTTGTCAGAACTGGTTATGATACAAGAATTAATTCTACTCATCTGTCAACTTTTTTCTATCTTGTATTGGCCCA
CAATAAAGAGTTCAAACGATCTGTAAAGGCAGCATTACCTTAGTGTTGTACAGTGAACCTGTTGTCCATA
```

BIBLIOGRAPHY

[1] Kato M, Mugitani R (2015) Pareidolia in infants. *PLoS One* 10(2):1–9. PMID: 25689630. 3

[2] Berry DS, Zebrowitz-McArthur L (1986) The impact of age-related changes on social perception. *Psychol Bull* 100(1):63–88. 3

[3] Huisinga-Fischer CE, Souren JPHJA, Werken FVD, Prahl-Andersen B, van Ginkel F (2004) Perception of symmetry in the face. *J Craniofac Surg* 15(1):128–34. PMID: 14704579. 3

[4] Berry LA, Witt PD, Marsh JL, Pilgram TK, Eder RA (1997) Personality attributions based on speech samples of children with repaired cleft palates. *Cleft Palate-Craniofacial J* 34(5):385–389. PMID: 9345604. 3

[5] Maris CL, Endriga MC, Omnell ML, Speltz ML (1999) Psychosocial adjustment in twin pairs with and without Hemifacial Microsomia. *Cleft Palate-Craniofacial J* 36(1):43–50. PMID: 10067761. 3

[6] Christensen K, Juel K, Herskind AM, Murray JC (2004) Long term follow up study of survival associated with cleft lip and palate at birth. *BMJ* 328(7453):1405. PMID: 15145797. 3

[7] Weiss J et al. (2009) Hospital use and associated costs of children aged zero-to-two years with craniofacial malformations in Massachusetts. *Birth Defects Res Part A - Clin Mol Teratol* 85(11):925–934. PMID: 19830851.

[8] Wehby G, Cassell CH (2010) The impact of orofacial clefts on quality of life and healthcare use and costs. *Oral Dis* 16(1):3–10. PMID: 19656316.

[9] Botto LD et al. (2013) Cancer Risk in Children and Adolescents with Birth Defects: A Population-Based Cohort Study. *PLoS One* 8(7). PMID: 23874873. 3

[10] March of Dimes Foundation (2015) Birth Defects | March of Dimes. 4, 73

[11] Jones KL, Smith DW, Ulleland CN, Streissguth AP (1973) Pattern of malformations in offspring of alcoholic mothers. *Lancet* 301(7815/7815):1267–1271. PMID: 4126070. 4

[12] Hackshaw A, Rodeck C, Boniface S (2011) Maternal smoking in pregnancy and birth defects: A systematic review based on 173 687 malformed cases and 11.7 million controls. *Hum Reprod Update* 17(5):589–604. PMID: 21747128.

[13] Lammer EJ et al. (1985) Retinoic acid embryopathy. *N Engl J Med* 313(14):837–841. PMID: 3162101. 122, 145

[14] Newman LM, Hendrickx AG (1985) Temporomandibular malformation in the bonnet monkey (Macaca radiata) fetus following maternal injestion of thalidomide. *J Craniofac Genet Dev Biol* 5(2):147. PMID: 4019728.

[15] Sulik KK, Johnston MC (1983) Sequence of developmental alterations following acute ethanol exposure in mice: craniofacial features of the fetal alcohol syndrome. *Am J Anat* 166(3):257–69. PMID: 6846205.

[16] Ejaz S, Ejaz A, Sohail A, Lim CW (2010) Vascular and morphogenetic abnormalities associated with exposure of cigarette smoke condensate during chicken and murine embryogenesis. *Biomed Environ Sci* 23(4):305–311. PMID: 20934119.

[17] Gilbert SF (2000) Environmental Disruption of Normal Development in *Dev Biol*. (Sinauer Associates, Sunderland, MA), 6th edition. 4

[18] Smith SM, Garic A, Flentke GR, Berres ME (2014) Neural crest development in fetal alcohol syndrome. *Birth Defects Res Part C - Embryo Today Rev* 102(3):210–220. PMID: 25219761. 4

[19] Smith-Thomas L, Lott I, Bronner-Fraser M (1987) Effects of isotretinoin on the behavior of neural crest cells in vitro. *Dev Biol* 123(1):276–281. PMID: 3476321.

[20] Sanbe A et al. (2009) Inhibitory effects of cigarette smoke extract on neural crest migration occur through suppression of R-spondin1 expression via aryl hydrocarbon receptor. *Naunyn Schmiedebergs Arch Pharmacol* 380(6):569–576. PMID: 19768455. 4

[21] Nei M, Glazko GV (2003) Estimation of divergence times for major lineages of primate species. *Mol Biol Evol* 20(3):424–434. PMID: 12644563. 4

[22] Narlikar L, Ovcharenko I (2009) Identifying regulatory elements in eukaryotic genomes. *Briefings Funct Genomics Proteomics* 8(4):215–230. PMID: 19498043.

[23] Gans C, Northcutt RG (1983) Neural crest and the origin of vertebrates: a new head. *Science (80-)* 220(4594):268–274. PMID: 17732898. 7, 122

[24] Gans C (1993) Evolutionary Origin of the Vertebrate Skull in *Skull, Vol 2*, eds. Hanken J, Hall BK. (University of Chicago Press). 4, 152

[25] Thorogood P (1997) The Head and Face in *Embryos, Genes and Birth Defects*. (John Wiley & Sons). 4

[26] Sulik KK, Johnston MC, Daft PA, Russell WE, Dehart DB (1986) Fetal alcohol syndrome and DiGeorge anomaly: critical ethanol exposure periods for craniofacial malformations as illustrated in an animal model. *Am J Med Genet* 2:97–112. PMID: 3146306. 4

[27] Juriloff DM, Harris MJ, McMahon AP, Carroll TJ, Lidral AC (2006) Wnt9b is the mutated gene involved in multifactorial nonsyndromic cleft lip with or without cleft palate in A/WySn mice, as confirmed by a genetic complementation test. *Birth Defects Res Part A - Clin Mol Teratol* 76(8):574–579. PMID: 16998816. 5, 73

[28] Lan Y et al. (2006) Expression of Wnt9b and activation of canonical Wnt signaling during midfacial morphogenesis in mice. *Dev Dyn* 235(5):1448–1454. PMID: 16496313. 5, 73

[29] Jolly RJ, Moore WJ (1975) Skull growth in achondroplasic (cn) mice; a craniometric study. *J Embryol Exp Morphol* 33(4):1013–1022. PMID: 1176871. 5, 71

[30] Hoffman WY, McCarthy JG (1994) The effects of facial nerve ablation on craniofacial skeletal development in neonatal rabbits. *Plast Reconstr Surg* 93(6):1236–1240. PMID: 8171143. 5

[31] Wiszniak S et al. (2015) Neural crest cell-derived VEGF promotes embryonic jaw extension. *PNAS* 112(19). PMID: 25922531. 5, 8, 9, 96, 145

[32] Poswillo D (1973) The pathogenesis of the First and Second Branchial Arch syndrome. *Oral Surgery, Oral Med Oral Pathol* 35(3):302–328. PMID: 4631568. 5, 9, 96, 141, 145

[33] Converse J, Coccaro P, Becker M, Wood-Smith D (1973) On Hemifacial Microsomia - the First and Second Branchial Arch syndrome. *Plast Reconstr Surg* 51(3):268–279. PMID: 4689671. 5

[34] Hartsfield J (2007) Review of the etiological heterogeneity of the Oculo-Auriculo-Vertebral spectrum (Hemifacial Microsomia). *Orthod Craniofacial Res* 10(3):121–128. PMID: 17651128. 95, 135

[35] Heike CL, Hing AV (2009) Craniofacial Microsomia Overview in *GeneReviews [Internet]*, eds. Pagon R, Bird T, Dolan C. (University of Washington, Seattle, WA). 20301754. 5, 6, 123

[36] Beleza-Meireles A, Clayton-Smith J, Saraiva JM, Tassabehji M (2014) Oculo-auriculo-vertebral spectrum: a review of the literature and genetic update. *J Med Genet* 51(10):635–45. PMID: 25118188. 5

[37] Grabb W (1965) The First and Second Branchial Arch Syndromes. *Plast Reconstr Surg* 36(5):485–508. PMID: 5320180. 6

[38] Poswillo D (1988) The aetiology and pathogenesis of craniofacial deformity. *Development* 103 Suppl:207–212. PMID: 3074909.

[39] Gorlin RJ, Cohen MM, Levin LS (1990) *Syndromes of the Head and Neck*. (Oxford University Press, Oxford, UK). 6

[40] Birgfeld CB, Heike CL (2012) Craniofacial microsomia. *Semin Plast Surg* 26(2):91–103. PMID: 23633936. 6

[41] Heike CL et al. (2013) Clinical care in Craniofacial Microsomia: a review of current management recommendations and opportunities to advance research. *Am J Med Genet (Part C)* 163C(4):271–82. PMID: 24132932. 6, 135

[42] Ballesta-Martínez MJ et al. (2013) Autosomal dominant Oculoauriculovertebral spectrum and 14q23.1 microduplication. *Am J Med Genet Part A* 161(June):2030–2035. PMID: 23794319. 6

[43] Descartes M (2006) Oculoauriculovertebral spectrum with 5p15.33-pter deletion. *Clin Dysmorphol* 15(3):153–154. PMID: 16760734.

[44] Digilio MC et al. (2009) Three patients with Oculo-auriculo-vertebral spectrum and microdeletion 22q11.2. *Am J Med Genet Part A* 149(12):2860–2864. PMID: 19890921.

[45] Kobrynski L et al. (1993) Trisomy 22 and facioauriculovertebral (Goldenhar) sequence. *Am J Med Genet* 46(1):68–71. PMID: 8494034.

[46] Rollnick BR, Kaye CI (1983) Hemifacial microsomia and variants: pedigree data. *Am J Med Genet* 15(2):233–253. PMID: 6881197.

[47] Kaye CI et al. (1992) Oculoauriculovertebral anomaly: segregation analysis. *Am J Med Genet Part A* 43(6):913–917. PMID: 1415339.

[48] Kelberman D et al. (2001) Hemifacial microsomia: progress in understanding the genetic basis of a complex malformation syndrome. *Hum Genet* 109(6):638–645. PMID: 11810276. 6

[49] Optiz J (1985) The developmental field concept. *Am J Med Genet* 21(1):1–11. 6

[50] Smith RJH (2015) Branchiootorenal Spectrum Disorders in *GeneReviews® [Internet]*, eds. Pagon RA et al. (University of Washington, Seattle, Seattle, WA). 20301618. 6

[51] Kohlhase J (2016) Townes-Brocks Syndrome in *GeneReviews [Internet]*, eds. Pagon RA et al. (University of Washington, Seattle, Seattle, WA). 20301618.

[52] Lalani SR, Hefner MA, Belmont JW, Davenport SLH (2012) CHARGE Syndrome in *GeneReviews [Internet]*, eds. Pagon RA et al. (University of Washington, Seattle, Seattle, WA). 20301296.

[53] Katsanis SH, Jabs EW (2012) Treacher Collins Syndrome in *GeneReviews [Internet]*, eds. Pagon RA et al. (University of Washington, Seattle, Seattle, WA). 20301704. 6

[54] Xue L et al. (2013) Global expression profiling reveals genetic programs underlying the developmental divergence between mouse and human embryogenesis. *BMC Genomics* 14(1):568. PMID: 23961710. 7

[55] Pavlov MI, Sautier JM, Oboeuf M, Asselin A, Berdal A (2003) Chondrogenic differentiation during midfacial development in the mouse: in vivo and in vitro studies. *Biol Cell* 95(2):75–86. PMID: 12799063. 7

[56] McBratney-Owen B, Iseki S, Bamforth SD, Olsen BR, Morriss-Kay GM (2008) Development and tissue origins of the mammalian cranial base. *Dev Biol* 322(1):121–32. PMID: 18680740. 7, 12, 152

[57] Delatte M, Von den Hoff J, Van Rheden REM, Kuijpers-Jagtman AM, Delatte M (2004) Primary and secondary cartilages of the neonatal rat: the femoral head and the mandibular condyle. *Eur J Oral Sci* 112:156–162. PMID: 15056113. 7

[58] Ahrens PB, Solursh M, Reiter RS (1977) Stage-related capacity for limb chondrogenesis in cell culture. *Dev Biol* 60(1):69–82. PMID: 198274. 8

[59] Ahrens PB, Solursh M, Reiter RS, Singley CT (1979) Position-related capacity for differentiation of limb mesenchyme in cell culture. *Dev Biol* 69(2):436–450. PMID: 437350. 8

[60] Percival CJ, Richtsmeier JT (2013) Angiogenesis and intramembranous osteogenesis. *Dev Dyn* 242(8):909–922. PMID: 23737393. 8, 145

[61] Rice DP (2008) Craniofacial sutures: development, disease and treatment. *Front Oral Biol* 12:xi. PMID: 18491429. 8

[62] Hiruma T, Nakajima Y (2002) Development of pharyngeal arch arteries in early mouse embryo. *J Anat* 201(1):15–29. PMID: 12171473. 8

[63] Bockman DE, Redmond ME, Kirby ML (1990) Altered development of pharyngeal arch vessels after neural crest ablation. *Ann N Y Acad Sci* 588:296–304. PMID: 2192648. 8

[64] Poswillo D (1975) Hemorrhage in development of the face. *Birth Defects* 11(7):61–81. PMID: 813794. 9, 96

[65] Miquerol L, Langille BL, Nagy A (2000) Embryonic development is disrupted by modest increases in vascular endothelial growth factor gene expression. *Development* 3946:3941–3946. PMID: 10952892. 9

[66] Werler MM, Sheehan JE, Hayes C, Mitchell AA, Mulliken JB (2004) Vasoactive exposures, vascular events, and Hemifacial Microsomia. *Birth Defects Res (Part A)* 70(6):389–395. PMID: 15211707. 9, 95

[67] Werler MM et al. (2004) Demographic and reproductive factors associated with Hemifacial Microsomia. *Cleft Palate-Craniofacial J* 41(5):494–450. PMID: 15352870. 9

[68] Castilla EE, Lopez-Camelo JS, Campan H (1999) Altitude as a risk factor for congenital anomalies. *Am J Med Genet* 86:9–14. PMID: 10440822. 9

[69] Cousley RR, Wilson DJ (1990) The effects of surgical section of the embryonic chick mandibular arch. *Anat Embryol (Berl)* 182(4):401–408. PMID: 2252223. 9

[70] Cousley R, Wilson D (1992) Hemifacial Microsomia: developmental consequences of perturbation of the auriculofacial cartilage model? *Am J Med Genet* 42(4):461–466. PMID: 609829. 9

[71] Heude E, Rivals I, Levi G (2011) Masticatory muscle defects in Hemifacial Microsomia: A new embryological concept. *Am J Med Genet A* 155:1991–1995. PMID: 21744489. 9

[72] Richtsmeier JT, Corner BD, Grausz HM, Cheverud JM, Danahey SE (1993) The role of postnatal growth pattern in the production of facial morphology. *Syst Biol* 42(3):307–330. 10, 37

[73] Thilander B (1995) Basic mechanisms in craniofacial growth. *Acta Odontol Scand* 53(43):144–151. PMID: 7572089. 10, 11, 95

[74] Dibbets JMH (1990) Introduction to the Temporomandibular Joint in *Facial Growth*, ed. Enlow DH. (WB Saunders & Co; Harcourt Brace Jovanovich, Inc), pp. 149–163. 10, 142

[75] Moss ML (1997) The functional matrix hypothesis revisited. 4. The epigenetic antithesis and the resolving synthesis. *Am J Orthod Dentofac Orthop* 112(4):410–417. PMID: 9345153. 10

[76] Lenton KA, Nacamuli RP, Wan DC, Helms JA, Longaker MT (2005) Cranial suture biology. *Curr Top Dev Biol* 66:287–328. PMID: 15797457. 11

[77] Mednick LW, Washburn SL (1956) The role of the sutures in the growth of the braincase of the infant pig. *Am J Phys Anthropol* 14(2):175–191. PMID: 13362486.

[78] Pritchard JJ, Scott JH, Girgis FG (1956) The structure and development of cranial and facial sutures. *J Anat* 90(Pt 1):73–86.3. PMID: 13295153.

[79] Koski K (1968) Cranial growth centers: facts of fallacies? *Am J Orthod* 54(8):566–583. PMID: 4874446. 11

[80] Babler WJ et al. (1982) Skull growth after coronal suturectomy, periostectomy, and dural transection. *J Neurosurg* 56(4):529–535. PMID: 7062124. 11

[81] Opperman LA, Sweeney TM, Redmon J, Persing JA, Ogle RC (1993) Tissue interactions with underlying dura mater inhibit osseous obliteration of developing cranial sutures. *Dev Dyn* 198(4):312–322. PMID: 8130378. 11

[82] Persson KM, Roy WA, Persing JA, Rodeheaver GT, Winn HR (1979) Craniofacial growth following experimental craniosynostosis and craniectomy in rabbits. *J Neurosurg* 50:187–197. PMID: 430131. 11

[83] Rosenberg P et al. (1997) The role of the cranial base in facial growth. *Plast Reconstr Surg* 99(5):1396–1407. PMID: 9105368. 11, 12, 71

[84] Bütow KW (1990) Craniofacial growth disturbance after skull base and associated suture synostoses in the newborn Chacma baboon: a preliminary report. *Cleft Palate J* 27(3):241–251. PMID: 2372972. 11

[85] DuBrul EL, Laskin DM (1961) Preadaptive potentialities of the mammalian skull: An experiment in growth and form. *Am J Anat* 109(2):117–132. PMID: 13888118. 12

[86] Lieberman D (1998) Sphenoid shortening and the evolution of modern human cranial shape. *Nature* 393(May 14):158–162. PMID: 1000252403. 12, 71

[87] McBratney BM, Margaryan E, Ma W, Urban Z, Lozanoff S (2003) Frontonasal Dysplasia in 3H1 Br / Br Mice. *Anat Rec Part A* 302:291–302. PMID: 12629672. 12, 144

[88] de Beer GR (1931) On the nature of the trabecula cranii. *Q J R Microsc Soc* 74:701–731. 12

[89] Al Dayeh AA, Rafferty KL, Egbert M, Herring SW (2013) Real-time monitoring of the growth of the nasal septal cartilage and the nasofrontal suture. *Am J Orthod Dentofac Orthop* 143(6):773–783. PMID: 23726327. 12

[90] Aizenbud D, Morrill LR, Schendel SA (2010) Midfacial trauma and facial growth: A longitudinal case study of monozygotic twins. *Am J Orthod Dentofac Orthop* 138(5):641–648. PMID: 21055606. 12

[91] Sarnat B, Wexler M (1968) Postnatal growth of nose and face after resection of septal cartilage in rabbit. *Oral Surgery, Oral Med Oral Pathol* 26(5):712–727. PMID: 5245694. 12

[92] Moss ML, Bromberg BE, Song IC, Eisenman G (1968) The passive role of nasal septal cartilage in mid-facial growth. *Plast Reconstr Surg* 41(6):536–542. PMID: 5654895. 12

[93] Copray JC (1986) Growth of the nasal septal cartilage of the rat in vitro. *J Anat* 144:99–111. PMID: 3693052. 12

[94] Wealthall RJ, Herring SW (2006) Endochondral ossification of the mouse nasal septum. *Anat Rec Part A* 1172:1163–1172. PMID: 17031811. 12

[95] Cousley R, Naora H, Yokoyama M, Kimura M, Otani H (2002) Validity of the Hfm transgenic mouse as a model for Hemifacial Microsomia. *Cleft Palate-Craniofacial J* 39(1):81–92. PMID: 11772174. 13

[96] Otani H et al. (1991) Microtia as an autosomal dominant mutation in a transgenic mouse line: a possible animal model of branchial arch anomalies. *Anat Anz* 172(1):1–9. PMID: 2031565. 13

[97] Nagata M et al. (1997) Isolated maxillary bending in CL/Fr strain mice: observation of cranofacial deformity and inheritance pattern. *Cleft Palate-Craniofacial J* 34(2):101–105. PMID: 9138502. 13, 14

[98] McLeod M, Harris M, Hernoff G, Miller J (1980) First arch malformation: a new craniofacial mutant in the mouse. *J Hered* 71(5):331–335. PMID: 7440954. 13

[99] Juriloff DM, Harris MJ, Froster-Iskenius U (1987) Hemifacial deficiency induced by a shift in dominance of the mouse mutation \textit{far}. *J Craniofac Genet Dev Biol* 7(1):27–44. PMID: 3597720. 13

[100] Theiler K, Sweet HO (1986) Low set ears (Lse), a new mutation of the house mouse. *Anat Embryol (Berl)* 175:241–246. PMID: 3103484. 14, 136

[101] Leary S et al. (2013) *AVMA Guidelines for the Euthanasia of Animals: 2013 Edition*. (American Veterinary Medicine Association, Schaumburg, IL), 2013 edition. 15

[102] Curtain MM, Donahue LR (2001) Small body and short ear pinna, a spontaneous mutation on chromosome 4 in the mouse. 19, 67, 69, 74, 75, 82, 96, 97

[103] Marden C, Curtain MM, Hurd J, Donahue LR (2012) Froggy; a new mutation on Chromosome 13 affecting skull shape and body size. 19, 74, 75, 80, 82

[104] Hensen K et al. (2004) Targeted disruption of the murine Plag1 proto-oncogene causes growth retardation and reduced fertility. *Dev Growth Differ* 46(5):459–470. PMID: 15606491. 16, 19, 69, 97, 116

[105] National Center for Biotechnology Information (2012) Mus musculus strain C57BL/6J chromosome 4, GRCm38.p3 C57BL/6J. 17, 132

[106] Kent W et al. (2002) The human genome browser at UCSC. *Genome Res* 12(6):996–1006. 17, 27, 100

[107] Kent WJ (2002) BLAT- The BLAST-Like Alignment Tool. *Genome Res* 12:656–664. 17, 100

[108] Palmer K et al. (2015) Discovery and characterization of spontaneous mouse models of craniofacial dysmorphology. *Dev Biol* 415:216–227. PMID: 26234751. 18, 75, 97

[109] Trapnell C et al. (2010) Transcript assembly and quantification by RNA-Seq reveals unannotated transcripts and isoform switching during cell differentiation. *Nat Biotechnol* 28(5):511–515. 23

[110] Love M, Huber W, Anders S (2014) Moderated estimation of fold change and dispersion for RNA-seq data with DESeq2. *Genome Biol* 15(12):550. PMID: 25516281. 23, 124

[111] Medicine MNIoG (2016) Online Mendelian Inheritance in Man, OMIM. 23

[112] The Jackson Laboratory (2016) Mouse Genome Database (MGD) at the Mouse Genome Informatics website. 23

[113] Huang DW, Sherman BT, Lempicki RA (2008) Systematic and integrative analysis of large gene lists using DAVID bioinformatics resources. *Nat Protoc* 4(1):44–57. 23

[114] Voz ML, Agten NS, Van de Ven WJ (2000) PLAG1 , the Main Translocation Target in Pleomorphic Adenoma of the Salivary Glands , Is a Positive Regulator of IGF-II 1. *Cancer Res* 60:106–113. 27

[115] UCSC Genome Browser (2012) Transcription Factor Binding Sites by ChIP-seq from ENCODE/Stanford/Yale. 27, 100, 101, 103, 167

[116] UCSC Genome Browser (2012) Histone Modifications by ChIP-seq from ENCODE/PSU. 167

[117] UCSC Genome Browser (2012) Transcription Factor Binding Sites by ChIP-seq from ENCODE/LICR. 100, 135, 167

[118] Blanchette M et al. (2004) Aligning multiple genomic sequences with the threaded blockset aligner. *Genome Res* 14(4):708–715. PMID: 15060014. 27, 100, 167

[119] Limaye A (2015) *Drishti Volume Exploration and Presentation Tool*. (National Computational Infrastructure's VizLab, Canberra, Australia), 8 edition. 30

[120] Rolfe S, Camci E, Mercan E, Shapiro L, Cox T (2013) A new tool for quantifying and characterizing asymmetry in bilaterally paired structures. in *Conf Proc Annu Int Conf*. (IEEE Engineering in Medicine and Biology Society), Vol. 2013, pp. 2364–7. 24110200. 30

[121] Webster M, Sheets HD (2010) A practical introduction to landmark-based geometric morphometrics in *Quant Methods Paleobiol*, eds. Alroy J, Hunt G. (Paleontological socIety short course, October 20th 2010), pp. 163–188. 30, 52

[122] Klingenberg CP (2011) MORPHOJ : an integrated software package for geometric morphometrics. *Mol Ecol Resour* 11:353–357. 30, 51

[123] Sheets H (2004) Simple 3D {1.0}. 30

[124] R Core Team (2013) *R: A Language and Environment for Statistical Computing* (R Foundation for Statistical Computing, Vienna, Austria). 31, 116

[125] Dryden I, Mardia K (1998) Tangent Space Inference in *Stat Shape Anal*. (Wiley, Chilchester). 31, 116

[126] Ovchinnikov D (2009) Alcian blue/alizarin red staining of cartilage and bone in mouse. *Cold Spring Harb Protoc* 2009(3):pdb.prot5170. PMID: 20147105. 31

[127] Bancroft JD, Gamble M (2007) *Theory and Practice of Histological Techniques*. (Elsevier Health Sciences), 6th edition. 31

[128] Vickerman L, Neufeld S, Cobb J (2011) Shox2 function couples neural, muscular and skeletal development in the proximal forelimb. *Dev Biol* 350(2):323–336. PMID: 21156168. 32

[129] Dodd J, Morton SB, Karagogeos D, Yamamoto M, Jessell TM (1988) Spatial regulation of axonal glycoprotein expression on subsets of embryonic spinal neurons. *Neuron* 1(2):105–116. PMID: 3272160. 32

[130] Nagy A, Gertsenstein M, Vintersten K, Behringer R (2007) Staining whole mouse embryos for beta-galactosidase (lacZ) activity. *CSH Protoc* 2007(s). PMID: 21357067. 32

[131] Sadler TW (2004) *Langmans Medical Embryology*. (Lippincott Williams & Wilkins,, Philadelphia), 9th edition. 37

[132] Perrine SM et al. (2014) Craniofacial divergence by distinct prenatal growth patterns in Fgfr2 mutant mice. *BMC Dev Biol* 14:8. PMID: 24580805. 37, 143

[133] Pirttiniemi P, Peltomäki T, Müller L, Luder H (2009) Abnormal mandibular growth and the condylar cartilage. *Eur J Orthod* 31:1–11. PMID: 19164410. 37

[134] Terry MJ, Ascherman JA (2006) A case of unilateral coronal synostosis in a child with Craniofacial Microsomia. *Cleft Palate-Craniofacial J* 46(6):752–756. PMID: 17105329. 37

[135] Cousley R, Calvert M (1997) Current concepts in the understanding and management of Hemifacial Microsomia. *Br J Plast Surg* 50:536–551. PMID: 9422952. 37, 123

[136] Katzen J, McCarthy J (2000) Syndromes involving craniosynostosis and midface hypoplasia. *Otolaryngol Clin North Am* 33(6):1257–1284. PMID: 11449786. 37, 143

[137] Vora SR, Camci ED, Cox TC (2016) Postnatal ontogeny of the cranial base and craniofacial skeleton in male C57BL / 6J mice: A reference standard for quantitative analysis. *Front Physiol* 6(417):1–14. PMID: 26793119. 38

[138] Lambert R (2009) Breeding Strategies for Maintaining Colonies of Laboratory Mice: A Jackson Laboratory Resource Manual.

[139] Somerville JM, Aspden RM, Armour KE, Armour KJ, Reid DM (2004) Growth of C57Bl/6 mice and the material and mechanical properties of cortical bone from the Ttbia. *Calcif Tissue Int* 74(5):469–475. PMID: 14961209. 50

[140] Robson CD (2006) Congenital hearing impairment. *Pediatr Radiol* 36(4):309–324. PMID: 16465539. 56, 135

[141] Juma AR, Damdimopoulou PE, Grommen SVH, Van de Ven WJM, De Groef B (2015) Emerging role of PLAG1 as a regulator of growth and reproduction. *J Endocrinol* 228(2):R45–R56. PMID: 26577933. 69, 70, 96, 99

[142] Nielsen MK, Kittok RJ, Kochera Kirby YL (1995) Uterine mass and uterine blood volume in mice selected 21 generations for alternative criteria to increase litter size. *J Anim Sci* 73(8):2243–2248. PMID: 8567459.

[143] Queimado L et al. (1999) Pleomorphic adenoma gene 1 is expressed in cultured benign and malignant salivary gland tumor cells. *Lab Investig* 79(5):583–589. PMID: 10334569.

[144] Vonnahme KA, Ford SP (2004) Differential expression of the Vascular endothelial growth factor-receptor system in the gravid uterus of Yorkshire and Meishan pigs. *Biol Reprod* 71(1):163–169. PMID: 14998908.

[145] Cowley DE, Pomp D, Atchley W, Eisen EJ, Hawkins-Brown D (1989) The impact of maternal uterine genotype on postnatal growth and adult body size in mice. *Genetics* 122:193–203. PMID: 2731729. 70

[146] Wang Y et al. (2005) Abnormalities in cartilage and bone development in the Apert syndrome FGFR2+/S252W mouse. *Development* 132:3537–3548. PMID: 15975938. 71, 143

[147] Yin L et al. (2008) A Pro253Arg mutation in fibroblast growth factor receptor 2 (Fgfr2) causes skeleton malformation mimicking human Apert syndrome by affecting both chondrogenesis and osteogenesis. *Bone* 42:631–643. PMID: 18242159. 71, 143

[148] Sahar DE, Longaker MT, Quarto N (2005) Sox9 neural crest determinant gene controls patterning and closure of the posterior frontal cranial suture. *Dev Biol* 280(2):344–361. PMID: 15882577. 71

[149] Slater BJ, Kwan MD, Gupta DM, Lee JK, Longaker MT (2009) The role of regional posterior frontal dura mater in the overlying suture morphology. *Plast Reconstr Surg* 123(2):463–469. PMID: 19182602.

[150] Sperber GH, Sperber SM, Guttman GD (2010) *Craniofacial Embryogenetics and Development*. (People's Medical Publishing House, Shelton, CT), 2nd edition. 71, 136, 152

[151] Nie X (2005) Cranial base in craniofacial development: developmental features, influence on facial growth, anomaly, and molecular basis. *Acta Odontol Scand* 63(5009):127–135. PMID: 16191905. 71

[152] Parsons TE, Downey CM, Jirik FR, Hallgrimsson B (2015) Mind the gap: genetic manipulation of basicranial growth within synchondroses modulates calvarial and facial shape in mice through epigenetic interactions. *PLoS Genet* 10(2):1–22. PMID: 25692674. 71

[153] Hallgrímsson B et al. (2006) The brachymorph mouse and the developmental-genetic basis for canalization and morphological integration. *Evol Dev* 8(1):61–73. PMID: 16409383. 71, 144

[154] Orkin RW, Willians BR, Cranley RE, Poppke DC, Brown KS (1977) Defects in the cartilaginous growth plates of brachymorphic mice. *J Cell Biol* 73(2):287–299. PMID: 67117. 71

[155] Lozanoff S (1993) Midface retrusion in adult brachyrrhine mice. *Acta Anat (Basel)* 147:125–132. PMID: 8379293. 71, 144

[156] Ma W, Lozanoff S (1996) Morphological deficiency in the prenatal anterior cranial base of midfacially retrognathic mice. *J Anat* 188:547–555. PMID: 8763472.

[157] Ma W, Lozanoff S (1999) Spatial and temporal distribution of cellular proliferation in the cranial base of normal and midfacially retrusive mice. *Clin Anat* 12(5):315–325. PMID: 10462729. 71, 144

[158] Lieberman DE, Hallgrímsson B, Liu W, Parsons TE, Jamniczky Ha (2008) Spatial packing, cranial base angulation, and craniofacial shape variation in the mammalian skull: testing a new model using mice. *J Anat* 212(6):720–35. PMID: 18510502. 72

[159] Suzuki A, Sangani DR, Ansari A, Iwata J (2016) Molecular mechanisms of midfacial developmental defects. *Dev Dyn* 245:276–293. PMID: 26562615. 73

[160] Wilkie AOM (1994) The molecular basis of genetic dominance. *J Med Genet* 31(2):89–98. PMID: 8182727. 74

[161] Noben-Trauth K, Johnson KR (2009) Inheritance patterns of progressive hearing loss in laboratory strains of mice. *Brain Res* 1277(301):42–51. 82

[162] Brunskill EW et al. (2014) A gene expression atlas of early craniofacial development. *Dev Biol* 391(2):133–146. 88

[163] Dunwoodie SL (2009) The Role of Hypoxia in Development of the Mammalian Embryo. *Dev Cell* 17(6):755–773. PMID: 20059947. 95

[164] Risau W (1991) Embryonic angiogenesis factors. *Pharmacol Ther* 51(3):371–376. PMID: 1792240. 95

[165] Poswillo DE, Hamilton WJ, Sopher D (1972) The marmoset as an animal model for teratological research. *Nature* 239(5373). PMID: 4628135. 96

[166] Voz ML et al. (2004) Microarray screening for target genes of the proto-oncogene PLAG1. *Oncogene* 23(1):179–91. PMID: 14712223. 96, 120

[167] Wang Y et al. (2013) Opposing functions of PLAG1 in pleomorphic adenoma: a microarray analysis of PLAG1 transgenic mice. *Biotechnol Lett* 35(9):1377–85. PMID: 23690029.

[168] Kas K, Voz ML, Hensen K, Meyen E, Ven WJMVD (1998) Transcriptional activation capacity of the novel PLAG family of zinc finger proteins. *J Biol Chem* 273(36):23026–23032. PMID: 9722527. 96, 166

[169] Noden DM (1989) Embryonic origins and assembly of blood vessels. *Am Rev Respir Dis* 140(4):1097–1103. PMID: 2192642. 96

[170] Griffiths A, Miller J, Suzuki D, Lewontin R, Gelbart W (2000) *An Introduction to Genetic Analysis*. (W. H. Freeman, New York), 7th edition. 97

[171] Eppig J, Shimoyama M (2015) Guidelines for Nomenclature of Genes, Genetic Markers, Alleles, and Mutations in Mouse and Rat in *Int Comm Stand Genet Nomencl Mice*, eds. Eppig J, Shimoyama M. (The Jackson Laboratory, Bar Harbor, Maine). 97

[172] Yang MQ, Elnitski LL (2007) *Bioinformatics Research and Applications: Third International Symposium, ISBRA 2007, Atlanta, GA, USA, May 7-10, 2007. Proceedings*. (Springer Berlin Heidelberg, Berlin, Heidelberg), pp. 361–371. 99, 100, 167

[173] Banci L et al. (2012) Structural characterization of CHCHD5 and CHCHD7: two atypical human twin CX9C proteins. *J Struct Biol* 180(1):190–200. PMID: 22842048. 99

[174] Yang MQ, Elnitski L (2014) Orthology-driven mapping of bidirectional promoters in human and mouse genomes. *BMC Bioinformatics* 15(Suppl 17):S1. 100, 167

[175] Gardiner-Garden M, Frommer M (1987) CpG islands in vertebrate genomes. *J Mol Biol* 196(2). PMID: 3656447. 100

[176] UCSC Genome Browser (2009) Visel Lab Tracks. 101

[177] UCSC Genome Browser (2012) DNAse I Hypersensitivity Sites by ChIP-seq from ENCODE/UW. 101, 103

[178] Visel A et al. (2009) ChIP-seq accurately predicts tissue-specific activity of enhancers. *Nature* 457(7231):854–858. PMID: 19212405. 103, 134

[179] Crawford GE et al. (2004) Identifying gene regulatory elements by genome-wide recovery of DNase hypersentitive sites. *PNAS* 101(4):992–997. 103

[180] Alam S, Zinyk D, Ma L, Schuurmans C (2005) Members of the Plag gene family are expressed in complementary and overlapping regions in the developing murine nervous system. *Dev Dyn* 234(3):772–782. PMID: 16193498. 105

[181] Stalmans I et al. (2003) VEGF: a modifier of the del22q11 (DiGeorge) syndrome? *Nat Med* 9(2):173–82. PMID: 12539040. 108

[182] Rosenbloom KR et al. (2015) The UCSC Genome Browser database : 2015 update. *Nucleic Acids Res* 43(November 2014):670–681. 109

[183] Dreos R, Ambrosini G, P´ erier RC, Bucher P (2014) The Eukaryotic Promoter Database: expansion of EPDnew and new promoter analysis tools. *Nucleic Acids Res* 43(D1):D92–D96. PMID: 27899657. 109

[184] Karim L et al. (2011) Variants modulating the expression of a chromosome domain encompassing PLAG1 influence bovine stature. *Nat Genet* 43(5). PMID: 21516082. 117

[185] Kas K, Röijer E, Voz M, Meyen E, Van de Ven WJM (1997) A 2-Mb YAC contig and physical map covering the chromosome 8q12 breakpoint cluster region in pleomorphic adenomas of the salivary glands. *Genomics* 358(43):349–358. PMID: 9268638. 117, 146

[186] Astrom AK et al. (1999) Conserved mechanism of PLAG1 activation in salivary gland tumors with and without chromosome 8q12 abnormalities: identification of SII as as a new fusion partner gene. *Cancer Res* 59:918–923. PMID: 10029085. 118

[187] Zatkova A et al. (2004) Amplification and overexpression of the IGF2 regulator PLAG1 in hepatoblastoma. *Genes Chromosom Cancer* 39(2):126–137. PMID: 14695992.

[188] Van Dyck F et al. (2008) aP2-Cre-mediated expression activation of an oncogenic PLAG1 transgene results in cavernous angiomatosis in mice. *Int J Oncol* 32(33-40):33–40.

[189] Dotlic S et al. (2014) Extraskeletal myxoid chondrosarcoma of the vulva with PLAG1 gene activation: molecular genetic characterization of 2 cases. *Appl Immunohistochem Mol Morphol* 22(7):537–42. PMID: 24185117.

[190] Hibbard MK et al. (2000) PLAG1 Fusion Oncogenes in Lipoblastoma PLAG1 Fusion Oncogenes in Lipoblastoma. *Cancer Res* 60:4869–4872.

[191] Kandasamy J, Smith A, Diaz S, Rose B, Brien CO (2007) Heterogeneity of PLAG1 gene rearrangements in pleomorphic adenoma. *Cancer Genet Cytogenet* 177:1–5. 118, 146

[192] Heim D et al. (2014) Retroviral insertional mutagenesis in telomerase-immortalized hepatocytes identifies RIPK4 as novel tumor suppressor in human hepatocarcinogenesis. *Oncogene* 34:1–9. PMID: 24413083. 118

[193] Tang W et al. (2015) SLIT2/ROBO1-miR-218-1-RET/PLAG1: A new disease pathway involved in Hirschsprung's disease. *J Cell Mol Med* 19(6):1197–1207. PMID: 25786906. 118

[194] Nagasawa H, Miyamoto M, Fujimoto M (1973) Reproductivity in inbred strains of mice and project for their efficient production (article in Japanese). *Jikken Dobutsu* 22(2):119–126. 119

[195] Verley FA, Grahn D, Leslie W, Hamilton K (1967) Sex ratio of mice as possible indicator of mutation rate for sex-linked lethals. *J Hered* 58:285–290. 119

[196] {Van Dyck} F, Delvaux ELD, {Van De Ven} WJM, Chavez MV (2004) Modification , and Degradation : Repression of the Transactivating Capacity of the Oncoprotein PLAG1 by SUMOylation. *J Biol Chem* 279(34):36121–36131. PMID: 15208321. 120, 166

[197] Dixon JR et al. (2012) Topological domains in mammalian genomes identified by analysis of chromatin interactions. *Nature* 485(7398):376–380. PMID: 22495300. 121, 123

[198] Lupianez DG et al. (2015) Disruptions of topological chromatin domains cause pathogenic rewiring of gene-enhancer interactions. *Cell* 161(5):1012–1025. PMID: 25959774. 121, 135, 147

[199] Abu-Abed S et al. (2001) The retinoic acid-metabolizing enzyme, CYP26A1, is essential for normal hindbrain patterning, vertebral identity, and development of posterior structures. *Genes Dev* 15(2):226–240. PMID: 11157778. 122

[200] Rhinn M, Dolle P (2012) Retinoic acid signalling during development. *Development* 139(5):843–858. PMID: 22318625. 122, 148

[201] Richman JM (1992) The role of retinoids in normal and abnormal embryonic craniofacial morphogenesis. *Crit Rev Oral Biol Med* 4(93). PMID: 1333827. 122

[202] Vieille-Grosjean I, Hunt P, Gulisano M, Boncinelli E, Thorogood P (1997) Branchial HOX gene expression and human craniofacial development. *Dev Biol* 183(1):49–60. PMID: 9119114.

[203] Balmer J, Blomhoff R (2002) Gene expression regulation by retinoic acid. *J Lipid Res* 43(11):1773–1808. PMID: 12401878. 125

[204] Savory JGA, Edey C, Hess B, Mears AJ, Lohnes D (2014) Identification of novel retinoic acid target genes. *Dev Biol* 395(2):199–208. PMID: 25251699. 122

[205] Kessel M, Gruss P (1991) Homeotic transformations of murine vertebrae and concomitant alteration of Hox codes induced by retinoic acid. *Cell* 67(1):89–104. PMID: 1680565. 122

[206] Morris-Kay G (1993) Retinoic acid and craniofacial development: molecules and morphogenesis. *BioEssays* 15(1):9. PMID: 8385449. 122

[207] Quadro L et al. (1999) Impaired retinal function and vitamin A availability in mice lacking retinol-binding protein. *EMBO J* 18(17):4633–4644. PMID: 10469643.

[208] Kedishvili N (2013) Enzymology of retinoic acid biosynthesis and degradation. *J Lipid Res* 54(7):1744–1760. PMID: 23630397. 122, 124, 125, 141

[209] Jones NC, Trainor PA (2005) Role of morphogens in neural crest cell determination. *J Neurobiol* 64(4):388–404. PMID: 16041760. 122

[210] Couly G, Le Douarin NM (1990) Head morphogenesis in embryonic avian chimeras: evidence for a segmental pattern in the ectoderm corresponding to the neuromeres. *Development* 108(4):543–58. PMID: 2387234. 123

[211] Couly GF, Coltey PM, Le Douarin NM (1993) The triple origin of skull in higher vertebrates: a study in quail-chick chimeras. *Development* 429:409–429.

[212] Yoshida T, Vivatbutsiri P, Morriss-Kay G, Saga Y, Iseki S (2008) Cell lineage in mammalian craniofacial mesenchyme. *Mech Dev* 125(9-10):797–808. PMID: 18617001. 123

[213] Villanueva S, Glavic A, Ruiz P, Mayor R (2002) Posteriorization by FGF, Wnt, and retinoic acid is required for neural crest induction. *Dev Biol* 241(2):289–301. PMID: 11784112. 123

[214] Niederreither K, Vermot J, Schuhbaur B, Chambon P, Dollé P (2000) Retinoic acid synthesis and hindbrain patterning in the mouse embryo. *Development* 127(1):75–85. PMID: 10654602. 123

[215] O'Gorman S (2005) Second branchial arch lineages of the middle ear of wild-type and Hoxa2 mutant mice. *Dev Dyn* 234(1):124–131. PMID: 15861402. 123

[216] Minoux M et al. (2013) Mouse Hoxa2 mutations provide a model for microtia and auricle duplication. *Development* 4397:4386–4397. 123, 130

[217] Pasqualetti M, Neun R, Davenne M, Rijli FM (2001) Retinoic acid rescues inner ear defects in Hoxa1 deficient mice. *Nat Genet* 29(1):34–39. PMID: 11528388. 123

[218] Cox T, Camci E, Vora S, Luquetti D, Turner E (2014) The genetics of auricular development and malformation: New findings in model systems driving future directions for microtia research. *Eur J Med Genet* 57(8):394–401. PMID: 24880027. 123, 130

[219] Anders S, Huber W (2010) Differential expression analysis for sequence count data. *Genome Biol* 11(10):R106. PMID: 20979621. 124

[220] Freemantle S, Kerley J, Olsen S, Gross R, Spinella M (2002) Developmentally-related candidate retinoic acid target genes regulated early during neuronal differentiation of human embryonal carcinoma. *Oncogene* 21:2880–2889. PMID: 11973648. 125

[221] Dennis Jr G et al. (2003) DAVID: Database for Annotation, Visualization, and Integrated Discovery. *Genome Biol* 4(5):P3. PMID: 12734009. 129, 168

[222] Morriss-Kay GM, Wilkie AOM (2005) Growth of the normal skull vault and its alteration in craniosynostosis: insights from human genetics and experimental studies. *J Anat* 207(5):637–53. PMID: 16313397. 130

[223] Ewings E, Carstens M (2009) Neuroembryology and functional anatomy of craniofacial clefts. *Indian J Plast Surg* 42:S19–S34. 130

[224] Streeter G (1922) Contributions to Embryology, No. 277: Development of the auricle in the human embryo in *Contrib Embryol*. (Carnegie Institution of Washington, : Carnegie Institution of Washington; 1922.). 130, 136

[225] Marzluff W, Gongidi P, Woods K, Jin J, Maltais L (2002) The human and mouse replication-dependent histone genes. *Genomics* 80(5):487–498. PMID: 12408966. 131

[226] Izzo A, Kamieniarz K, Schneider R (2008) The histone H1 family: Specific members, specific functions? *Biol Chem* 389(4):333–343. PMID: 18208346. 131

[227] Rosin J et al. (2016) A distal 594bp ECR specifies Hmx1 expression in pinna and lateral facial morphogenesis and is regulated by Hox-Pbx-Meis. *Development* 143. 132

[228] Belyaeva OV, Lee SA, Adams MK, Chang C, Kedishvili NY (2012) Short chain dehydrogenase/reductase Rdhe2 is a novel retinol dehydrogenase essential for frog embryonic development. *J Biol Chem* 287(12):9061–9071. PMID: 22291023. 134

[229] Belyaeva OV, Chang C, Berlett MC, Kedishvili NY (2015) Evolutionary origins of retinoid active short-chain dehydrogenases/reductases of SDR16C family. *Chem Biol Interact* 234(2015):135–143. PMID: 25451586. 134

[230] Ito K, Morita T (1995) Role of retinoic acid in mouse neural crest cell development in vitro. *Dev Dyn* 204(2):211–218. PMID: 8589445. 134

[231] Goulding EH, Pratt RM (1986) Isotretinoin teratogenicity in mouse whole embryo culture. *J Craniofac Genet Dev Biol* 6(2):99–112. PMID: 3459732. 134, 148

[232] Hochedlinger K, Plath K (2009) Epigenetic reprogramming and induced pluripotency. 19168672. 134

[233] Rada-Iglesias A et al. (2012) Epigenomic annotation of enhancers predicts transcriptional regulators of human neural crest. *Cell Stem Cell* 11(5):633–48. PMID: 22981823. 134

[234] Passos-Bueno MR, Ornelas CC, Fanganiello RD (2009) Syndromes of the first and second pharyngeal arches: A review. *Am J Med Genet Part A* 149(8):1853–1859. PMID: 19610085. 135

[235] Wiley MJ (1983) The pathogenesis of retinoic acid-induced vertebral abnormalities in golden Syrian hamster fetuses. *Teratology* 28(3):341–353. PMID: 6665734. 135

[236] Poswillo D (1975) The pathogenesis of the Treacher Collins syndrome (Mandibulofacial dysostosis). *Br J Oral Surg* 13(1):1–26. PMID: 807232. 136

[237] Kastschenko N (1887) Das Schicksal der embryonalen Schlundspalten bei Sfiugetieren. *Arch für Mikroskopische Anat und Entwicklungsmechanik* 30. 136

[238] Mangold U, Dried A, Kaufmann P (1981) The gill arch development in rats and mice II. The existence of gill slits. *Acta Anat (Basel)* 110. 136

[239] Nanci A (2013) *Ten Cate's Oral Histology*. (Elsevier - Mosby), 8th edition. 136

[240] Kaufman MH, Bard JB (1999) *The Anatomical Basis of Mouse Development*. (Academic Press, San Diego, CA). 136

[241] Enlow DH (1990) *Facial Growth*. (W.B. Saunders Company), 3rd edition. 136, 144

[242] Kagurasho M, Yamada S, Uwabe C, Kose K, Takakuwa T (2012) Movement of the external ear in human embryo. *Head Face Med* 8(1):2. 136

[243] Baverstock H, Jeffery NS, Cobb SN (2013) The morphology of the mouse masticatory musculature. *J Anat* 223(1):46–60. PMID: 23692055. 136

[244] Rinon A et al. (2007) Cranial neural crest cells regulate head muscle patterning and differentiation during vertebrate embryogenesis. *Development* 134(17):3065–75. PMID: 17652354. 136

[245] Nishizaki K, Anniko M (1997) Developmental morphology of the middle ear. *Auris Nasus Larynx* 24(1):31–8. PMID: 9148725. 136

[246] Thompson H, Tucker AS (2013) Dual origin of the epithelium of the mammalian middle ear. *Science (80-)* 339(6126):1453–1456. PMID: 23520114. 136

[247] Mukherji SK et al. (1993) Evaluation of first branchial anomalies by CT and MR. *J Comput Assist Tomogr* 17(4):576–581. 137

[248] Sze RW, Paladin AM, Lee S, Cunningham ML (2002) Hemifacial Microsomia in pediatric patients: asymmetric abnormal development of the first and second branchial arch. *Am J Roentgenol* 178:1523–1530.

[249] Richter CA et al. (2010) Defects in middle ear cavitation cause conductive hearing loss in the Tcof1 mutant mouse. *Hum Mol Genet* 19(8):1551–1560. PMID: 20106873. 137

[250] Klamt F et al. (2008) Vitamin A treatment induces apoptosis through an oxidant-dependent activation of the mitochondrial pathway. *Cell Biol Int* 32(1):100–106. PMID: 17942326. 137

[251] Oliveira MRD (2015) Vitamin A and retinoids as mitochondrial toxicants. *Oxid Med Cell Longev* 120267. 137

[252] Freyer L, Aggarwal V, Morrow BE (2011) Dual embryonic origin of the mammalian otic vesicle forming the inner ear. *Development* 138(24):5403–5414. PMID: 22110056. 137

[253] Silver LM, {Adapted for the web by Mouse Genome Informatics at The Jackson Laboratory Bar Harbor ME} (2004) *Mouse Genetics: Concepts and Applications*. (Originally published by The Oxford University Press, Bar Harbor, ME). 142

[254] Vissers LELM et al. (2011) Heterozygous mutations of FREM1 are associated with an increased risk of isolated metopic craniosynostosis in humans and mice. *PLoS Genet* 7(9). PMID: 21931569. 143

[255] Veistinen L et al. (2012) Loss-of-function of Gli3 in mice causes abnormal frontal bone morphology and premature synostosis of the interfrontal suture. *Front Physiol* 3 MAY(May):1–6. PMID: 22563320. 143

[256] Moss ML (1959) The pathogenesis of premature cranial synostosis in man. *Acta Anat (Basel)* 37:351–70. PMID: 14424622. 143

[257] Richtsmeier JT, Grausz HM, Morris GR, Marsh JL, Vannier MW (1991) Growth of the cranial base in craniosynostosis. 2004097. 143

[258] Stewart RE, Dixon G, Cohen A (1977) The pathogenesis of premature craniosynostosis in acrocephalosyndactyly (Apert's syndrome). *Plast Reconstr Surg* 59(5):699–707. PMID: 850706. 143

[259] Perlyn CA et al. (2006) The craniofacial phenotype of the Crouzon mouse: analysis of a model for syndromic craniosynostosis using three-dimensional MicroCT. *Cleft Palate-Craniofacial J* 43(6):740–8. PMID: 17105336. 143

[260] Holmdahl R, Malissen B (2012) The need for littermate controls. *Eur J Immunol* 42(1):45–47. PMID: 22213045. 143

[261] Shopfner CE, Wolfe TW, O'Kell RT (1968) The intersphenoid synchondrosis. *Am J Roentgenol* 104(1). PMID: 5691615. 143

[262] Tsukamoto Y et al. (2008) Growth and development of the cranial base in mice that spontaneously develop anterior transverse crossbite. *Am J Orthod Dentofacial Orthop* 134(5):676–83. PMID: 18984401. 144

[263] Ma W, Lozanoff S (2002) Differential in vitro response to epidermal growth factor by prenatal murine cranial-base chondrocytes. *Arch Oral Biol* 47(2):155–63. PMID: 11825580. 144

[264] Gudbjartsson DF et al. (2008) Many sequence variants affecting diversity of adult human height. *Nat Genet* 40(5):609–615. 145

[265] Cho YS et al. (2009) A large-scale genome-wide association study of Asian populations uncovers genetic factors influencing eight quantitative traits. *Nat Genet* 41(5):527–534.

[266] Rubin CJJ et al. (2012) Strong signatures of selection in the domestic pig genome. *PNAS* 109(48):19529–19536. PMID: 23151514.

[267] Kemper KE, Visscher PM, Goddard ME (2012) Genetic architecture of body size in mammals. *Genome Biol* 13(244):1–13.

[268] Metzger J et al. (2013) Analysis of copy number variants by three detection algorithms and their association with body size in horses. *BMC Genomics* 14:487. PMID: 23865711. 145

[269] Koyama E et al. (1999) Retinoid signaling is required for chondrocyte maturation and endochondral bone formation during limb skeletogenesis. *Dev Biol* 208(2):375–91. PMID: 10191052. 146, 148

[270] McIntyre DC et al. (2007) Hox patterning of the vertebrate rib cage. *Development* 134(16):2981–2989. PMID: 17685480. 146

[271] Hensen K, Van Valckenborgh ICC, Kas K, Van de Ven WJM, Voz ML (2002) The tumorigenic diversity of the three PLAG family members Is associated with different DNA binding capacities. *Cancer Res* 62:1510–1517. 146, 166

[272] Rhee EJ, Nallamshetty S, Plutzky J (2012) Retinoid metabolism and its effects on the vasculature. *Biochim Biophys Acta - Mol Cell Biol Lipids* 1821(1):230–240. PMID: 21810483. 148

[273] Richtsmeier JT, Baxter LL, Reeves RH (2000) Parallels of Craniofacial Maldevelopment in Down Syndrome and Ts65Dn Mice. *Dev Dyn* 145(August 1999):137–145. 152

[274] Zheng G, Yang YC (2005) Sumoylation and acetylation play opposite roles in the transactivation of PLAG1 and PLAGL2. *J Biol Chem* 280(49):40773–40781. PMID: 16207715. 166

[275] Braem CV et al. (2002) Identification of a Karyopherin α 2 Recognition Site in PLAG1 , Which Functions As a Nuclear Localization Signal. *J Biol Chem* 277(22):19673–19678. 166

[276] Hardison RC (2000) Conserved noncoding sequences are reliable guides to regulatory elements. *Trends Genet* 16(9):369–372. PMID: 10973062. 167

[277] Ziebarth JD, Bhattacharya A, Cui Y (2013) CTCFBSDB 2.0: A database for CTCF-binding sites and genome organization. *Nucleic Acids Res* 41(D1):188–194. PMID: 23193294. 178

COLOPHON

This document was typeset using the `classicthesis` package for LaTeX 2ε developed by André Miede (https://bitbucket.org/amiede/classicthesis/). Modifications were made to Table of Contents, header, figure formatting, and reference management. The BibTeX style file `pnas2011.bst` was modified to include PubMed ID and links, when available.

Final Version as of December 19, 2016 (`classicthesis`).